Optical probing of thermodynamic parameters and radical production in cavitating micro-flows

Darjan Podbevsek

N°d'ordre NNT :
2018LYSE1210

THESE de DOCTORAT DE L'UNIVERSITE DE LYON
opérée au sein de
l'Université Claude Bernard Lyon 1

Ecole Doctorale Nº52
École Doctorale de Physique et Astrophysique de Lyon

Spécialité de doctorat : **Physique**

Soutenue publiquement le 18/10/2018, par :
Darjan Podbevšek

Optical probing of thermodynamic parameters and radical production in cavitating micro-flows

---

Devant le jury composé de :

FERRIGNO Rosaria, PU, Universite Lyon 1	Président
DANTELLE Géraldine, CR CNRS, Université de Grenoble	Rapporteure
DULAR Matevž, Professor, University of Ljubljana	Rapporteur
CAUPIN Frédéric, PU, Universite Lyon 1	Examinateur
FARHAT Mohamed, Lecturer, Ecole polytechnique federale de Lausanne	Examinateur
LEDOUX Gilles, DR CNRS, Universite Lyon 1	Directeur de thèse
AYELA Frédéric, PU, Université Grenoble Alpes	Invité
DEMESSENCE Aude, CR CNRS, IRCELYON	Invitée

UNIVERSITE CLAUDE BERNARD - LYON 1

Président de l'Université	**M. le Professeur Frédéric FLEURY**
Président du Conseil Académique	M. le Professeur Hamda BEN HADID
Vice-président du Conseil d'Administration	M. le Professeur Didier REVEL
Vice-président du Conseil Formation et Vie Universitaire	M. le Professeur Philippe CHEVALIER
Vice-président de la Commission Recherche	M. Fabrice VALLÉE
Directeur Général des Services	M. Alain HELLEU

COMPOSANTES SANTE

Faculté de Médecine Lyon Est – Claude Bernard	Directeur : M. le Professeur J. ETIENNE
Faculté de Médecine et de Maïeutique Lyon Sud – Charles Mérieux	Directeur : Mme la Professeure C. BURILLON
Faculté d'Odontologie	Directeur : M. le Professeur D. BOURGEOIS
Institut des Sciences Pharmaceutiques et Biologiques	Directeur : Mme la Professeure C. VINCIGUERRA
Institut des Sciences et Techniques de la Réadaptation	Directeur : M. le Professeur Y. MATILLON
Département de formation et Centre de Recherche en Biologie Humaine	Directeur : Mme la Professeure A-M. SCHOTT

COMPOSANTES ET DEPARTEMENTS DE SCIENCES ET TECHNOLOGIE

Faculté des Sciences et Technologies	Directeur : M. F. DE MARCHI
Département Biologie	Directeur : M. le Professeur F. THEVENARD
Département Chimie Biochimie	Directeur : Mme C. FELIX
Département GEP	Directeur : M. Hassan HAMMOURI
Département Informatique	Directeur : M. le Professeur S. AKKOUCHE
Département Mathématiques	Directeur : M. le Professeur G. TOMANOV
Département Mécanique	Directeur : M. le Professeur H. BEN HADID
Département Physique	Directeur : M. le Professeur J-C PLENET
UFR Sciences et Techniques des Activités Physiques et Sportives	Directeur : M. Y.VANPOULLE
Observatoire des Sciences de l'Univers de Lyon	Directeur : M. B. GUIDERDONI
Polytech Lyon	Directeur : M. le Professeur E.PERRIN
Ecole Supérieure de Chimie Physique Electronique	Directeur : M. G. PIGNAULT
Institut Universitaire de Technologie de Lyon 1	Directeur : M. le Professeur C. VITON
Ecole Supérieure du Professorat et de l'Education	Directeur : M. le Professeur A. MOUGNIOTTE
Institut de Science Financière et d'Assurances	Directeur : M. N. LEBOISNE

Acknowledgments

First and foremost, I would like to thank my thesis director and mentor, Gilles Ledoux. He was always available for discussion, helpful advice or just listening to ideas, sorting the good ones from the bad ones. With his knowledge, patience and willingness to help, he creates around him a nurturing environment for his students and interns. I'm glad I was a part of this environment. It was truly a pleasure working with and learning from you.

I would also like to extend my gratitude to the number of experts in the jury, donating their time to engage in and evaluating our work. Special acknowledgments should go to dr. Dantelle and prof. Dular for evaluating the manuscript and of the jury.

I would like to thank both all the collaborator teams I had the pleasure to work with: Oleksandra and dr. Demessence from IRCELyon, dr. Martini and Huong form FENNEC team at ILM, prof. Ayela and dr. Colombet from LEGI Grenoble. I think our work shows how fruitful interdisciplinary studies can be.

A very big thank you must go out to the mechanics, Yann, Jean-François, and Valentin, for the continuous help throughout the thesis, as different experimental setups were evolving. On the same line, thanks going out to Jean-Marc and Pierre and the rest of the electrical department.

Upon my arrival to the Luminescence team, the other doctoral students were just finishing, leaving me without counterparts in the team. To may rejoice, the following year Gaetan, Justine and Quentin started their PhD's with the team, followed the year after Amira. Thanks for livening things up in the office and in fact the institute with the TeamDoc activities. Next ski trip is in Slovenia!

I also appreciate the working conditions within the team, everybody always willing to help and add their expertise if needed. Thank you, Christophe, for maintaining a positive team spirit, making the luminescence team an enjoyable working environment. Thank you, Benoit for countless discussions, when chemicals were misbehaving, you could always run to the team chemist. Et aussi de m'encourage d'utiliser Français plus fréquent que possible. Also, K Kheirredine and Guillaume for frequent help on sapphire related topics.

Clement, Marin and Valentin, I hope you enjoyed your respective internships in our team. Teaching was a new and pleasant experience for me.

Additional thanks to Christophe from Nanoptec and the people from the Cecomo platform for the technical support and the ILM internal call project, allowing me to pursue the “tension cell” project, listed in perspectives. Extending the thanks to the liquid and interphase team for the use of the high-speed camera equipment.

Finally, I would thank my family for supporting throughout my studies up to and during the thesis. My mother Jelka and grandmother Stanislava, helping me focus in times of hardship and my grandfather Silvester for being my encyclopaedia of knowledge since young age. To my girlfriend Alja, who inspired, advised and motivated since the day we met.

The following thesis is dedicated to my brother, Peter Mahne, who succumbed to illness, during my time abroad.

Mesure optique de paramètres thermodynamiques et production de radicaux dans des micro-écoulements cavitants

Les microcanaux sont des outils précieux pour étudier la dynamique des fluides. Une réduction de taille dans un micro-canal va accélérer localement le liquide ce qui, d'après la loi de Bernoulli, va créer une dépression locale. Si la pression tombe sous la pression de vapeur, le liquide passera dans une zone métastable où pourront éventuellement apparaître des bulles de vapeur. Ces bulles apparaissent dans la zone de faible pression et vont imploser violement plus loin lorsque les conditions de pression redeviennent standard. Ceci génère une zone d'écoulement bi-phasique au-delà de la constriction. A cause de la chaleur latente liée à la transition de phase, on s'attend à trouver des gradients de température dans les zones où les bulles apparaissent ou implosent. En ajoutant des sondes fluorescentes dans le liquide il est possible d'utiliser des techniques optiques pour extraire des informations locales sur l'écoulement. La température est ainsi mesurée en chaque point via le spectre de luminescence, qui dépend de la température, des colorants. La méthode utilisée est nommée mesure par intensité ratiométrique et permet d'être insensible aux variations d'intensité de la luminescence provoqués par des variations de concentrations dues à la présence de bulles dans le milieu bi-phasique.

Afin de protéger les colorants de l'implosion violente des bulles, ceux-ci sont encapsulés dans une coque pour former une nanoparticule hybride. Les colorants ont été choisis pour, d'une part, leur compatibilité chimique avec la coque et, d'autre part, pour leur luminescence rapide (quelques nanosecondes) indispensable compte tenu de la vitesse du fluide (20-40 m/s). En effet cette vitesse implique un temps de résidence dans le volume optique d'excitation très court (dizaine de nanosecondes). La coque est constituée de polysiloxane qui protège le colorant et qui permet d'éviter toute agglomération *via* une fonctionnalisation de la surface. Le cœur de la particule est lui constitué d'or qui permet une plus grande densification du polysiloxane ce qui protège les fluorophores des attaques chimiques. La taille limitée (60nm de diamètre) des particules permet une thermalisation rapide et, si la concentration n'est pas trop importante, une absence de modification des propriétés rhéologiques du fluide.

Comme nous étudions un écoulement stationnaire, on peut déterminer la température locale à partir de la spectroscopie mesurée en un point avec des accumulations longues. Cette spectroscopie effectuée à l'aide d'un microscope confocal, qui comprend un filtre spatial, permet de définir un volume d'observation limité dans les trois directions de l'espace. En balayant ce volume d'observation on produit des cartographies thermiques de l'écoulement en 2 et 3 dimensions. D'autre part comme les sondes ne vont pas dans la phase vapeur, l'information d'intensité donne aussi une indication sur la quantité de vapeur, en chaque point, dans l'écoulement.

Une étude paramétrique des gradients de température générés derrière la constriction a été effectuée en fonction des paramètres géométriques des microcanaux. La dynamique de l'écoulement ainsi que l'influence de la pression d'entrée et de la température du liquide entrant ont été étudiés. Les températures mesurées dans les zones de refroidissement du fluide bi-phasique sont plus importantes que prévues suggérant que la technique utilisées est peut-être plus sensible à la couche limite thermique entourant les bulles en expansion. Une technique de thermométrie complémentaire a été utilisée, basée sur la spectroscopie Raman, et a confirmé ce résultat dans le cas de l'isopropanol.

Dans l'idée de pouvoir aussi mesurer la pression par des voies optiques, une nouvelle famille de matériaux luminescents ont été testés. Il s'agit de polymères de coordination à base de thiolates de métaux précieux (or, argent et cuivre). Des études de luminescence en fonction de la température et de la pression ont été effectuées afin de comprendre l'origine de celle-ci et afin d'évaluer leurs potentiels en tant que sonde luminescentes.

Enfin, nous avons cherché à évaluer la quantité de radicaux produits dans les microcanaux cavitants, là aussi par des méthodes optiques. En effet la formation de radicaux est souvent observée lors de l'étude de la cavitation et est souvent associée aux conditions extrêmes observées lors de l'implosion des bulles. Afin de quantifier la production des radicaux, nous avons utilisé la réaction bien connue de chimiluminescence du luminol avec $^{\bullet}OH$ et observée celle-ci dans les microcanaux par une méthode de comptage de photons. En plaçant un photomultiplicateur au plus près de la zone cavitante du microcanal et en collant un microphone afin de synchroniser les mesures avec les périodes de cavitation, nous avons pu corréler le signal sonore avec le signal de chimiluminescence. Une relation linéaire entre la pression d'entrée et le taux de production de photons a été mis en évidence et ce pour tous les microcanaux testés. Une amélioration de la

technique a permis ensuite de cartographier la production de radicaux au sein des microcanaux. Le maximum de production correspond à la zone d'implosion des bulles de cavitation. Cette technique simple pourrait être étendue afin d'optimiser les taux de production de réacteurs de cavitation en jouant sur leurs géométries et les paramètres d'écoulements.

Contents

List of abbreviations

ABS	– Absorption
AC	– Acoustic cavitation
AOP	– Advanced oxidation processes
CARS	– Coherent anti-Stokes Raman spectroscopy
CL	– Chemiluminescence
CNT	– Classical nucleation theory
CRET	– Chemiluminescence resonance energy transfer
CT	– Charge transfer
FL	– Fluorescence
FRET	– Forsters or fluorescence resonance energy transfer
FTC	– Fluorescence thermographic camera
HC	– Hydrodynamic cavitation
HIFU	– High intensity focused ultrasound
HOMO	– Highest occupied molecular orbit
IC	– Internal conversion
ISC	– Intersystem crossing
LCL	– Luminol chemiluminescence
LUMO	– Lowest unoccupied molecular orbit
LWD	– Long working distance (objective)
MBSL	– Multi bubble sono luminescence
PHO	– Phosphorescence
PMT	– Photomultiplier tube
QY	– Quantum yield
RIM	– Ratiometric intensity measurement
RPE	– Rayleigh-Plesset equation
S/AS	– Stokes/anti-Stokes
SBSL	– Single bubble sono luminescence
SL	– Sonoluminescence
SNR	– Signal to noise ratio
S-RIM	– Stokes-Ratiometric intensity measurement
TBD	– Thermal boundary layer
VIB	– Vibrational relaxation

1. General introduction

In the following thesis, the focus of our study is cavitation and its affiliated phenomena, probed by various light-based measurement techniques. The introduction serves as an overview of the problematic, referring the reader to the specific sub-chapter for a detailed theoretical discussion. A per chapter orientation is given at the end.

Similar to the well-known boiling process, cavitation is a phase change transition from liquid to vapor, occurring when the pressure in the liquid falls below liquid vapor pressure, allowing the formation of vapor bubbles. These bubble formations lay at the origin of the name, as the first attempts to describe the phenomenon, "*cavities"* were observed forming in the liquid. In the engineering field the term cavitation is often used to describe formation and activities of the vapor bubbles in a liquid.

During the growth phase the bubble expands, increasing the interface, lowering surface tension thus facilitating the phase transition. An intense rapid pressure gradient will lead to non-linear effects and an explosive bubble growth. The energy for the transition is acquired from the heat of the surrounding liquid and stored in the vapor phase as latent heat. When the pressure normalizes, the situation is reversed, initiating compression of the bubble content and condensation on the interface. As the bubble interface diminishes, condensation is hindered and the accumulated energy is focused on the bubble content. In the last phase of the collapse, nonlinearities from the increasing surface tension accelerates the implosion, which can lead to an adiabatic bubble collapse with extreme thermodynamic conditions reached. This event is the cavitation bubble collapse, which is responsible for many beneficial and also undesirable side effects of cavitation.

The name given to specific cavitation classifications is based on the bubble excitation source and can be roughly divided into acoustic and hydrodynamic cavitation. The former uses the pressure oscillations of ultrasound to periodically induce cavitation events, and the latter is formed due to Bernoulli's principle; pressure decrease in a flow constriction due to flow acceleration.

Hydrodynamic cavitation is the focal phenomenon under study. The use of special formulated microchannels allows for cavitating conditions to be observed at the microscale. These channels

are a phenomenal tool to observe hydrodynamic phenomena in an environment, where due to their inherent micro dimensions, surface effects can start to dominate over volume effects.

A further benefit of microfluidics is the inherent low fluid consumption, allowing for specialised fluids to be used. The specialized fluids in our case refers to nano fluids, where the liquid is seeded with luminescent nano particles, without perturbing its inherent properties. These particles can then be used to yield information about the local environment in the liquid under study, by the use of optical probing. Luminescence thermometry uses a ratiometric technique to obtain temperature information from the emitted spectrum of the nano probes, in a non-intrusive manner. An alternative thermometry method uses the Raman scattering signal to yield the local temperature information. Both techniques can be coupled with a confocal microscope setup, which enables a confined acquisition volume, allowing 2D or even 3D mapping of the temperature in the micro-cavitating flow.

Another aspect of cavitation bubble collapse is the formation of chemical species in the extreme thermodynamic conditions of the bubble collapse. This is a well-known phenomenon for the periodic bubble events of acoustic cavitation used for sono-chemical reactions. However, it is less well known for hydrodynamic cavitation. Replacing the working fluid with an aqueous solution of luminol, which has a chemiluminescent reaction with the produced radicals, allowed us to quantify the radical production rate. This is done by a photon counting technique, as the chemiluminescent reaction will produce a photon per reaction with a radical.

In chapter 2 the theoretical discussion on cavitation is performed from nucleation to the effects of bubble collapse. We touch the main mechanisms and effect for which cavitation is known and used for. Hydrodynamic cavitation and microfluidic is further discussed. After the theoretical introduction our microfluidic experimental setup is described, followed by the characterization of the channels used in the thesis.

Chapter 3 starts with an overview on light matter interactions, with a focus on photoluminescence. The relevant radiative and nonradiative relaxation mechanism following photon absorption are discussed. The concept of using luminescence to probe the local environment is introduced. Experimental setups for characterising luminescent materials at different temperatures and pressures are presented, followed by a study on specific luminescent materials, for the purpose of

evaluating their suitability as a temperature or pressure probes. Lastly, the temperature sensitive luminescent nano probes forming our nano liquid suspensions are described.

Next, chapter 4 includes a short discussion on the thermal effect and temperature gradients expected in micro cavitating flows. The achromatic confocal microscope setup is explained along with the luminescence thermometry technique and the data analysis. A parametric study on several channels is performed, varying the driving pressure and liquid temperature. A discussion on 3D effects in the channel is also presented. Attempts to explain the results are found in the discussion. The second part is dedicated to the Raman scattering based thermometry techniques. After the explanation of the experimental setup, results confirming the observed trends with the luminescence-based technique are presented and discussed.

Chapter 5 starts with the discussion on the cavitation bubbles as high-temperature and high-pressure reactors. Radical production mechanism of the collapsing bubbles is described. Chemiluminescence and luminol are discussed in terms of the luminol chemiluminescnent reaction with the produced radicals. The experimental technique used is presented and the results on the radical quantification are also shown and discussed. An expansion on the idea, allowing for mapping of the chemiluminescent signal in the microchannel is shown as well. The data is compared to the data from chapter 4 and discussed.

Chapter 6 contains the general conclusions, summing up the study, while chapter 7 briefly presents the perspectives. These are the suggestions for the continuation and some unfinished side project related to the topic. First is a novel single bubble excitation method, second is the luminescence thermographic camera and the last a chemiluminescence enhancement technique.

2. Hydrodynamic cavitation in microfluidics

2.1. Cavitation

Cavitation is a phase transition phenomenon from liquid to vapor and its subsequent return to liquid phase, due to the environmental pressure decreasing below vapor pressure and later recovering to ambient pressure. In the engineering field the term is often used to describe formation and activities[1] of the bubbles in a liquid [2]. These are the bubble inception and growth of the bubble in low pressure regions and much more so the phenomena associated with the energetic bubble collapse (Figure 2.1), such as cavitation erosion and cavitation noise [1]. The latter is due to rapid spherical bubble collapse forming shock waves, whereas the former is thought to be a complex interaction of spherical and non-spherical bubbles collapsing near a surface and forming very fine, but energetic jets in combination with shock waves, which can erode even the hardest materials in use for hydraulic applications [3].

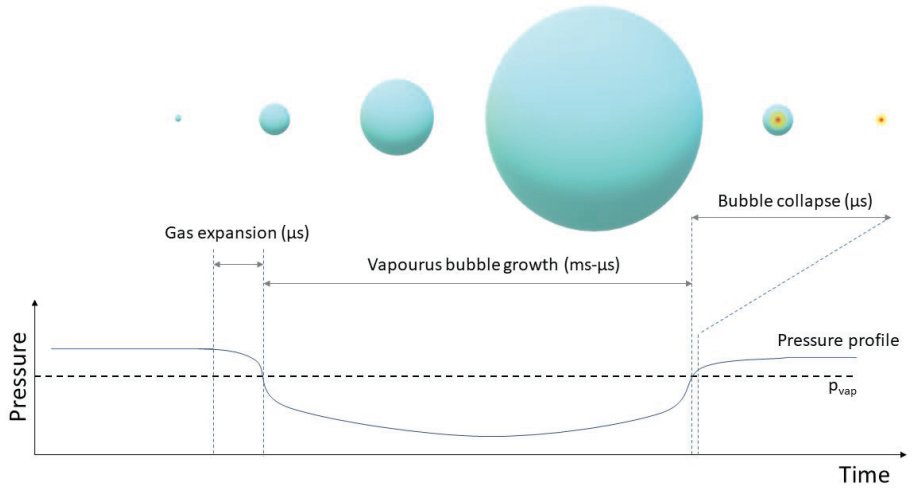

Figure 2.1 - Image of bubble growth and collapse (vs pressure) with typical bubble collapse phenomena.

First encountered by Huygens in his experimental observations of negative pressure in liquids in 1662 and reported in 1672 [4]. He observed that the tension in the liquid is maintained until a bubble (nuclei) is introduced. Soon after in 1704 it was reported by Isaac Newton [5], in his work Optics as: "*rings appearing in water between a plane surface and a convex lens, when the latter*

[1] Due to the two-phase flow, the efficiency of hydraulic machinery is reduced [1].

was rotated". Unknown to him at the time, these were gas bubbles appearing and expanding due to the low pressure region formed between the rolling surfaces [2]. First interests into the unknown process coincided with the growing popularity of the screw propeller in steam ships around the turn of the 20th century. The first investigations of the process were indeed fuelled by the need to understand the efficiency decrease that could occur in certain circumstances on such ships. It was found that the water under the extreme conditions of fast spinning propeller encountered such stress that it was torn apart[2], causing vapor bubble to appear. This was also the first time the phenomenon was assigned the name cavitation[3], as the observed bubbles were called cavities at the time.

The bubble growth expands the liquid-vapor interface, easing the subsequent phase transition as the breaking surface tension force is decreased. These leads to an accelerating non-linear growth, called the explosive bubble growth [7]. The transition to vapor requires the breaking of the cohesive forces in liquid state and can consume a lot of energy. This energy is provided by the surrounding liquid, which consequently undergoes cooling. The situation is reversed at bubble collapse, where the interface shrinks and hinders condensation. For a rapid bubble implosion, this can lead to some of the vapor being trapped by the shrinking interface, thus exposing it to the extreme thermodynamic conditions at the bubble collapse [8]. The energy of vaporisation (latent heat) is deposited on a much smaller number of molecules than the number vaporized beforehand. In a slow transition the balance would be null, as condensation and thermalization could unfold, however due to the inherent fast dynamics of the interface, the bubbles have a built-in mechanism for **energy focusing**. This property has beneficial and adverse effects, prompting research to mitigate or intensify cavitation processes, respectively.

Since the early interest springing from hydrodynamics, cavitation research has flowered, ranging from fundamental to applicative, due to interest in various independent fields:

- hydraulic machinery (efficiency, noise and cavitation erosion) [9],
- waste water treatment (viral [16], microbial [17], chemical treatment [18]) advance oxidising processes (pharmaceutical waste) [19].

[2] Cohesive intermolecular forces of the liquid are overome to produce vapor.
[3] The name suggested by R. E. Froude, and first cited in Barnaby and Thornycroft work on "Torpedo-boat destroyers" [6].

- chemical engineering, Sonochemistry [10], and cleaning [11], sonoluminescence and plasma research [12], [13], process intensification (emulsification [14], transesterification of biodiesel [15]),
- biomedical studies (lithotripsy[4], contrast enhancement in imaging, therapeutics [20])
- biological studies (xylem in vascular plants [21], mantis shrimp [22], limiting velocity of tuna and dolphin [23]),
- food [24] and beverage [25] processing,
- naval applications (ship propeller design [26], super-cavitating torpedo [27], hydrofoil design [28]),
- geology (coastal erosion) and hydrology [29],

Essentially, cavitation is often encountered when studying liquid dynamics as the limiting factor; as the liquid is pushed to their physical limit and the cohesive forces of the liquid are overcome.

Indeed, for the most part, studies into cavitation were of preventative nature, since it is one of the more notable limitations in hydraulic machinery design. Due to real-life conditions, often the working fluid parameters cannot be controlled, prompting applicative studies mostly directed to flow geometries optimisation.

However, with time beneficial effects were identified, such as sonochemistry, waste water treatment and various medical procedures. Sonochemistry has indeed become a field of its own. Here the bubble acts as a high pressure and temperature reactor, producing species which are hard or impossible to produce at ambient conditions (chapter 5.1). Fundamental research into cavitation bubbles has peaked around the turn of the century, when indications of nuclear fusion reactions in the collapsing bubble were driving investigations of the thermodynamic conditions during the collapse phase [12]. Although, yielding much important information about the peak bubble collapse temperatures [30] and pressures [31] from sonoluminescence, there has yet to be a clear demonstration of nuclear fusion in the bubble implosions[5].

In terms of driving mechanism, cavitation can be divided into tension (hydrodynamic - HC, acoustic - AC) or energy deposition induced [2]. The latter occurs when a large energy flux

[4] Triturating of kidney stones with ultrasonic cavitation.
[5] Author claiming nuclear fusion [32], later shown to be irreproducible [33] and controversial [34].

(photons [35], neutrons [32], protons [36]) is focused in the liquid, driving the nucleation and growth of a vapor bubble[6]. In most real-world situations, the cavitation we encounter is tension induced (inertial), as focused energy sources aren't common in Nature.

Fundamentally, the liquid vapor pressure is the parameter responsible for driving the phase transition. Although seemingly very different, the comparison to boiling is apt. From the bubble dynamics viewpoint, it's the same if the ambient pressure drops below the saturation vapor pressure (cavitation) or the vapor pressure is raised due to a temperature increase (boiling). One could say, from a thermodynamic terminological stance, they are both limiting cases, cavitation an isothermal and boiling an isochoric process. However, in practise boiling is often limited by the heat transfer rate to the liquid, making it a relatively slow process. Cavitation on the other hand, is driven by the density fluctuations (inertia) if the liquid, therefore it is often a much faster and a more violent process.

Nucleation and cavitation threshold

In this subchapter we will generally discuss the liquid (water) vapor transition, unless otherwise stated. Homogeneous and heterogeneous nucleation and the cavitation threshold are discussed as relevant parameters for cavitation. A thermodynamic phase will have a uniform physical property throughout, however the phase transfer (appearance of a new phase) will usually cause an abrupt (discontinuous) change in these properties.

Nucleation is the appearance of a new phase in the medium, being stochastic in its nature. Usually expressed either as the characteristic times one has to wait for the first appearance of a new phase or it's inverse - the nucleation rate - Γ, which can be calculated by the classical nucleation theory (CNT).

$$\Gamma = \Gamma_0 \exp\left[-E_b / (k_B T)\right] \tag{2.1}$$

A succinct summary of the theory of nucleation and its formula relevant to the topic of the thesis is below and is summarized from [37]. Homogeneous nucleation is produced by voids (density fluctuations) spontaneously springing up in the liquid due to thermal fluctuations (k_BT)[7]. At this

[6] A vapor bubble is created by boiling, which collapses forming a shock wave driving the cavitation events [35].
[7] Characterised by the thermal energy - k_BT.

stage there is a competition between surface effects[8] and volume effects (eq 2.2), the former hindering (Gibbs free energy - G↑) and the latter promoting growth (G↓).

$$E(R) = \underbrace{\frac{4\pi R^3}{3}(P - P_{sat})}_{volume\ \ term} + \underbrace{4\pi R^2 \sigma}_{surface\ \ term} \tag{2.2}$$

$$E_b = (16\pi\sigma^3) / \left[3(P_{sat} - P)^2\right] \tag{2.3}$$

$$R_c = 2\sigma / (P_{sat} - P) \tag{2.4}$$

Since one scales as an area term (R^2) and the other as a volume term (R^3) there is a R value at which the volume overcomes the surface term – critical radius (R_c) (Figure 2.2). Therefore, the voids that will overcome the energy barrier (eq. 2.3) associated with the interfacial free energy (E_b) are the ones that form the nuclei, the rest simply re-dissolve. These are the nuclei that increase beyond the critical radius (eq. 2.4), forming vapor bubbles.

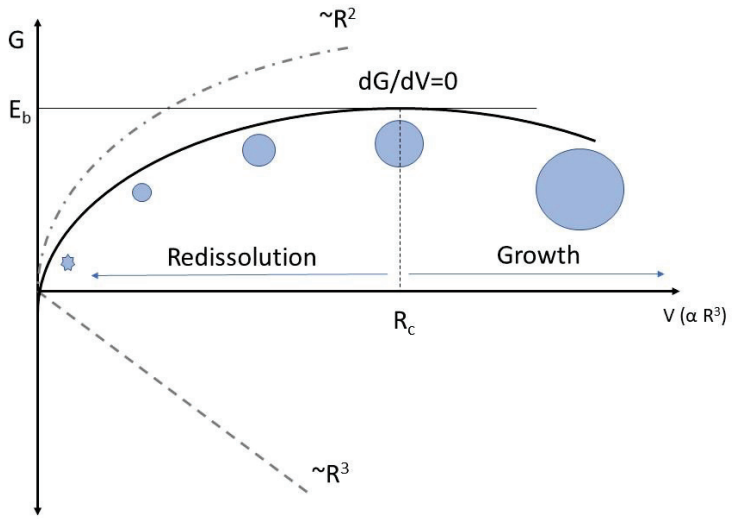

Figure 2.2 - Gibbs free energy in relation to nuclei volume – competition between surface and volume term, illustrating the energy barrier and critical radius of the nuclei in the nucleation theory.

[8] Surface tension – σ.

The coexistence of two phases can exist on a well-defined line on the thermodynamic diagrams, (Figure 2.3) called the binodal line; straying away from this line, one of the phases would be preferential. However, the interfacial energy (surface tension) allows the so called metastability, where the initial phase can go beyond the binodal line (metastable region) and exist there for a finite amount of time, before nucleation occurs [37]. The lifetime decreases with the deviation from the binodal, down to the spinodal limit (spinodal). The basic rule when dealing with phase transitions warrants the equilibrium of Gibbs free energy per mass between the two phases[9].

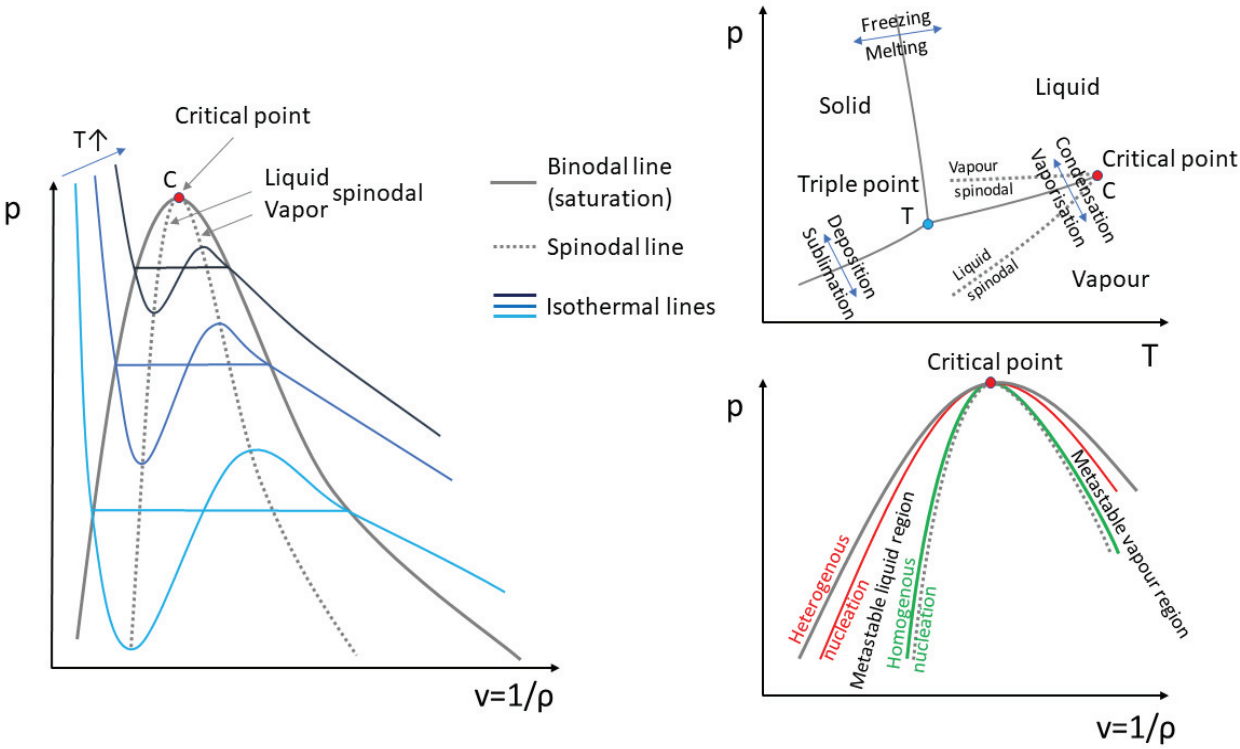

Figure 2.3 - Water phase diagram, with binodal and spinodal lines.

Nucleation tends to be very sensitive to inhomogeneities (impurities) in the metastable phase. When an ultra-pure (homogeneous) liquid is subjected to tensional stress, it can warrant a phase transition (Gibbs free energy equilibration). The theoretical tensile strength of very pure water is believed to be about -140MPa at 25ºC (experimentally shown with isochoric cooling of ultrapure water in quartz inclusions [38], [39]), due to the high density of the cohesive bonds (hydrogen

[9] Energy balance between the phases required to reach a equilibrium (static case). If there is an inequality, there will be dynamics of the surface until an equilibrium is obtained.

bond network) in water. This would mean that **homogeneous nucleation** is very hard to induce. A large body of work deals with observations of water under tension, attempting to probe several unexplained anomalies of water [39]–[45], which is beyond the scope of the discussion here.

$$p_b = \sigma\left(\frac{1}{R_1} + \frac{1}{R_2}\right) \xrightarrow[R_1 = R_2]{\text{spherical bubble}} \frac{2\sigma}{R_b} \tag{2.5}$$

However most real liquids are far from the homogeneous perfect liquid. They contain impurities or nuclei, either in the form of undissolved gas bubbles or solid particles. These nuclei can drastically lower the tensile strength of the liquid, thus enabling **heterogeneous nucleation**. Essentially, they are a weakness in the continuum (analogous to a crack in solid material) or in other terms, they will lower the energy barrier needed to be overcome to make the phase transition.

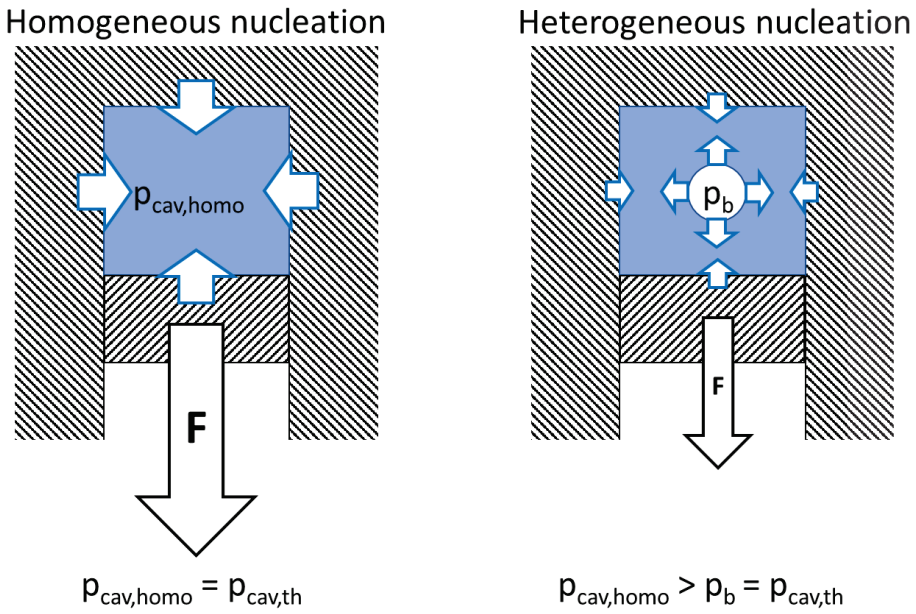

Figure 2.4 - A simplified schematic of the homogeneous and heterogeneous nucleation in a liquid under tension.

In a liquid-vapor system the interfacial free energy is essentially the surface tension, i.e. the force trying to reduce the interface area. By the Young-Laplace law (eq. 2.5), the pressure induced in the bubble will be inversely proportional to the curvature of the interface, meaning that small bubbles will have a high internal bubble pressure. For the case of water, the surface tension σ = 72mN/m and a bubble radius of 100nm, the internal bubble pressure would be ~15bar and ~150bar

for a 10nm bubble. This is in fact the pressure needed to be overcome to start the bubble expansion – nucleation. Going to the few nm scale, the bulk surface tension value can't be assumed constant and this kind of simple model fails to predict accurately the internal pressure [44], however we can still see that it approaches the theoretical values for homogeneous nucleation[10]. Therefore, the cavitation threshold will be proportional to the nucleation bubble radius, via the surface tension (Figure 2.4 and eq.2.5), reducing the forces needed to grow the bubble with the bubble radius. Big nuclei of 10μm will have only about 0,14bar of internal pressure[11]. It is clear then, that a liquid containing nuclei beyond a certain size is effectively unable to withstand any tensional stress and cavitates when the saturated vapor pressure is reached.

Several articles, overviewing cavitation nuclei in water were published by K.A. Morch [46]–[48]. As discussed above, the first suspect for lowering the tension strength of the liquid would be a free-flowing bubble. This would introduce an interface into the system, lowering the energy boundary needed for phase transitions and facilitating the phase change. They are known to be abundant in many real liquids, however in practice these bubbles would have the tendency to either dissolve in the liquid or be removed by buoyancy when becoming too big. A stabilising mechanism was proposed; where a layer of organic impurities (for example fatty acid) starts depositing at the interface of the gas bubble. As the bubble slowly dissolves, the layer starts to encompass it forming a boundary layer preventing further dissolution of the bubble content [49]. This process has two effects; it stabilises small gas bubbles (small enough to be neutrally buoyant), preventing further mass exchange and also neutralising the surface tension caused by the dangling bonds at the water gas interface (polar heads) by interacting with the polar "head" of the amphiphilic molecules. The stabilisation effect seems even more valid for solid particles, that can act as gas trapping sites as is suggested by the so-called crevice model [50]. It is generally accepted that this model is responsible for the low tensile strength of water. This is where a bubble is trapped by a concave crevice on a surface in contact with the liquid. The crevice could be on the boundary walls or on free-flowing particles (Figure 2.5).

From the stated above, we can see that the nuclei concentration and size will play an enormous role in the liquid susceptibility to nucleation and cavitation bubble growth.

[10] 1nm → ~1500bar ≈ $p_{cav,homo}$ = -140MPa = 1400bar [38]
[11] In addition to the ambient pressure.

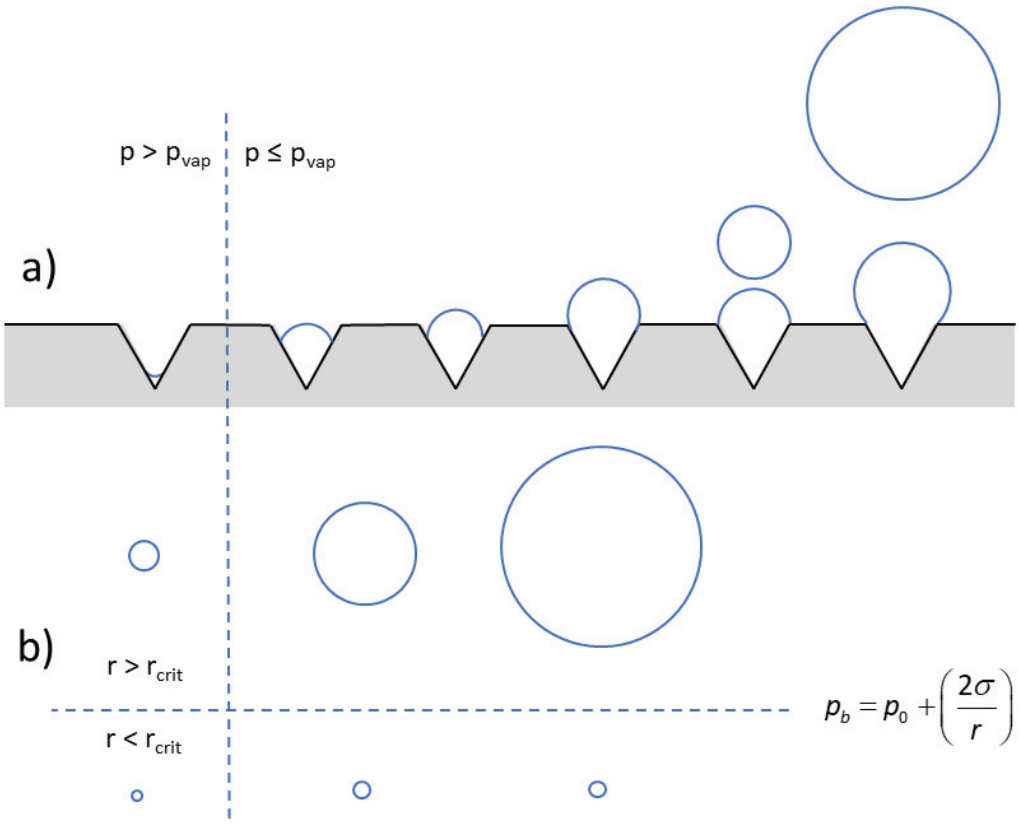

Figure 2.5 - Bubble growth mechanisms after exposure to pressures below vapor pressure. a) crevice model; solid surface harbouring a pocket of gas, b) free gas nucleation bubble – below and above the critical radius. p_b is the bubble internal pressure and p_0 the ambient liquid pressure.

2.1.1. Bubble dynamics

Describing the bubble interface dynamics has always been at the core of cavitation studies. An accurate model would allow a theoretical prediction of the thermodynamic parameters inside the collapsing cavity, which can help explain phenomena and optimise different cavitation processes. However due to the nonlinear nature of the dynamics, the governing equations are not fully solvable [51]. First attempts to describe the motion of a collapsing empty cavity was made by Besant in 1859, deriving it from Bernoulli's theorem [52] (eq.2.6). As was stated by the author, describing the bubble collapse:

"An infinite mass of homogeneous incompressible fluid acted upon by no forces is at rest, and a spherical portion of the fluid is suddenly annihilated; it is required to find the instantaneous alteration of pressure at any point of the mass, and the time in which the cavity will be filled up, the pressure at an infinite distance being supposed to remain constant."

So, starting with an empty cavity (no mass) in an infinite liquid, all the parameters should be based on the only special parameter r (distance from centre of cavity). Considering a spherical bubble in an infinite liquid, at a homogeneous pressure P_∞ and T_∞. The dot notations signify a time derivative; r is referring to the radius from the centre of the bubble while R is the radius of the bubble (interfacial parameters in capital, lower case for general parameters - Figure 2.6). Also, the liquid is incompressible (ρ=constant) and no mass transfer is supposed over the interface.

Due to laws of mass conservation, the fluid velocity is subject to the inverse square law, making it inversely proportional to the square of r [2]:

$$\frac{\dot{r}}{\dot{R}} = \frac{\frac{1}{r^2}}{\frac{1}{R^2}} \rightarrow \dot{r}(r,t) = \frac{R^2\dot{R}}{r^2} \tag{2.6}$$

Considering the bubble interface is undergoing pure radial motion (irrotational) the velocity potential is [53]:

$$\phi = \int_r^\infty \dot{r}dr = -\frac{R^2\dot{R}}{r} \tag{2.7}$$

Then the bubble motion can also be derived from Bernoulli's principle (special case of Navier-Stokes equation) since the same assumptions hold for both:

$$\underbrace{\frac{P-P_\infty}{\rho} = -\frac{\partial\phi}{\partial t} - \frac{\dot{r}^2}{2}}_{\frac{v^2}{2}+\psi+\frac{p}{\rho}=const} = \frac{2R\dot{R}^2 + R^2\ddot{R}}{r} - \frac{R^4\dot{R}^2}{2r^4} \xrightarrow[at\ interface]{r=R} R\ddot{R} + \frac{3\dot{R}^2}{2} = \frac{P_L - P_\infty}{\rho} \tag{2.8}$$

Where pressure P is the pressure in the liquid at liquid density ρ ($P=P_L$) and P_∞ the pressure at infinity (far field pressure).

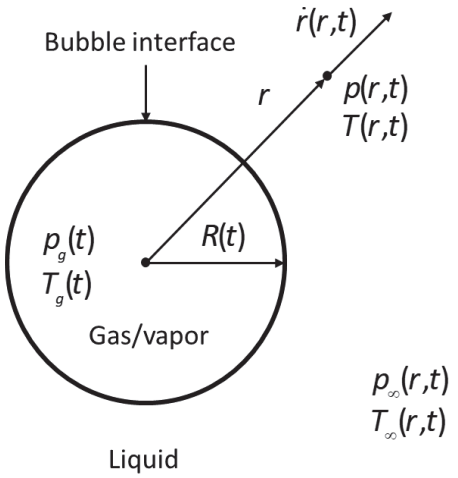

Figure 2.6 - schematic of interface and r and R as stated for the RPE derivation (modelled on [45]).

In attempt to predict the damage to ship propellers, the idea was expanded by Lord Rayleigh, where he derived the collapse time of the cavities [54]. Later analysis considered also the viscous [55] and surface effects [56], [57] at the interface and the damping effects of the gas content (eq. 2.9) to yield the typical form of the Rayleigh-Plesset equation (RPE). P indicates the pressure, R is the bubble radius and C is the ideal gas constant[12]; with the subscripts g - of gas in bubble, B - interior of bubble, 0 for initial and ∞ for infinite or far field) and γ the polytropic exponent[13]. Bubble content and thermodynamic parameters (pressure, temperature) are presumed homogeneous and constant through the bubble:

$$P_g\left(\frac{4\pi R^3}{3}\right) = C_R T \xrightarrow[adiabatic\ conditions]{T=const} P_B = \left(P_0 + \frac{2\sigma}{R}\right)\left(\frac{R_0}{R}\right)^{3\gamma} \tag{2.9}$$

$$R\ddot{R} + \frac{3\dot{R}^2}{2} = \frac{1}{\rho}\left[\left(P_0 + \frac{2\sigma}{R_0}\right)\left(\frac{R_0}{R}\right)^{3\gamma} - P_\infty - \frac{2\sigma}{R} - \frac{4\mu\dot{R}}{R}\right] \tag{2.10}$$

Seemingly an inconsistency with the proposed model arises, since the derivation from Bernoulli's principle assumes an inviscid liquid (also deriving from Navier-Stokes equations the viscous term

[12] Typical notation would be R, however we will use C_R, in order not to confuse with radius.
[13] 1 for isothermal, 1,4 for adiabatic, values between polytropic

disappears [7]), while a viscous term (μ - dynamic viscosity) is present in the equation (2.10). However, this term originates from the interface (boundary conditions) not from bulk liquid [55]. If a non-viscous liquid is assumed (as was the case for the derivation of lord Rayleigh) the last (viscous) term in equation 1.9 disappears and we are left with the Rayleigh equation (valid for Rayleigh collapse[14]) [58].

Other considerations can be taken into account for more specialised problems (such as liquid compressibility), however they will not be discussed in the scope of the thesis.

The RPE can also be derived by differentiation with respect to R or by integration of the Navier-Stokes equations [59]. The considerable amount of assumptions [2]:

- The bubble interface is completely spherical at all times,
- spatially uniform conditions hold within the bubble,
- no body forces are present (exp.: gravity driven),
- the liquid is incompressible or compressibility is small compared to the bubble gas phase,
- bubble gas content is constant,

might lead the reader to believe the equation is far removed from a realistic description. However many have shown that this robust equation can in most cases accurately describe the bubble dynamics (exp.: laser ablation bubble production [60]), even holding for stable cavitation at the nanoscale [61]. Other derivations have been used, for example the acoustic approximation, which prescribes a fixed stiffness to the liquid ($\partial p / \partial \rho = c^2$, where c is the sound velocity in the liquid). In fact, the static case of the RPE is the Young-Laplace equation where R=const. → dR/dt=0:

$$\cancel{R\ddot{R}} + \frac{3\cancel{\dot{R}^2}}{2} = \frac{1}{\rho}\left[\underbrace{\left(P_0 + \frac{2\sigma}{R_0}\right)\left(\frac{R_0}{R}\right)^{3\gamma}}_{P_B} - \frac{2\sigma}{R} - \cancel{\frac{4\mu\dot{R}}{R}} - P_\infty\right] \longrightarrow P_B - P_\infty = \frac{2\sigma}{R} \qquad (2.11)$$

One example when the RPE definitely fails is the very final phase of the bubble collapse. In this stage the densities in the liquid phase and the gas phase (due to extreme compression) are

[14] immediate pressure variations, no traveling pressure waves in medium.

comparable, which is inconsistent with the RPE [13], [30]. Regardless of that, many have used it to model the thermodynamic conditions in the peak bubble collapse as well as collapse times.

Usually for a periodic excitation (ultrasound) the bubble can be either stable or transient. The stable bubble will be (as the name suggests) stable, following the excitation for thousands of periods without a net growth (oscillating around the average bubble size) [8]. However, if the bubble dynamics are fast enough, the interface increasing (decreasing) during growth (collapse), the former will ease and the latter hinder mass transfer over it, effectively producing a net mass flux into the bubble, making it grow. This can lead the bubble into the transient regime, where the bubble dynamics become non-linear and go through an explosive growth and subsequent violent collapse event.

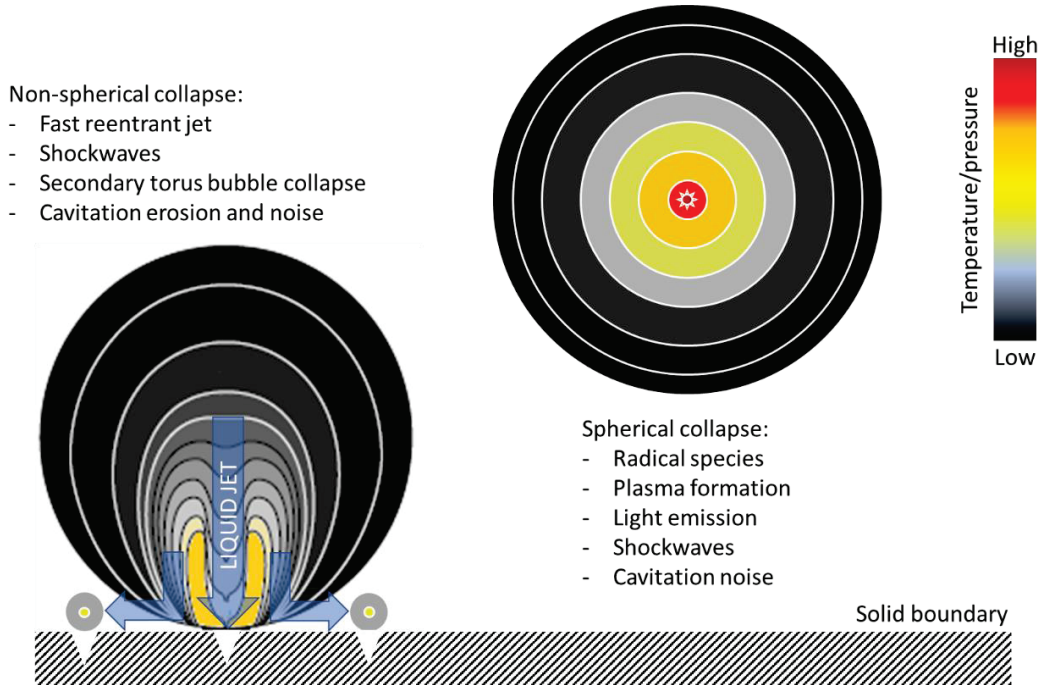

Figure 2.7 - Image of a spherical and non-spherical bubble collapse with associated effects.

However, for the case of hydrodynamic cavitation, the excitation is not periodic[15] and generally the growth phase can be longer than for ultrasound. Therefore, different dynamic effects can be expected. As shown in Figure 2.7, a perfectly spherical collapses will cause shock waves, luminescent emission from plasma excitation (in accordance with the hot-spot theory [63]) and

[15] There can be periodic bubble cloud shedding with coordinated collapse, inducing pressure fluctuations [62].

exotic species production [64]. While, the presence of a solid interface can perturb the collapse dynamics, causing the bubble to implode faster in one axis than the other two. This leads to an inward accelerating jet of fluid (direction perpendicular to the solid interface) and is believed to be the energetic mechanism behind bubble erosion (shockwaves being the second suspect)[16] [3].

2.1.2. Sonoluminescence and the extreme bubble collapse conditions

In the final phase of the rapid collapse, the gas and vapor that failing to condense on the interface, are trapped in the shrinking bubble, leading to chemical reactions and light emission [63]. Often observed in ultrasonic cavitation, the light emitted from a single cavitation bubble is thought to originate from a high temperature plasma at peak collapse, lasting roughly 100ps [65]. This is called **sonoluminescence** (SL) and it seems to originate from the following mechanism: after several bubble oscillations, the nitrogen and oxygen react to form highly soluble NOx species which are removed through the interface into the liquid, leaving inside the nonreactive noble gasses, most commonly monoatomic Argon [66], [67]. This gas is prone to ionisation due to its inertness, even at high temperatures. Therefore, a strong pulse of light is emitted in the last phase of the bubble collapse, as the gas is subjected to the extreme thermodynamic conditions [30]. A spherical collapse of a noble gas bubble is known to produce much higher light intensities, due to adiabatic compression and inertness of the gas [63].

Although first reported in 1933, the full potential of sonoluminescence was not realised until it's boom period between 1990 to 2005 (resource article by L.A. Crum [12]), which was largely due to indications that nuclear fusion reactions could be occurring in the collapsing bubbles. Currently no repeatable experiments show evidence of fusion [68], however it has led to great advancement into understanding the thermodynamic conditions at peak bubble collapse. The source of the light production was subject to many theories [69]. Currently, the hot-spot plasma emission is widely accepted. Sonoluminescence (SL) nowadays is believed to originate from bremsstrahlung emission, due to the decelerating electrons by the ion or atomic, plus a contribution of radiative recombination [8], [13]. The measurements originating from single (SBSL) or multi (MBSL) bubble collapses frequently indicate extreme conditions for the bubble core. Due to the optically opaque plasma, the main emission might not be coming from core [30], thus the maximum values[17]

[16] A secondary torus shaped cloud formed at the surface is also suspected to be a source of erosion.
[17] Could be in the range of 10^8K for a few hundred fs [70].

in the bubble might not yet have been probed [71]. Despite this, sonoluminescence remains the best tool to probe the peak collapse conditions inside the collapsing bubble [71] and can in many cases be proportional to the sonochemical yield [12]. Several emission peaks can be detected to estimate temperatures and pressure in the bubbles. Almost all organic species added to water will present a weak C_2 MBSL emission (Swan band) [72]. Isolated Ar^* lines, Xe^* and Xe^+, O_2^+, OH excited species can be ionised, emitting spectra from which temperature can be obtained [8]. The peak temperatures are quoted from a few thousand [30] to hundreds of thousands K [8], [13], with similarly enormous pressure reported from a few hundred to several thousand bars [31]. The numerical modelling approximations go even beyond those figures. Recently even non-equilibrium plasma models have been suggested [13] in the form of $^{\bullet}OH$ radicals in different energy states. This moves away from the adiabatic model and suggests that these temperatures shouldn't be considered from a viewpoint of a single value, but as a multi-temperature environment, governed by different particle energies and degrees of freedom [73]. Meaning that the observed temperatures obtained from plasma emission spectra might not correspond to the gas temperatures (translational) in the bubble, but to electron, vibrational or rotational temperatures of the excited species.

However, all of stated above testifies to the truly extreme conditions achieved at bubble collapse, prompting the birth of a separate field – sonochemistry; producing exotic species with ultrasound excitation of a liquid medium. The same principles are at work in microchannels as we will see further down the line [74] (discussed in chapter 5.1).

2.1.3. Parameters affecting cavitation

As summarized by Apfel in [75], the golden rules in cavitation experimentation should be "*know thy liquid*", "*know thy sound field*" and "*know when something happens*". Good control of these three should yield significant and, what is often problematic for cavitation research, repeatable results [2].

The first refers to the parameters concerning liquid quality; such as nuclei size, type and distribution and dissolved or non-condensed gas content [76]. Often tap water is used as the working fluid, which can vary wildly between locations. Therefore repeatability and inter-experimental comparison suffers, due to the lack of control over nuclei and gas content [2]. A

general recommendation would be to use deionised water[18], systems are readily available nowadays and some form of degassing to control the gas content.

The second – "*Know thy sound field*" is obviously in context of acoustic cavitation, and perhaps should be generalized as "*Know thy driving pressure*" dynamics. This concerns the nuclei/liquid excitation by the low-pressure excitation. Parameters influencing the pressure profiles, like geometrical parameters[19] and nuclei exposure time are also relevant.

The last is a comment on experimentation techniques, as often the effect (especially at cavitation inception), could be at the micro or even nano scale and consequently easy to overlook. Sonoluminescence is a good example, as usually very sensitive equipment must be used to detect the photon production for the case of water [63]. However in specialised fluids and with periodic excitation, it may be observed by the naked eye [8].

Liquid parameters like temperature and pressure can in fact be responsible for several parameter variations. For instance, liquid temperature would influence the vapor pressure, surface tension, viscous damping, nucleation via the tensile strength of the liquid, gas solubility, etc.

As was mentioned in the introduction, cavitation was first reported by Newton in Optics [5]. Essentially what he saw was gaseous cavitation or degassing. The dissolved gases will follow Henry's law when subjected to decreased pressure. A distinction can be made between gaseous and vaporous cavitation [8], the former associated with a bubble of non-condensable gas (degassing), while the latter with phase transition. In ultrasonic cavitation only the gaseous cavitation is associated with SL and cavitation noise [77]. The polytropic index and thermal conductivity of gasses can also influence collapse temperatures, SL and the radical yield [78].It can also lower the cavitation threshold, by forming non-condensed gas bubbles, serving as nuclei for subsequent cavitation events.

In summation, clearly many parameters can influence the cavitation process. Perhaps by altering the initial/steady-state conditions, single/inter bubble dynamics or by some other indirect mechanism, the control of these parameters is essential for repeatable and representative results.

[18] Indicated by 18,2MΩ resistivity.
[19] Pressure profile for HC, acoustic field for AC.

2.2. Hydrodynamic cavitation in microchannels

Hydrodynamic cavitation has historically been of interest for hydraulic machines (turbines, pumps, propellers), so often these are applicative macroscale studies. Recently the development of microfluidics has opened up interest in fundamental microscale cavitating flow. Unlike boiling at the microscale (due to interest in microprocessor cooling), micro-cavitating flow is much less studied. However, it is expected, as the miniaturisation trend continues, the high speed microfluidic devices could begin to be influenced and eventually limited by cavitation effects [79]. In order to construct a representative experiment, we often rely on the scaling laws to make accurate models of the macroscopic problems. Some debate is raised over the scaling of cavitation to the microscales [80], however it seems that laws of hydrodynamics are valid down to a few microns [81], [82].

A body of work was published on hydrodynamic cavitation in etched silicon microchannels from the laboratories of Peles [79], [83]–[92], Ayela [93]–[99] starting around the beginning of the millennium and more recently Koşar [100]–[102] (and individual attempts by groups [103], [104]). The studies examine channel geometries and liquid parameters, mostly studied by optical means and flow characterisation, some backed up with CFD simulations [103].

2.2.1. Why microfluidics?

Nuclei and viscous effect are mostly responsible for scaling effects of cavitation inception [80]. The nuclei can be, as indicated in chapter 2.1, free flowing or attached to channel walls. Due to the small characteristic sizes of microchannels, some form of filtration must be assured as not to clog the system, therefore removing free flowing nuclei above the filter size. Also, the surfaces in silicon channels can be made to be reasonably smooth [93], lessening the effect of surface attached nuclei. In addition, the surface energy (hydrophilicity/hydrophobicity) might play an important role. Surface tension at macroscales is of relevance only at the very beginning of the bubble inception and growth (then becomes of lesser importance), whereas at the microscale it's always a relevant mechanism [80]. All these effects lead to an increase in the tensional strength of the liquid, delaying cavitation inception and allowing for a metastable flow to occur in the channel [93] (Figure 2.8). This is a typical scaling phenomenon encountered in micro-scale cavitation [90]. Fast flows and small geometries present short dwell time of nuclei to grow in the low-pressure

region of the microchannel, also contributing to metastability. These effects in the microfluidic setups allow for experiments unavailable at the macroscale.

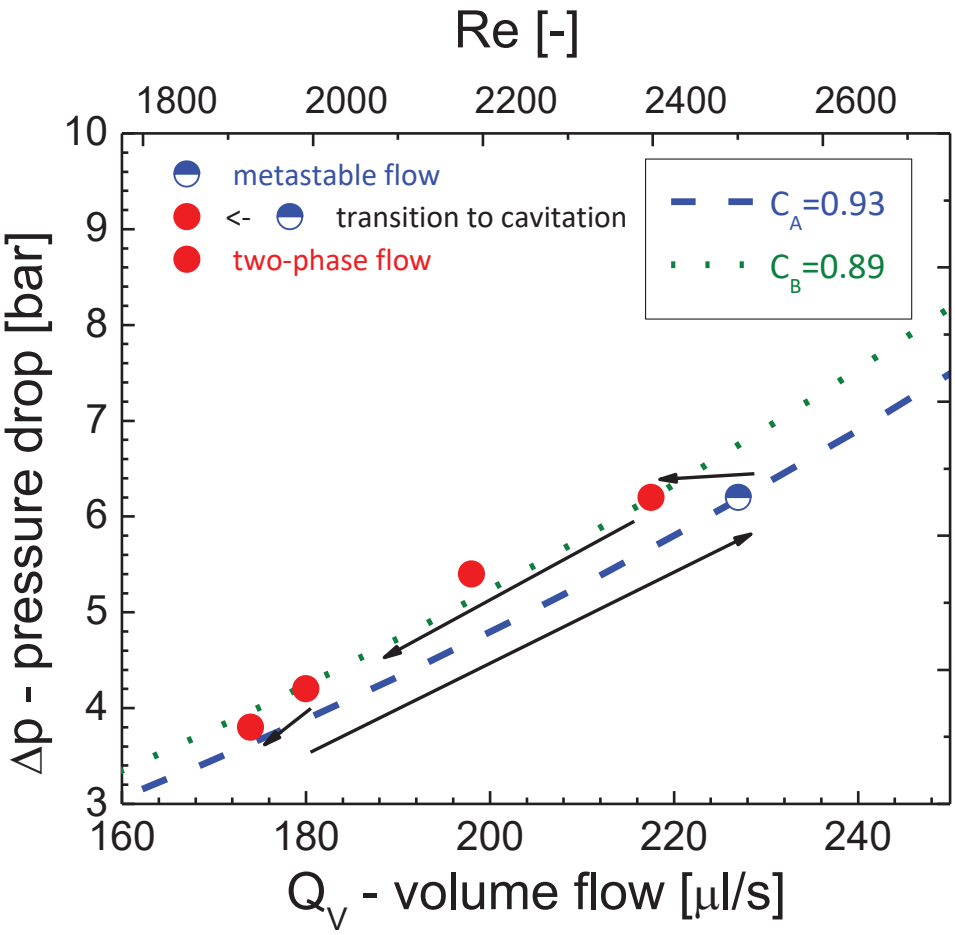

Figure 2.8 - Δp to Q and Re graph, showing the hysteresis and metastability in microfluidic channels when using clean, well filtered liquid. .Re is the Reynolds number (see page 24). Adapted from [85].

A general rule in microfluidics is the smaller you go, the higher the driving pressure needed, due to the losses on the walls of the channel. With downscaling, the ratio between the wall size and volume increases, upscaling the pressure drop through the microchannel. However, the small channels surface areas also withstand higher pressure (force per area).

Transparent windows allows optical observations and probing into the channel (long working distance objective with a confocal setup [94]). One of the main advantages of microfluidic is also the low fluid consumption (low flow). This makes it useful of when specialised (or toxic) fluids are used (nanofluids, liquid crystals,…) [93], [94], [105], [106].

2.2.2. Channel fabrication

The fabrication of the channels was done at the Neel institute in Grenoble in association with Damien Colombet and Frederic Ayela from LEGI[20].

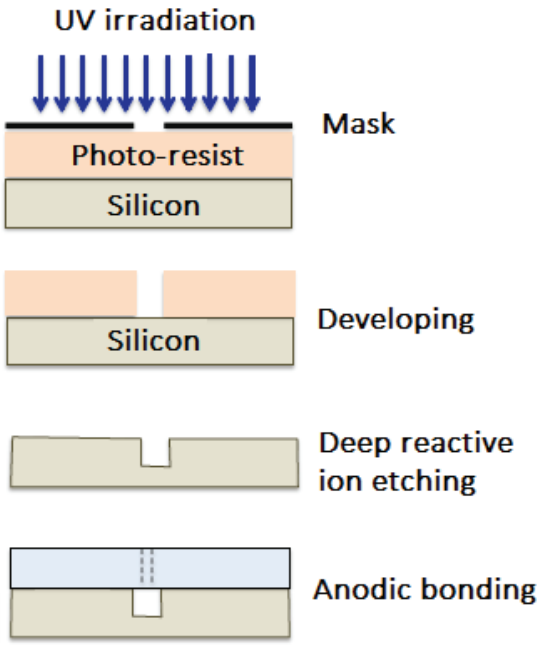

Figure 2.9 - Microchannel manufacturing phases. Adapted from [86].

There is a wide array of fabrication processes and substrates to choose from, when designing a microfluidic device, each presenting its own challenges and attributes. With photolithography, etching, embossing, imprinting, injection molding, micromachining and laser processing, we can create channels of different degree of complexity onto materials like glass, polymers, silicon or metal based substrates [107]. The majority of uses are in biological studies. They are often fabricated by simple lithography processes onto polymers, making them dispersible and suitable for rapid prototyping. For mass production, embossing and injection molding might be most suitable. While for complex shapes micromachining and more so, laser processing might be most suitable.

The microchannels used in the scope of our study were produced by the so called Bosch or deep reactive ion etching process [108] of a silicon wafer. This involves the alternation of etching and

[20] LEGI - Laboratoire des Écoulements Géophysiques et Industriels.

passivation of the walls with SF_6-C_4F_8 plasma. The result is nearly perpendicular side walls and high aspect ratios in order to produce rectangular hydraulic cross sections.

The fabrication process used for our Si-Pyrex microfluidic devices is described shown on Figure 2.9 [93], [95]:

1. Starting with a polished 350µm thick (100) silicon wafer. Classical ultraviolet lithography process is used to transfer the desired geometry onto the photo-resist.
2. The deep reactive ion etching step. The etch rate of a few µm/min gives way to scalloping patterns on the side walls of a few nm. A SEM image (Figure 2.10) of the geometry before topping of the channel with Pyrex glass is shown below.
3. The last step is the anodic bonding of the Pyrex glass onto the etched silicon wafer and the machining of the inlet/outlet holes through the glass. A negative voltage of -500V is applied to the Pyrex glass at 400ºC, allowing for ion migration to the Si wafer. This assures a powerful bond between the two plates, making the channel useful for high pressure (>10bar) experiments. Before the bonding the inlet/outlet holes are drilled into the Pyrex glass.

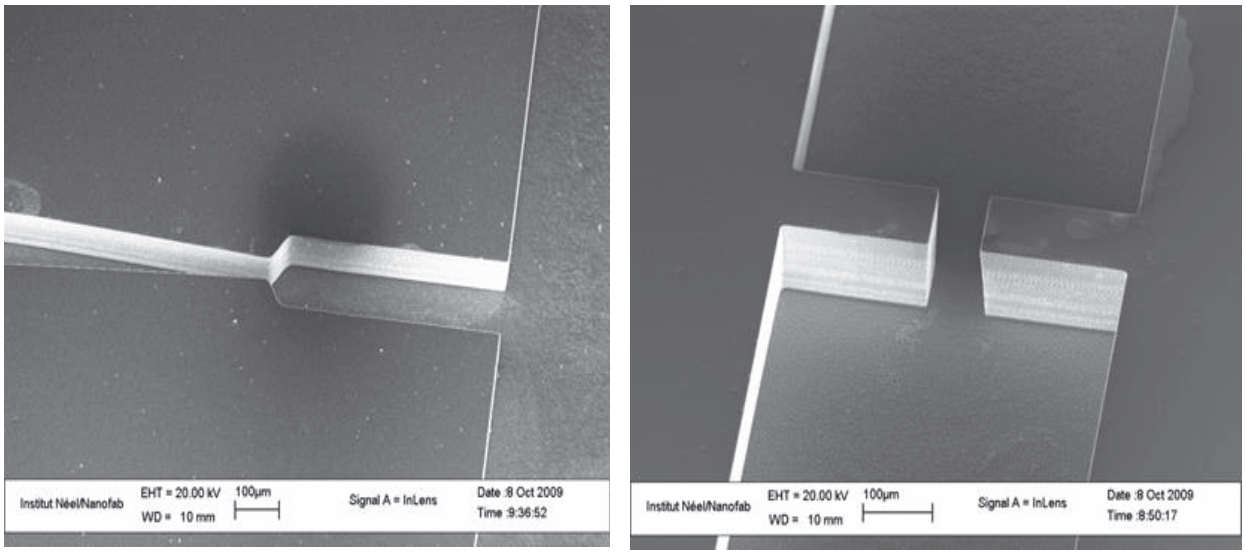

Figure 2.10 - Scanning electron microscope images of channels after etching (step 2). The high aspect ratio and nearly perpendicular walls can be observed [84].

In Figure 2.10 we can see the typical channel geometries used[21]. On the left is the converging-diverging (microventuri) channel and the right a microdiphragm (abbreviated MD). Both

[21] For the thesis only microdiaphragm results will be shown.

geometries promote cavitating flow (constricting the flow) by accelerating the liquid and producing a low-pressure region in the *vena contracta*[22], just downstream of the channel opening.

The channel design in hydrodynamic cavitation is one of the key features when making interexperimental comparison. Due to a lack of protocol, channel design is often left to the discretion of the experimentalist, often not yielding corroborating or consistent results [109].

To ease the study between experiments, **dimensionless numbers** are often used, which enable flow characterisation at different scales (dimensionless analysis). Often two mechanisms will be compared in the analysis in order to determine the relationship between them and if one dominates over the other.

One of the basic and frequently used dimensionless number is the **Reynolds number**. Although introduced by Sir George Stokes back in 1851 [110], it was named after Osbourne Reynolds, who established its use in flow analysis. Essentially it describes the ratio between the viscous and inertial forces in the flow:

$$\mathrm{Re} = \frac{inertial\ \ forces}{viscous\ \ forces} = \frac{\rho \cdot v \cdot D}{\mu} \tag{2.12}$$

Low Reynolds numbers indicate a steady, laminar flow ($Re_{lam} < 2300$), where viscous forces become dominant. Higher values will indicate inertial forces dominating, producing vortices and instabilities indicative of turbulent flow ($Re_{turb} > 2600$), with a transient regime in between. Laminar flows are often encountered in microfluidics, due to the low values of D (characteristic dimension in channel). Due to this, the turbulent mixing doesn't occur, leaving only diffusive mixing which is an inherently slow process [111]. This presents an inherent problem for lab-on-a-chip devices, however it might be interesting for micro-cavitating flow for which the Re numbers should stay below 10^4 compared to macro scale systems which operate well above, firmly in the turbulent regime, at the Re range of 10^6-10^9 [80].

[22] The point in the fluid flow where the stream diameter is least, leading to the highest velocities, as dictated by Bernoulli's principle. For our case this is located just downstream of the constriction in the channel.

Cavitation number is another dimensionless number often used to characterise the fluid flow of susceptibility to cavitation. It's the relation between the kinetic energy per volume and the pressure difference to vapor pressure:

$$\sigma = \frac{pressure\ to\ vapor\ \ pressure}{kinetic\ \ energy\ \ per\ \ volume} = \frac{p - p_v}{\rho v^2 / 2} \tag{2.13}$$

This simple characterisation applies for most engineering approximations, but fails to take into account the ability of fluids to withstand tension (metastability) [7], it assumes cavitation will occur instantaneously when the liquid is brought below vapor pressure. However, it remains an important parameter when comparing experimental data on cavitation, since often the geometrical parameters between setups can vary wildly.

Some authors also mention Weber number - We (inertial /surface tension forces) and Strouhal number - St (vortex shedding/flow velocity) as relevant dimensionless numbers [80].

2.3. Liquid line – Microfluidic experiment

A detailed series of articles have been published on the microchannels used within this study [93]–[96], detailing the meta stability of pure liquids as well as nanofluids, showing that dispersed nanoparticles with proper surface chemistry shouldn't influence the cavitation threshold (under sufficiently low concentrations). Figure 2.11 shows the schematic of the microfluidic part of the experiment. Our working liquid is ultrapure water with dispersed nanoprobes (chapter 3.4), for which the properties relevant in hydrodynamics don't deviate from ultrapure water[23]. Water purification system Barnstead Smart2Pure from Thermo Scientific was used. The liquid is contained in a butyl rubber membrane reservoir (Figure 2.11 - l). When pressure from the nitrogen tank (a) is introduced in the gas line (grey lines from a to e), it exerts isostatic pressure on the membrane and the liquid. This prevents gas mixing with the liquid and allows for a pulseless propelling of the liquid through our system. When the lower valve (k) is open, the liquid will make its way through the liquid line past the sensors (n,o) and preparation systems (m,p) to the channel. The narrow constriction in the flow keeps the upstream pressure high, therefore a pressure difference across the constriction drives the high-speed jet, which may or may not induce

[23] Electrical resistance of 18,2MΩ indicative of pure deionized water.

cavitating flow in the channel (depending on the parameters). The filter holder (m) contains a nylon 10µm filter with a 2,7 or 1µm glass fibre filter to prevent small particles from blocking constriction in the microchannel. A piezoelectric pressure sensor (n) determines the upstream pressure (driving pressure) and the mass flow meter (o) the liquid mass flux. Temperature control is achieved with a chiller (l) and a liquid to liquid heat exchanger (p). A thermocouple determines liquid temperature after the heat exchanger and a thermistor regulates the heat exchanger surface temperature. Just before the channel inlet another thermistor is glued on the metallic inlets (unmarked). The liquid after the constriction is led out of the channel and into an open reservoir (i) (at outlet is at ambient pressure).

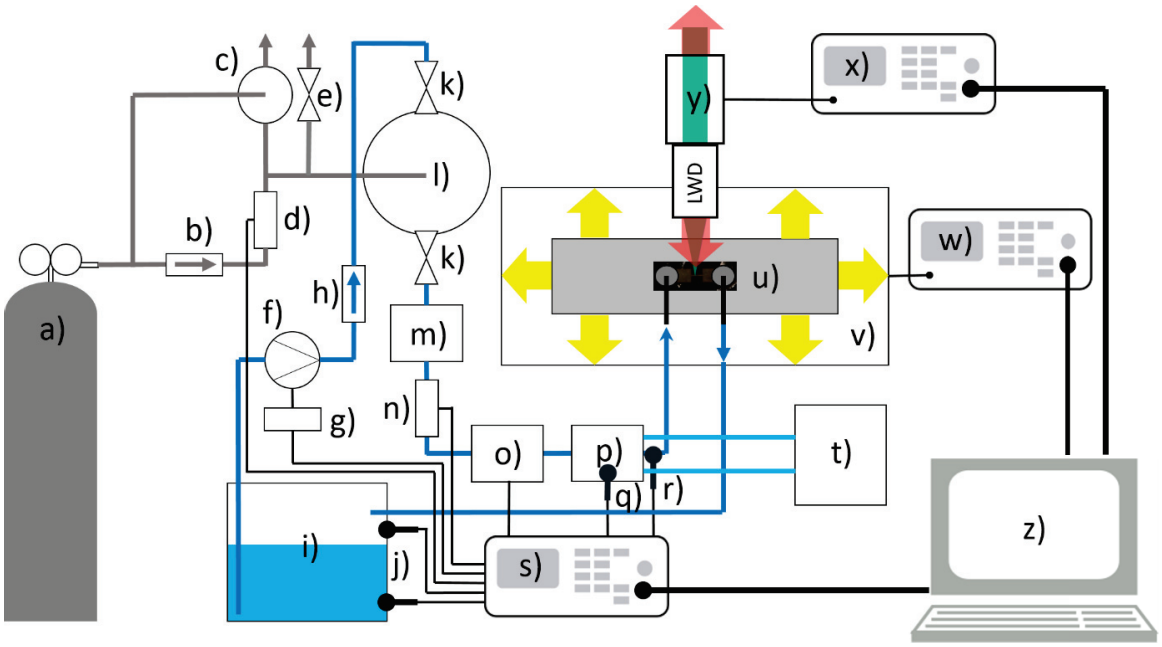

Figure 2.11 - Liquid line of the microfluidic experimental setup. a) to e) + l) elements of the gas line; f) to r) + u) elements of the liquid line; and the rest sensor acquisition and channel x, y and z movement control. Blue- liquid line, grey – gas lines, black – electrical signal. The individual elements are tabulated in the appendix - Table 5.

A recirculating pump (f) controlled by (g) is engaged by the liquid level switches (j) and transported through a one-way valve (h) to the high-pressure reservoir (l) to allow for continuous flow conditions. The recirculation was added later on, since optical acquisitions can take a long time and there is a danger of the liquid running out. So liquid volume was one of the limiting factors. However, when the liquid is transported the pressure if unmitigated will increase, introducing pressure variations that could even cross the maximum allowed pressure for the

system. So, a back-pressure regulator (c) is positioned in the gas line to deal with these pressure variations, levelling the pressure to the reference set by the pressure from the nitrogen bottle. Another pressure sensor (d) is positioned in the gas line to compare the set gas pressure and the liquid line pressure (a difference between the two might indicate filter clogging problems). The microchannel is mounted in the channel holder (u) and can be moved in the X and Y direction by the micromechanical manipulators (v) and its control (w). The Z manipulator (y) and controller (x) is achieved by moving the objective, as is explained in the chapter 4.2.1. all data acquisition and motion control is handled by an in-house LabVIEW program on the computer (z).

2.3.1. Flow characterisation

The pressure – flow (p-Q_m) characterisation was performed for the studied channels. Pressure sensor (d) and mass flow meter (o) in the liquid line (Figure 2.11) were used to measure flow at specific pressure points. The appearance of the hysteresis, as mentioned before, shows metastable flow can be reached, indicating a pure liquid with sufficiently small nuclei.

$$\Delta p = \frac{\rho Q^2}{(2C^2W^2H^2)} \tag{2.14}$$

The pressure – flow rate should follow the relationship shown in equation (2.14) [94], where the Q is the volume flow, Δp is the driving pressure, W and H are the width and height of the constriction (Table 6, Figure 2.12) and C – the discharge coefficient.

In the table below, we classify the channels used in all subsequent microfluidic experiments (Chapter 4 and 5). An inherent short coming of the Silicon-Pyrex hybrid channel design is their inherent brittleness. The channels have the tendency to fracture or even disintegrate during mounting/dismounting. This issue was addressed later on by adapting the channel holder design, however many channels from the early part of the study could not be remeasured. Therefore, a full overview of flow parameters in all of the studied channels cannot be presented.

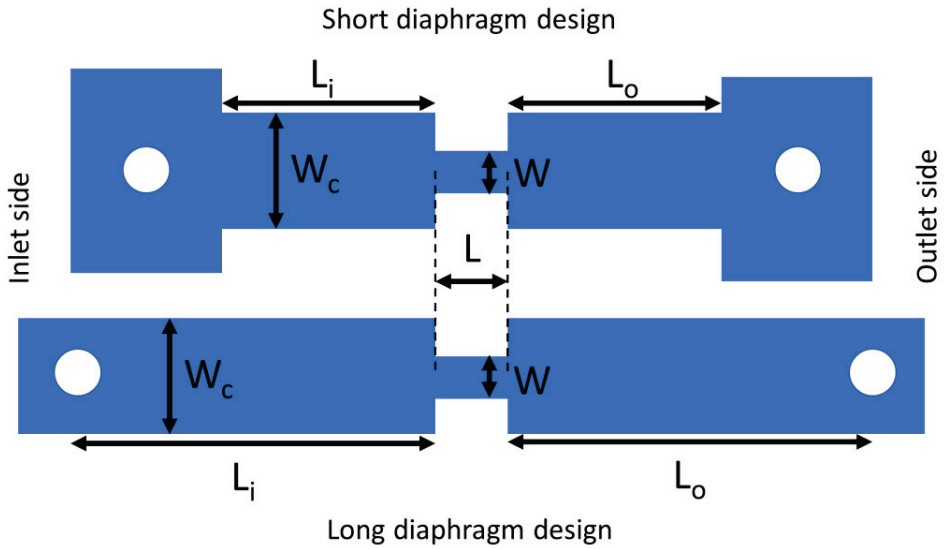

Figure 2.12 - Short and long microdiaphragm design schematic. The geometric parameters W_C is fixed for all channels at 500µm (+/- 10µm between channels). For long diaphragm L_i=15000µm and L_o= 25000µm, while for the short diaphragm they are equal at 1500µm. Other variable parameters are shown in Table 1.

Table 1 - Microdiaphragm (MD) channel constriction dimensions. W - width, L - length of constriction (Figure 2.12) and H- height of channel. Channels name prefix T indicating transparent channel (Pyrex-Si-Pyrex system), L indicating long diaphragm and no prefix indicating short diaphragm. Channel identification does not indicate any correlation to geometrical parameters, they originate from internal laboratory classification.

Channel identification (MD)	W [µm]	L [µm]	H [µm]	Comment
10	70	80	145	
11	92	77	158	
13	72	78	152	
14	54	94	150	Non-transparent copy of T2
T2	54	94	150	Short diaphragm, transparent channel.
T3	72	17	114	Short diaphragm, transparent channel.
L3	62	94	170	Long diaphragm
L4	101	58	164	Long diaphragm
L6	81	78	154	Long diaphragm

Flow characterisation of channels 11, 13, 14 and T2 are shown in Figure 2.13. The first three vary in the constriction width (W) from 54µm to 92µm, while the last two have the same geometries but vary in channel design (SI-Pyrex for 14 and Pyrex-Si-Pyrex for T2). Metastability is present on all studied channels, shown by the presence of the hysteresis. The difference between the varying W channels is obvious; increased flow rate for the same driving pressure.

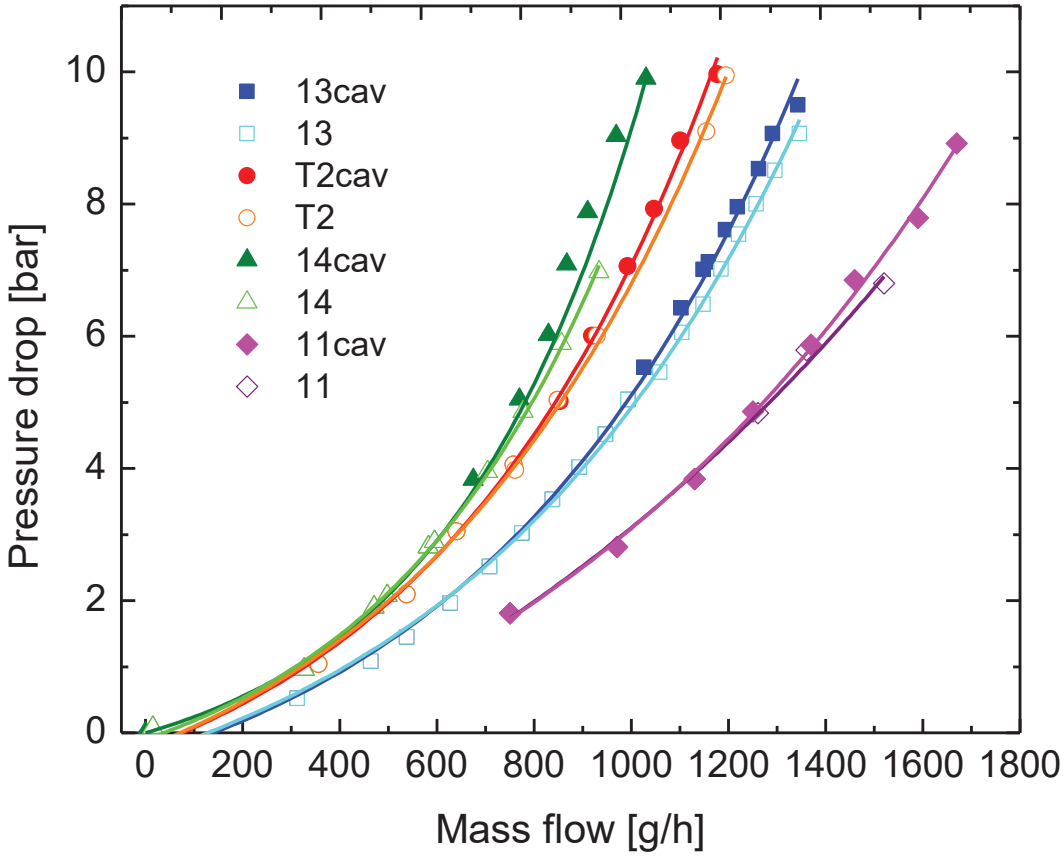

Figure 2.13 - Pressure vs mass flow curve diagram (p-Q_m) for the short diaphragm microchannels. Coloured symbols show two-phase flow while hollow ones show single phase flow.

Rather more surprising is the difference in the flow for the geometrically identical channels 14 and T2. This could be attributed to the altered flow caused by a symmetrical (Pyrex-Si-Pyrex) and asymmetrical (Pyrex-Si) channel or simply the double glass surface of T2 inducing a lesser drag and therefore a higher flow rate compared to the Si-Pyrex system of 14. However, Si and Pyrex surface roughness is in the same order of magnitude [93], therefore this seems unlikely. The discrepancies then most likely originate from minute geometric differences, which have shown to

greatly influence the flow discharge [96]. Particularly, the orifice edge is known to influence the jet contraction and subsequent flow dynamics.

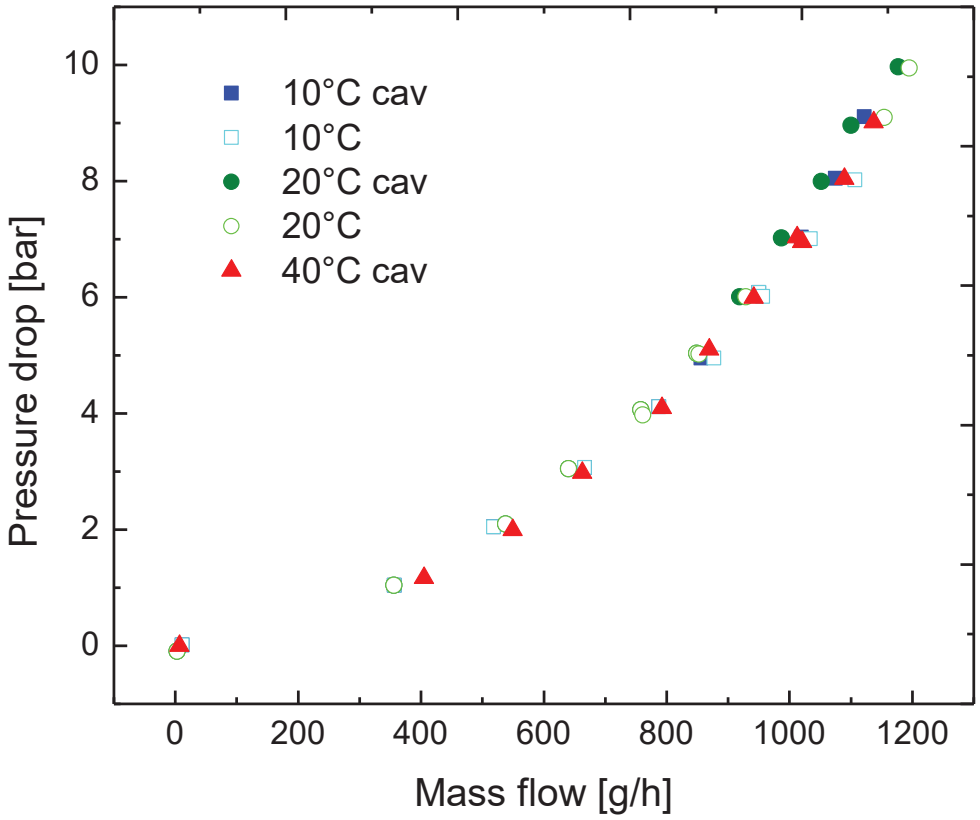

Figure 2.14 - Pressure vs mass flow curve diagram (p-Q_m) for the T2 short diaphragm microchannel with varying temperature. Coloured symbols show two-phase flow while hollow ones show single phase flow.

Figure 2.14 below shows the T2 flow curves as the liquid temperature is varied. With temperature liquid viscosity varies; in fact, the dynamic viscosity halves from 10 to 40ºC. In macroscopic systems this wouldn't greatly influence the flow parameters, however since we are operating in or near the laminar flow regime (Re ≈ 2300), the viscosity variations should be visible on the flow curves. Surprisingly, the results aren't dramatic, showing only slight increase of flow with the temperature rise. More importantly, the metastable flow couldn't be reached for 40ºC, probably due to lowering of the cavitation threshold.

2.3.2. Highspeed images of flow

One of the main differences between hydrodynamic and acoustic cavitation is the timescales of the exposure to the decreased pressures [109]. For micro cavitating flows, these times could be short due to the fast flow velocities and the short paths through the pressure depression region. For this reason, we wish to probe the fast bubble dynamics and estimate the bubble characteristic times, with a fast camera shadowgraphy setup, shown in Figure 2.15.

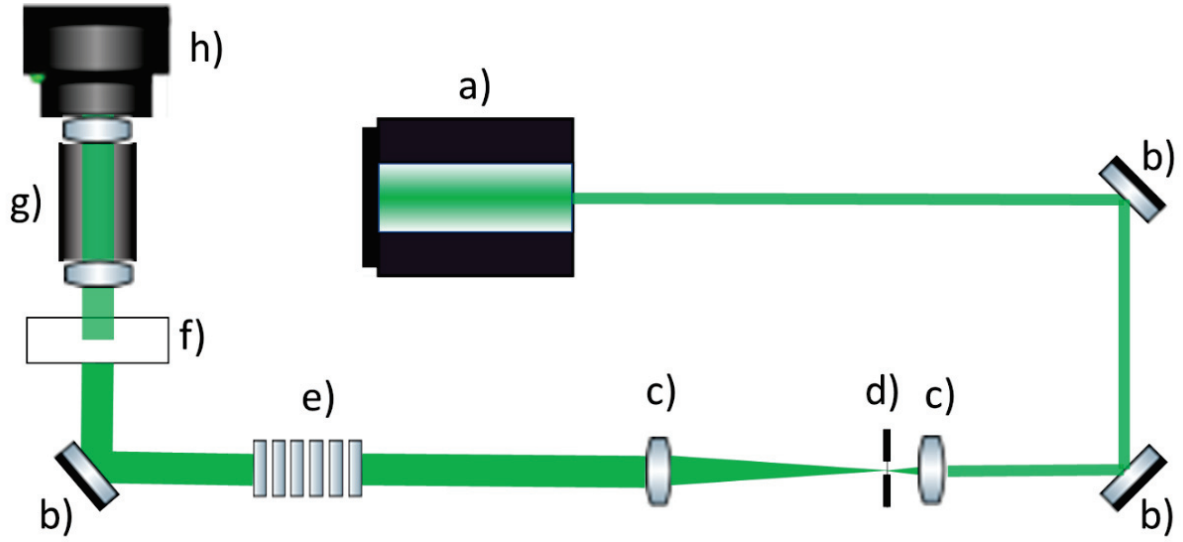

Figure 2.15 - Fast camera shadowgraphy recording setup of the T2 transparent microdiaphragm channel. Each part specified in Table 6.

For the low to moderate driving pressure, the bubble growth time can be approximated. In Figure 2.16 we can see (red circle) a bubble appearing in frame 2 and growing to about 100μm in frame 5, corresponding to 5μs growth time. In subsequent frames the growth seems to be less rapid as is its advection. This is the same timeframes as a typical low frequency acoustic bubble, commonly excited at 20kHz. Moreover, the exposure time to lower pressure is probably much longer for hydrodynamic cavitation.

By averaging over many frames of the highspeed recording, one can obtain the equivalent of a long exposure time image. In our case the dark regions correspond to bubbles (disregarding the walls and defects), when averaging we get a grey intensity information, proportional to the times the pixel was occupied by the bubble in the summed frames. So essentially it is also the image of the void fraction averaged over the cumulative time of the recording. This is shown in Figure 2.17, for different driving pressures in the T2 microchannel.

Bubble production was roughly estimated from the images and was shown to be 160000 bubbles/s at 4bar, rising linearly to 320000 bubbles/s at 7bar. Above 7bar the bubble overlap in the images is severe and the bubble production rate cannot be distinguished.

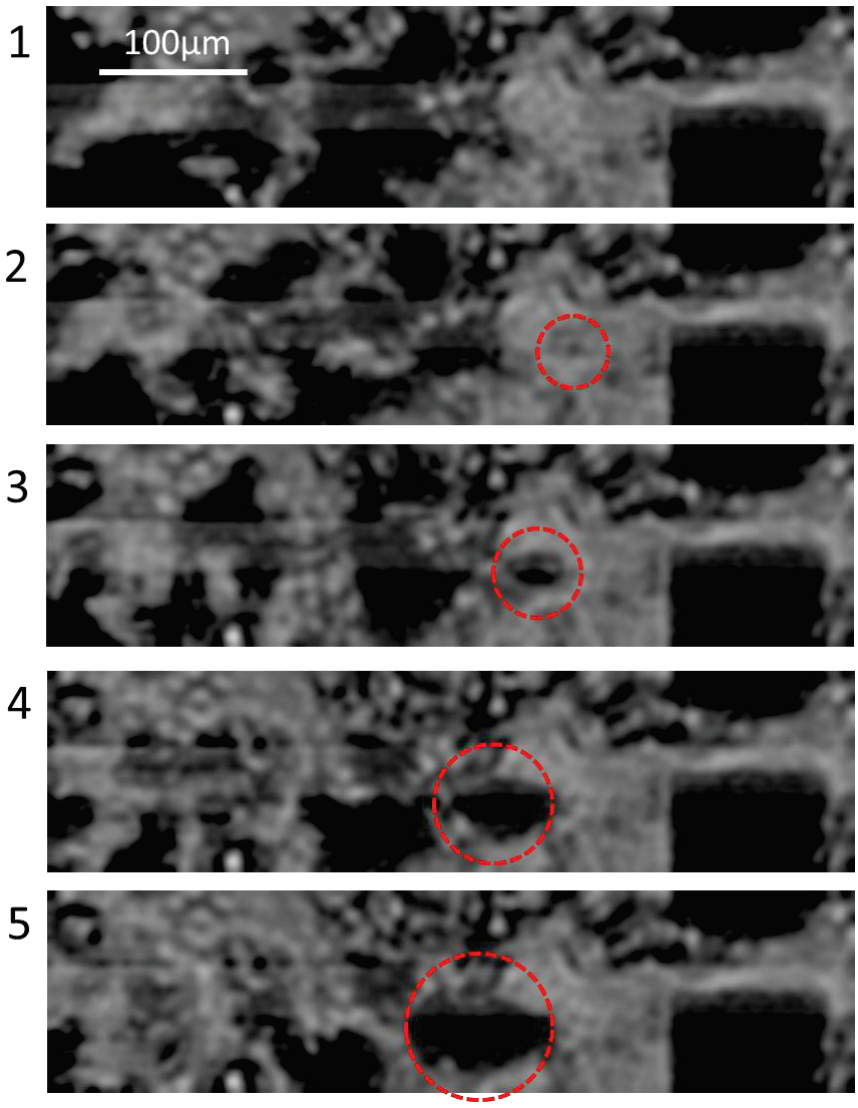

Figure 2.16 - Fast camera shadowgraphy at the mouth of the microdiaphragm. 128x32 8bit, 600kHz (1,667µs between frames). Recording of the transparent (Pyrex-Si-Pyrex) microchannel T2 at 6bar driving pressure. Numbers in corner indicating the frame in recorded series. Flow is from right to left, black squares on right side are the diaphragm walls. The static grey spots in the background are defects on the glass surface from the fabrication process. The red dashed circle indicates the growing bubble.

An important finding is visible in the high-speed recordings (Figure 2.18). The inception of the cavitating flow is hard to catch as it is stochastic, so it's not known how the cavitation is initiated.

However, upon examination of the fast images one can see that what appears to be residual gas bubbles, emerging from the collapse region, is redirected back towards the diaphragm opening and the high shear flow of the jetting liquid. This appears to be one of the mechanisms sustaining the two-phase flow. At low driving pressure the emergence of bubbles from the constriction is also observed, but with pressure increase the number of the residual gas bubbles increases and it is likely that they become the dominant mechanism. Furthermore, at the highest driving pressure (10bar) two regimes are observed. One forming a super-cavitation bubble instead of a bubble stream and the "typical" two bubbly flows surrounding the high-speed jet emerging from the constriction. As the liquid jet curves to one side, the inner most stream is more intense, as shown on Figure 2.18.

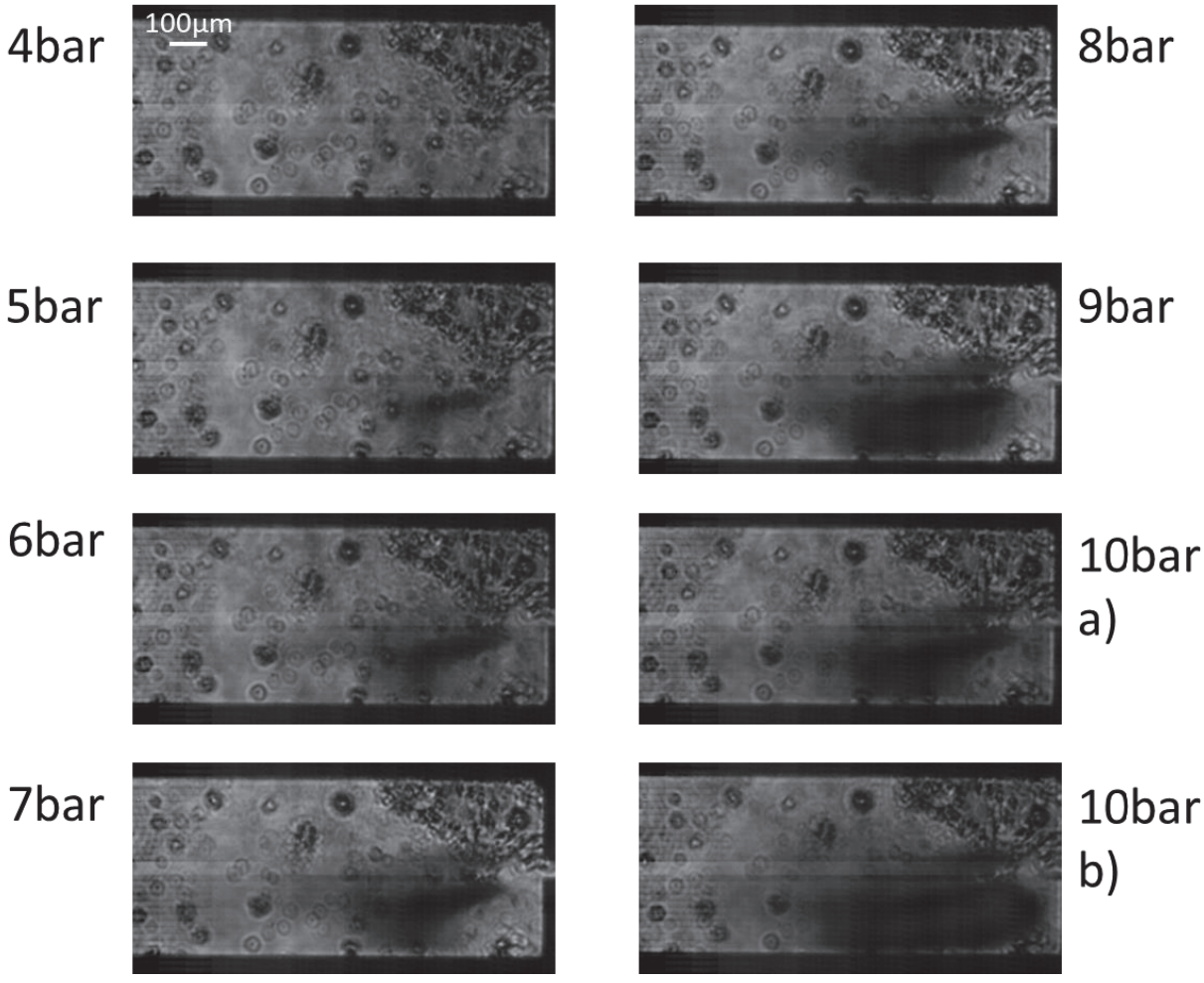

Figure 2.17 - Images averaged over 1000 frames at 150kHz. At 10 bar the two regimes are shown; a) the typical flow and b) the bubble coalescence.

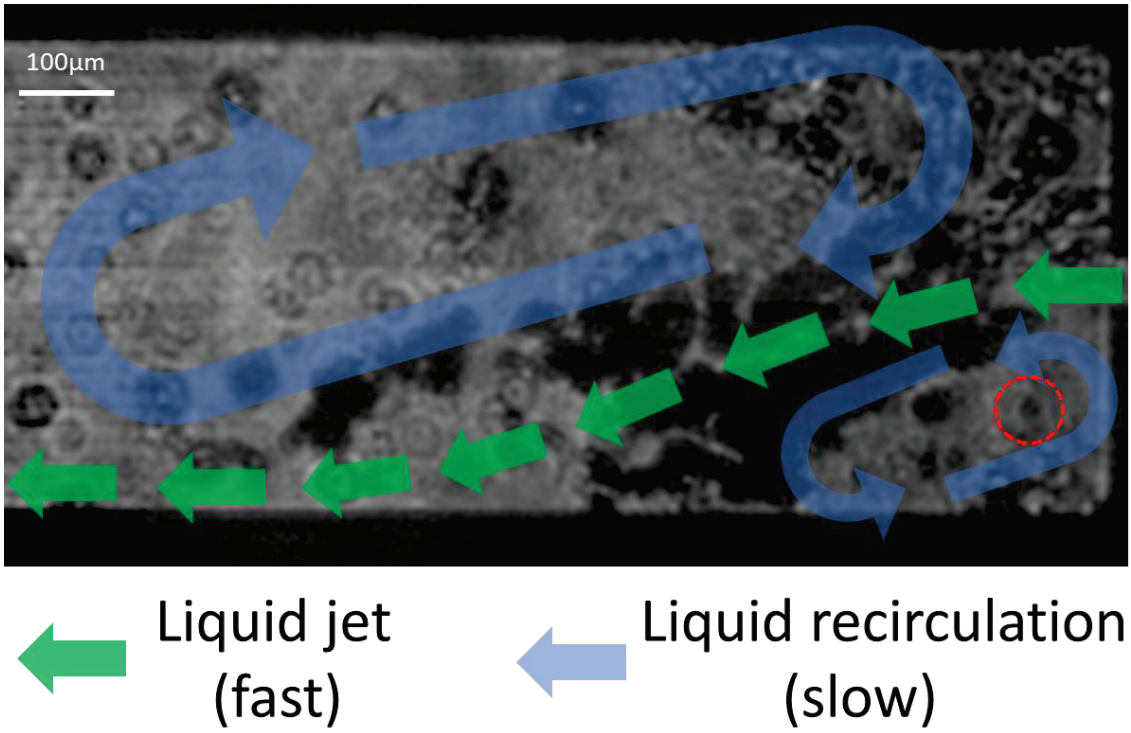

Figure 2.18 - The two main recirculation zones in typical cavitating flow of a microdiaphragm (6bar driving pressure). The red dashed circle indicating the residual gas bubbled, most likely produced by degassing in the cavitating flow. These bubbles recirculate and get injected in the shearing flow, serving as nuclei and sustaining the cavitating flow.

3. Luminescence as a probing tool

In the most basic form, light and matter can interact in the following ways (figure 3.1):

Light transmission; light will pass through the material (being refracted if a difference in the refraction index exists at the interface), without energy exchange.
Light reflection; occurring at the interface, it can be specular (retaining image) or diffuse (losing image), but in both cases the energy is maintained.

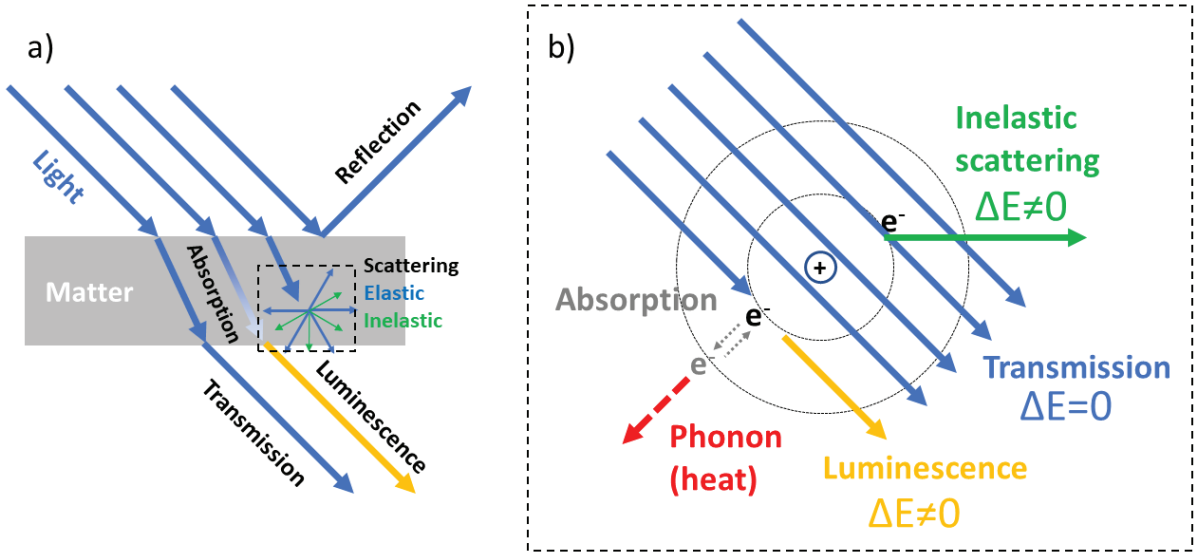

Figure 3.1 - Basic light-matter interaction. reflection, absorption, scattering and transmission; interactions at the: a) macroscopic and b) atomic scale.

Light scattering; this can be either elastic (Rayleigh scattering) or inelastic (Raman, Brillouin scattering). When a photon is scattered from an atom/molecule, elastic scattering will account for the majority of the scattering interactions. It's called elastic due to the fact that there is no energy exchange in the process (wavelength fixed), while the inelastic scattering will be dependent on the material properties (Raman - change in polarizability and for Brillouin – density fluctuations in matter i.e. sound waves). As it is relevant for our discussion, Raman scattering is discussed in chapter 4.3.
Light absorption; the energy of the photon is absorbed by the electrons in the atoms/molecules. The absorbing molecule/atom is considered to be in an excited state. Several relaxation mechanisms can follow, to bring the electron from the excited state to the lowest energy state

called the ground state of a molecule/atom. These will be discussed in the following sub-chapters.

In the scope of our study we were interested in the events after photon absorption, specifically the different relaxation mechanisms (radiative and non-radiative) that enable the use of luminescence as a tool to probe the local environment of the emitter. With the study of time and energy resolved response of the luminescent signal, information about the relaxation mechanism in relation to environmental parameters can be obtained. Inelastic scattering effects can also yield the local temperature information. So essentially, using spectroscopy one can follow conversions of the photon energy as it interacts with matter, to yield information on the thermodynamic parameters of the local environment.

In this chapter we discuss the excitation/emission mechanism on a single emitter basis, starting from a simple atom and expanding to complex molecular/crystalline structures. The discussion of the relationship between the emitters sensitivity to the environment and the use of spectroscopic method to probe it. In depth development of individual optical processes is omitted. Some results on a specific family of metal organic chalcogenolates are discussed in context of pressure probe development and at the end luminescent nano-particle suspension used in chapter 4.2 are discussed.

.

3.1. Light absorption and relaxation mechanisms

In this sub-chapter an overview is made on luminescence, absorption and relaxation mechanism relevant to the thesis topic. As defined in [112]: "*Luminescence is a spontaneous emission of radiation from an electronically excited species or from a vibrationally excited species not in thermal equilibrium with its environment"*. The non-equilibrium conditions in the definition are due to photon's energy absorption (excited state), which prompts the relaxations mechanisms, bringing it back to equilibrium (ground state). The term coined in 1888 [113], the prefix "lumin-"; latin for light and the suffix "-essence", process or state of being, denotes the light emitting property of a material. Often termed "cold-light" as light was produced without a temperature increase, contrary to incandescence which is the emission of visible light due to black body radiation. Many forms of luminescence exist, named according to the excitation used (Table 2 below).

Table 2 – Different forms of luminescence categorized by excitation [106], [107]. Marked bold are the ones relevant in the thesis.

Luminescence	Excitation mechanism
Photoluminescence	Absorption of light
Radioluminescence	Ionizing radiation
Cathodoluminescence	Electron bombardment
Electroluminescence	Electric field
Thermoluminescence	Heating after prior storage of energy, like radioactive irradiation
Chemiluminescence	Chemical process
Lyoluminescence	Dissolution of solid in liquid
Crystalloluminescence	Crystalization
Bioluminescence	Biological process
Triboluminescence	Frictional and electrostatic forces
Mechanoluminescence	Mechanical action
Fractoluminescence	Crystal fracture
Piezoluminescence	Nondestructive (elastic) dynamic pressure
Sonoluminescence	Ultrasound (cavitation)

Photoluminescence - the absorption of a photon and its re-emission at higher wavelengths, is of main interest to our work, due to its application in sensorics. The optical excitation and acquisition can be performed quickly, non-invasively or non-intrusively and in a very localized manner. In chapter 5.2 and 2.1.2 we discuss chemi- and sono-luminescence, respectively.

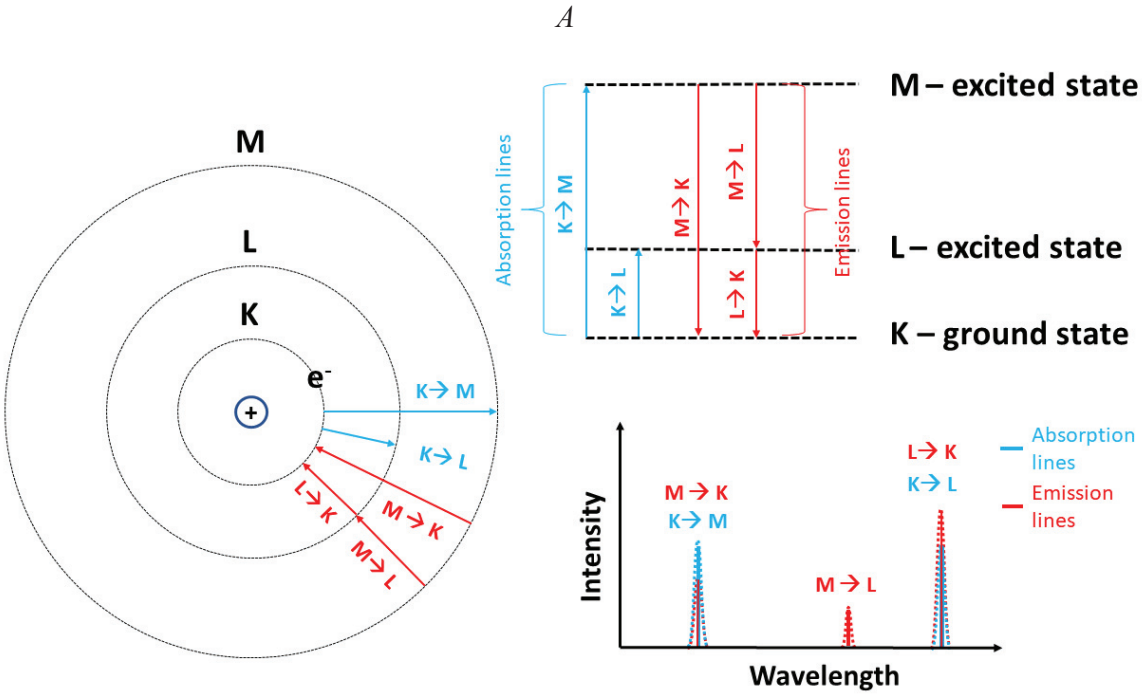

Figure 3.2 - A simplified schematic of the discreet electronic energy states in an atom. The blue transitions show photon absorption and the red, photon emission.

As the photon is absorbed, the species finds itself in an excited state, meaning the electron of the molecule is not at the lowest energy level. In various fields of spectroscopy, different units and notations are usually used (SI notations for energy is J – joule; also used; eV, cm^{-1}), however for the purpose of this thesis we will use (unless otherwise specified) the units - nm for specifying the wavelength λ to describe the photon energy. These are connected by the Planck-Einstein relation; $E = hf = h * c/\lambda$, where h is Planck's constant, c is speed of light in vacuum and λ is the wavelength of the photon. We can see that photons of lower wavelength carry more energy. Also, from quantum mechanics principles, we know that energy of electrons around an atom is only allowed in discreet energy levels. Due to the electron confinement around the nucleus (can be simplified as a potential well) the allowed energy states are called the **electronic states**. This means the electron in such a system (Figure 3.2) can only absorb a photon of specific energy which will

allow the transition to the higher energy state (K→L or K→M). Radiative relaxation should follow the reverse route (L→K or M→K), with an additional emission peak appearing due to the M→L transition. Since atomic spectroscopy is a complicated field by itself [114], we will omit it from further discussion and use this rudimentary example.

In reality, there are many effects (Natural, (thermal) Doppler, pressure - broadening [115], [116]) that can cause these lines to broaden, leading to more commonly observed spectra. The most prominent of these would be the formation of chemical bonds. From the laws of thermodynamics, we know that Nature strides to the lowest energy state. When atoms combine into a molecule they are doing exactly the same, the reduction of their overall energy. This is also why most matter (at standard conditions) is found in molecular not in its constituent atomic form. When forming a bond, the constituent atoms are "sharing" electrons. From Heisenberg's uncertainty principle ($\Delta E \Delta t = \Delta p \Delta x \geq \frac{h}{4\pi}$), this sharing of electrons expands the electron distribution volume of the valence electrons, creating a lower energy level ($\uparrow \Delta x \rightarrow \Delta E \downarrow$) [117]. This forms an energy favourable bonding and an unfavourable anti-bonding energy level.

When discussing photoluminescence in fluorophores, it is common to talk about the highest occupied and lowest unoccupied molecular orbitals (former **HOMO** and latter **LUMO -** Figure 3.3). An elegant way to demonstrate the molecular orbital model is with a formaldehyde molecule (Figure 3.3), since it contains all of the most common bonds in organic dyes[24]. This can lead to the singlet-singlet and triplet-singlet transitions. The electronic transition energy is commonly in this order [118]: $n \rightarrow \pi^* < \pi \rightarrow \pi^* < n \rightarrow \sigma^* < \sigma \rightarrow \pi^* < \sigma \rightarrow \sigma^*$.

The analogy can be made to the electrons in the valence (for HOMO) and conduction band (for LUMO) when discussing solid state emitters. The conduction band for isolators and semiconductors is empty, as would be the HOMO of the molecule in ground state. A molecule in excited state would be equivalent of populating the conduction band. The d → f transitions would in this case present the spin allowed (singlet-singlet) and f → f the spin forbidden (singlet-triplet) transitions. Returning to the luminophore[25] example; as opposed to an atom, a molecule will also have vibrational and rotational motion, affecting the electron distribution around it.

[24] n – nonbonding electrons, σ – sigma bond (s-s, s-p, p-p), π – pi bond (p-p with colinear axis symmetry)
[25] Molecule exhibiting luminescent properties.

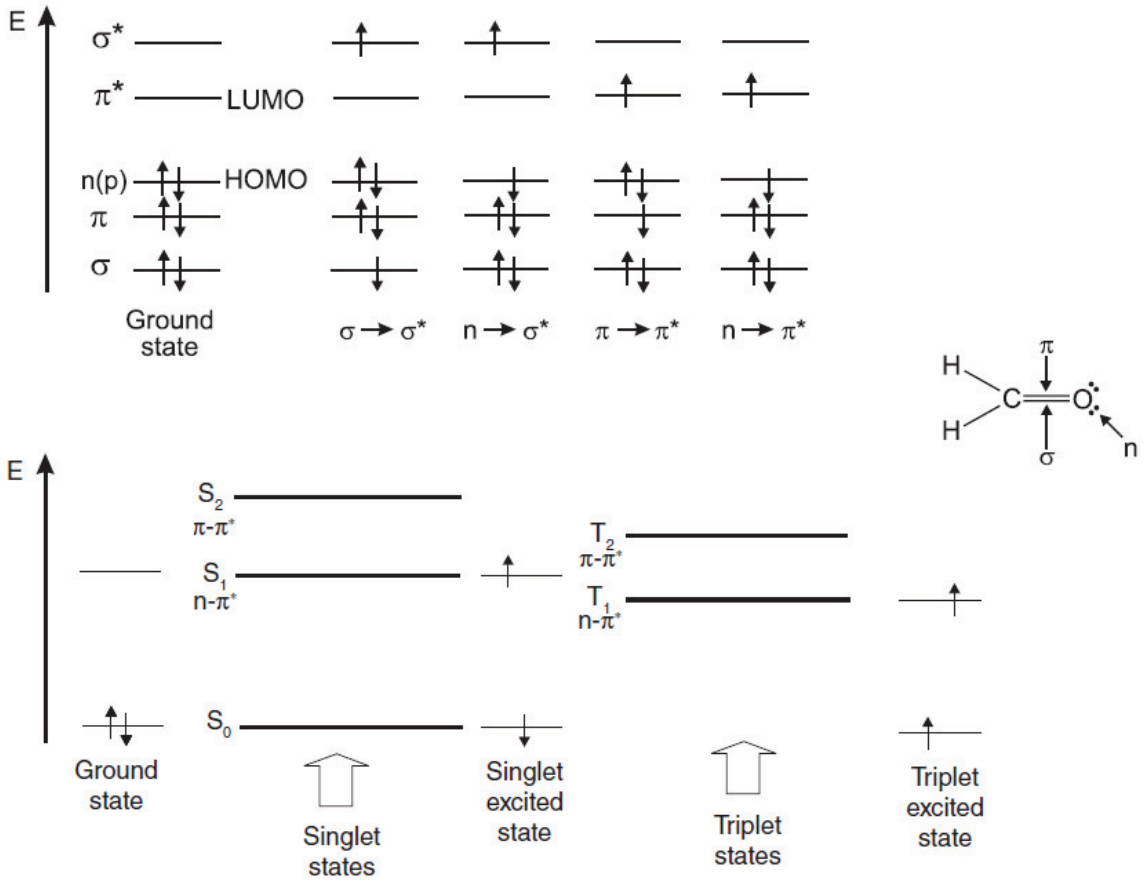

Figure 3.3 - HOMO/LUMO of formaldehyde molecule and the singlet/triplet excited states. Image adapted from [106].

Therefore, in addition to the electronic states, molecules will have additional sub-levels called **vibrational** and **rotational energy levels**. At 0K most of the population will tend to the lowest energy state (v=0) within the electronic state, due to the rapid vibrational relaxation mechanism and the distributions between the vibrational levels. As the ambient temperature rises, the probability of populating higher vibrational/rotational levels rises in respect to the thermal energy. This is an important aspect of luminescence, as the electron population in the available states follows **Boltzmann distribution** [118]:

$$\frac{N_1}{N_0} = \exp\left[-(\Delta E)/k_b T\right] \tag{3.1}$$

where N is the number of molecules in the 0 and 1 a given state (electronic, vibrational, rotational), ($\Delta E = E_1-E_0$), k_B – Boltzmann constant [1,3807 * 10^{-23} J/K] and T – absolute temperature [K] and the product of the two is the thermal energy[26]. The latter indicates the temperature dependence and the effect it can have on the spectra, as the probability of emission and excitation from different levels opens up. Therefore, as the ambient temperature becomes non-zero, the excitation and emission spectrum will tend to red shift. One phenomenon linked to the discourse of population distribution is the spectral overlap between the emission and excitation spectrum (seemingly violating the energy conversion principles) example in Figure 3.5 (grey overlap area). However, at room temperature, there will be population of states above the ground vibrational state, in the excited and ground electronic levels, accounting for the deviation from Stokes law [118]. This discrepancy vanishes at lower temperatures.

As we will see later on (Table 3), radiative relaxations are orders of magnitude slower compared to vibrational relaxations, leading to the population of the lowest vibrational states. This is the premise for **Kasha's rule**, where the absorption and emission occur from the lowest vibrational energy level within the electronic state. As a consequence, the excitation wavelength generally doesn't influence the emission spectrum. The close spacing of the levels vibrational and rotational levels leads to the spectrum becoming a broad peak. Generally, the excitation and emission spectrum should follow a mirror symmetry, since the vibrational and rotational levels should be alike (Figure 3.4). However, according to the **Frank-Condon principle** the absorption of the electron is virtually instantaneous (vertical transition) compared to the nucleus reaction. The probability of a transition occurring depends on the square of the vibrational wave function overlap of the different vibrational modes between the two electronic states [118]. Vibrational relaxation, as we will see later on, is a fast process, since the transition between two consecutive levels is highly probable, due to the strong overlap between neighbouring levels. Therefore, when the nucleus responds to the absorption (Δq) the emission no longer mirrors the absorption band (Figure 3.4), due to the different proportion of probability density functions. The existence of additional vibrational and rotational sublevels in the electronic state, broadens the excitation/emission spectra

[26] The thermal energy k_BT is often regarded as an energy scale factor in molecular systems. Being roughly 4,045 *10^{-23}J or 25,25meV at 20ºC.

of luminophores. Due to slight differences between their kinetic energy, even these levels broaden usually leading to a spectral overlap and a broad peak appearing. And more importantly for us, these sublevels are susceptible to their surroundings.

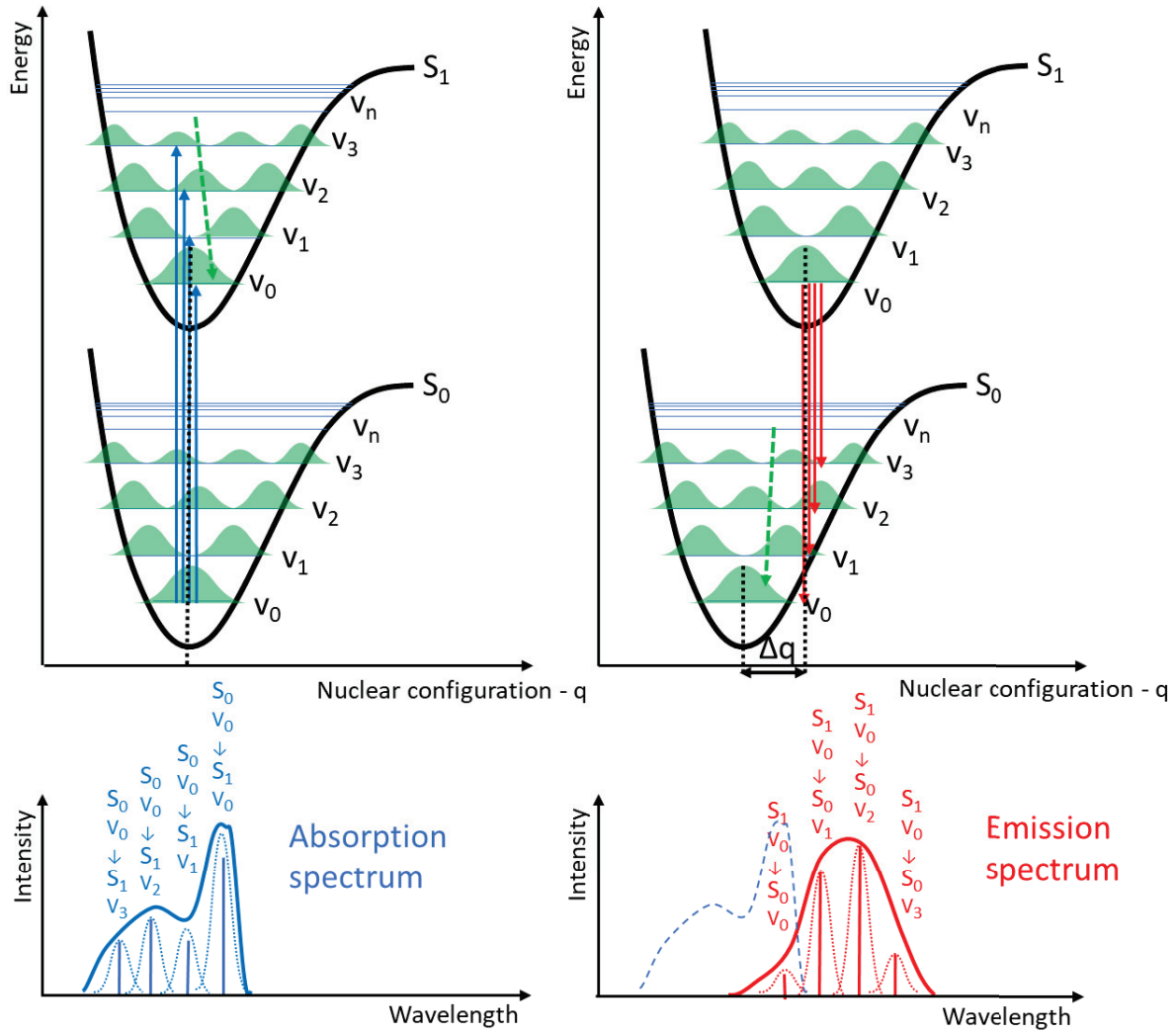

Figure 3.4 - Schematic representation of the Franck-Condon principle and Kasha's rule. On upper graphs the green filled shapes represent the electron distribution in different vibrational levels in an electronic state (S). The greater the overlap of the distribution functions the favorable the transition is (absorption/emission). The green arrow shows the vibrational relaxation after absorption will bring the electron population to the v_0 state, from where the emission will occur. Below the theoretical spectra of a fluorophore in dissolved (broad) and vapor (line emission) state.

.

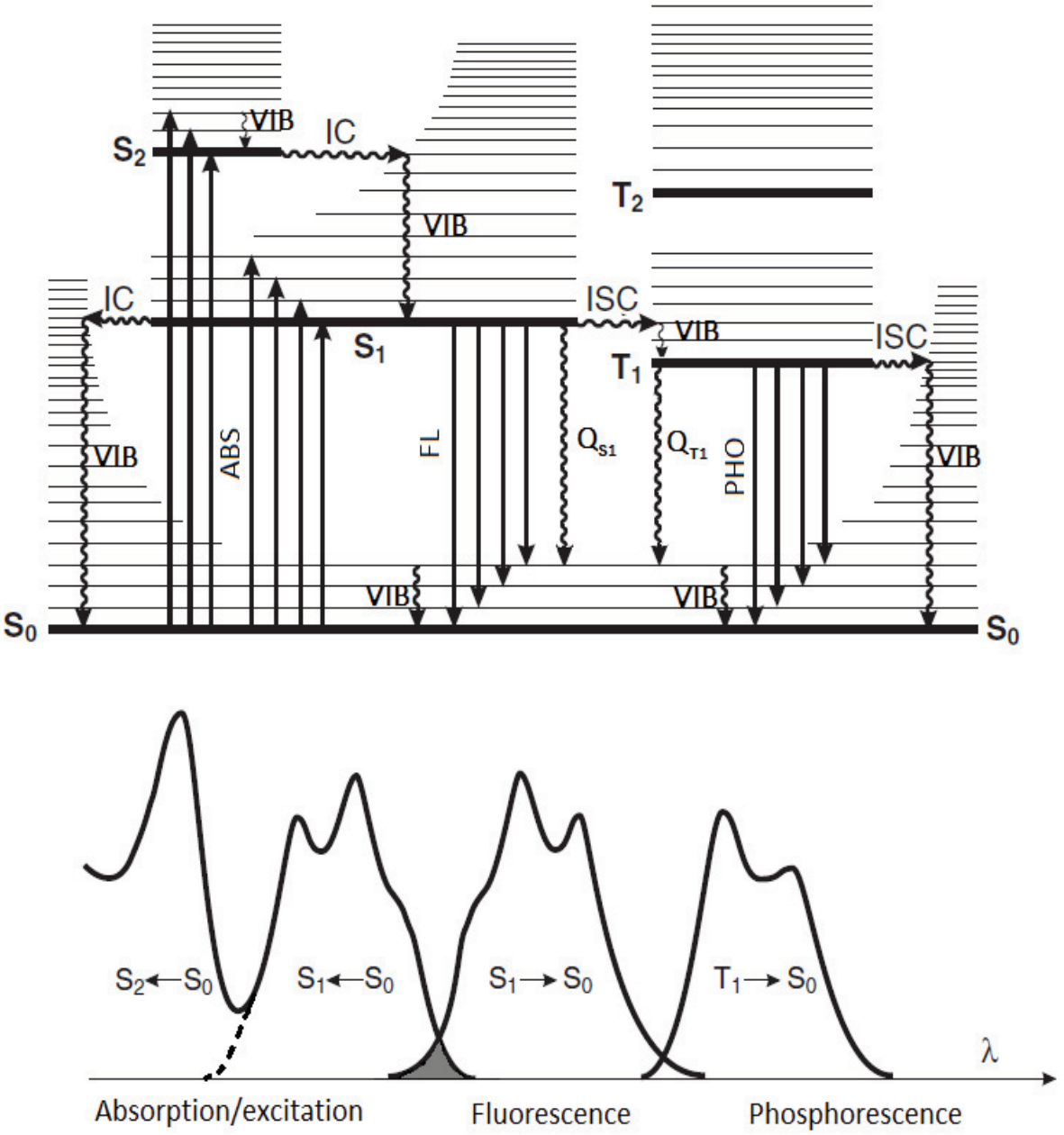

Figure 3.5 - Jablonski diagram and corresponding spectral peaks. Electronic states (S – singlet, T – triplet; subscript 0 – ground and 1,2 for excited) presented in bold horizontal lines, while fine lines mark the vibrational/rotational states. Wavy arrows present non-radiational transitions (VIB – vibrational relaxation, IC – internal conversion, ISC – intersystem crossing, Q – quenching (subscript S1 – singlet, T1 – triplet)) and straight arrows the radiational relaxation (absorption, fluorescence and phosphorescence). Grey area on spectrum is the excitation/emission spectral overlap. Image adapted from [118].

The assortment of energy transitions possible to an excited electron can be found in Figure 3.5 and is described below. As was indicated earlier in the text, the photo-luminescence process starts with **photon absorption** (ABS)**.** This is the excitation process that brings the electrons to the higher energy levels. The excitation spectrum of a fluorophore usually follows the absorption spectrum, with a decrease in the intensity for the peaks that don't lead to emission. An important aspect of absorption is its extremely fast nature (femtoseconds) in respect to other mechanisms (Table 3), as shown before with the Franck-Condon principle. From here on different de-excitation or relaxation mechanisms take hold. Commonly, most non-luminescent species go through the non-radiative transformation of the absorbed energy into heat. The rapid **vibrational relaxation** (VIB)[27] (sometimes called external conversion) occurs as the electron falls down the energy diagram through different vibrational/rotational states, releasing energy in the form of heat passing it along to the environment as it thermalizes. Due to the energy conservation laws, the removal of heat from the molecule to the environment is the limiting factor, controlling the rate of relaxation. After the relatively fast transition through the vibrational states, the electron then pauses at the lowest states[28] where it can undergo radiative relaxation or **internal conversion** (IC), which is a non-radiative transition to a lower electronic state (in solvents usually followed by VIB). **Fluorescence** (FL) is radiative relaxation between two electronic energy states of the same spin multiplicity [118]. In fact, for the most part, fluorescent transitions occur from S_1 to S_0, with a characteristic lifetime in a few ns range.

Quenching is the mechanism describing many paths of de-exciting the molecule/atom following absorption, effectively decreasing fluorescence intensity either by depopulation or reduction of **quantum yield**[29] [118], which is the radiative energy conversion efficiency of the emitter. Some examples of these are; ground state non-fluorescent complex formation, paramagnetic species or heavy atom collisions, energy or **charge transfer** (electron, proton). It can be roughly divided into **static** and **dynamic** (or combination of both) quenching, both of which require molecular contact of the quencher with the excited molecule [119]. As can be seen it's highly or entirely dependent on the environment, therefore it can also yield information regarding the fluorophore surroundings (use in biological systems) [118].

[27] Sometimes refered to as external conversion.
[28] Governed by Boltzmann distribution
[29] Quantum yield = QY = radiative relaxation probability / (radiative + non-radiative relaxation probability)

Table 3 - electron energy conversions and relaxation mechanisms characteristic times [113].

Transition	Energy conversion mechanism	Characteristic time	Comments
$S_0 \rightarrow S_1$ (or S_n)	Photon absorption – ABS / emission - EM	10^{-15} s	Absorbing/emitting a photon and exciting an electron to a higher energy state
$S_1 \rightarrow S_1$	Vibrational relaxation - VIB	10^{-12} to 10^{-10} s	Heat dissipation in form of vibrational/rotational energy
$S_1 \rightarrow T_1$	Intersystem crossing - ISC	10^{-10} to 10^{-8} s	Common for heavy elements – I, Br, …
$S_n \rightarrow S_1$	Internal conversion - IC	10^{-11} to 10^{-9} s	
S_1 (or S_n) $\rightarrow$ S_0	Singlet (S) excited state lifetime – Fluorescence	10^{-10} to 10^{-7} s	
$T_1 \rightarrow S_0$	Triplet (T) excited state lifetime - Phosphorescence	10^{-6} to > 100 s	Common for heavy elements – I, Br, …
S_1 (or S_n) $\rightarrow$ S_0	Non-radiative relaxation Quenching Singlet	10^{-7} to 10^{-5}	
$T_1 \rightarrow S_0$	Non-radiative relaxation Quenching Triplet	10^{-3} to > 100 s	Common for heavy elements – I. Br, …
$T_1 \rightarrow S_1 \rightarrow S_0$	Delayed fluorescence	Fluorescence + Phosphorescence times	

Oxygen is a well-known quencher for most fluorophores, by causing them to undergo **intersystem crossing** (ISC) into the long-lived triplet state. This leaves them vulnerable to collisional quenching with solvent molecules [119]. Most molecules in their basic form are at the singlet state[30], meaning the occupying electrons are of opposite spin, making the overall (2S+1; +1/2 -1/2 → S=0) spin state = 1 or a singlet state. The singlet to triplet transition (ISC) is denoted as a "forbidden", meaning that it is less likely[31] to occur. However, due to the spin-orbit coupling, ISC is particularly favourable for heavier atoms (high atomic number – exp: Br, I, Au Ag, Cu,..). After the crossing, another form of radiative relaxation can occur, called **phosphorescence** (PHO), which has considerably longer lifetimes, spanning even into seconds and more. As indicated before, the characteristic times expose the excited electrons to quenching effects, therefore generally speaking phosphorescence has lower quantum yields (except when shielded from

[30] Molecular oxygen is an example of an exception, being in triplet state.
[31] But not impossible,as the name implys.

quenching effects – rigid crystalline structure or low temperatures for example), than its singlet counterpart fluorescence. Due to the lower energy level of the T* state it's also attributed with a higher wavelength of emission [118]. Furthermore, the reverse transition (ISC) is possible, populating again the S_1 electronic level, yielding the so-called **delayed fluorescence (**characteristic times linked to phosphorescence + fluorescence). This mechanism will produce the same emission spectrum, as the relaxation is occurring from the same S_1 level as fluorescence.

Another energy transfer system worth mentioning is **FRET** – Förster resonance energy transfer. If two emitters have a good overlap of the emission/excitation spectra and are found within a critical radius (Förster distance[32]), an inter molecular energy transfer may take place. The spectral overlap requirement may at first be misinterpreted as the emission and absorption of the electrons at close range, however it is indeed a non-radiative transfer[33]. Often used in biology or chemistry as a spectroscopic ruler in the 1 to 10nm range [118], as the technique is extremely sensitive to separation distance[34]. A related phenomenon (CRET – chemiluminescence resonance energy transfer) is discussed in chapter 5.2.1 and 7.4.

[32] Intermolecular distance where a 50% of radiative relaxation and 50% for the energy transfer probability exists.
[33] Dipole-dipole coupling [118].
[34] $(1/d^6)$ – d being the distance between the molecules.

3.2. Probing the local environment

Figure 3.6 shows the possibilities of the excitable molecule after photon absorption. For remote sensing the preferred method is to use photoluminescence, since excitation can be induced by a simple light source and the light produced can be orders of magnitude larger compared to other radiative mechanisms, like Raman scattering. The excited species going through energy conversions will reemit at a lower wavelength in accordance with Stokes law[35]. The reflected or transmitted[36] excitation light can be filtered out by a long pass filter leaving just the part of the lower energy part for analysis.

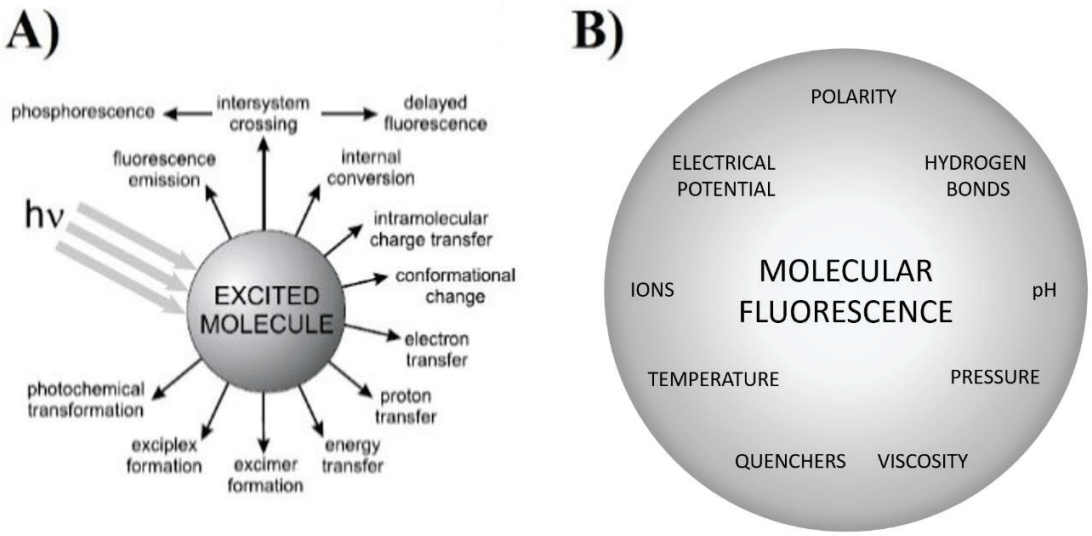

Figure 3.6 - A) possibilities for relaxation mechanism following a photon absorption. B) parameters with possible effect on fluorescence from excited molecule. Image adapted from [106].

In principle, any perturbations of the outer most electrons (HOMO, LUMO) should yield a luminescent response. As shown in Figure 3.6 B), chemical (ions and chemical species, pH, hydrogen bonds, …) and physical (temperature, pressure, viscosity, electric potential, polarity) factors can all do just that, inducing intensity or spectral variations which opens the possibility to

[35] The energy displacement between the excitation and emission maxima is called the **Stokes shift**
[36] Depending on the setup. Infact usually the acquisition is done at a 90º degree angle to alleviate this problem, however elastic scattering remains.

measuring one or more of these parameters. For example, many fluorescent dyes have pH dependent emission [118].

According to the kinetic theory (Boltzmann distribution) temperature is proportional to the average kinetic energy of the constituent particles in the measured medium (atoms, molecules, electrons…). So, it stands to reason that this quantity will be a prominent factor describing interactions between particles at microscales and below.

Many properties are temperature dependent, in fact often measurements of other parameters have to be adjusted for the temperature (pH for example). However, that also means many measurable properties can be proportional to temperature, making them useful for thermometry (resistance, refractive index, thermal expansion, infrared radiation…). Indeed, the temperature is always measured indirectly via other properties. This definitively holds for luminescence thermometry.

Temperature influences many relaxation processes. It's said that any luminescent system will have some temperature dependency, either simply by ground and excited level population or more complex systems like dynamic quenching (exp: rhodamine B [120]) or inhomogeneous broadening (effects on vibrational/rotational levels).

Broadly speaking, due to the intrinsic properties of the energy level population following the Boltzmann distribution, any luminescent system with two or more energy levels is effectively capable of determining the temperature [121]. But what makes a **good luminescent temperature probe:**

- Sensitivity, temperature resolution and the dynamic range suitable for the temperature range we are interested in (valid for any thermometer). Sensitivity usually helps with the signal to noise ratio (SNR).
- Repeatability and chemical stability to environment, which are often closely linked,
- Non-intrusiveness/non-invasiveness of the probe introduction to the measured system – no or limited perturbations of the system being measured. Essentially smaller probes or even intrinsic emitters (Raman) would perturb least the measured system.
- Quantum efficiency, Temporal and spatial resolution – a strong and fast emitter can help with the SNR.

In practice, time integrated (ratiometric intensity measurements) or time-resolved (luminescence lifetime) are most commonly used due to their self-referencing properties. This makes these methods independent on concentrations of the emitters and changes in measurement conditions, as the temperature information is obtained from a ratio of intensities and the lifetimes, respectively [122]. Two examples of these self-referenced temperature measurement systems are given:

- The first is the time resolved measurement [123]. A specific defect in the crystalline structure of microdiamonds (S3 defect: N-V-Ni-V-N) is responsible for producing two closely spaced (ΔE=0,114eV) and highly luminescent energy levels, with luminescence lifetimes orders of magnitude apart (~100ns and ~300μs). As shown in Figure 3.7, this can be used for high frequency temperature acquisition (100Hz), throughout a wide temperature range (120K to 900K) with accuracy of 1K. The micro sized probes with high thermal conductivity of monocrystalline diamond (2200W/(m K)) allows for fast thermalization. As the temperature increases the k_BT follows, affecting the population of the closely spaced levels and their lifetimes. The drawback is that the accuracy depends on the number of photons collected. The higher the excitation rates, lower the standard deviation of the measurement. Furthermore, as the lifetime increases with cooling, the excitation rate must be adjusted, slowing down the acquisition at lower temperatures.

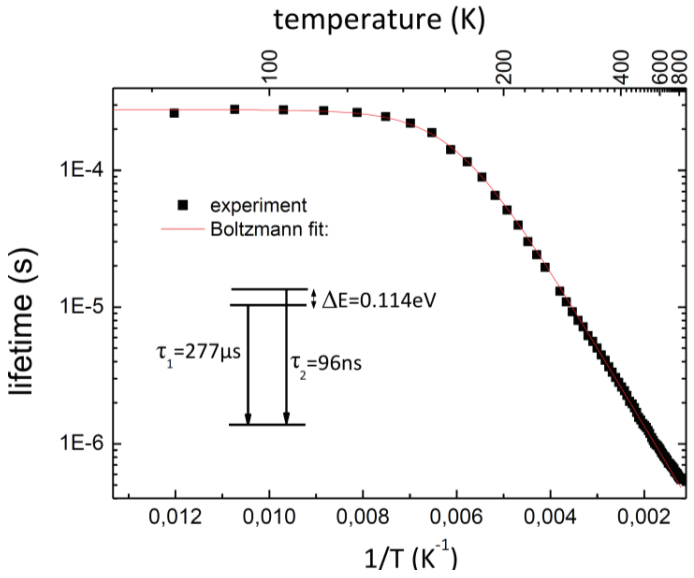

Figure 3.7 - Lifetime of emitting system plotted versus the inverse temperature. The measured points follow nicely the Boltzmann fit. The closely separated energy levels schematic showing the different lifetimes of each and the energy gap between them. Figure taken from [123].

- The second example is a pair of rhodamine dyes commonly used in liquid thermometry. For ratiometric intensity measurements, ideally an emitter or an emitting system with a stable peak and a peak varying with temperature is desired. While you can get complex multi-peak emission from an emitter, you can also combine two fluorophores with those properties. An often used example is the Rhodamine B and 101[37], the latter being temperature insensitive, while the former's emission intensity drops significantly from 10ºC to 60ºC [122]. Rhodamine B intensity is modulated by dynamic quenching while the effect on the reference Rhodamine 101 is significantly lower. Also, both organic dyes are good emitters, producing a strong intensity signal, helping with the SNR. This can either be implemented for improving accuracy by signal accumulation or speeding up the acquisition, gaining in temporal resolution. The disadvantage of this method is that presence of two dyes gives way to concentration variations as the ratio of probe concentrations should remain constant, in order not to affect the spectrum. Either photobleaching or other chemical reactions can cause such discrepancies, prompting a need for recalibration or remake a new batch of solution.

In summation, many luminescent temperature probes exist, covering the temperature range from cryogenics to flame or plasma analysis. There is however, no universal temperature probe, it's left to the user to determine what properties can be sacrificed to gain in others.

Luminescent **pressure probes** however are harder to find. Some luminescent paints have been developed, allowing for simultaneous temperature and pressure determination [124]. Their studied pressure range is ambient (+/- 1bar) gas atmosphere. However, these paints rely on quenching mechanisms (oxygen quenchers), which might not be applicable for probing a liquid environment.

Alternatively, micro-balloon pressure probes are suited for liquids and the pressure range used in low-pressure microfluidic devices (1-2bar), as they rely on the deformation of the gas filled volume and its subsequent optical response (Fabry-Perot resonator) [125]–[127]. However, the

[37] Also, Sulphorhodamine versions of these dyes can be used which are better suited for some chemical environments. Furthermore, the reference Rhodamine 101 can be replaced by Rhodamine 110, to yield similar results.

complicated manufacturing, limited lifetime and pressure operating range, as well as their fixation on the vessel walls, limit their use.

Ruby (Al_2O_3:Cr) fluorescence (R1 line) is often used for determining pressure in high isostatic pressure conditions [128]. The R1 red-shift is detectable only at high pressure – compression of the crystalline structure (due to the high bulk modulus of ruby), shifting linearly with increasing pressure [129]. Coupled with the chemical inertness makes it a suitable pressure gauge for diamond anvil cells, however not useful below roughly 500bar. Some rare earth doped materials have also been used as so called "luminescent manometers" [122].

Unlike the myriad of luminescent materials exhibiting temperature dependent emission, pressure responsive luminophores are rare. It's clear that a reliable and easy to implement luminescent pressure probe for the intermediate pressure range in microfluidics (1-100bar) is hard to find.

In hope of filling the gap, a new family of materials was tested – d^{10} metal (Au, Ag, Cu) thiolate coordination polymers [130] in the following chapter 3.3. These are luminescent[38] materials, with the luminescent properties originating from intra and inter molecular interactions in the crystalline structure. The working hypothesis was that pressure could perturbate the crystalline structure, causing a spectral variation in response to pressure stimulation. A previous study on a similar family of materials, showed significant peak shifts as the pressure increased [132]. It was believed that the relatively soft crystalline structure of these coordination polymers would make them an interesting material for pressure sensing applications.

[38] Some highly luminescent with up to 70% quantum efficiency [131].

3.3. Coinage (d^{10}) metal – thiolate coordination polymers under different thermodynamic parameters

The motivation for this work was to use the luminescent properties of d^{10} metal (Au, Ag, Cu) (I) thiolate coordination polymers as pressure probes. The basis for the idea was the fact that the luminescent properties originate from metalophilic interactions in the molecule and the crystalline structure. Therefore, it's believed that any perturbations on the crystalline structure should be detectable in the spectral response [132]. If the polymer structure is soft enough, the spectral response could foreseeably yield a detectable spectral perturbation, which can then be used as luminescent pressure probes.

The metalophilic interactions, resulting from the relatively strong effect of metal atoms in metal-thiolate coordination polymers and in some cases ligand hydrogen bonds, are the main driving forces behind the polymer's self-assembly properties [133]. These metalophilic bonds can also influence the photoluminescent properties in such compounds [134]. Thiolate ligands also have luminescent properties [135] and they have an important role in the crystallisation process [133]. Primarily they are used for functionalization of gold cluster and nanoparticles [136]. Other uses are in medicine and pharmacology, where Gold (I) thiolate coordination polymers are used as a treatment for rheumatoid arthritis [137], demonstrating their non-toxicity.

Several articles were published on this body of work [131], [135], [138]–[140]. Often these samples were studied as a function of varying temperature in hope of better understanding the energy transitions and underlying relaxation mechanisms in these complex systems. At the end we also show some preliminary results on pressure variations.

3.3.1. Spectroscopy of luminescent species

In the following subchapter the experimental setups used for characterising the samples are presented in sequence. Further along in the text, the reader might be referred to devices (figures) in this sub-chapter.

When talking about photon absorption and the different radiative mechanisms that follow, one would use a **spectrofluorimeter** to characterise the **excitation** and **emission spectra** of an emitter.

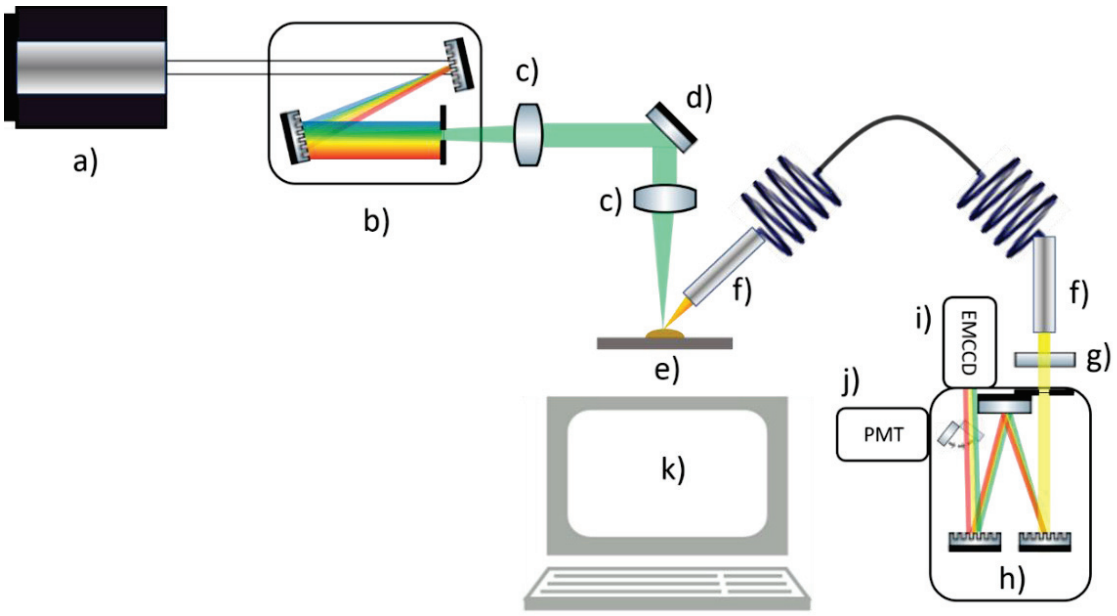

Figure 3.8 - Excitation emission spectrometer. a) to d) – laser driven xenon lamp with monochromator for excitation wavelength selection; e) sample; f) to j) – acquisition line (optical fibre, analysis monochromator, detection device (EMCCD and PMT); k) excitation/emission spectrometer control. Devices specified in Table 7.

The former is a plot of the intensity of the emission spectrum as a function of excitation light, while the latter shows the energy distribution of the emitted light at a specific excitation wavelength. Figure 3.8 shows the homemade spectrometer, with a broad emission laser driven xenon lamp (a) for variable excitation wavelengths. Using optical gratings, the monochromator (b) disperses the broad emission light. It can then be spatially filtered by the use of a narrow slit to select specific (bandwidth and central) wavelength, which will be the excitation light source. The light is then passed through a series of lenses (c) and mirrors (d) to be focused onto the sample (e) positioned on a non-luminescent silicon wafer. The emitted light is collected by a multimode optical fibre (f) and transported to the acquisition monochromator (h) for spectral analysis. Before the entrance a variety of filters can be selected, in order to cut the reflection and higher order diffraction of the excitation light. An EMCCD (i) or a photomultiplier tube (j) can be selected for the detection system. The combination of the optical grating and the CCD sensor will define the spectral resolution and range, while the slower point by point measurements of the more sensitive PMT detector will mechanically prescribe those parameters and will not be limited in range by the

grating. The device is calibrated for excitation power variation[39] – excitation lamp correction and the background subtraction is performed for the emission spectrum.

A CW 355nm laser (tripled Nd:YAG) laser can replace the xenon lamp light source (Figure 3.8 – a → r), for excitation in the UV, for species with excitation peaking in this range. The slightly modified setup is mainly used on weakly luminescent samples to increase the signal to noise ratio and produce well defined spectral curves.

As the sample is irradiated by the specified wavelength, the recording is made by the CCD, with the prescribed central wavelength, gain and amplification (binning option). The 16-bit resolution of the CCD limits the acquisition time, as not to saturate the camera. Ideally, the acquisition time would be timed as to make the luminescent signal close to maximum (without saturating). This then allows to add up the signals (number of acquisitions) to improve the SNR, producing smoother spectra. The second option is the PMT (j), which usually takes more time to acquire a spectrum, but due to increased sensitivity it might be more suited for recording weak emitters.

In order to obtain the excitation/emission maps, the resolution parameters are prescribed in both spectra and an emission spectrum is collected for each excitation wavelength used. Due to Kasha's rule the emission spectra should be independent of excitation, however in complex system this is not always the case.

Luminescence lifetime measurements are often used to probe the radiative (and even nonradiative) relaxation mechanisms. Besides spectroscopic analysis (energy domain), the arrival times of the photons (time domain) can also yield information about the probe's environment. A popular characterisation technique in spectroscopy is the so-called lifetime measurements. Using a photomultiplier tube with a pulsed excitation source, we can determine the arrival times of a large number of emitted photons, yielding a curve which after fitting with a n-exponential function, will yield a n – number of characteristic lifetimes. As we saw in the previous chapter, the relaxation mechanisms following the photo-excitation have widely different characteristic times (Table 3). If we can follow the photon arrival times with our instruments, we can probe into the relaxation

[39] Power output at specific wavelength

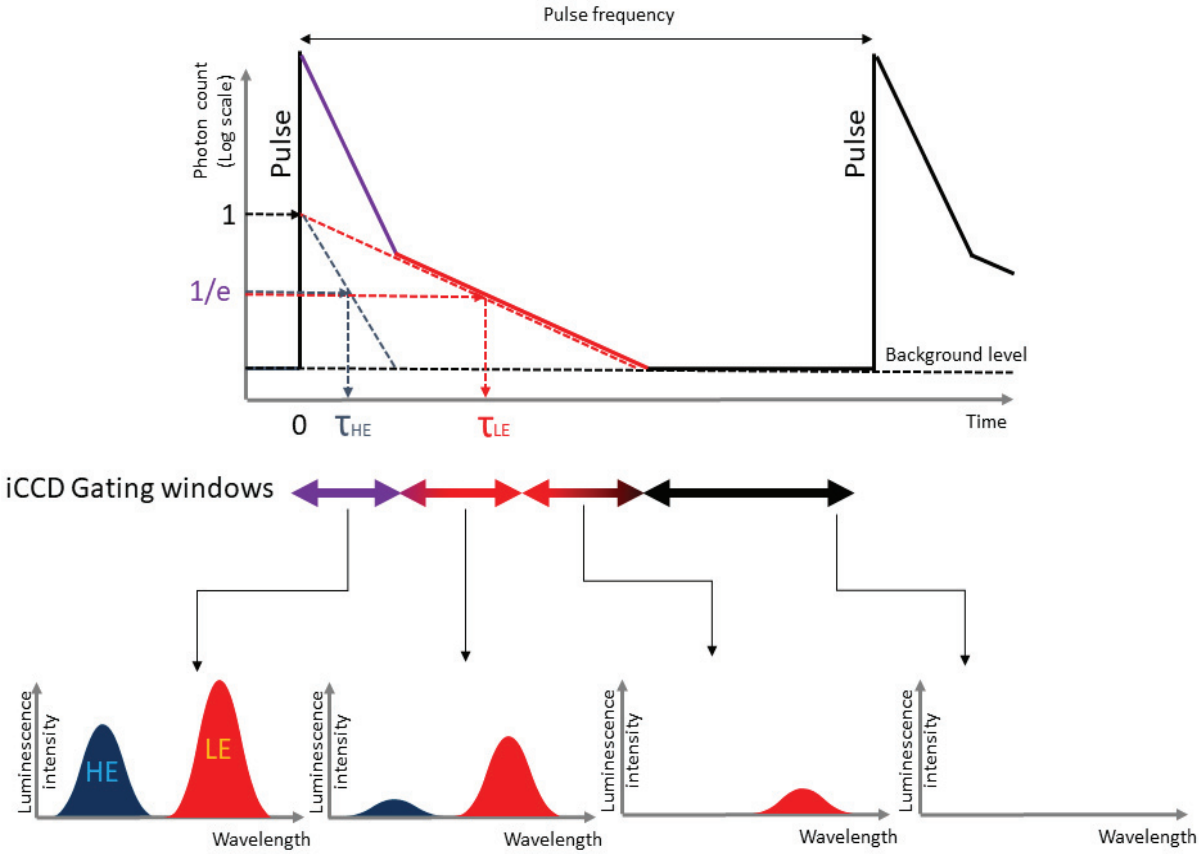

Figure 3.9 – Time-correlated single photon measurements, luminescence lifetime and time resolved spectroscopy schematic. The photons are sorted as a function of arrival time in regards to the pulse arrival time. The dashed lines show the individual exponent functions and the full line their superposition. Below the concept of time resolved spectroscopy is shown; the spectral response of a double exponent function (two radiative mechanism) intensities of the HE and LE (high and low energy) peaks in different gating windows for the iCCD camera.

mechanisms taking place and possibly yielding information about the emitter and its environment. The lifetime value is the time it takes for the (normalized) intensity to fall from 1 to 1/e (36,8% of original value) as shown in Figure 3.9.

The depopulations should be sensitive to quenching mechanisms (dynamic quenching) and therefore to temperature. Fitting the arrival time histogram with exponential functions (Figure 3.9), can yield the lifetimes and through the knowledge of characteristic times (Table 3) for the corresponding mechanisms, the origin can be speculated (fast τ_{HE} → fluorescence, slow τ_{LE} → phosphorescence). This is not always conclusive, as the times can be in the middle ground between

two mechanisms. A single exponential function is indicated by a straight line on the logarithmic scale and as shown in Figure 3.9, where we have a two exponential superposition of lifetimes.

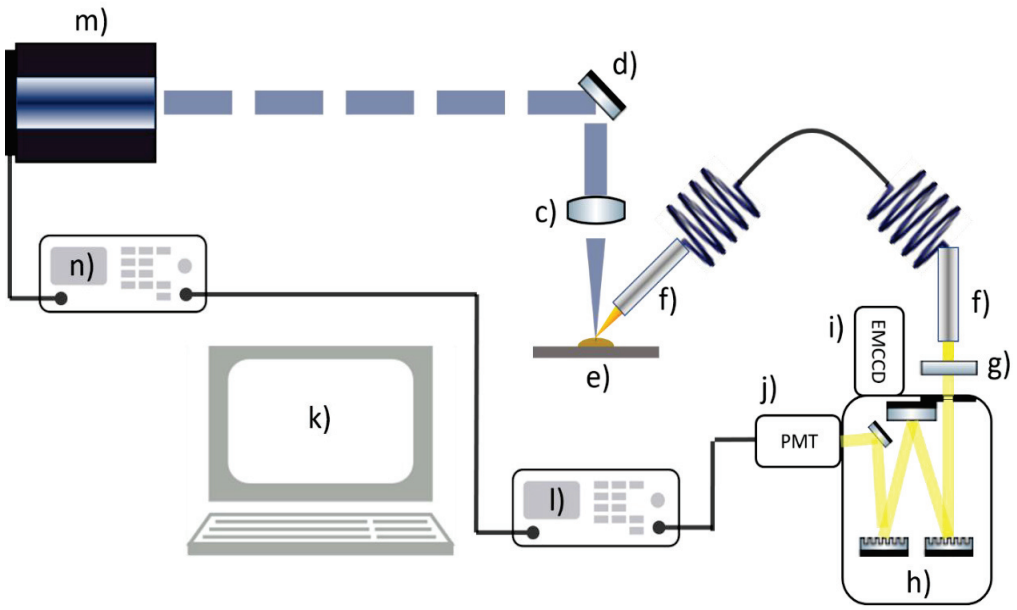

Figure 3.10 - Time-Correlated single photon counting (luminescence lifetime) experiment schematic; m) pulsed laser excitation source with - n) pulse modulation; f), g), o) and p) acquisition line. Devices specified in Table 7.

In the lifetime experimental setup (Figure 3.10), a pulsed laser diode light source (m) of 379nm is used, to create excitation pulses on the sample. The frequency/power modulator (n) is used to control the pulse frequency and power output. A trigger is linked to the multichannel scaler (r), which receives the voltage pulsed signal from the PMT and groups the incoming pulses according to the arrival time. Many pulses are required to draw out the lifetime curve, the weaker the emitter the longer acquisition time required. A pulse leaving the laser triggers the multiplexer recording and hits the sample with a short time delay[40]. The sample is excited and the emitted light is collected by the fibre and passed along through the monochromator (gratings acting as mirrors in this case) to the PMT, where the photons are transformed to a tension pulse. These are then counted by the aforementioned multiplexer.

Time resolved spectroscopy can also be used (Figure 3.11). The excitation remains the same, however an intensified charge-coupled device is used (iCCD) and time dependent spectra can be

[40] Roughly 1ns delay for 30cm of travel in air.

collected. The laser pulse again is used to trigger the recording on the camera. Operating with a fast gating option, the spectrum at a given time delay and width (window) from the laser pulse can be acquired. This can help determine which emission peak corresponds to which lifetime, as is shown in the theoretical two exponential decay[41] in Figure 3.9.

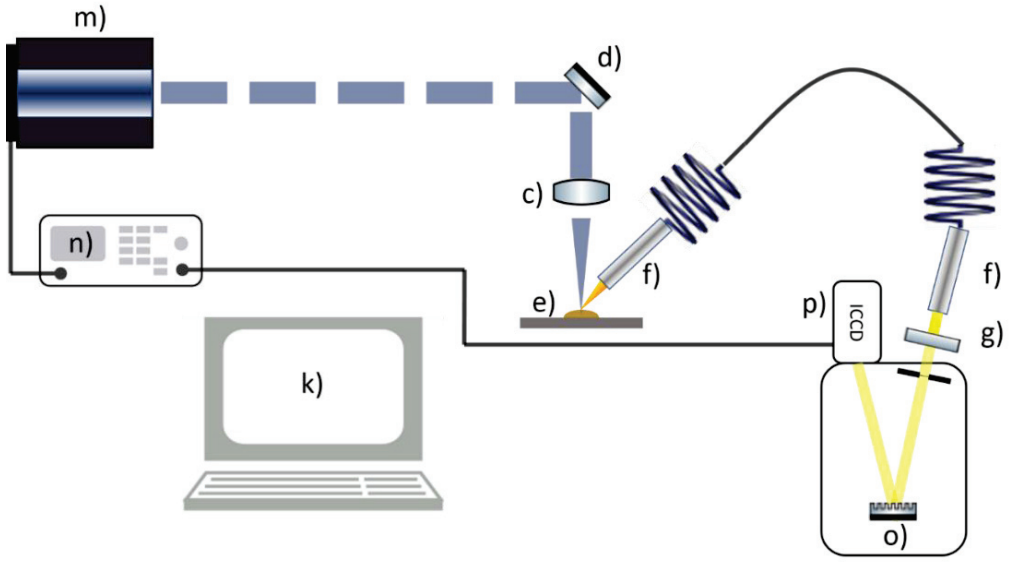

Figure 3.11 - Time-correlated spectroscopy experiment schematic; m) pulsed laser excitation source with - n) pulse modulation, f), g), o) and p) - acquisition line. Devices specified in Table 7.

A Heating/cooling stage is used for the temperature control over the samples (Figure 3.12). It uses a combination of electric resistance heaters and liquid nitrogen flow to modulate the temperature on the sample holder (a). Liquid nitrogen flows from the Dewar (f) through the sample holder, pumped by a cryogenic pump (g). The temperature control (i) keeps the sample at reference temperature (regulated by a thermistor in the sample holder), by modulating the current to the heater and the liquid nitrogen flow. At higher temperatures a water-cooling system (e) is used to prevent overheating of the housing (d). The sample (b) can be probed through the sapphire window (c), which is transparent to wavelengths throughout the UV-vis spectrum. The liquid nitrogen used for cooling (now gas) can be passed through the sample holder chamber to assure an inert, oxygen and water free atmosphere.

[41] Two relaxation mechanism, two lifetimes, two peaks.

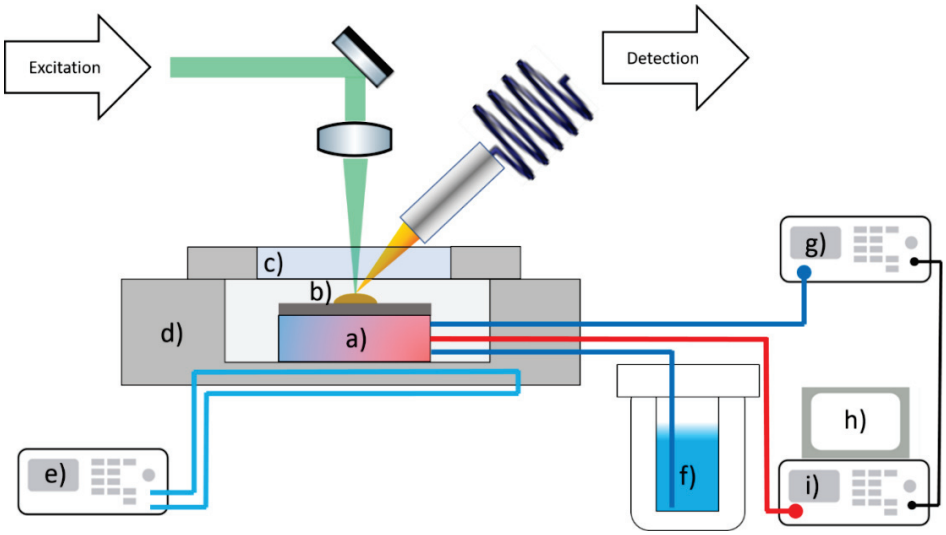

Figure 3.12 – Linkam temperature control system (heating/cooling stage); a) Linkam THMS-600 heating/cooling sample holder with liquid nitrogen lines and electrical resistive heater, b) sample on silicon wafer, c) cover with sapphire optical window, d) temperature control stage housing with water recirculation, e) water recirculation system, f) liquid nitrogen Dewar; Linkam T95-PE system: g) liquid nitrogen pump, h) control module and i) temperature control system.

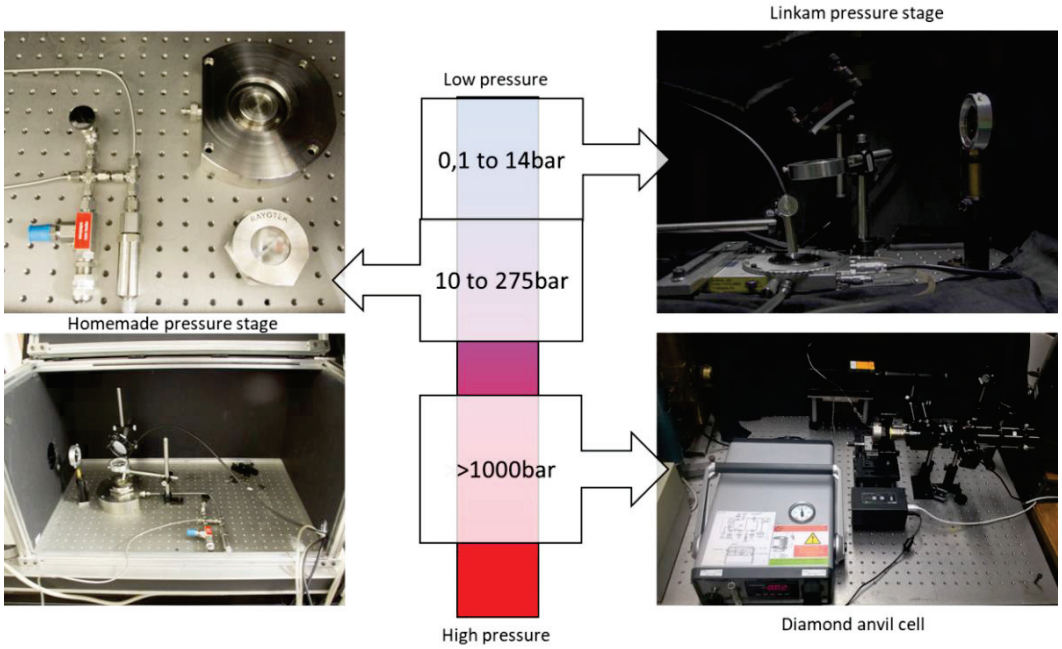

Figure 3.13 – Different pressure stages options covering a wide range of pressures. Upper right image shows the Linkam pressure (nitrogen gas driven) temperature control. Bottom right shows the diamond anvil cell for testing samples at very high pressures (in liquid). Left side shows a homemade pressure stage (nitrogen gas driven).

For pressure dependent luminescent spectroscopy, we need a way to exert a pressure increase on the sample, while leaving an optically transparent window[42] for observations. As can be seen in Figure 3.13, we have at our disposal a pressure/heating cell from Linkam, capable of testing samples at 0,1bar to 14bar. On the other side of the scale, the diamond anvil cell can expose the samples to extreme pressures of several hundreds to thousands of bars. The sample is confined in a small volume of liquid[43], where the interactions with the environment will be different from that of high-pressure nitrogen gas.

Due to a gap in pressure range we conceived a homemade **intermediate pressure stage** (Figure 3.14)**.** A high-pressure sapphire window sight from Rayotek (c), along with the high-pressure back pressure regulator - BPR (h), pressure sensor (e), safety (f) and release (g) valves. A robust housing (d) was constructed of inox steel, allowing us to subject the sample up to 275bar under the direct gas content from the nitrogen bottle.

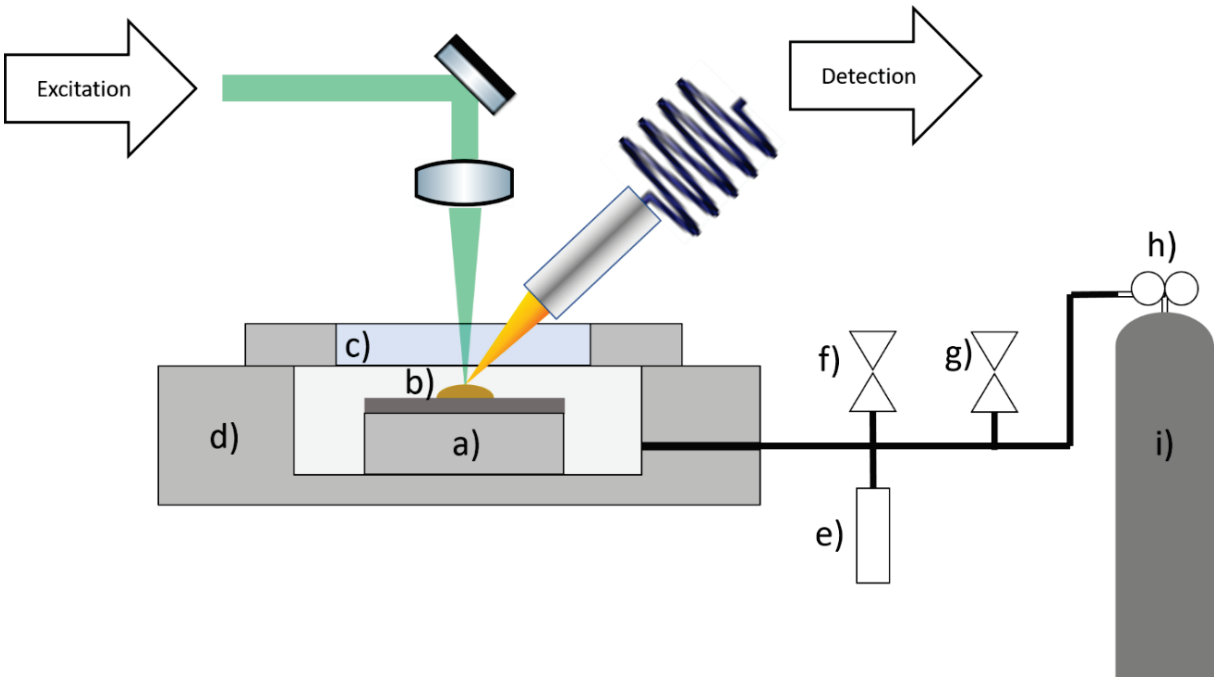

Figure 3.14 – Pressure control sample holder schematic. a) sample holder, b) sample on silicon wafer, c) high pressure sapphire optical window, d) pressure stage housing, e) piezoelectric pressure sensor, f) safety calve, g) relies valve, h) pressure reducing valve and i) nitrogen tank.

[42] Quartz or sapphire, depending on the wavelength range of interest.
[43] Squalene – oil providing isostatic pressure.

3.3.2. Luminescence as a function of temperature and pressure

The work presented here is resulting from a close collaboration with Aude Demessence and Oleksandra Veselska from IRCELyon[44]. The samples were prepared, characterized and structurally analysed by Oleksandra Veselska as a part of her PhD thesis. The luminescence characterization was performed at ILM. Often these samples were studied as a function of varying temperature in hopes to deconvolute the mechanisms behind their luminescent properties from the emission/excitation spectroscopy and time resolved measurements. Several articles were published on this body of work [130], [131], [133], [135], [138], [139], [141], [142] .

In the scope of this thesis, a side project was pursued, where the luminescence properties of these materials would be assessed for their response to pressure variations. As their origin has been traced to the crystalline structure, it was assumed that its perturbation would yield a spectral response. These materials could foreseeably be used as luminescent pressure probes in microfluidic experiments, which was the major motivation behind this work.

Here we present a short overview on the luminescent properties of the thiolates as a function of temperature, in an attempt to determine the relaxation mechanism. Primarily what is shown is the impact of organic ligands in the structure on self-assembly of the coordination networks, influencing geometrical parameters and the rigidity of the structure [143]. In Figure 3.15. we can compare the different coordination polymers (gold +1, silver +1 and copper +1) with the same ligand. The main absorption mechanism seems to be from the ligand (Figure 3.17 – a)), followed by a charge transfer[45] (LL/ILCT for the HE peaks and LMCT + MC for the broad LE peak) and phosphorescence back to ground state. This is expected due to the heavy atom effects, causing spin-orbital coupling and promoting the singlet to triplet transition. This is in agreement with the long luminescence lifetimes (Figure 3.18). On the emission/excitation maps (Figure 3.15), we can observe peaks between 450 and 500nm (High Energy - HE peaks), present on all three compounds at low temperatures. Furthermore, the spectral position seems to overlap with the pure ligand, shown on Figure 3.16, linking the HE peaks to the to the LL/ILCT transitions.

[44] IRCELyon - L'Institut de recherches sur la catalyse et l'environnement de Lyon
[45] Charge transfer abbrevitations: CT – charge transfer, LL – ligand to ligand, IL – inter ligand, LM(M)/ML – ligand to metal (metal) / metal to ligand, MC – metal center.

The vibronic peaks can be observed for the HE peaks in Figure 3.17 – 480nm, 500nm, 530nm, 560nm. For the silver samples, the crystalline structure and the emission/excitation graphs are strongly related, almost identical. However, due to the formation of hydrogen bonds, it is assumed that the higher rigidity of the system gives rise to higher dependency on the excitation wavelength for sample $[Ag(I)(p\text{-}SPhCOOH)]_n$ compared to $[Ag(I)(p\text{-}SPhCOOCH_3)]_n$ [142][46].

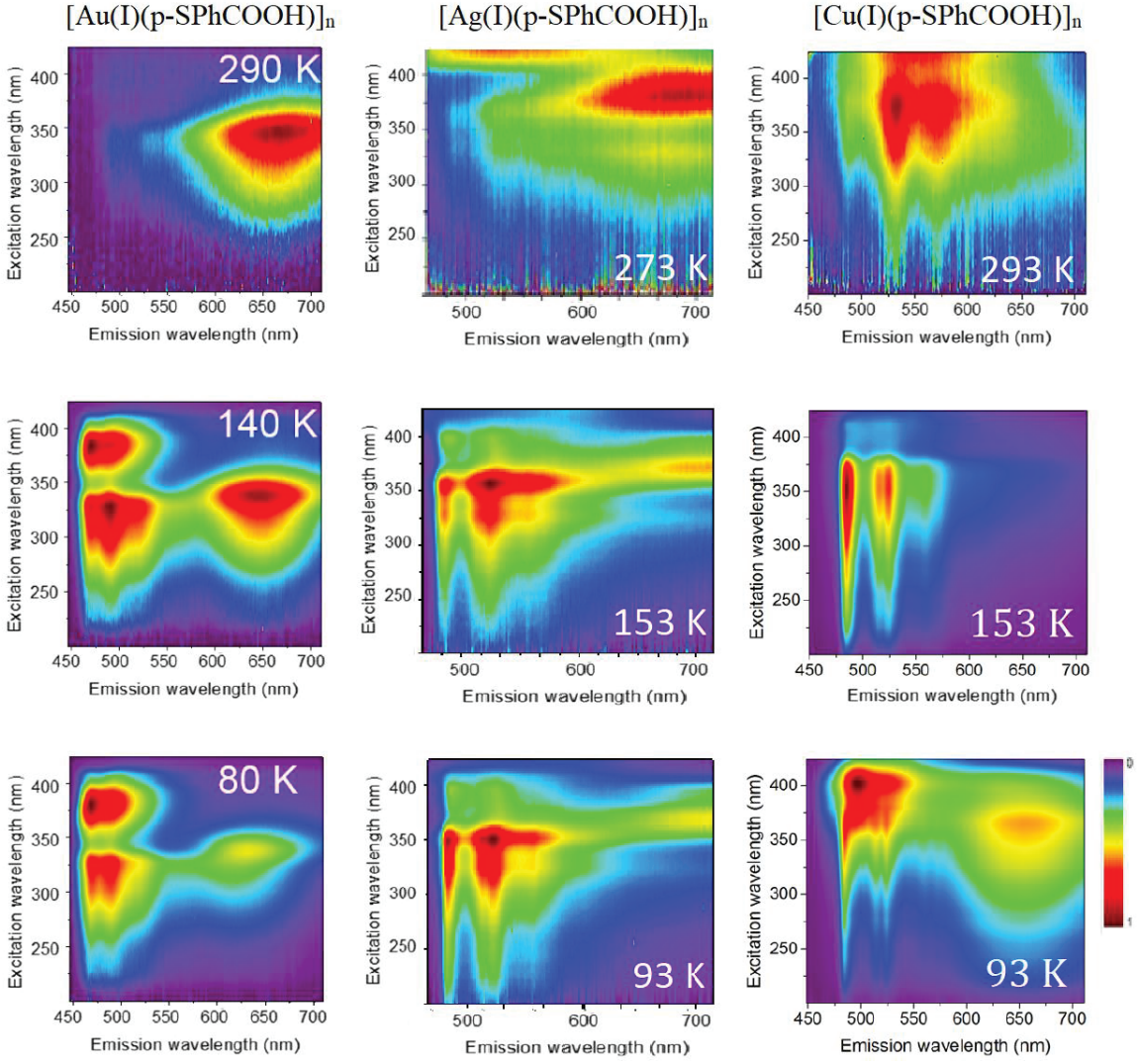

Figure 3.15 - Emission excitation maps at corresponding temperatures, demonstrating the similarities due to the use of a common ligand. High energy (HE) peaks between 450 and 500nm and the rest are the low energy (LE) peaks. Left column presents the[Au(I)(p-SPhCOOH)]n , middle [Ag(I)(p-SPhCOOH)]n and the [Cu(I)(p-SPhCOOH)]n coordination polymer on the right, adapted from their respected publications [135], [143], [142].

[46] Article submitted.

Luminescence lifetimes were obtained by fitting the time-resolved photon distribution curves, measured as a function of temperature (Figure 3.18). On the right the lifetime multiplied by the fitting factor is plotted to yield the proportional light intensity of individual mechanisms. The long characteristic lifetimes indicate T*→S transitions (phosphorescent relaxation). A small contribution of a short lifetime component indicating fluorescent relaxation is present. This component is most likely undergoing ISC and populate the T* states. By using time-resolved spectroscopy (Figure 3.11) the findings of the lifetime measurements are confirmed.

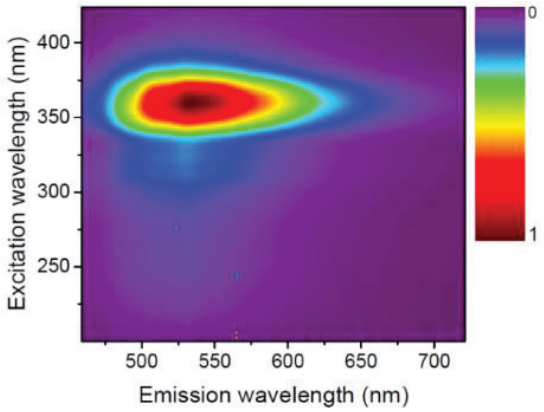

Figure 3.16 - emission excitation map for ligand p-HSPhCOOH at 93K. The position of the emission and excitation peaks seems to be in agreement with the IL/LLCT transitions seen with the metal-based samples. Reprinted from article [135].

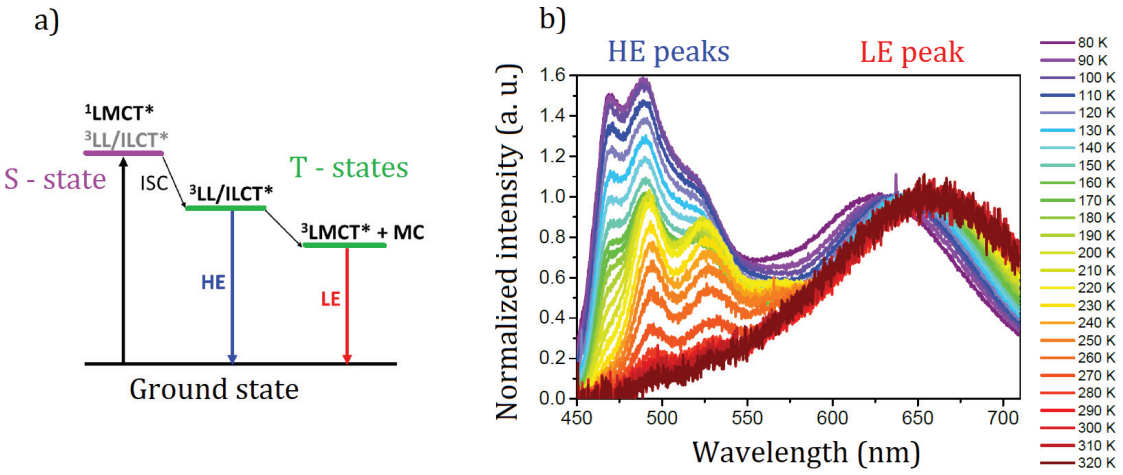

Figure 3.17 - temperature dependence of $[Au(I)(p\text{-}SPhCOOH)]_n$ spectrum,. a) simplified schematic of singlet and triplet electronic states and the proposed emission peak yield (H-high and L-low E-energy peaks). b) emission spectra as a function of temperature. Both images adapted from [135].

On Figure 3.19 we can see the first acquisition (black line) from the laser pulse to 5µs the presence of both HE and LE peaks. In the second acquisition (red line), only the HE peak is present when the recording window is from 5 to 30µs after the pulse. Linking this to the lifetimes data, we can see that the intermediate (0,3-1µs) component is the LE peak associated with aurophilic interactions, while the longer component (3-10µs) is attributed to the HE ligand peaks. The very fast component was not detected on the iCCD due to its low intensity compared to other luminescent mechanisms.

Table 4 - a short overview of the samples tested in the scope of the study. The table presents the chemical structure; publication reference, luminescent transitions and crystalline structure: T - excited triplet state, S – singlet state, IL- intra ligand, LLCT – ligand to ligand charge transfer, LM(M)CT – ligand to metal(-metal) charge transfer, MC – metal centre.*

Sample	Ref	Emission	Crystalline structure
$[Au(I)(p\text{-}SPh)]_n$	[141]	T*→S: LMMCT + MC (685nm)	1D helical chains
$[Au(I)(p\text{-}SPhCOOH)]_n$	[135]	T*→S: LMCT (470-520nm) T*→S: IL/LLCT + MC (650nm)	2D network
$[Au(I)(p\text{-}SPhCOOCH_3)]_n$	[131]	T*→S: IL and MLCT (650nm) Rigid network → high QY	2D lamellar
$[Ag(I)(p\text{-}SPhCOOCH_3)]_n$	[142]*	T*→S: IL/LLCT (480, 520, 560nm) T*→S: LMCT (630nm)	2D lamellar honeycomb
$[Ag(I)(p\text{-}SPhCOOH)]_n$	[142]*	T*→S: IL/LLCT (480, 520, 560nm) T*→S: LMCT (700nm)	2D lamellar honeycomb
$[Cu(I)(p\text{-}SPhCOO\ CH_3)]_n$	[138]	T*→S: IL/LLCT (460 and 560nm) T*→S: LMCT and MLCT + MC (740nm)	2D lamellar
$[Cu(I)(p\text{-}SPhCOOH)]_n$	[143]	T*→S: IL/LLCT (485-570nm) T*→S: LMCT and/or MLCT + MC (660nm)	2D network

On Figure 3.15 we see the resemblance between the three ([Au(I)(p-SPhCOOH)]$_n$, [Ag(I)(p-SPhCOOH)]$_n$ and [Cu(I)(p-SPhCOOH)]$_n$) coordination polymers. The HE peak is present on all samples further linking them to the ligand interactions, while the broad LE peak again validates it originates from the metalphilic interactions.

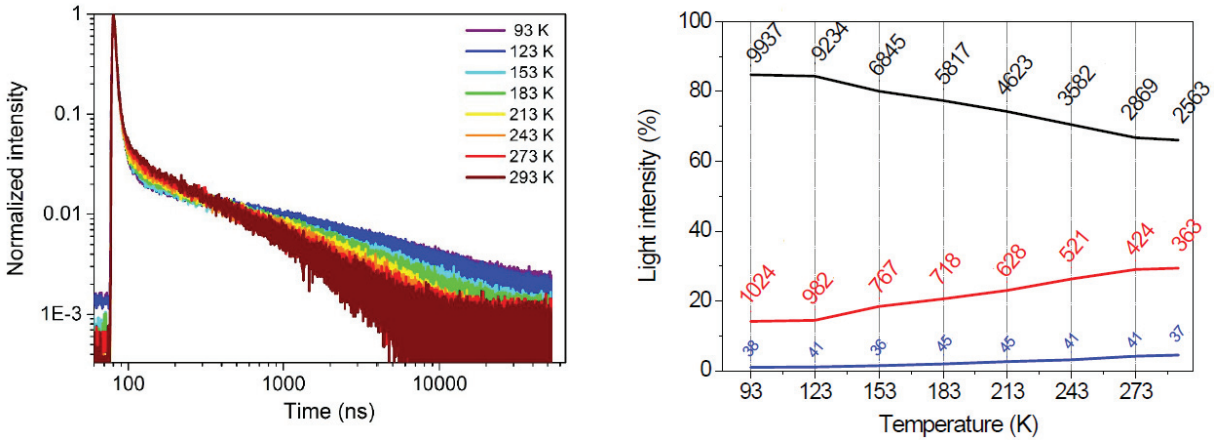

Figure 3.18 - On left: time-resolved luminescence evolution with temperature of [Au(I)(p-SPhCOOH)]$_n$.On right: three luminescent mechanisms of different lifetimes; Adjacent values are the lifetimes in ns. Adapted from [131].

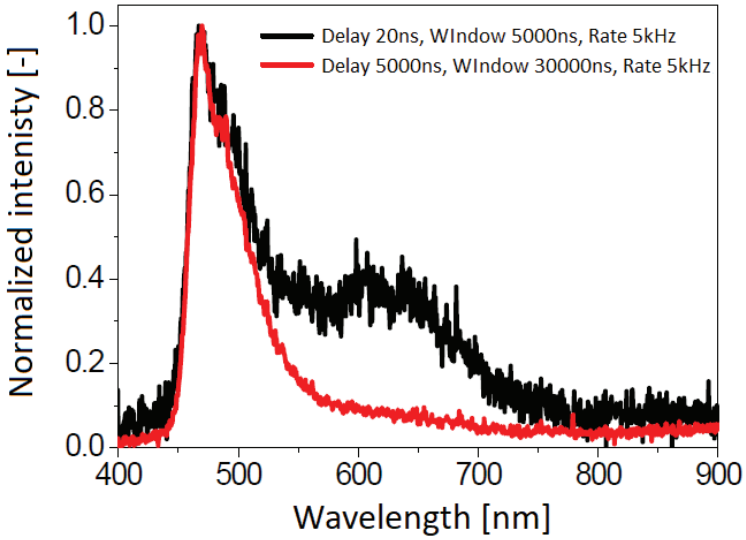

Figure 3.19 - Timer resolved spectroscopy data of [Au(I)(p-SPhCOOH)]$_n$; in the legend the nanosecond time for the delay from pulse, the temporal window of the observation and the laser pulse rate is shown. Adapted from [131].

The results on pressure exposure are shown in Figure 3.22 and Figure 3.21. On both figures, the left graph shows the sample in the diamond anvil cell. Squalene oil is used in these high pressure

cells, since it has well known rheological properties, weak absorption and no fluorescence response in the visible range [144]. Several kbar can be induced with this system. On the right the response of the "intermediate pressure stage" are shown. The working medium is nitrogen gas directly from a compressed air bottle, with maximum pressure of 190bar. A peak shift is observed when immersed in squalene. This is however not surprising, as solvatochromic shifts are known and depend on solvent polarity[47] [118].

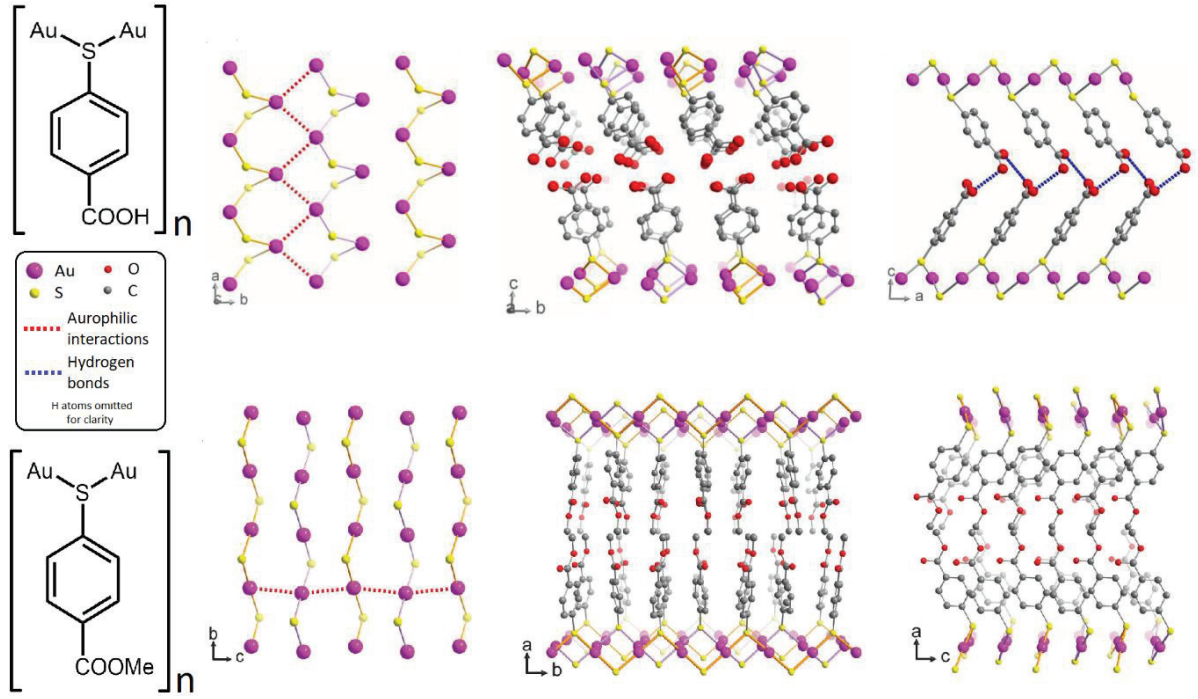

Figure 3.20 – the [Au(I)(p-SPhCOOH)]$_n$ 2D network (upper) and the [Au(I)(p-SPhCOOCH3)]$_n$, 2D laminar (lower) crystalline structure.

A general trend of a blue shift with increased pressure is observed on all samples, except [Au(I)(p-SPhCOOCH$_3$)]$_n$ in squalene. A surprising red shift is observed (Figure 3.21 - left) compared to the same sample exposed to nitrogen (right). Peak broadening is observed on both samples as the pressure increases and interactions with the solvent increase with it. The crystalline structure of the samples tested are shown in Figure 3.20. The explanation for the shift is hard to obtain from these preliminary results. The shift is most likely to occur due to the deformation of the crystalline structure.

[47] Often blue shifted when going from gas to liquid medium.

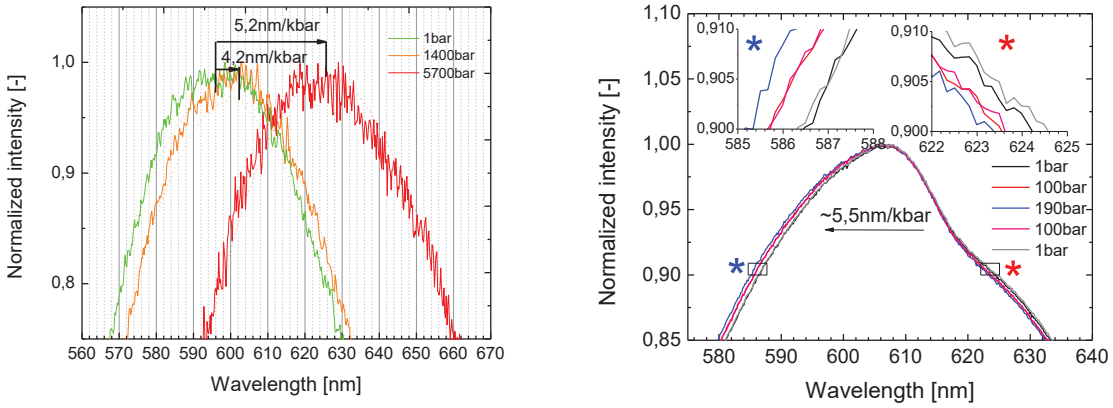

Figure 3.21 - Luminescent response at increased pressure for [Au(I)(p-SPhCOOH)]$_n$. On left the diamond anvil cell results with pressures up to 5700bar in squalene medium. On right the exposure to 200bar of pressure in nitrogen gas medium.

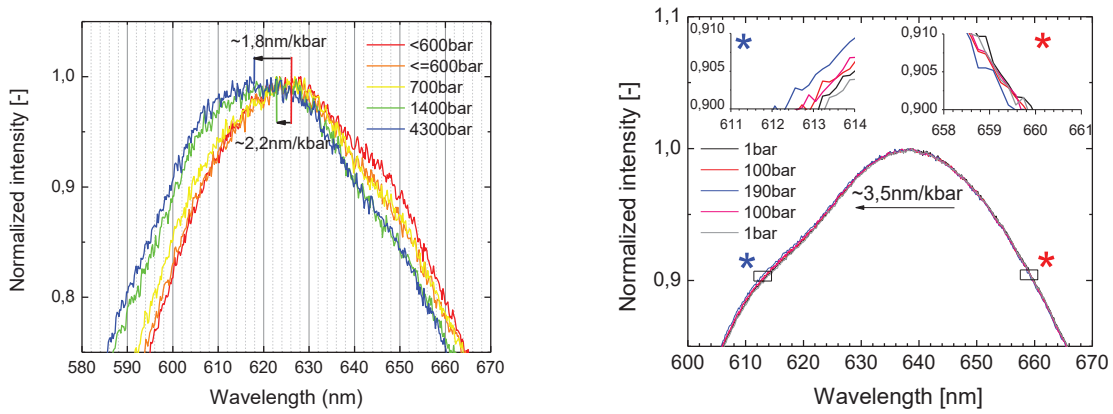

Figure 3.22 - Luminescent response at increased pressure for [Au(I)(p-SPhCOOCH$_3$)]$_n$. On left the diamond anvil cell results with pressures up to 4300bar in squalene medium. On right the exposure to 200bar of pressure in nitrogen gas medium.

The reported rigid structure of crystalline structure of the [Au(I)(p-SPhCOOCH$_3$)]$_n$ is reflected in its lesser sensitivity to pressure. Also, it seems to be progressive with pressure increase, as the shift is more responsive in the lower pressure nitrogen medium (Figure 3.22). The reverse seems to hold for the [Au(I)(p-SPhCOOH)]$_n$ in the diamond anvil cell (Figure 3.21 left). As for the former the ligands would be wedged, gradually increasing resistance to pressure deformations. Also, it brings the ligands closer together, most-likely causing the blue shift. The latter structure, with its slanted ligand organisation and hydrogen bonds, doesn't offer a straight forward explanation for the red-shifting, which would indicate an increasing distance in the crystalline structures or at least the emission relevant sites. Also, to keep in mind is the fact that if the crystalline rigidity is high it

might affect positively the QY, by protecting the long-lived excited T states from quenching [122]. However, this should decrease the pressure sensitivity, at least for deformation-based mechanisms as opposed to a quenching mechanism.

One imaginable use could be in diamond anvil cells, where the ruby R1 method for determining the pressure is reportedly insensitive below roughly 600bar. This opens up a potential use as a "intermediate" pressure probe, also due to the high quantum yield[48] and consequently strong luminescence. However, many other parameters would have to be assessed to establish its use, such as repeatability and chemical stability. Response in 5nm/kbar red shift which is in the same range of sensitivity as the related family of compounds, reported in [132] also red shifting (~5 nm/kbar red shift). Compared to the 0,02nm/kbar of the R1 ruby line pressure standard method the results seem like a huge improvement, however the minute shifts are easier to observe on the narrow emission peaks of ruby, than the broad peaks of our study.

What is clear is that the thiolate coordination polymers are complex luminescent systems, with interwoven luminescent mechanism. Predicting or even untangling such systems is no easy task. Some have great potential for luminescence thermometry. Due to their multi peaked emission spectrum, the ratiometric intensity measurements could yield temperature measurements unperturbed by intensity fluctuations. Their rigid crystalline structures protect the long-lived excitation states, producing phosphorescence at reasonable and some cases very good quantum yields. However, this seems to make them not as responsive to pressure as initially thought. Furthermore, were the structures more flexible, perhaps the QY decrease would render them not usable for probing applications.

Though only preliminary results, it's already clear that the response of the coordination polymers is not sensitive enough for use in microfluidic devices[49], unless a structure to amplify the crystalline deformation is used. However, this family of materials has only started to be explored. Chemical modifications of ligands can completely rearrange the self-assembly process and can yield materials with completely unexpected properties. Therefore, it is an exciting perspective to pursue.

[48] 70% at room temperature [140]
[49] Perhaps for very high-pressure systems – homogenisers.

3.4. Thermo-sensitive nano-probes

The thermo-sensitive probes were developed by FENNEC[50] team at ILM, Lyon and fabricated at their facility. The gold-SiOx-FITC temperature sensitive nanoprobes were used for the thermal mapping experiments (chapter 4.2) and in publication [94]. As is shown in Figure 3.23, the nanoprobes are composed of a gold core and a polysiloxane shell, containing the fluorophores. The choice of the fluorescent dye (FITC – fluorescein isothiocyanate) was due to its high quantum efficiency, covalent bonding to the silica shell (cyanate group) and foremost, the fast luminescence lifetimes (typical for organic dyes). This is important due to fast flows and a limited acquisition voxel dimension (chapter 4.2.1). If the lifetime was too long, some information might be lost due to advection, while the emission was still taking place.

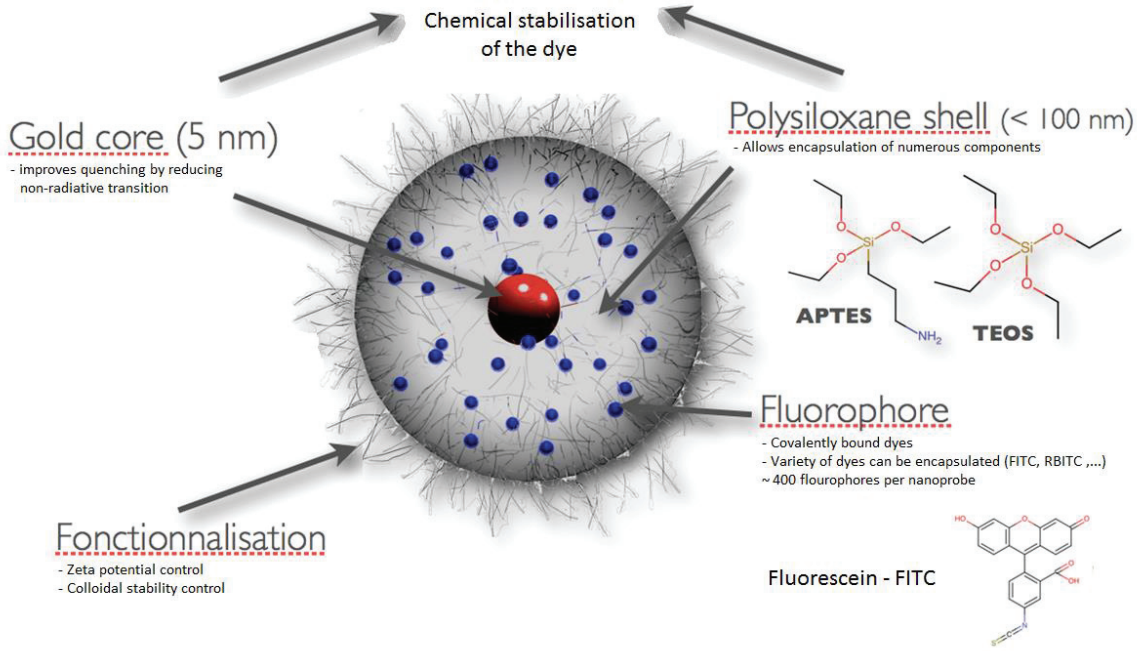

Figure 3.23 - temperature sensitive fluorescent (Au:SiOx) nanoparticles; 5nm gold core with a ~25-30nm thick poly silica shell containing fluorescent dyes (FITC), with functionalization on the surface to prevent precipitation. Internal laboratory data.

The benefit of a fluorescent nano-object is the increase of fluorescence intensity (~400 dyes per probe) and protection of the dyes from environmental influences (chemical, pH,…) [145]. This

[50] Team FENNEC - Formation Elaboration de NaNomatériaux et Cristaux; prof. Olivier Tillement, dr. Matteo Martini, Huong Lai.

could be an issue in our cavitating flows, as they are known to produce chemically reactive species (chapter 5.1). Due the nano sizes, thermalization happens very quickly (in nanoseconds [51]). The gold core was initially intended to induce plasmonic effects, however to no success[52]. On the other hand, the 5nm gold cores are easy to prepare with the water in oil emulsion process [145], facilitating the production. This helps with quenching effects at increased temperature, as the gold creates a denser shell. Since the FITC organic dyes are embedded covalently to the shell, a denser polysiloxane shell adds to their chemical stability, by preventing photobleaching. This can be seen in Figure 3.24, comparing the dye embedded silica particles with and without a gold core. Quantum yield is somewhat lowered, but still retains 80% of the isolated dye[53] [145].

As the probes are added to the working liquid, they produce a nanofluid (suspension of nanoparticles). The porous silica shell of about 25-30nm makes the particles around 60-70nm in diameter, thus small enough not to perturb the fluid properties (below certain concentrations) [93]. Also, the silica shell makes it optically transparent in the visible range of wavelength. The functionalization maintains the nano- suspension stability, preventing precipitation of the probes and adding to the hydrophilic nature of the silica shell.

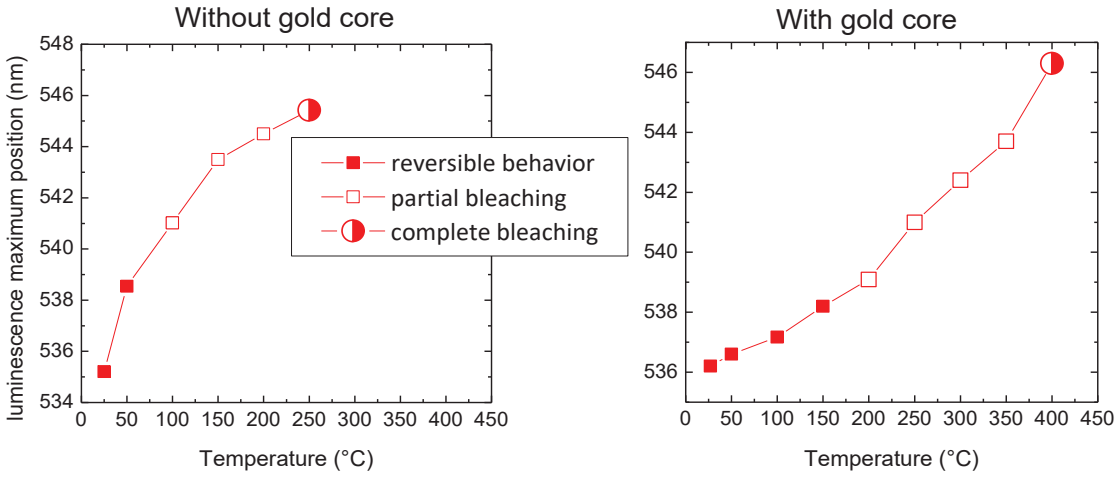

Figure 3.24 - luminescence quenching at elevated temperature, with and without the presence of a gold core. The gold core has an effect on the density of the silica shell, helping to shield the fluorophores from quenching effects. Internal laboratory data.

[51] Thermalization characteristic times [146]: $\tau = R^2/a = (6\times10^{-8})^2/(8.3\times10^{-7}) = 4ns$

[52] Unsuccesful, as the 5nm gold nanoparticles are too small to show plasmonic effects at the desired wavelength.

[53] Decreasing the non-radiative decay due to the presence of the gold core.

Figure 4.2 shows typical calibration curves (emission spectra) of the temperature sensitive nano-probes. Calibration curves are usually measured in broader microchannels without constrictions. This allows for better thermalisation and for representative optical conditions, since the channels are of similar dimensions and are made with the same materials [147]. The temperature control of the inlet liquid is controlled by the liquid to liquid heat exchanger and a recirculating liquid chiller (Figure 2.11). The acquisition is demonstrated in chapter 4.2.1, and is identical for the calibration and the measurements. Calibrations are performed from 8 to 40^{o}C, since the probes are prone to precipitation at higher temperature, the temperatures out of this range are approximated by linear extrapolation. As is observed in chapter 4.2.2, Figure 4.2, the vibrational levels (red region) increases with rising temperature, no doubt governed by the Boltzmann distribution increasing the population of higher vibrational stated, red-shifting the spectrum.

4. Temperature gradients in micro-cavitating flow

Cavitation bubble growth is a rapid phase change phenomenon. Accordingly, the bubble has an associated latent heat requirement in order to transit to vapor. The fast dynamics of a growing bubble are expected to induce thermal gradients in the cavitating flow. In this chapter, we discuss these temperature gradients and the techniques used to probe them.

Microfluidics allows us to use specialized luminescent thermosensitive colloidal suspensions and a confocal microscope setup for luminescence-based thermometry. Micro-cavitating flow might be uniquely suited for such measurements, as the boundary layers around growing bubbles might be more significant than at macroscopic scales. Furthermore, when studying two-phase flow, additional problematics arise, due to the phase mismatch. Compared to single phase measurements, the difficulties posed by the bubbles in the flow originate from the abrupt changes in some fluid properties (ref. index, density, viscosity…). However, these are shown not to be problematic for the specific technics used in the study.

The results of a parametric study, considering the driving pressure and the working liquid temperature in several different channels, are compiled and discussed herein. Also, 3D characterisations of the flow are also presented. Complementary techniques are shown to yield similar values.

4.1. Temperature gradients and the thermal effect

Cavitation, as discussed in chapter 2.1, is theoretically an isothermal process. This holds when considering the large-scale system, however for a rapid phase transition, the associated latent heat effects[54] can be faster than the thermalization, yielding temperature gradients around the growing vapor bubble. This is often disregarded in the discussion of bubble growth, where a layer of lower temperature can hinder the growth of the bubble due to the reduced vapor pressure. Inertially driven cavitation is not influenced by this phenomenon, but for certain susceptible liquids, this may induce thermally controlled cavitation, often associated with the so called thermal delay. As the thermodynamic parameters of the growing vapor bubbles aren't fully investigated, engineers sometimes have problems estimating the thermal effect [148].

[54] And also for macroscopic bubbles, the initial cooling by gas expansion before reaching saturation vapor pressure.

Thermally driven as opposed to inertially driven cavitation bubbles refers to the damping effect of the cooled liquid around the growing bubble. As the bubble grows it finds itself surrounded by a thermal boundary layer (TBD - δ) of liquid at lower temperature from that at the beginning. This raises the vapor pressure, moderating the bubble growth. This is more profound for liquids near the critical point, for example cryogenic liquids [149], making the thermal effect or thermal delay interesting for applications in turbopumps for liquid hydrogen and oxygen pumps in space launcher engines [149].

The thermal effect of a liquid is often assessed by comparison to a liquid, with negligible thermal effects, like water at 20ºC (shown below), thus a characterization by dimensionless numbers is feasible. One of these is the characteristic temperature difference

$$\Delta T^* = \frac{\rho_v L}{\rho_l c_{p,l}} \tag{4.1}$$

where ρ is the density of the phase (subscript l for liquid, v for vapor), L is heat of vaporisation and $c_{p,l}$ the heat capacity of the liquid. This parameter only considers the fluid parameters, not considering any thermal inhomogeneities. At 20ºC it amounts to about 0,01K[55] (0,04K[56] for isopropanol), showing it's not a thermally sensitive fluid at this conditions, whereas for a cryogenic fluid like liquid hydrogen at 22.2K the value would be a significant 1,2K [149]. This shows the bubble would be also thermally, not merely inertially controlled. This means the temperature drop of the surrounding liquid would suppress bubble growth.

The temperature difference ($\Delta T = T_b - T_\infty$) between the bubble interface and bulk temperature was derived for an isolated bubble from Fourier's law [58]. The thermal boundary layer should be in the range of $(at)^{1/2}$ [149], with q being the heat flux per unit surface qt the interface, α_l = thermal diffusivity = $\lambda_l/(\rho_l c_{p,l})$, λ_l – liquid thermal conductivity:

$$q = \lambda \frac{\Delta T}{\sqrt{a_l t}} \xrightarrow{q 4\pi R^2 = \frac{d}{dt}\left(\frac{4}{3}\pi R^3\right)\rho_v L} q = \dot{R}\rho_v L \xrightarrow{\dot{R} \cong R/t} \Delta T \cong \frac{\dot{R}\sqrt{t}}{\sqrt{a_l}} \Delta T^* = \frac{R}{\sqrt{a_l t}} \frac{\rho_v L}{\rho_l c_{p,l}} \tag{4.2}$$

[55] Values used water: $c_{p,l}$=4,18J/(g K), L=2454J/g, ρ_v=17,3g/m^3, ρ_l=998000g/m^3

[56] Values used isopropanol: $c_{p,l}$=2,68J/(g K), L=45000J/mol/60g/mol=750J/g, ρ_v=100g/m^3, ρ_l=750000g/m^3.

Another characterisation can be made by the B-factor, which is the ratio between the vapor entering the bubble (proportional to R) and the liquid to be cooled (proportional to the boundary layer) [149].

$$B = \frac{\Delta T}{\Delta T^*} \approx \frac{R}{\sqrt{a_l t}} \approx \frac{\alpha}{1-\alpha} \tag{4.3}$$

This simplified approach means that the B factor is of order unity[57], therefore $\Delta T \approx \Delta T^*$, meaning the former parameter is a reasonable estimate of the temperature gradients due to bubble growth in cavitating flows.

Estimating the vapor pressure difference from Clapeyron relation, disregarding the vapor density as it is orders of magnitude lower to liquid phase, we can write [58]:

$$\Delta p_v = \frac{R}{\sqrt{a_l t}} \frac{(\rho_v L)^2}{\rho_l c_{p,l} T_\infty} \tag{4.4}$$

While Brennen proposed a related parameter Σ [m/s$^{3/2}$] which is dependent only on the liquid temperature [7]:

$$\Sigma = \frac{\left(\rho_v L\right)^2}{\rho_l^2 c_{p,l} T_\infty \sqrt{a_l}} \tag{4.5}$$

Research in the field of the thermal effects in cavitating flow are scares. Mainly fuelled by research into cryogenic liquids [150], [151]. Thus far, there is only a handful of studies probing the temperature in cavitating flow. The recent IR camera measurement identified temperature gradients in water for single bubble [152] and multi bubble cavitation [153], [154], the former in room temperature conditions and the latter close to 100ºC. A study on diesel injectors, using LIF (laser induced fluorescence) to measure temperatures and void fractions information in multiple points along a mili-meter wide channel, also presented cooling region in the two phase flows [155]. Diesel surrogate liquids were used with inherent luminescent properties, which is an ideal situation in terms of luminescence thermometry, as the liquid serves as the measurement probe. This allowed them to obtain temperature as well as void fraction information from the measurements.

[57] Unless the void fraction α=1

Water is perhaps the most interesting and complex liquid to study, yet has no luminescent properties. For this reason Ayela et al. [94] used temperature sensitive nanoprobes to investigate the temperature gradients in micro cavitating flow. Our studies are a continuation of their work.

4.2. Thermo-sensitive nano-probe measurements

4.2.1. Achromatic confocal microscope

An in-house built achromatic confocal microscope is used for the probing inside the microchannels. The achromatic notation implies the excitation wavelength modulation. On Figure 4.1 – a) is the doubled Nd:YAG 15W laser light source using 532nm light to excite the b) Ti:Sapphire laser with the tuneable emission in the range of 700 to 1000nm pulsed laser light. The 880nm wavelength is selected due to the efficient energy conversion and passed along through the c) Faraday isolator to the d) frequency doubler producing 440nm pulsed laser light, with the 80MHz rate and 300fs pulse width. The beam dump – f) absorbs the unconverted laser light, while useful blue laser light is reflected by the e) filter, passed through the i) pinhole in the beam expander, j) optical densities and again reflected by the k) dichroic and injected into the l) long working distance objective – LWD. it focuses the light into the m) channel, exciting the nanoprobes in the liquid, which absorb and reemit the light at lower wavelengths. The sample can be moved in x and y, while the z movement of the focal spot is done by moving the LWD. The light is collected by the same objective, passed through the dichroic to the acquisition branch of the microscope. In the first part it goes through the i) 20µm pinhole, which serves as a spatial filter, not allowing the light from above or below the focal point to pass. The acquisition voxel is the 3D confinement of the volume from which we are obtaining our data, with the dimensions of 1x1x5µm (X,Y,Z)) [94]. This allows us to make several 2D cuts at different heights in the channel, essentially fully characterising the flow in 3D. Considering the rapid flow conditions, reaching roughly 40m/s at peak driving pressures, the probes spend very little time in the excitation volume. FITC, an organic dye embedded in the probes with the characteristic luminescence lifetime of about 4nm is well suited for the dwell times of about 25ns[58] per probe. This prevents any signal lose due to advection out of the acquisition voxel. If the pinhole is removed, the image can be sent to the p) camera for visual observations of the flow, otherwise it's passed through the q) filter to remove

[58] 10^-6m /40m/s=25*10^-9s

the remaining excitation light and the signal is injected into the r) monochromator. A spectrum is produced by the 300gr/mm (blazed at 500nm) gratings projected on the s) EMCCD with the possibility of using also the t) PMT. Acquisition and control is performed by the u) computer with a LabVIEW program.

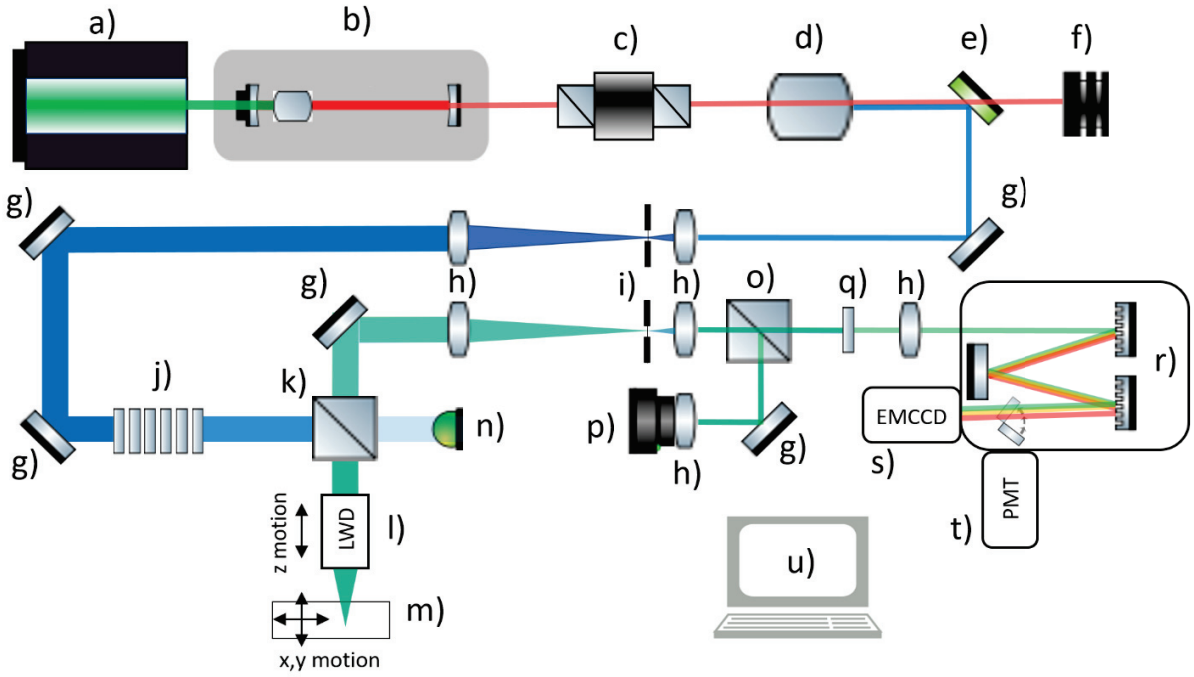

Figure 4.1 - Achromatic confocal microscope setup. individual components can be found in appendix, Table 8.

The x and y movement of the sample is achieved by a micromanipulator Nanoview and the Microdrive control from Mad city labs. It creates a point by point movement over the desired area in the channel with the desired resolution. The recording of the spectrum in each point is defined by the acquisition time and the number of accumulations. Generally, the gain and other electronic amplifications also lower the SNR.

In later experiments the laser excitation setup (a to e) was replaced by a weaker CV 473nm laser, without disturbing operations. The weaker excitation power is somewhat improved by the more suitable excitation wavelength match and the continuous laser mode didn't noticeably deteriorate the nanoprobe operations[59]. Kasha's rule states the excitation wavelength doesn't influence the

[59] Pulsed excitation is better suited for exciting the organic dyes., to help with photobleaching and avoid overheating. For both lasers used the light flux was sufficiently low not to induce heating.

emission spectrum (as long as it's not in the spectral overlap zone). Furthermore, as the probes are calibrated before measurements, the excitation light source replacement shouldn't be of concern.

4.2.2. Data analysis

The spectral analysis yields two important parameters in flow characterization. The first is of course the **temperature information**. This is obtained by the so-called RIM (ratiometric intensity measurements). Theoretically, this method is insensitive to the signal intensity[60], as the information is obtained from the temperature sensitive sections on the emission spectrum (red and blue region - Figure 4.2). As the signal is integrated over these regions, a ratio is produced corresponding to a specific temperature. Prior to the measurements, calibration curves are acquired in the same kind of channel and conditions, only in the absence of the cavitation inducing constriction. The calibration curves example is shown in Figure 4.2 below.

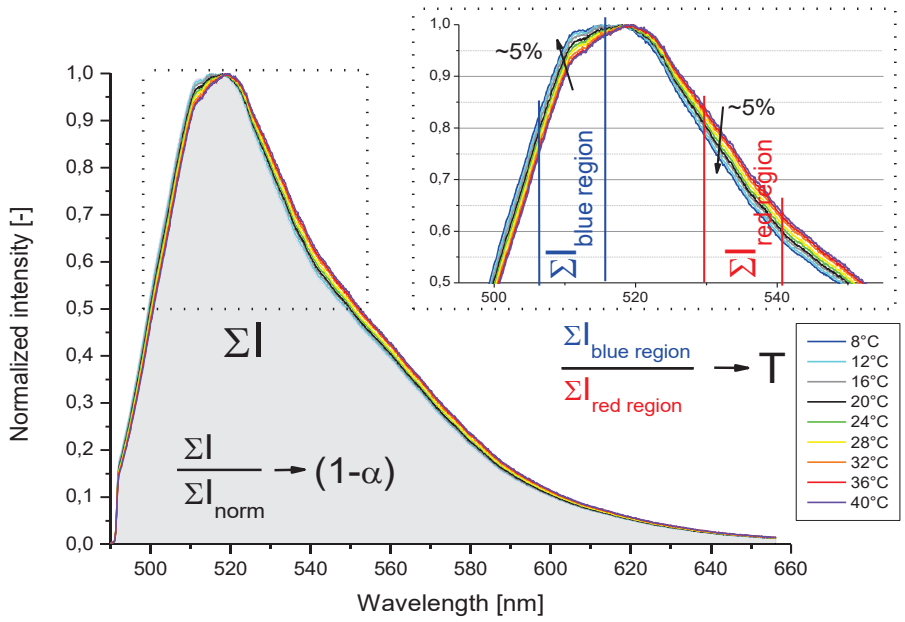

Figure 4.2 - Calibration curves example with data analysis demonstrating the RIM technique. The red and blue region are summed and their ratio yield the temperature information. Grey area is used to obtain void fraction information when normalized by area representing zero void fraction (α=0).

After data acquisition and the spectral analysis is performed, we can obtain also the luminescence intensity as shown in Figure 4.2. As the probe distribution in the liquid is homogeneous, the

[60] If SNR is disregarded.

intensity should remain constant or corresponding to the excitation power. This is also the reason for the n) diode in Figure 4.1, allowing for the excitation source oscillation correction[61]. As the two-phase flow appears, one can imagine a bubble being present in the acquisition volume during recording. Since the vapor phase doesn't contain any light emitting species[62], there will be a corresponding drop in intensity of the signal, proportional to the dwell time of the bubble in the voxel during the recording time. Therefore, this information is approximately the indication of the liquid phase or one minus **void fraction** information, averaged over the data acquisition time. Thus, for each measurement point, the spectrum counts are summed to yield the luminescence intensity (area under the curve marked grey on Figure 4.2) and normalized to the intensity in a point of single-phase flow. This is usually the maximum value in the measurement series, as the points are acquired so, that a reference temperature and a zero void fraction region is present[63]. From this, the temperature and void fraction maps can be produced, which are presented in the following sub-chapters.

Generally measuring at the very top and bottom is difficult due to the perturbations of the walls. This also holds for the side walls and the constriction itself. Reflections and other surface effects perturb the spectrum and intensity of the signal therefore the relevant information is lost. Due to the excitation cone formed by the objective, the deeper the measurement in the channel the larger the extent of the perturbation region around the walls. For this reason, cropped maps are used in further analysis, which have the bad data points measure at the walls removed. These are the point where the luminescence intensity was insufficient to yield any relevant information.

A typical analysis performed is the **scatter plot** of the measured points as a function of their void fraction and temperature (example Figure 4.5). The distribution of points shows the fluorescence intensity and temperature are not directly linked. This was also shown in [94]. Furthermore, a rudimentary analysis of the cavitation cloud and peak temperature position is performed. A cropped temperature (upper) and void fraction (lower) analysis window from the LabVIEW program is shown in Figure 4.3.

[61] Used if laser oscilations are high.
[62] Or at worst, a strongly diluted concentration.
[63] Upstream of the diaphragm, where zero void fraction and a stable temperature is expected.

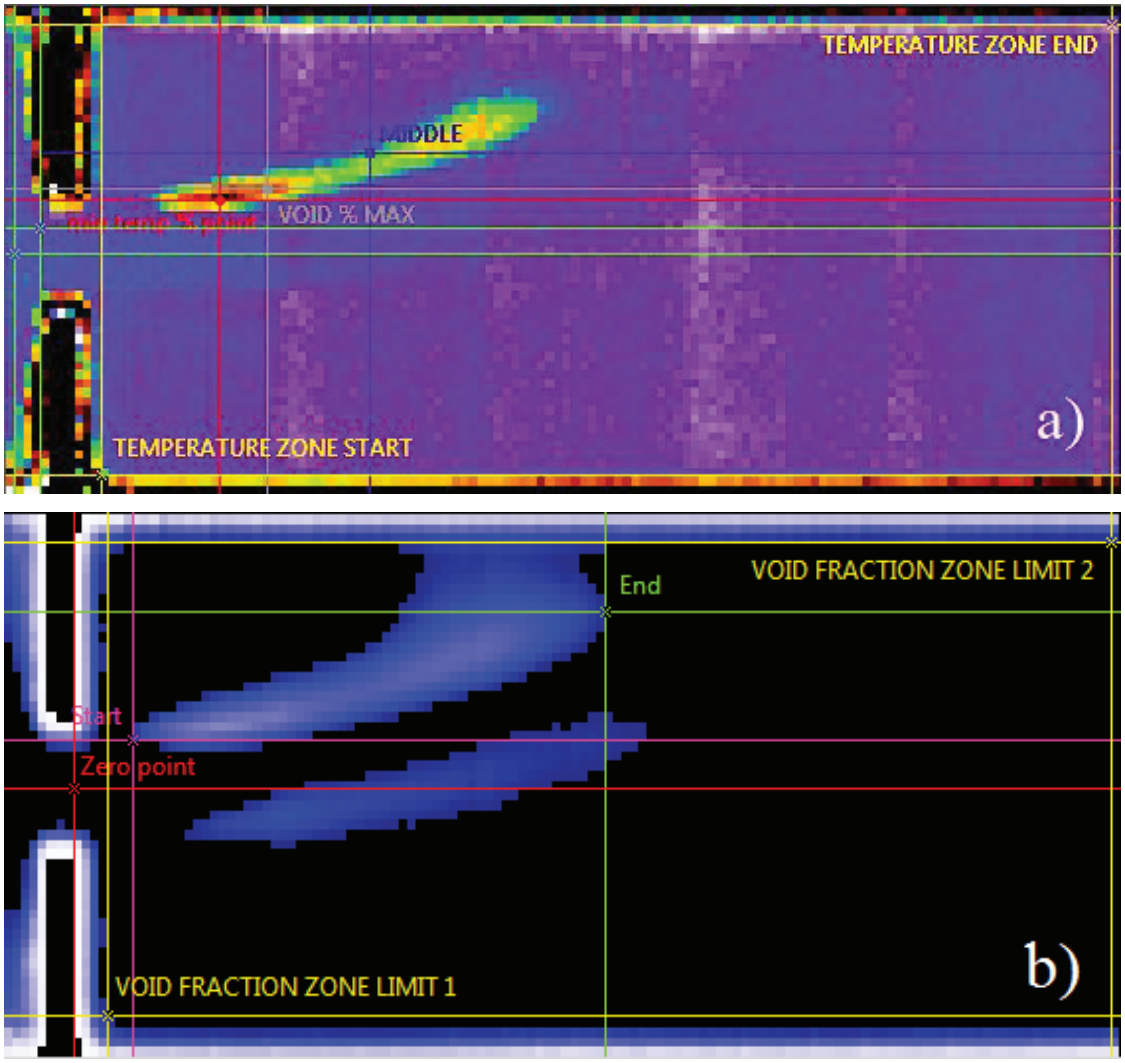

Figure 4.3 - example of a) temperature and b) void fraction map analysis with relevant cursors.

On the a) temperature map of the Figure 4.3, the yellow cursors are used to crop the mapped points, which are considered in all subsequent analysis (in scatter plots for example). The green cursors limit the points from where the average temperature value for the ambient temperature is obtained. This is usually at the entrance of the diaphragm, where the temperature of the incoming liquid should be most representable. The other three following points present are a part of the cavitation cloud **area analysis** data. The red cursor indicates the average **point of the temperature area** – the area in the temperature map above the set threshold (10% of maximum temperature drop - $T_{min\ 10\%}$), indicating the area of the highest temperature decrease. The grey cursor indicates the middle **point of void fraction area** – obtained from the 10% of the highest void fraction points, highlighting the area of highest void fraction. The last blue point is manually prescribed by the

"start" and "end" cursors which are positioned at the beginning and end of the cavitation cloud (above 0,3 void fraction) in the void fraction map, indicating the **cavitation cloud middle** – halfway between the prescribed points. All coordinates are referenced from the zero point, which is positioned at the diaphragm opening, as shown in Figure 4.3 b) red cursor "zero point".

In Figure 4.3 b) the void fraction map presents only the values above the set threshold limit – the sum yields the value called the **cavitation cloud area**[64]. The limiting void fraction of 0,3 is used unless otherwise specified, since it corresponds to the value that is still present for the low intensity cavitating flow and still within the confines of the channel for the high intensity flow. Also, from the cavitation cloud area a value called the **equivalent cavitation cloud area** is derived, corresponding to the area if all point had the void fraction of 1, therefore considering also the void fraction value in each point considered.

A graphical representation of the analysis points is presented in the first scatter plot considered in the height analysis of MD L4 channel – Figure 4.5.

4.2.3. 3D analysis in microchannel

The height analysis was performed for selected channels to explore the 3D aspects of the two-phase flow. The recordings were done at uniform pressure and at 20ºC liquid and ambient temperature. The temperature and void fraction maps are located in chapter 8 (in Appendix, with an exception of Figure 4.4) and only the analysis figures are shown in the following sub-chapters. MD L4 maps and analysis is shown first, as it is an example of a typical recorded flow as a function of height for a Si-Pyrex microchannels. Next, we analyse the MD 10 and L6, which show some deviations from the typically observed trends. At the end, the comparison of MD 14 and T2, two geometrically identical channels, but differing in channel design are discussed.

Figure 4.5 shows the typical scatter plot and explains graphically how most analysis points are obtained from the temperature and void fraction maps, while Figure 4.6 shows cavitation cloud area, with the corresponding average void fraction and temperature drop information. The cavitation cloud area is simply summing the points on the map above the selected threshold[65], as

[64] Number of acquisition points, multiplied by the measurement step in x and y.
[65] Selected as low as possible, so that the intensity variations don't perturb the analysis and high enough that it doesn't go out of the analysis range at high flow conditions. The value 0,3 seems to fit nicely, even for comparison among different channels.

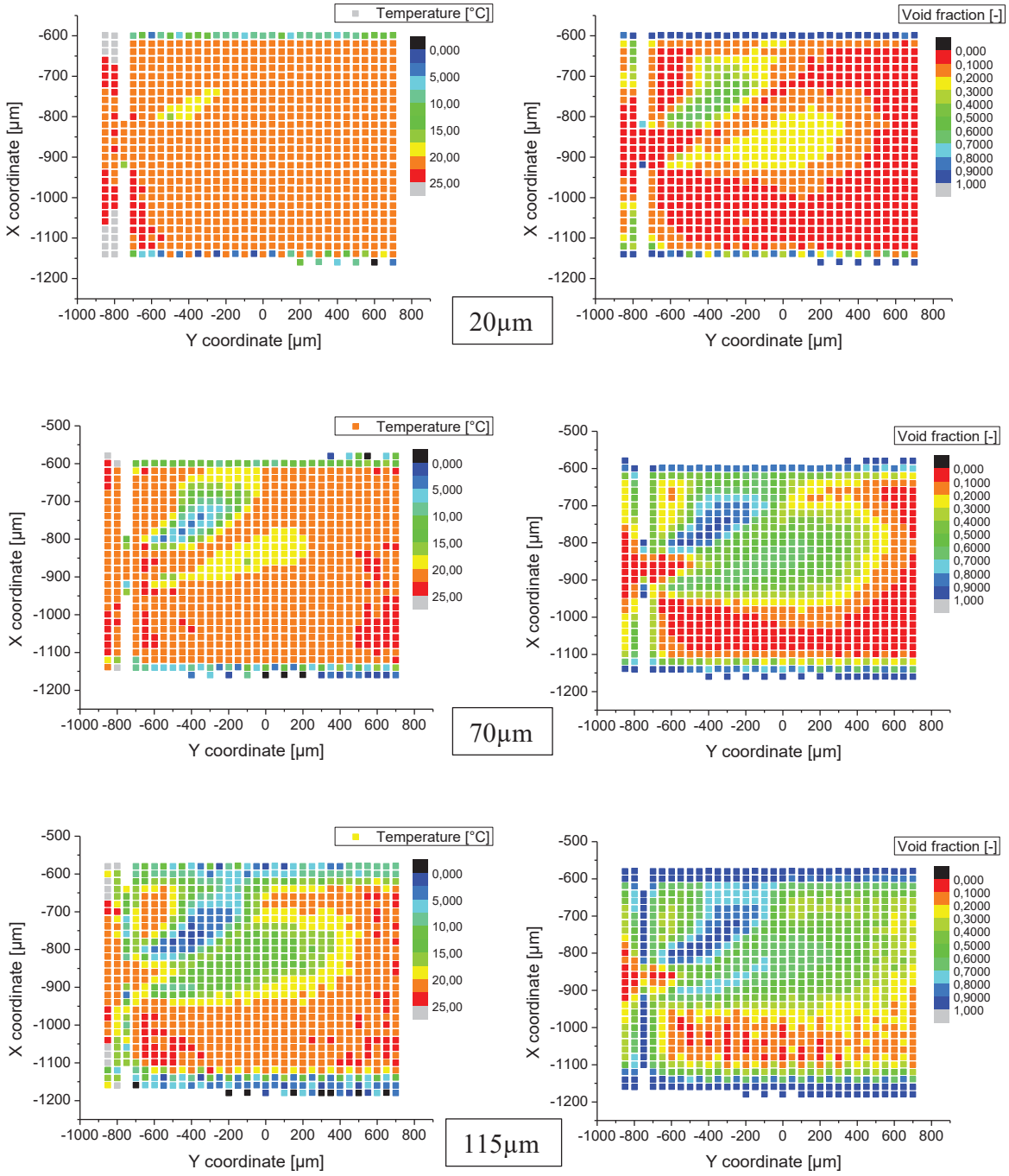

Figure 4.4 - MD L4 at 10bar; temperature (left) and void fraction (right) mapping at 20, 70 and 115µm from glass (order from top to bottom). Flow is from left to right at 10 bar driving pressure. Diaphragm walls are best seen on lower right temperature map.

a way to quantify the vapor clouds formed. After it is multiplied by the scanning resolution to obtain physical dimensions. In a typical SI-Pyrex channel, the cloud seems to increase in size and intensity with channel depth.

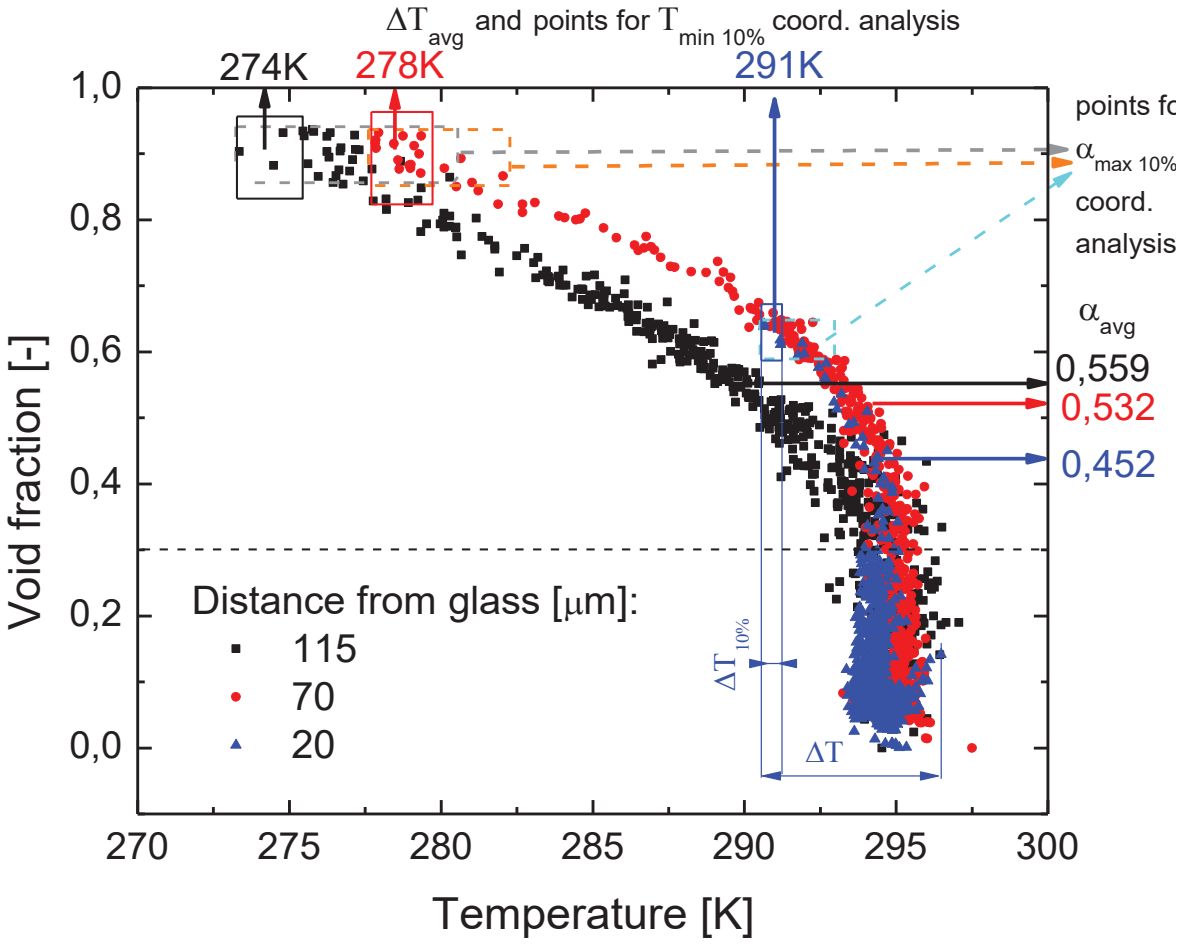

Figure 4.5 - MD L4 temperature vs void fraction plot, 10bar driving pressure measured at different heights in the channel. The legend indicates the scanning plane height in reference to the glass liquid interphase, expressed in micrometres. The dashed line showing the void fraction limit, above which the points for the cavitation cloud analysis are considered. The coloured full line squares show the points considered for the temperature drop - $T_{min\ 10\%}$, while their corresponding pale coloured dashed squares show the points considered for the coordinate analysis ($\alpha_{max\ 10\%}$). ΔT_{avg} and α_{avg} origin is shown, data plotted alongside cavitation cloud and temperature area in Figure 4.6.

The coordinates of the relevant area analysis points show no dramatic changes. There is a general drift from the centre line (towards the wall) for the y coordinates. After the initial increase, no significant movement in the x coordinates is typically observed, indicating a sheet like cavitation

cloud, perhaps. This would be the expected cloud shape in shear cavitation regime, which should be present in a micro diaphragm [93]. The overlap of the void fraction maximum and the temperature minimum coordinates, indicating the temperature gradients corresponding to the cavitation cloud.

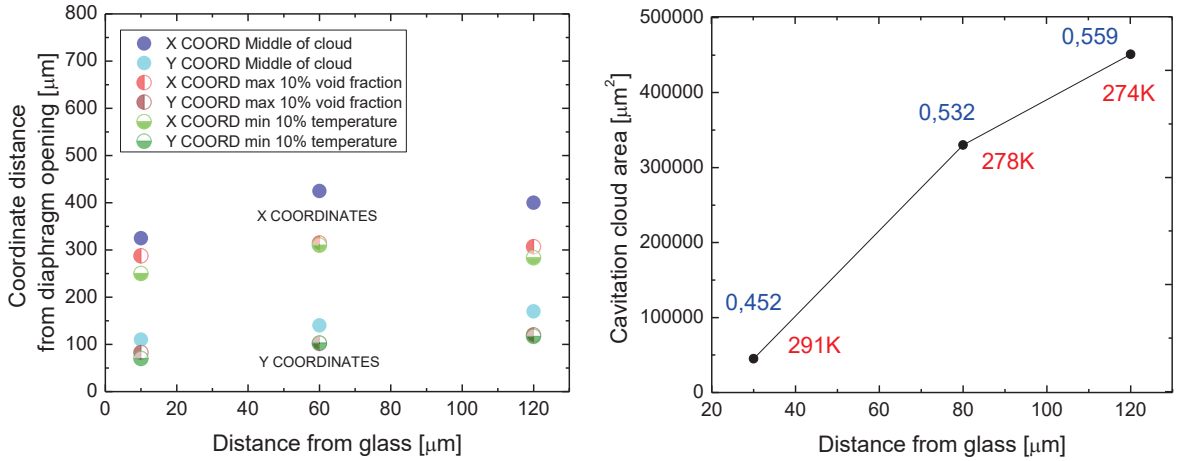

Figure 4.6 - figure on left showing the coordinates of the area analysis from diaphragm opening along the height of the MD L4 channel. Figure on right showing the cavitation cloud area, its average void fraction (blue value) and the temperature drop - $T_{min\ 10\%}$ (red value). (defined in "Data analysis" sub-chapter).

In the analysis of MD 10 and L6, some deviations from the typical flow are shown. In Figure 4.7, the scatter plot of the MD 10 recorded maps shows a spread instead of a line of points, meaning that for the same void fraction, the many different temperatures were obtained. This example showcases an important point for the technique, that is the temperature variations are not directly linked to void fraction (intensity signal). This is also confirmed in [94] as the same type of probes, channels and measurement technique was used. The typical coupling is most-likely observed due to the short thermalization times, as the cooling occurs during bubble growth. However, from the images in Figure 4.8, we can see the formation of a stable vapor bubble occurring in the region where the anomalies on the maps occur Figure S.1. (supplemental data) this bubble can periodically appear and disappear leaving some signal for the temperature information. Also, from the scatter graph and the maps we can speculate that the bubble is located below the 60μm level or about half-height in the channel, since it's where the anomalies start. The periodic appearance of the bubble most-likely gives periods of α=1, followed by liquid of lesser cooling washing

through the acquisition volume. This leads to the back-swing in the scatter plots at higher VF below 60μm.

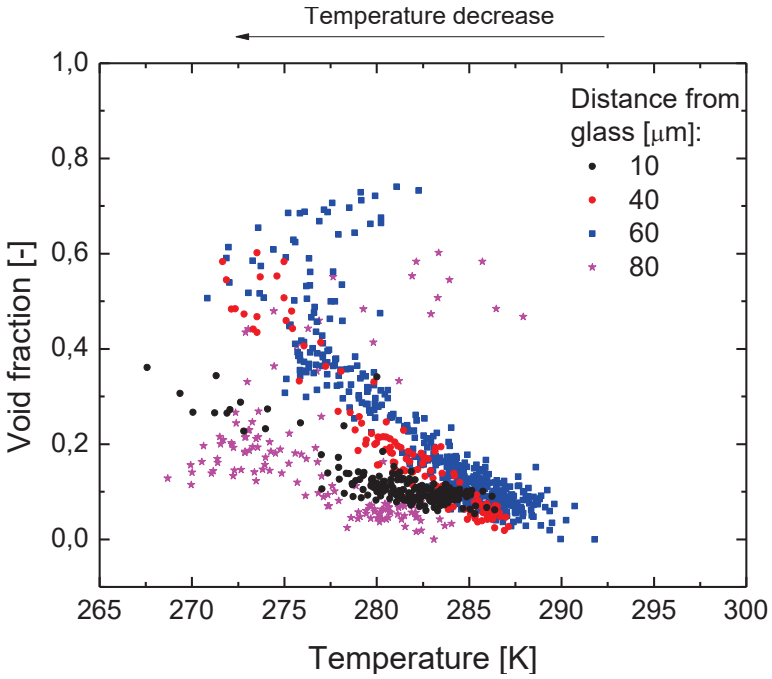

Figure 4.7 – MD10 temperature vs void fraction plot, 10bar driving pressure measured at different heights in the channel. The legend indicates the z plane height in reference to the glass liquid interphase, expressed in micrometres.

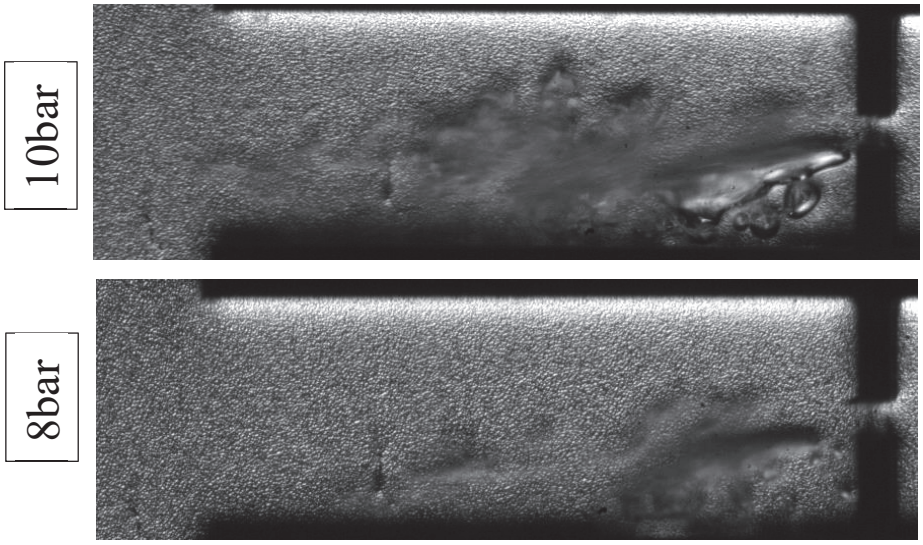

Figure 4.8 - highspeed camera snapshot of MD 7 (an identical copy of the MD 10); flow at 10bar (upper) and 8bar (lower). No bubble coalescence is detected for the flow at 8bar while a stable cavitation bubble is observed at 10bar.

Like the MD 10, L6 also has bubble proposed coalescence in the flow at high flow rates. A snapshot at 9bar is shown in Figure 4.10. No snapshot for the flow at 10bar was available, but a stable cavitation bubble is already seen forming at lower flow conditions, which is only expected to augment with the increasing driving pressure.

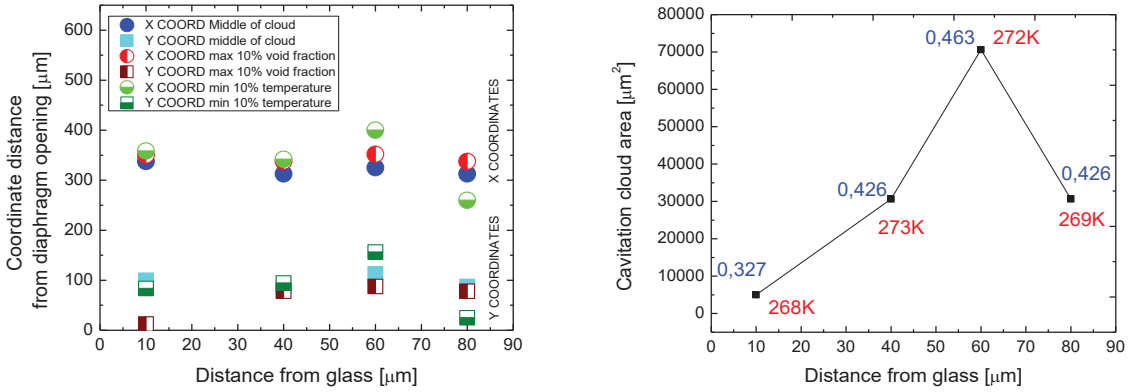

Figure 4.9 – figure on left showing the coordinates of the cloud area analysis from diaphragm opening along the height of the MD 10 channel at 10 bar driving pressure. Figure on right showing the cavitation cloud, its average void fraction (blue value) and the temperature drop (red value).

Both Figure 4.9 and Figure 4.12 are hard to interpret due to the perturbation of the proposed vapor bubble. Again, some indications are present, that the maximum intensity of the flow is near the half-height for channel MD10, since the cavitation cloud intensity peaks at 60µm. The temperature drops are most intense at the uppermost and lowest measured plane. This in however not the case for L6. For this channel the temperature and void fraction maps (Figure S.2) offer most clear evidence of the coalesced bubble at 70 an 90µm, as the high VF region is partially missing the usual temperature drop in the region where the coalescent bubble would appear

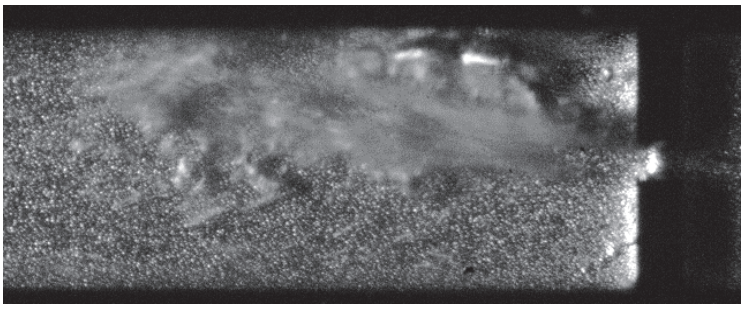

Figure 4.10 - highspeed camera snapshot of MD L6 flow at 9bar. Bubble coalescence is beginning and will increase at 10bar.

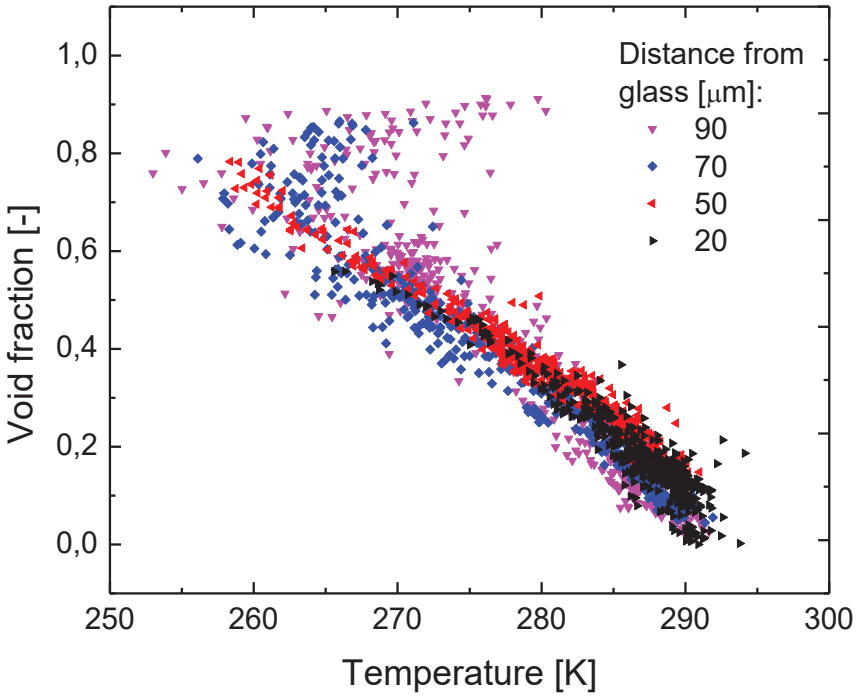

Figure 4.11 – MD L6 scatter plot of temperature against void fraction, 10bar driving pressure measured at different heights in the channel. The legend indicates the z plane height in reference to the glass liquid interphase, expressed in micrometres.

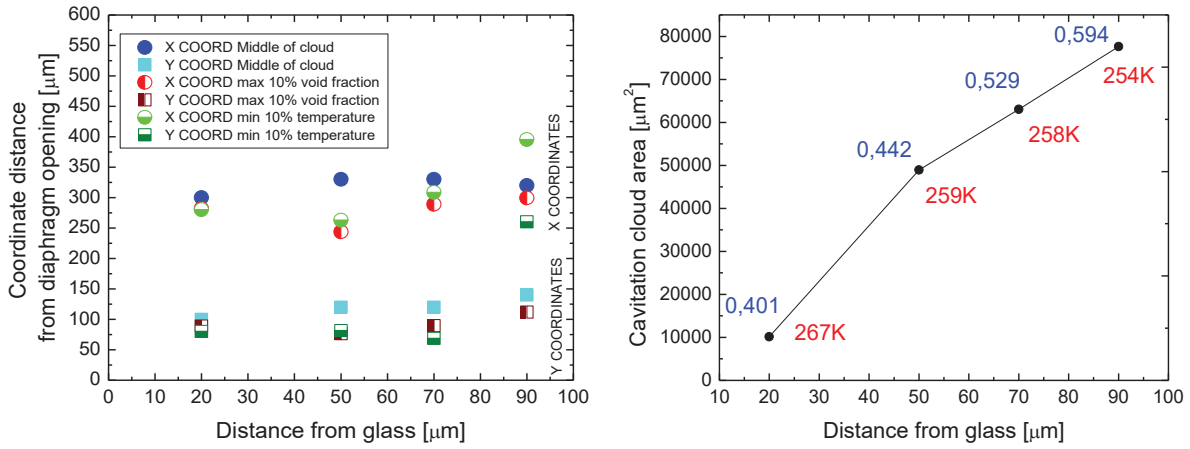

Figure 4.12 - figure on left showing the coordinates of the area analysis from diaphragm opening along the height of the MD L6 channel at 10 bar driving pressure. Figure on right showing the cavitation cloud, its average void fraction (blue value) and the temperature drop (red value).

Figure S.3 shows the VF and temperature maps at different heights (20, 50 and 80μm – 8bar pressure drop) for channel MD 10. The 3D curvature of the flow is seen by the cavitation cloud

retreating from the constriction with depth into the channel. This is not typically seen for our channels, however it was observed with other studies [94]. The two-phase flow also seems thinner in the middle of the channel height than typical flow (L4 -. Figure 4.8) shows a less intense flow at 8bar, which doesn't show signs of vapor bubble coalescence. Consequently, no back-swing is observed on the scatter plots below (Figure 4.13).

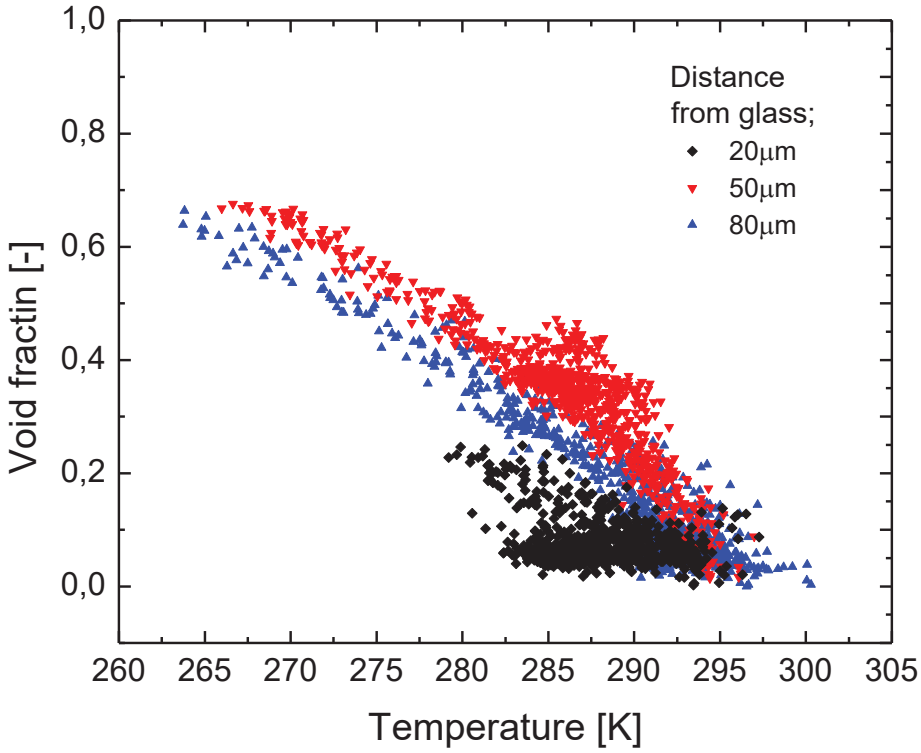

Figure 4.13 - MD 10 channel at 8bar driving pressure. scatter plots of maps at different heights in the channel.

Due to this specific pattern, the analysis points response in Figure 4.14 is obvious for x and y directions. The cavitation cloud area reaching maximum coverage at the midpoint of the measurement, most-likely due to the recording cutting the sheet like cavitation at that particular height. At the lowest point, the cavitation cloud seems to be jetting down towards the silicon wall, so a strong 3D effect of the flow, compared to the usual sheet like distribution. However, the temperatures seem to follow the common trend of decreasing with depth of the channel, as does the average void fraction value.

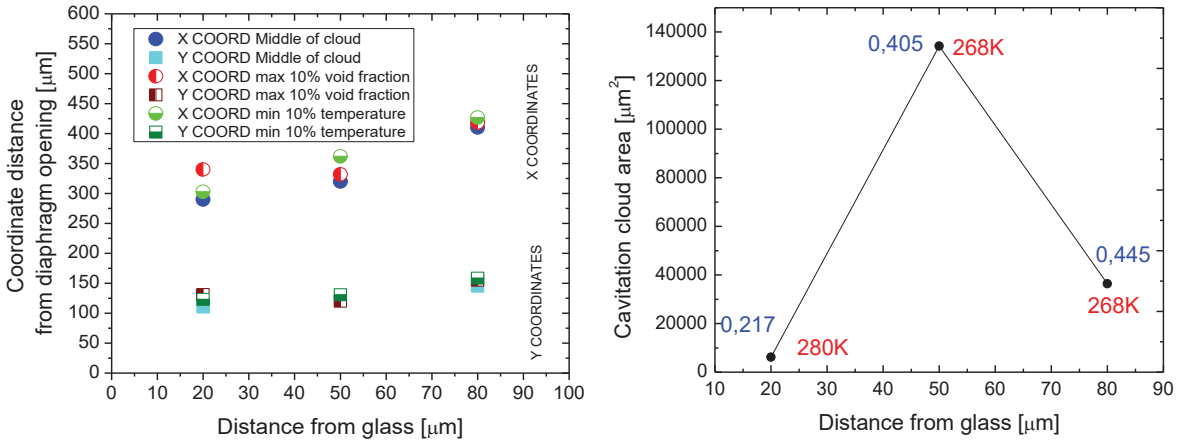

Figure 4.14 - figure on left showing the coordinates of the area analysis from diaphragm opening along the height of the MD 10 channel at 8 bar driving pressure. Figure on right showing the cavitation cloud, its average void fraction (blue value) and the temperature drop (red value). (defined in "Data analysis" sub-chapter). In this case the 0,3 void fraction threshold was lowered to 0,2 for the 20μm measurement plane, due to low intensity.

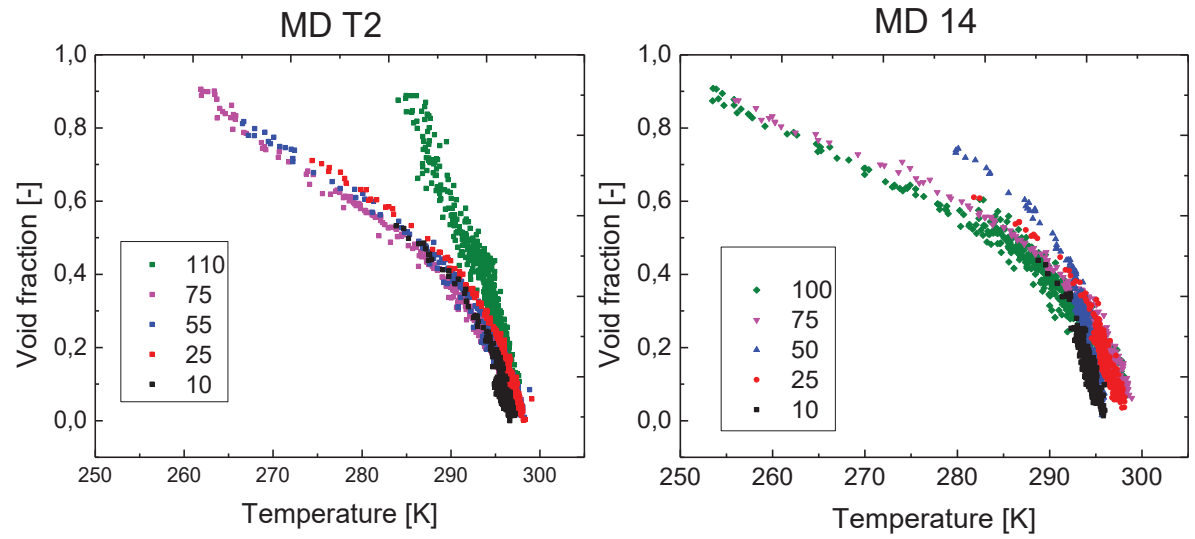

Figure 4.15 - Void fraction vs temperature at different heights in microchannels at 8bar driving pressure. Comparison of MD T2 (left) and 14 (right). The legend in the black square indicates the distance from the forward glass-liquid interface in μm.

In figures Figure 4.14 and Figure 4.15 we can see the difference between the MD 14 and T2 channels, which have the same geometrical parameters (Table 1 – chapter 2.3), yet we can see the curves are not identical. The T2 flow seems to develop the cavitation cloud symmetrically over the height, which doesn't hold for the MD 14. The deeper the light has to pass through the channel

the more it will scatter on the two-phase flow. Thus, a void fraction discrepancy between the top and bottom measurement is appearing, as the temperature drop remains similar. Furthermore, the area analysis for MD T2 seen on Figure 4.16 (green symbols) and Figure 4.17 (red line) shows the temperature related measurements seem to follow the same trend [66]. The void fraction derived data is increasing to the linearly towards the bottom wall, with the average void fraction dropping slightly at the last point.

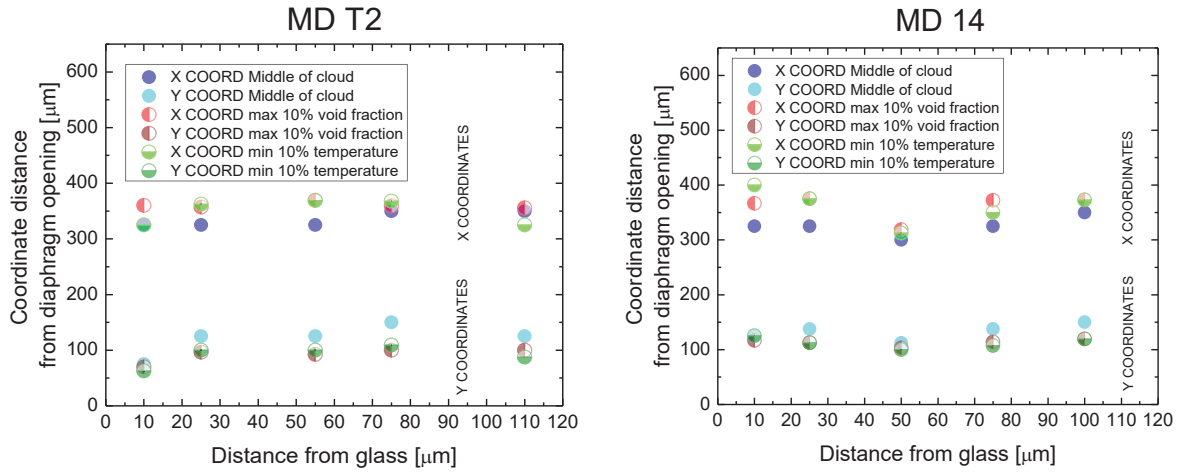

Figure 4.16 – the coordinates of the area analysis from diaphragm opening along the height of the MD T2 (left) and 14 (right) channels at 8 bar driving pressure.

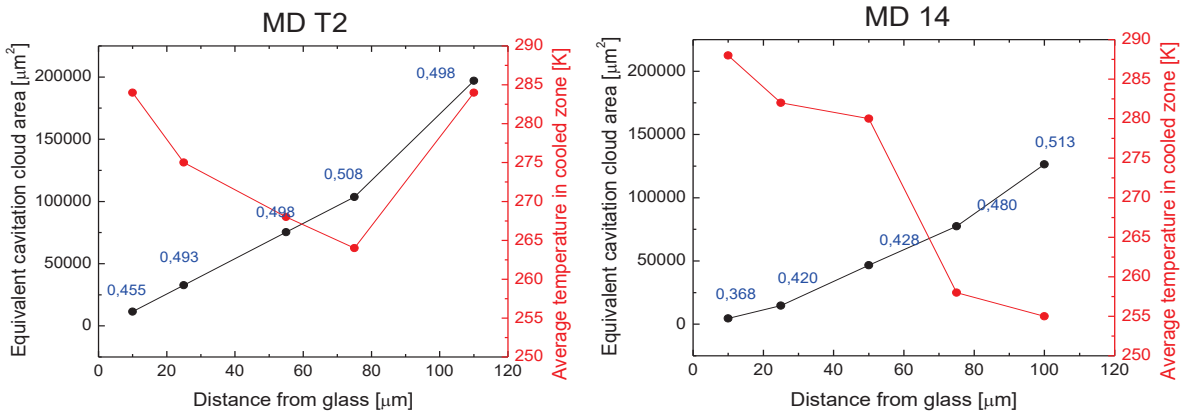

Figure 4.17 – the equivalent cavitation cloud (black) and temperature (red) area for MD T2 (left) and 14 (right) along the height of the channel at 8bar driving pressure. The blue values are the average void fractions and the red line the average temperature of the 10% coolest points.

[66] For MD 14 the 50 micron point was measured with the flow swinging in opposite direction to the rest of the measurements.

It stands to reason that the discrepancy between them should originate from the different materials used for the 4th wall of the channel, as the MD 14 is etched into silicon (3x silicon walls/1x Pyrex) and MD T2 is sandwiched between two Pyrex plates (2x silicon/2x Pyrex). For this channel pair we saw before in chapter 2 (Figure 2.13) the two flow curves also don't correspond. The T2 Pyrex-Si-Pyrex microchannel might present lower drag due to double glass surfaces[67], although this would be surprising since the surface roughness between Silicon and Pyrex glass is in the same range and shouldn't induce significant drag difference [93]. But this slight difference might induce a symmetric flow in MD T2 and not in MD 14. Alternatively, a difference in the constriction geometry[68], since the manufacturing processes are slightly different. There is some evidence of this in Figure 4.15 as the curves for T2 are more uniform with depth than MD 14. The latter evolves the temperature with depth, while the former has more stable temperature profiles.

What could perhaps be happening is either the manufacturing process. The MD 14 presents a typical 3D mapping of Si-Pyrex channels, that is the flow intensity seems to be more intense near the silicon wall (void fraction increased). More likely there could be an effect of flow symmetry in T2, as the cooling trails off at channel walls.

Conclusions for 3D analysis

The 3D analysis of the channels produces conclusive results. A dominating geometrical parameter was not identified, as the geometrical differences between the channels influencing the flow dynamics seem to be more complex than initially thought. However, some interesting phenomena were observed, showing along the way an important property of the technique, that the void fraction gathered form the signal intensity is not directly linked to the temperature information.

Comparison of the MD T2 and 14, channels with identical geometries did not yield corroborating results. Flow curve observations seem to indicate other parameters influencing the flow. Without identifying these complementary parameters, a clear conclusion is difficult, however it seems the channel design is the only clear difference between the two.

The coordinates of the points characterising the flow don't show much variations as the typical two-phase flow seems to be confined. The exceptions being the MD L6 and 10. However both

[67] Higher mass flux at same pressure difference compared to MD 14 - Figure 2.13
[68] or the material mismatch

were recorded at 10 bar driving pressure. The fast camera recordings for the MD T2 showed bubbles in the more intense inner cavitating stream coalescing into a long-lived stationary bubble[69]. A similar regime was observed in MD L6 and 10, which could explain the high void fraction in those points and the corresponding to temperature dispersion in the rest of the cavitating flow[70].Since the bubble disappeared periodically, this exposing the acquisition volume to the liquid therefore yielding a signal, where the temperature readings were quite different compared to the individual bubble growth regime usually observed in the two-phase flow. A specific 3D flow was observed for MD 10 at 8bar, not linked to bubble coalescence.

When considering the MD T2 measurements, we can see the same temperature ranges obtained at top and bottom of the channel, with drastically different void fraction ranges. When measuring at the bottom of the channel, the probing light had to pass the whole height of the channel, including two phase flow, which can scatter part of the light. As the void fraction is approximated from the signal intensity, we can say that the void fraction after a certain depth or flow intensity is no longer accurate. It is hard to estimate the accuracy of the void fraction information, since part of the intensity drop will come from the scattering of the excitation and part of the emission light. A rough estimate could come from MD T2 data in Figure 4.15. If indeed a symmetrical (by height) flow is purposed the measurements done at the bottom should follow the ones near to the top of the channel. The temperatures at 10 and 110μm are in the same range. Due to the use of RIM the temperature information should be conserved even at different signal intensities[71]. From this we could assume the void fraction overestimation can be almost two-fold, depending on the flow conditions.

4.2.4. Driving pressure effect on micro cavitating flow

It can be generally stated that the increase in pressure drop over the constriction should induce more intense cavitation. Perhaps some specific flow events might cause a deviation from the stated[72], however it can be generalized that individual growing bubbles will feel a stronger driving force at higher pressure differences across the diaphragm opening, growing larger at higher rates.

[69] Perhaps begining of a supercavitation regime.
[70] Small individaul bubbles growing and collapsing
[71] With a higher temperature distribution due to an increase in SNR at lower signal intensities.
[72] Choking point of cavitation – where an increase in pressure doesn't yield an increase in cavitation intensity .

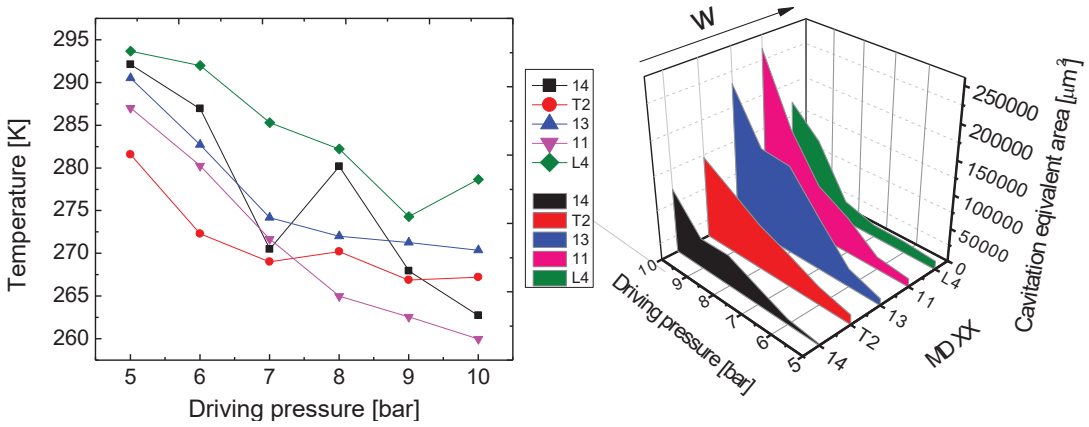

Figure 4.18 – the average temperature in cooling zone evolution for MD L4, 11, 13, 14 and T2 (left) and the equivalent cavitation cloud area graph (right) as a function of driving pressure. The increasing diaphragm opening width (w) is indicated by the arrow (Table 1).

For this analysis the influence of driving pressure on different microchannel was studied. All recordings were done at uniform height in the channel (middle) and at 20ºC liquid and ambient temperature.

Figure 4.18 shows the channel equivalent cavitation cloud area at different driving pressures and the corresponding temperature drop. As expected the cloud increases with increased pressure as does the average void fraction (with the exception of MD L4 at low pressure points). MD T2 seems to obey a linear relationship to pressure increase for equivalent cavitation cloud analysis[73]. The same general trend of average temperature decrease is observed for all samples.

The MD L4 channel seems to be standing out. Considering the geometrical parameters (chapter 2.3 - Table 1) one would expect the highest flow for set channel (w=101µm), or at least comparable to MD 11 (w=92µm). But this is not observed. There are two features to the channel that are drastically different to the others. The diaphragm walls (L) are the thinnest of all samples tested and the second is the fact that it is the long diaphragm setup. Both could individually could alter the flow drastically, let alone the combined effect. Perhaps it could also be the measurement plane height, however it was shown in chapter 4.2.3, that the cavitating flow at the middle of the channel should already be developed. A general trend of temperature decrease with increasing pressure is followed by most channels, with some discrepancies seen for MD 14. Further investigations would be needed to conclude on the influence of the geometrical parameters on the cavitating flow.

[73] Which is infact the cavitation cloud area if all points had α=1

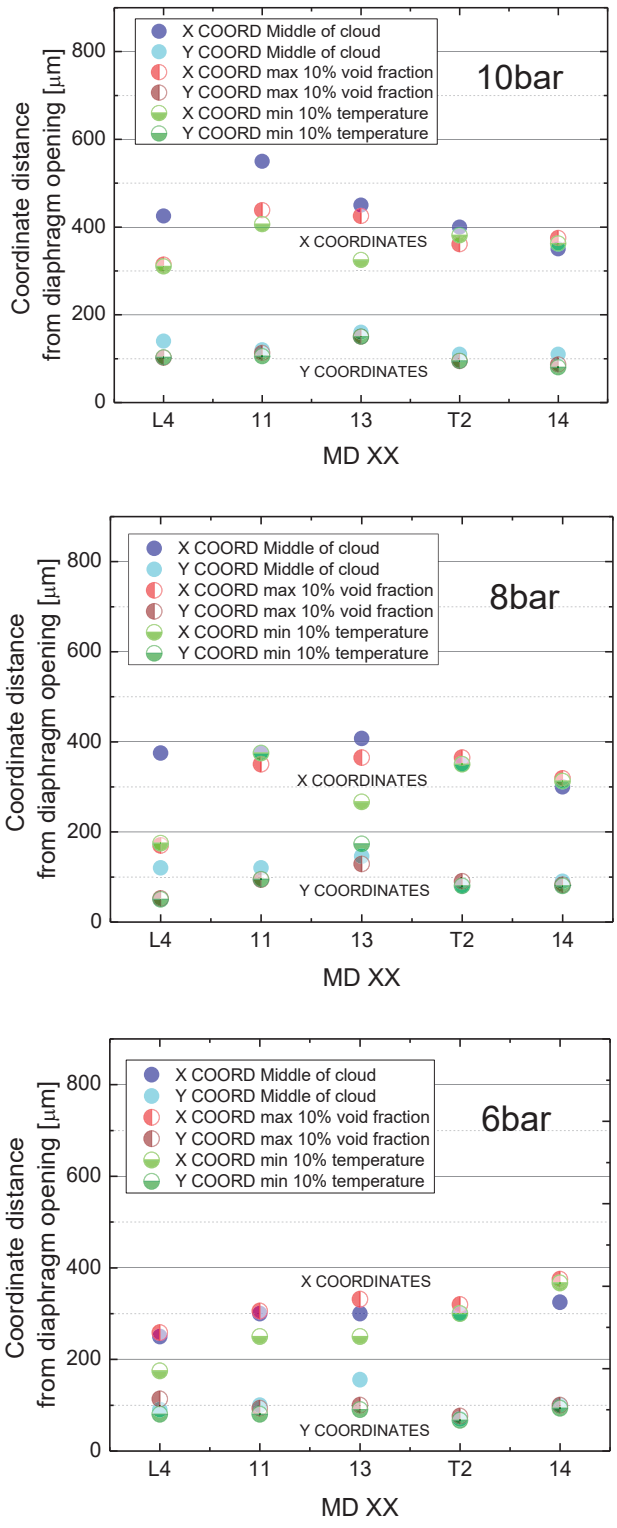

Figure 4.19 – Coordinates of the analysis points in different microchannels as a function of pressure.

The coordinates of the area analysis show some interesting results. In Figure 4.19, the 10bar measurement shows a progressive drop from the MD 11 to 14 for x coordinates involving void fraction, meaning the cloud cavitation is elongating as the diaphragm width or volume flow is increased. MD L4 sample doesn't seem to follow these findings, however the displacement between the cloud middle (full blue circle) and void fraction maximum (half red circle) show about the same displacement at the MD 11 channel. The displacement between its x coordinates varies with pressure drops. At other driving pressures no obvious trends are observed. A general trend of retreating is found for x coordinates as the pressure drops, except for MD 14. The y coordinates seem reasonably fixed and uniform, with the exception of MD 13, for which the x and y coordinates are not overlapping and at increased values (compared to other channels) at all driving pressures. At low flow (6bar), the x coordinates seem to retreat with the increasing constriction width, meaning it's most-likely inversely proportional to the flow.

Conclusion for driving pressure analysis

A general trend of increased cavitation intensity is observed with driving pressure increase. The cavitation cloud, void fraction and temperature drop are all increased as the driving pressure rises. Even the x coordinates of the area analysis follow the flow characteristics for the individual short diaphragms. The MD T2 channel shows uniquely a linear response to most of these parameters, raising the question to of connection to the height symmetric flow, proposed in the previous analysis. The L4 on the other hand is underperforming, considering its dimensions. The proposed explanation is its unique geometry influencing the flow in the microchannel.

4.2.5. Liquid temperature effect on micro cavitation flow

The inlet liquid temperature should have the most significant effect, as higher temperatures ease the phase transition. Also, bubbles are becoming more and more thermally controlled with rising temperature, due to the vapor pressure decrease. In the following analysis was performed on the MD L4, T2 and 14 channel, with the temperatures normalized to their respective liquid temperature. All recordings were done at uniform height in the channel (middle) and at 8 bar driving pressure.

On the following graphs, we can see the MD L4 and 14 follow a common trend, somewhat different to the T2, indicating perhaps that the channel design used is an important factor, as was

seen in previous analysis. The T2 shows variations on the scatter graphs only at VF above ~0,5 evolving with temperature (Figure 4.20). The scatter plot curves seem to be of similar length, indicating roughly constant temperature drop. Due to normalizing issues, most-likely caused by condensation in the channel external wall, the measurements for 10ºC was adjusted to fit the other curves. The measurements for MD L4 and 14 show different behaviour. It is mostly the extent of the temperature drop and void fraction that increase with temperature.

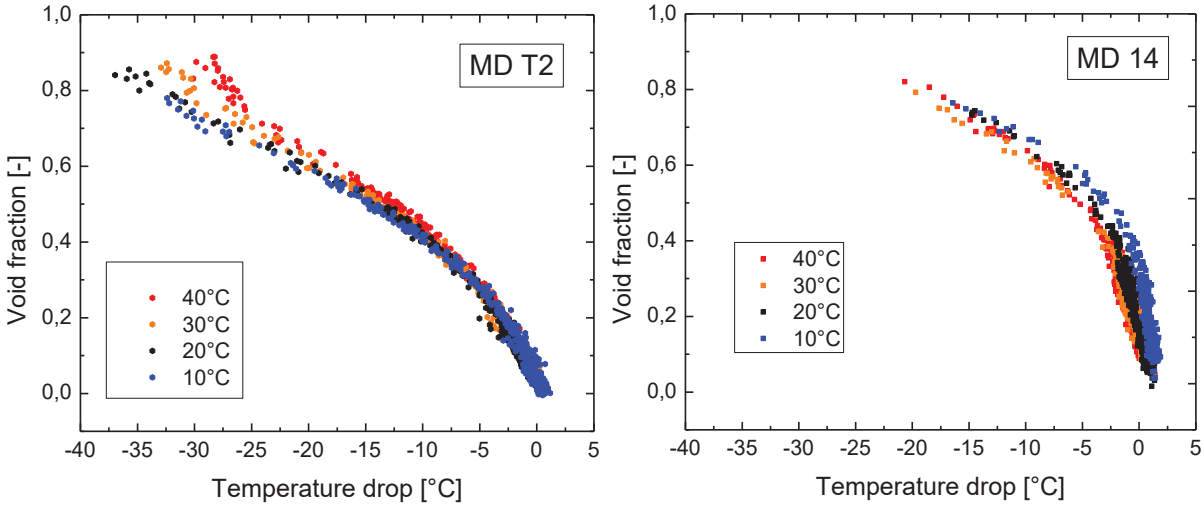

Figure 4.20 - Scatter plot for MD T2 and 14 at 8bar and the mid-height of the channel with varying inlet liquid temperature.

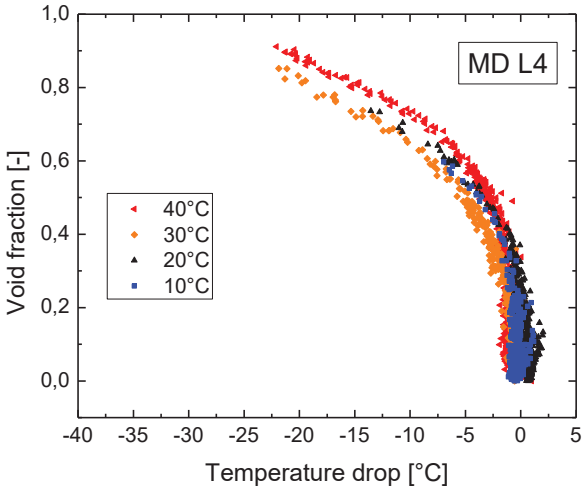

Figure 4.21 - Scatter plot for MD L4 at 8bar and the mid-height of the channel with varying inlet liquid temperature.

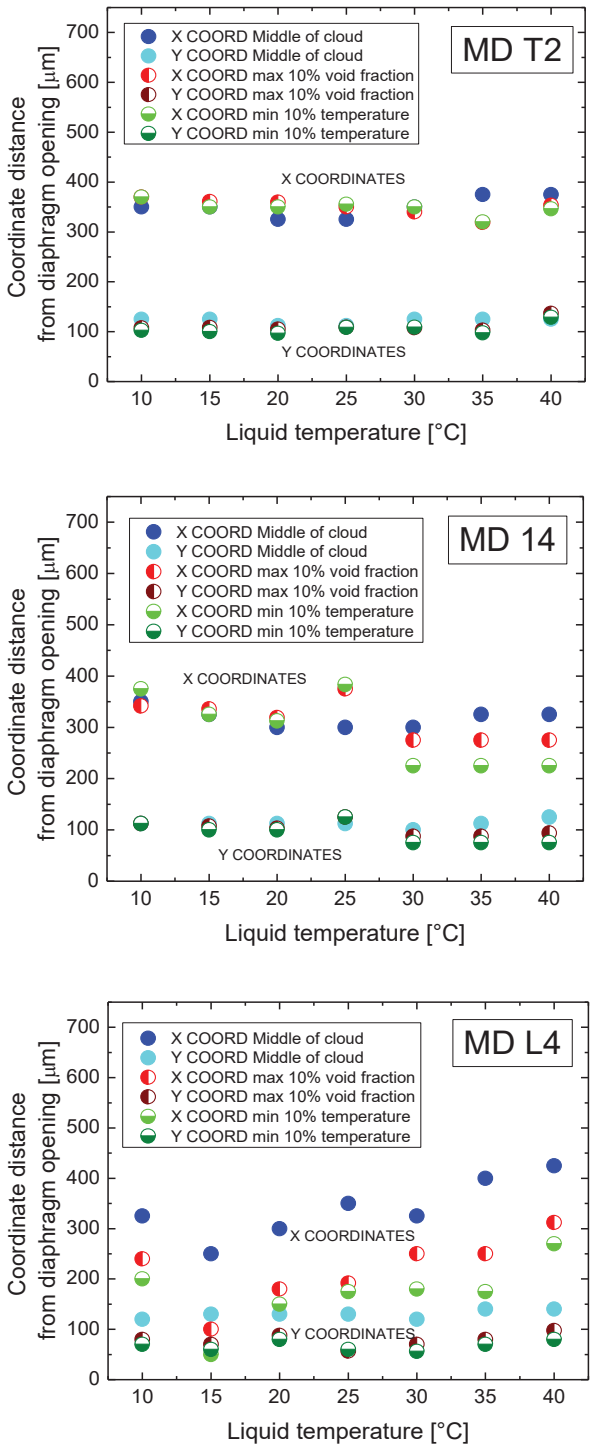

Figure 4.22 - Coordinates of the analysis points in different microchannels as a function of temperature.

The area analysis coordinates in this study does not yield any conclusions. The MD T2 seems to be constant at all temperature values for x and y coordinates, while the MD 14 doesn't show a

clear trend. For MD L4 a rising trend for the x coordinates can be observed with rising liquid temperature. The discrepancy at 10ºC could be caused by condensation forming on the channel surface, as this has been observed to perturb the measurement, Moreover, in Figure 4.23 the cavitation cloud area is examined for MD L4 as the other two did not show conclusive results. The cavitation area curves tend to increase with liquid temperature, as the phase transition is facilitated at higher temperatures, due to an increase in the saturation vapor pressure. In fact, the dashed line showing the vapor pressure curve is followed nicely by the equivalent cavitation cloud area, showing a clear correlation. As the driving pressure is kept constant, it is essentially the saturation vapor pressure that is increased to yield higher cavitation intensities.

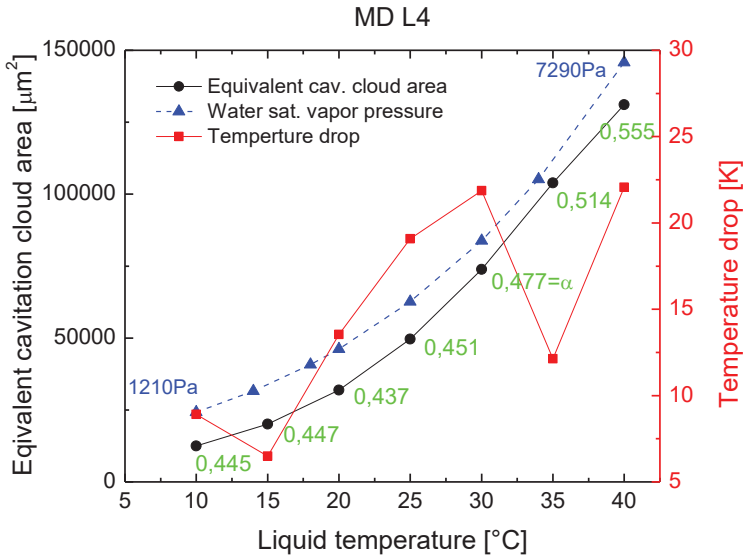

Figure 4.23 - Cavitation cloud area in MD L4 as a function of temperature. The blue line and values are the saturation vapor pressure and the red curve is the average temperature decrease in [K]. The black curve is the equivalent cav. cloud area and the green values the average void fraction.

Conclusion for liquid temperature analysis

By varying the temperature of the working liquid, we have shown (for a single channel) that the cavitation intensity, assessed by the cavitation cloud area, increases as a function of saturation vapor pressure with increasing temperature. The effect is likely to increase at higher temperatures, however the experimental setup temperature control is peaked at 45ºC. In any case the stability of the probes deteriorates at increased temperatures, therefore going above 60ºC is not advisable.

For one sample, the liquid temperature varied the temperature drop (roughly 10K) and to a lesser extent the void fraction achieved. For the other two, the void fraction and temperature drop increased with increasing temperatures.

4.2.6. Temperature gradients and the Thermal boundary layer

In chapter 4.1, it is suggested that using the ΔT* (eq. 4.1) as a reasonable approximation of temperature gradients expected due to bubble growth. However, this assumption disregards significance of the thermal boundary layers, as they encompass the growing bubble, effectively forming a microenvironment around it. The explosive growth occurring at the microscale when the moderating influence from the surface tension is released, should give rise to these thermal boundary layers. Generally speaking, fast bubble dynamics should yield higher thermal gradients and smaller scales should limit their thermalization due the absence or at least low levels of turbulent mixing, which is the case for our microfluidic low Re number flows. It stands to reason that, for the short time of existence for the TBL, a much more intense thermal gradient appears, closer to the interface temperatures T_∞-than ΔT*. It has been suggested that a boundary layer should be accompanying the inertially controlled growth for all but very slow bubble dynamics [7]. However, since the saturation vapor pressure changes with temperature, to a lesser degree at the lower water temperatures compared to high temperatures, the thermal delays aren't expected at 20ºC [58]. Therefore, water is considered a thermosensitive liquid only near the boiling point.

The measured results showing deep cooling in the cavitating regions are puzzling. At first glance the measured temperatures should be in the range of ΔT*, so below 1K. While cooling is expected, as was established in the introduction of this chapter, the extent of the temperature drop is surprising. Even though the heat of vaporization is orders of magnitude above the heat capacity of water (about 500 times as much), the volume of the fluid in the excitation voxel cannot be cooled down to the measured temperatures with the corresponding void fractions.

The working hypothesis presumes the nanoprobes will be probing the thermal boundary layer around the growing bubble. As the liquid evaporates into the bubble it leaves the nanoprobes at the, or near the interface, pushing them along as it grows. Due to the rapid evaporation, a thermal boundary layer (TBD - δ) should appear just around the growing bubble [149];

$$\delta = \sqrt{a \cdot \tau_g} \tag{4.6}$$

For our discussion we use the available data from the fast camera recordings[74] at 6bar, therefore we can consider the fast camera images in chapter 2 - Figure 2.18. The growth time τ_g in this case is about 3-4 frames at 600kHz so roughly 3,5 to 5μs. Entering this into the equation and the thermal diffusivity a=143 10^{-9} m^2/s, we get the TBD should be in the few hundred nm range.

On the images we also see the fast bubble growth from the radius off about 1μm to 30-40μm in the specified time; eventually ending up at 90-100μm.

When considering the energy balance in the growth process we can calculate the latent heat if we know the mass flux of the vapor into the bubble and the heat of vaporization (average value between 20 and 0ºC – 44600J/mol). For the conditions stated above[75], a very rudimentary analysis from the ideal gas law[76], with p_b the bubble pressure[77];

$$pV = nC_R T \xrightarrow[e-end]{i-initial} \Delta n = \frac{p_{b,e}V_{b,e}}{C_R T_{TBL}} - \cancel{\frac{p_{b,i}V_{b,i}}{C_R T_{AMB}}} \xrightarrow[no\ vapor\ content]{i=initial=0} \frac{p_b V_b}{C_R T_{TBL}} \tag{4.7}$$

shows 0,00114nmol of vapor entering the bubble, corresponding to 390nJ of heat absorbed by the process. The minute initial content ($p_{b,I}$ $V_{b,i}$) of the bubble is roughly 4 orders of magnitude lower and can be neglected. Moreover, any gas expanding in the bubble would only aid the cooling. The latent heat was taken from a layer of liquid surrounding the bubble. Thus, by simply considering the highest temperature depression we measured for the 6bar driving pressure in the T2 – 20K and the heat capacity of the liquid c_p – 4,186J/(g K), we calculate the mass of the cooled layer. About 5ng of water is cooled which corresponds to the volume of 5000μm^3 and the boundary layer thickness of about 190nm around the 90μm bubble. This is in the range of the boundary layer calculated above (eq. 4.6). Furthermore, it is thick enough to encompass the ~60nm nanoprobes. The characteristic thermalization time of such a layer is considered in the equation below [146];

$$\tau_{th} = \frac{L_{TBL}^2}{a} \tag{4.8}$$

[74] Low driving pressures, where we can still distingush the individual bubbles.
[75] 1micron bubble radius grows to 90micron.
[76] C_R notation used to avoid confusion with radius.
[77] Saturation vapor pressure + surface tension – 6500Pa.

where L_{TBL} is the thermal boundary layer thickness. For our case, the characteristic time would be just below 1µs range, but this equation considers the thermalization of a spherical object and surely doesn't model accurately our particular case. Moreover, as our calculations don't consider the growing interface pushing and thinning out the TBL, counteracting the thermal diffusion. Also, the calculations assume instantaneous heat generation in the volume of TBL, which of course isn't the case. All this would, in real-life situation, further prolong the existence of the TBD and increase the likelihood of measuring it.

This scenario would be perfectly suited for numerical simulations; however, it was out of scope for our project due to time constraints. Our simple analysis still shows it is reasonable to assume that our technique is at least partially probing the TBL around the growing bubbles.

The bubbles are not completely spherical during the last stage of the growth, as the surface tension forces decline. Considering the Re numbers indicating laminar or close transient regime, we can say that thermalization would mainly take place by diffusion, which can further prolong the presence of temperature gradients in our microfluidic flows.

Furthermore, temperatures reached in the TBL in some flow dip below 0ºC. Of course, due to the fast dynamics and the demonstrated metastability of our system, this can be simply explained by water supercooling. Since, the very low temperatures are usually measured in high VF points, there is also the added error from the SNR increase, which might overshoot the measurements in such cases. The error associated with the VF should be +/- 0,2ºC for $\alpha < 0,5$ and at $\alpha > 0,5$ rising up to +/- 2,5ºC.

Comparison to previous study

The appearance of cooling regions is not surprising in cavitating flow. Moreover, one would expect heating regions appearing in the flow due to condensation of the bubbles. In fact, this was observed in a previous study on a single channel [94], using the same setup, liquid and channels. However, no heating has been observed in our multi-channel study, even for the ones with similar dimensions (MD 14 and T2). Even when comparing the flow curves, it is clear the flow conditions aren't mimicked (ΔQ=+/- 10%). In fact, this is most-likely due to geometrical parameters mismatch[78], making it reasonable to assume the MD T2 and 14 are not similar enough to compare with the

[78] The channel heights (16%) and to a lesser extent the width (5%) and length (6%) of the diaphragm opening.

microchannel used in the previous study. The heating region from the former study is argued by the presence of a recirculating vortex, where bubbles collapse and the latent heat[79] is confined in the stable vortex. This would lead to steady state temperature gradients, which are easily measurable by this technique. In our study, we also see the recirculations (Figure 2.18), as they seem to be inherent to the flow in microdiaphragm channels. It is currently hypothesized that perhaps small changes in geometry could lead to the altered flow dynamics. These could be specific to the channel geometry or a consequence of clogs in the system. This is actually a common problem in the system. Often the use of fiberglass filters can release a fibre which can partially clog the diaphragm and drastically alter the flow conditions. Our recent studies incorporated a 10μm nylon filter to trap this kind of fibres but for the study beforehand this filter wasn't present. If partially clogged[80], it might have gone unnoticed and produce the results reported in the article [94]. In the previous study, slight cooling was also noticed in other regions of the channel, alongside the heating.

Missing collapse region

Continuing from why we couldn't replicate the specific recirculation zone heating, the question is why do we not observe heating regions from the condensing bubbles. After taking a look at the high-speed recordings, we can see that while the growth zone is very much localized at the exit of the constriction and following the liquid jet, the area where the bubbles collapse is spread out through a large area, far from localized. This means the accumulated energy is spread-out downstream the channel. Also due to the point like collapse, the energy even if focused, will dissipate quickly in the liquid and not produce a stable but a transient heated zone which is undetectable by our averaging technique. Another effect might be contributing to the lack of the heating zones. The first is only valid for laminar or close to laminar flow and very quick bubble growth and collapse. Due to the lack of mixing, the energy consumed by the growth would be redeposited upon collapsing, onto the same layer of water that was initially cooled. If fast enough, the lack of thermalization would yield an average zero net temperature change.

[79] Perhaps accompanied with viscous heating
[80] Single glass fibre, a few micron thic and hundreds of microns long.

4.3. Raman Stokes/Anti-stokes measurements

As mentioned before, water doesn't possess luminescent properties. Therefore, in order to perform luminescence-based measurement, specialized materials have to be added into the liquid in order to collect the information. The other option is to use inherent signals like IR thermometry[153] or as we will demonstrate Raman scattering techniques [156].

4.3.1. Raman scattering and spectroscopy

Raman scattering is an inelastic scattering process, meaning there will be an associated energy (wavelength) variation to the incident light. Often used complementary with IR spectroscopy, it is a powerful tool for determining molecular structures. Their principle is based on the fact that molecular motion is not random, but predetermined vibrational modes exist in every molecule. Raman scattering signal will occur depending if the vibrational modes cause a change in the polarizability potential (deformation of the electron cloud), whereas IR spectroscopy is based on the absorption of photons in the infrared range of the spectrum, where a change in the dipole moment is required for the particular vibrational mode to be detected. This means a particular vibrational mode might be either Raman (or IR, or Raman/IR) active/inactive.

Raman spectroscopy usually relies on the Stokes peak (red shift – energy decrease) to probe the molecular structure of the molecules[81]. The peaks produced are often temperature dependent, as we will see is the case for the water stretching band (chapter 7.3). In fact, the same analysis method is used as with the nanoprobes – RIM[82]. Since, the method uses only the Stokes stretching part of the Raman spectrum it will be abbreviated as S-RIM (for Stokes or Stretching band RIM) from here on. Another relatively simple method can be used, relying on the different intensities of the Stokes and Anti Stokes peak because of the population variation of the vibrational levels from the ground state as a function of temperature (Stokes/Anti-Stokes measurements – from here on referred to as S/AS). In our study we used the two different principles of Raman scattering for thermometry.

The Raman scattering experimental setup (Figure 4.24) is essentially a slightly modified achromatic confocal microscope discussed above (Figure 4.1 and Table 8). For Raman scattering

[81] Particularly the functional groups.
[82] Ratiometric intensity measurements.

spectroscopy, we simply use the powerful 532nm laser, normally used to excite the Ti:Sapphire laser. By changing a few optical elements, like q) filters and the k) dichroic to accommodate the new wavelengths and by-passing the pulsed laser setup, we essentially obtain a confocal Raman spectroscopic setup. The microfluidic setup remains unchanged, with the exception that it's thoroughly clean of nanoprobes and ultrapure water or propane-2-ol (isopropanol) is used as the working fluid. In the event some nanoprobes remain, they would not disturb the Raman scattering signal as the excitation light is beyond their excitation peak (and in fact the emission peak also). By simply varying the detection spectrum on the detection system, we can use the S-RIM or the S/AS measurements.

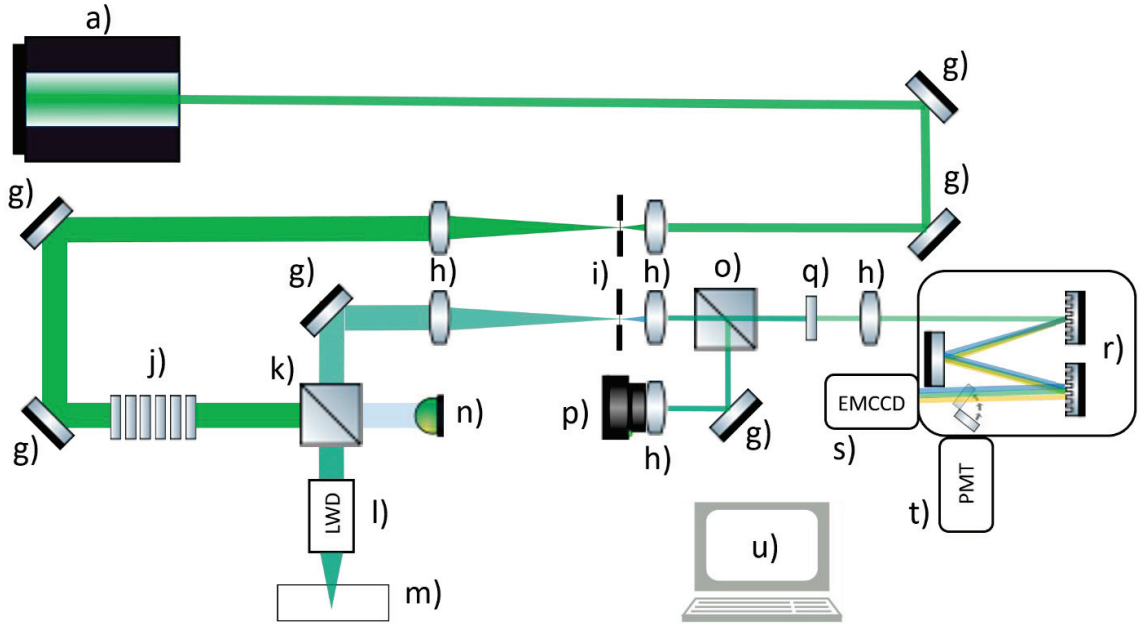

Figure 4.24 - Raman scattering confocal microscope setup. The device list can be found in Table 8.

First, the **Stokes/Anti-stokes thermometry** principle is highlighted in the following equation, where I is the intensity of the measured peak (subscript S – for Stokes, AS – for Anti-Stokes), ν – wavenumber [cm^{-1}], h is Planck constant, c is speed of light, k – Boltzmann constant, and T the absolute temperature [K] [157]:

$$\frac{I_{AS}}{I_S}=\left[\frac{\nu_0+\Delta\nu_i(T)}{\nu_0-\Delta\nu_i(T)}\right]^4\exp\left[-\frac{hc\Delta\nu_i(T)}{kT}\right]=\left[\frac{\nu_0+\Delta\nu_i(T)}{\nu_0-\Delta\nu_i(T)}\right]^4\exp\left[-1{,}4387\frac{\Delta\nu_i(T)}{T}\right] \quad (4.9)$$

Basically, it relies on the Boltzmann distribution of the population in the vibrational states associated with the electronic ground state of the molecule (water/isopropanol ...), to yield directly the temperature information from the equation (4.9). As all other parameters are either constants or can be gathered form the measurement, like the Stokes and Anti-Stokes shifts and intensities, the absolute temperature information can be obtained. For this reason, the technique does not rely on the use of calibration curves.

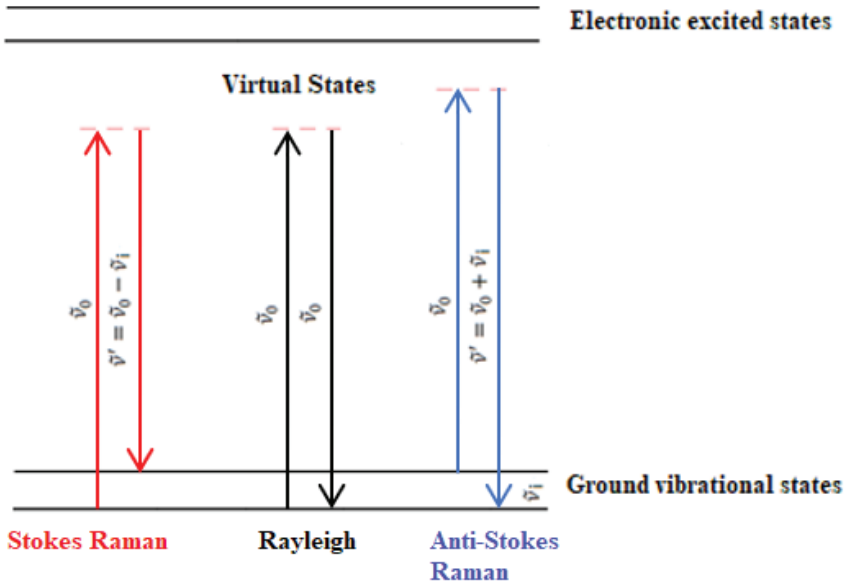

Figure 4.25 - Rayleigh scattering (elastic), Stokes (red shift) and Anti-Stokes (blue shift). From the intensity of the Anti-Stokes and Stokes peaks, one can probe the ground vibrational state population, which would depend of the Boltzmann distribution (temperature dependent).

Often it is used for high temperature measurements [157], where the population of the Anti-stokes peak will be much higher, yielding more accurate measurements. The Stokes Anti-Stokes technique has been used as a nanoscale thermometry probe [158]. Known since the start of the 1980, the use of the CARS (Coherent Anti-Stokes Raman Spectroscopy) for thermometry in flames and combustion processes was well established [159], [160]. Essentially, CARS is an enhancement mechanism of the inherently weak (near room temperatures) Anti-Stokes peak, however it requires expensive excitation laser equipment. For the use in our microfluidic setup it is sufficient to detect both peaks even at room temperature range, considering the expected temperature gradients. As the only strong emitting mode for water is the stretching band, with a high Stokes shift (~3200 cm^{-1}), the Anti-Stokes peak would be undetectable. For this reason, water

can't be used in our desired temperature range. The use of isopropanol[83] is preferred, as it produces Raman scattering peaks with much smaller spectral shift, compared to water.

Raman Stokes/Anti-Stokes thermometry results

Problem of inherently low signal from Raman scattering, requiring long exposure times and high laser power to obtain reasonable results from the water stretching peak. Furthermore, the signal will drop with void fraction, making temperature measurement even more unreliable in the intense two-phase flow. Also, it remains unclear what the effect of the vapor phase would be on the scattering signal, as all previous uses were with single phase flow. Vapor phase should have a much less intense response and most-likely a perturbed spectrum, due to the lack of the hydrogen bond network. Interfacial effect could also perturb the spectrum due to the dangling bonds present at the interface

Figure 4.26 shows the cooling regions occurring. The S/AS technique as mentioned above doesn't' rely on thermosensitive material being dispersed in the working liquid. The information is gathered from the inherent inelastic scattering of molecules composing the liquid. Unfortunately, due to the different properties of water and isopropanol, the flow dynamics are not comparable. Surface tension, density and viscosity vary greatly between them so a similarity in the flow conditions cannot be expected. However, the S/AS thermometry technique does show cooling in the same range, for a liquid of comparable latent heat properties (~45kJ/mol). Due to a lower heat capacity and denser vapor, the volatile isopropanol should produce higher global cooling compared to water.

The S-RIM measurements (chapter 7.3) should yield some answers, since both use water as the working fluid, it could confirm the TBL hypothesis presented for nanoprobes based thermometry. In fact, we unsuccessfully attempted to measure temperature gradients in isopropanol with temperature sensitive nanoprobes. This way a relevant comparison of the two techniques would have been observed, however problems of nanoprobes precipitation occurred continuously, preventing these measurements.

[83] Other organic liquids could be used.

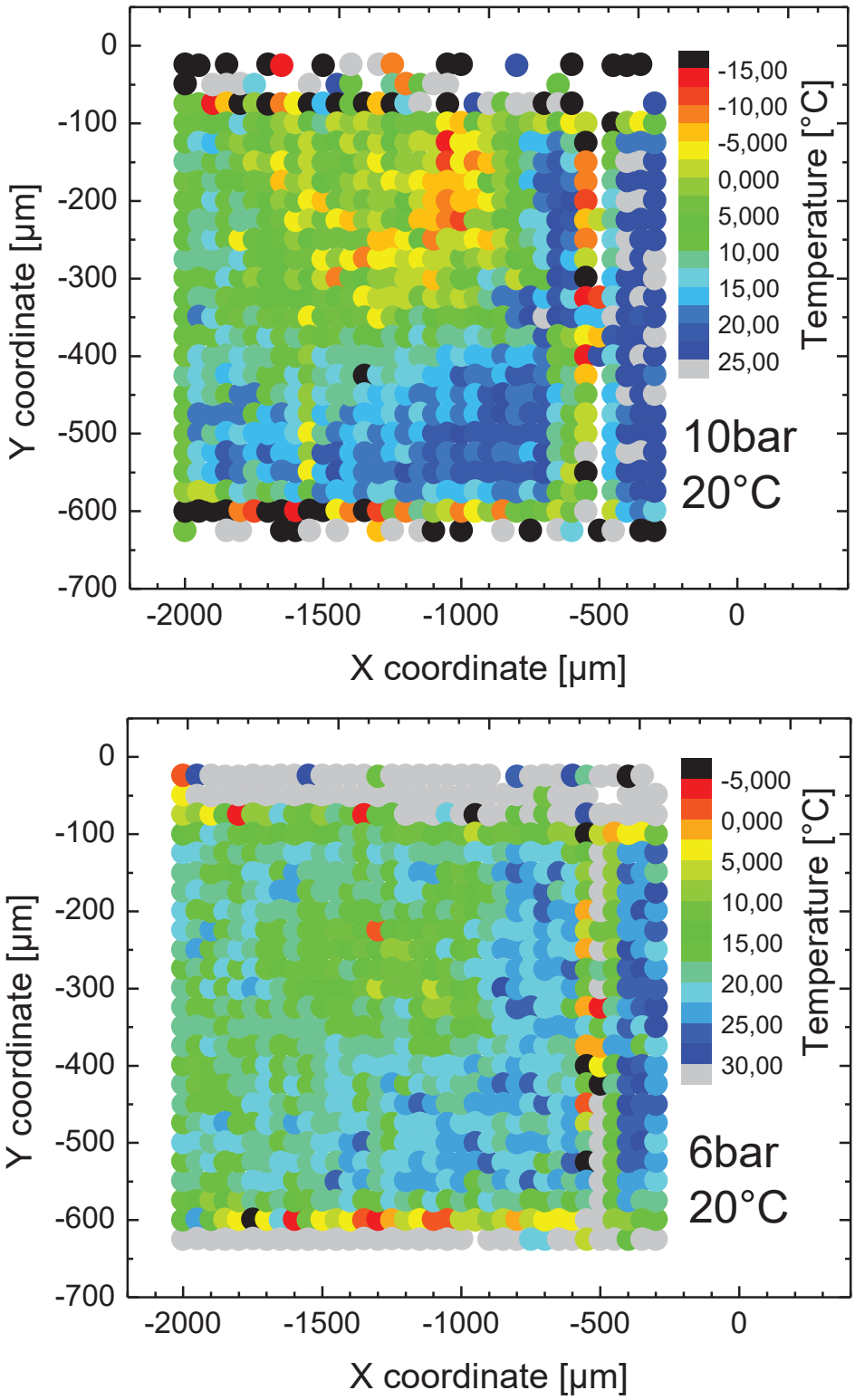

Figure 4.26 - S/AS temperature plot of MD T2 diaphragm with isopropanol as the working fluid at 10 and 6bar.

4.4. Conclusions on temperature gradients in cavitating micro-flows

The thermal gradients observed in our study of water in cavitating flow at 293K are too high to be explained by bulk liquid cooling, as this would be minute for all but the highest void fractions. Since the vapor density is low, the amount of matter transitioning will also be small, therefore, even the 500x higher latent heat compared to the heat capacity of water will not be enough to cool down the bulk water significantly. For this reason and the fact that vapor pressure at 293K does not vary substantially, water is not considered a thermally sensitive liquid.

A viable hypothesis is presented for the observed bubble dynamics. The deep cooling observed localized in the bubble growth region of the flow is most-likely consequence of probing into the thermal boundary layers around the bubble. This would yield a much greater temperature decrease, than a thermalized liquid would. The bubble growth would counteract the effect of thermal diffusion, by thinning out the layer as it grows, thus prolonging the TBD existence.

The question is raised regarding the expected heating due to bubble condensation upon collapse. An explanation for these missing heating regions, corresponding to bubble collapse area, is most-likely due to a non-localized collapse region. As the bubbles grow in two confined regions around the liquid jet just downstream of the diaphragm opening, their combined localized effect seems to be easily measurable, while the dispersed collapses are not registered with presented averaging techniques.

As will be discussed in chapter 5, the idea behind the chemiluminescence mapping was also to locate the collapse region. The area of highest intensity should correspond to the collapsing bubbles, due to the radical production. The same could be achieved in the case of strong luminescence from a bubble collapse, which might occur for argonated water.

Further on, a parametric study was attempted to observe the effects in cavitating flow in microchannels. High void fraction values of up to 0,95 are observed, with the accompanying temperature routinely dropping to -10ºC and more in extreme cases. This would indicate supercooled water around the rapidly growing bubbles. Due to the observed metastable effects for cavitation inception it seems reasonable to have metastable liquid for the supercooled water region, especially considering the short lifetimes of thermal non-equilibrium. A general trend on the

scatter graphs seems to be a double (sometimes triple) slope of the temperature/void fraction line, with the transition between $\alpha = 0,3$ and 0,5. The interpretation of this is observation is not clear at this time, but it could possibly be linked to the double cavitating streams and the liquid volume between the bubbles.

The 3D flow distribution showed a typical trend for the silicon Pyrex microchannel, which is the cavitation cloud increasing in size and intensity towards the bottom wall, while the temperature drop maxima are situated in the mid-height in the channel. Particularities found in specific channel flows highlighted an important feature of the measurement technique: no direct link between the void fraction measurements the temperature information.

The influence of driving pressure and liquid temperature on the flow was also studied. The cavitation parameters tend to increase with increased pressure and liquid temperature. A correlation with the saturation vapor pressure is found when liquid temperature is varied.

The validity of our measurements is also confirmed by a complementary study with Raman scattering stokes/anti-stokes thermometry, for isopropanol as the working fluid. A similar temperature range was observed, although a comparison between the techniques is difficult due to the flow and liquid parameter variations, as well as the lack of void fraction information makes.

Commenting on the thermal delay in such flow is difficult and is not the focus of our study, since traditionally temperature gradients in the direct vicinity of the bubbles are not considered. However, a long-term goal is to use these techniques with liquid nitrogen as a surrogate liquid for the more dangerous liquid oxygen and hydrogen rocket fuels. This way a thermally sensitive liquid could be studied for the thermal delay effects. In cryogenic liquids the generated cavitation bubbles are finer and less coalescence takes place as compared to water [161], therefore even greater effects on single bubbles are expected.

5. Cavitation induced radical production

Radical production is well known to occur for acoustic cavitation (AC). It is believed to be linked to sono-chemical reactions [10] biological and chemical waste water treatment [18] and the driving force behind sono-chemiluminescence [162]. Radical formation in AC however, is considered an inefficient way to transfer energy to the liquid [73] especially for bulk liquid processing.

Hydrodynamic cavitation (HC) could be the answer for bulk fluid processing and improved energy transfer efficiency [109]. The same source suggested extrapolating from known mechanisms in acoustic cavitation and applying them for hydrodynamic cavitation, However this is not always straight forward, as some controlling parameters in AC can't easily be converted for HC [98], [163]. One of the more important ones is bubble exposure time to driving pressures. These are usually orders of magnitude apart; AC - μs (kHz sound waves) and ms for HC (liquid velocity through the constriction). However, at the microscale as we saw in chapter 2, the bubble growth times could be in μs range, perhaps making it comparable with low frequency AC [109].

In this chapter we discuss the radical formation from collapsing bubbles and the optical acquisition of chemiluminescence to observe their formation. An article was published on this topic during the thesis [98]. The results from the article and new developments are presented and discussed.

5.1. Cavitation bubbles as chemical reactors

For an imploding bubble, the collapse conditions can be considered "quasi"-adiabatic, therefore limited mass and heat transfer across the interface, resulting in vapor being trapped in the bubble during collapse. As vapor (gas) is compressed by the shrinking interface, the thermodynamic parameters increase, exposing it to extreme temperatures and pressures. This can lead to various chemical reactions and exotic species being produced in what is called sono-chemical reactions [18], [73].

In fact, there are evidence of temperatures >10000K and >1000bars[84] of pressures for short times (200ps plasma flash time [165]) at peak collapse [164]. Numerical simulations have put these numbers much higher (pure Xe gas, ~10^8K for a few hundred femtoseconds [70]), considering also

[84] Some claiming 10Gpa [164]. however these are values obtained from non-equilibrium plasma, which wouldn't correspond to actual gas temperatures (see chapter 2.1.2)

the proposed shockwave in the rapidly collapsing bubble, amplifying the thermodynamic conditions at the peak collapse. These predictions might hold, were it not for the endothermal reactions taking place in real bubbles, containing vapor and gas [10]. Therefore, the latter two may experience chemical bonds dissociation, reaction initiations and even production of ionized species, producing plasma, which is at the core of the sonoluminescence phenomena (chapter 2.1.2).

During collapse, even the bubble interface was shown to be at elevated temperatures, above supercritical conditions (647K, 221bar). In the RPE (Chapter 2.1.1), the liquid at the interface is assumed to have uniform temperature to the surrounding liquid. At peak collapse however, the temperatures due to condensation and the conduction from the hot bubble core might heat up a fine layer of liquid, immediately surrounding the collapsing bubble. This has been demonstrated experimentally (~1900K [166]) and numerically (~1500K [167]). However the scales are in the ns and nm range [164]. In Figure 5.1 the reaction zones of the collapsing bubble are shown. The inner bubble forms the initial radicals, the interface and boundary layer around is where the aqueous solution of the radicals reacts and transports the remaining radicals to the bulk liquid.

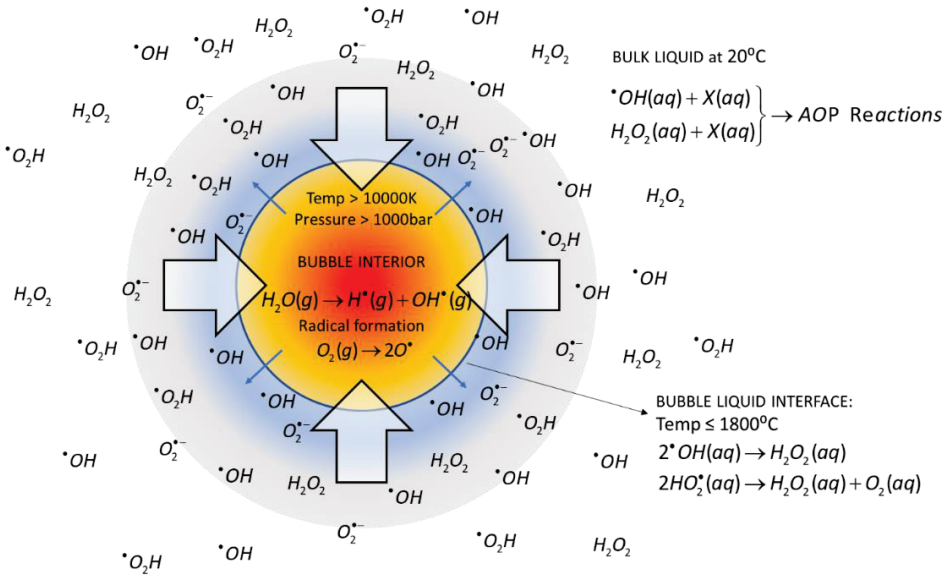

Figure 5.1- Bubble collapse regions and the radical/reactions associated with it (eq 5.1 to 5.9). Bubble gas phase with the homolyses of water vapor, producing hydroxyl radicals. The transition in to the liquid at the interface and the hydroxyl radical and hydrogen peroxide dominant presence in bulk phase. Based on [18].

Cavitation induced radical production

As mentioned, the fast, adiabatic collapse traps the vapor inside the bubble and subjects it to extreme temperatures and pressures during compression. The chemical reactions and exotic species being produced are at the root of the process called sonochemistry. Most of what we understand about cavitation radical yield originates from AC. However, not all parameters in AC are easily transferable to HC, like frequency, exposure time, pressure fields [109].

Of course we can expect many chemical reactions from such an energetic system [168]. For an air filled bubble, 93 chemical oxidation/reduction reactions were identified [169]. In air saturated water the main dissociation reactions would be from the homolytic cleavage of water vapor (eq. 5.1) and the dissociation of dissolved oxygen (eq – 5.2) [162] listed below:

$$H_2O(g) \rightarrow H^{\bullet}(g) + HO^{\bullet}(g) \tag{5.1}$$

$$O_2(g) \rightarrow 2O(g) \tag{5.2}$$

The products may further recombine [162]:

$$HO^{\bullet} + HO^{\bullet} \rightarrow H_2O_2 \tag{5.3}$$

$$O + H_2O \rightarrow HO^{\bullet} + HO^{\bullet} \tag{5.4}$$

$$H^{\bullet} + O_2 \rightarrow HO_2^{\bullet} \tag{5.5}$$

$$2HO_2^{\bullet} \rightarrow H_2O_2 + O_2 \tag{5.6}$$

And pH dependent reactions will yield an increase in the superoxide anion radical $O_2^{\bullet -}$:

$$HO_2^{\bullet -} \underset{\longleftarrow}{\overset{pKa=4,8}{\longrightarrow}} H^+ + O_2^{\bullet -} \tag{5.7}$$

$$HO^{\bullet} + H_2O_2 \xrightarrow{k_1} O_2^{\bullet -} + H_3O^+ \tag{5.8}$$

$$HO^{\bullet} + HO_2^{\bullet -} \xrightarrow{k_2} O_2^{\bullet -} + H_2O \tag{5.9}$$

The absence of H is explained by supplemental reactions[85], where $H^{\bullet}$ is consumed by: $H_2O + H^{\bullet} \rightarrow {}^{\bullet}OH + H_2$, $HO_2 + H^{\bullet} \rightarrow 2{}^{\bullet}OH$ and $2H^{\bullet} \rightarrow H_2$ [8]. Apart from implications in reactions above, the role of oxygen in sono-chemical reactions is still not completely clear [170]

Sonochemistry has been used for wastewater treatment (degrading organic pollutants), process intensification and mixing and production of nanoparticles [73]. In chemical and mostly pharmaceutical industry, waste water treatment is an important, yet costly process, making any improvements on this part highly desirable. To this end hybrid AOP (advance oxidizing processes) / cavitation based techniques are becoming popular [18]. The process for the most part relies on hydroxyl radicals oxidizing the pollutants, as it has a very high oxidation-reduction potential, one of the highest among the radicals expected from cavitation [168], higher to that of hydrogen peroxide [164]. AOP can produce radical by chemical or catalytic reactions. These could be photochemical or mentioned hybrid AOP method. The strong oxidizing reactions of these hybrid systems can reduce the pollutant content by as much as 60%, compared to 10-20% for stand-alone cavitation [18]. As seen in Figure 5.1, the pollutants are removed either by exposure to extreme conditions in the bubble at collapse[86] or by the subsequent reactions in bulk liquid. The former applies mostly for volatile substances, that could enter the bubble to begin with, however most is done by the AOP. An extensive parametrical review on the topic was recently made, where it has been suggested that HC could be more energy efficient than AC for radical formation, especially when industrial scale up is considered [18], [109].

[85] example eq. 5.7.
[86] Temperature, pressure and radicals present at peak bubble collapse.

5.2. Chemiluminescence

Chemiluminescent (CL) reactions are chemical reactions that produce species in excited states, which eventually relax to the ground state by a radiative process. Often referred to as »cold light« reactions as opposed to incandescence. The chemical reaction transfers energy to an electron in the molecule, prompting it into an excited state, much like as it would be after the photon absorption in photoluminescence. So, the luminescent molecule is essentially excited to a singlet state. From this point onwards, the aforementioned relaxation mechanisms (chapter 3.1) take over, one of possibilities being radiative (light emission). There are several known chemiluminogenic such as species from acylhydrazide group, acridinium and peroxyoxalic derivatives, dioxetenes and coelenterazines [171]. In fact many organic species are known to have CL reactions, but the low (practically non existing) yield makes most of them unsuitable as a CL probe [171]. For example, lucigenin forms a CL reaction with reductive species[87], and has thus been used in sono-chemilumienscent experiments [8].

However, most frequently used and best studied is luminol (acylhydrazide group) and its derivatives, due to its low cost and availability [172]. It has a chemiluminescent reaction with many species and radicals, most importantly for the scope of the thesis with the OH^{o} , a radical which is known to be produced at the vapour bubble collapse in water (previous chapter). This specific CL reaction is further discussed in the following subchapter.

5.2.1. Luminol chemiluminescent reaction

As mentioned, luminol (5-amino-2,3-dihydro-1,4-phthalazinedione) is a popular substance used in clinical and analytical sciences (immunoassay, monitoring metabolic pathways, detection of free radicals, inorganic substances and trace metals, forensic and environmental applications)[171]. For this reason there are several reviews on the subject of luminol in the scope of chemiluminescence [171], [172]. These two sources were used for the bulk of the general information on luminol and CL in this subchapter.

The first chemiluminescent reaction was observed back in 1877 by Radziszewski [173]. A full 50 years later came the first report of luminol chemiluminescence (LCL, from here on) by Albrecht

[87] Isopropanol reaction with O_2 , producing the superoxide radical (O_2^{-o}), producing a CL reaction with lucigenin [8].

in the 1928 [174]. Since then LCL has become the most studied CL reaction, with numerous reaction mechanism studies performed, making it the benchmark for CL reactions.

Luminol is a yellow-coloured crystalline powder, solvable in most polar organic solvents, but not so in water. It is present in three isomers; the first (Figure 5.2 -I) being more stable, fluorescent and exhibits a CL oxidation reaction and is found in crystalline form as a tautomer (Figure 5.2 - II) [175]. For the second (Figure 5.2– III) a modification of the amino group position degrades the quantum yield [171], while the third (Figure 5.2 – IV) has no luminescent properties altogether [176]. For all further reading luminol is considered in (I) isomer form.

Luminol is a diprotic acid (LH2) with the pKa1=6,74 and pKa2=15,1 (6,3 and ~13 respectively according to [162]) values for the first and the second deprotonation. Thus, in acidic conditions it becomes fully protonated, while it starts dissociating to the mono (LH^-) and di-anion ($L2^-$) in alkaline solutions. So obviously, luminol solution (and the LCL reaction) is highly sensitive to pH, as well as light exposure, increased temperatures, oxidising/reducing agents and also strong acids and bases [172].

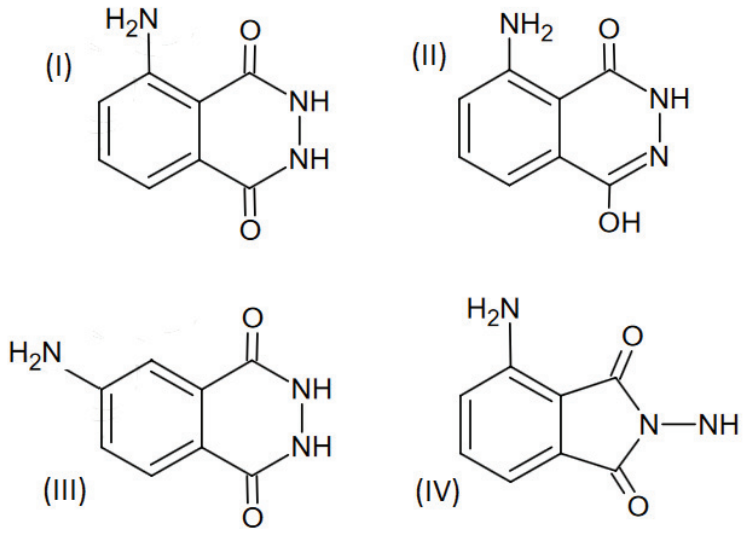

Figure 5.2 - luminol isomers and tautomer (combined from [171], [175]).

Considering the extreme basic conditions needed for the di-anion, we can assume that in most CL applications luminol will be in the mono-anion form. A specific chemiluminescence path for (ultrasonic) cavitation was proposed by McMurray and Wilson [162]:

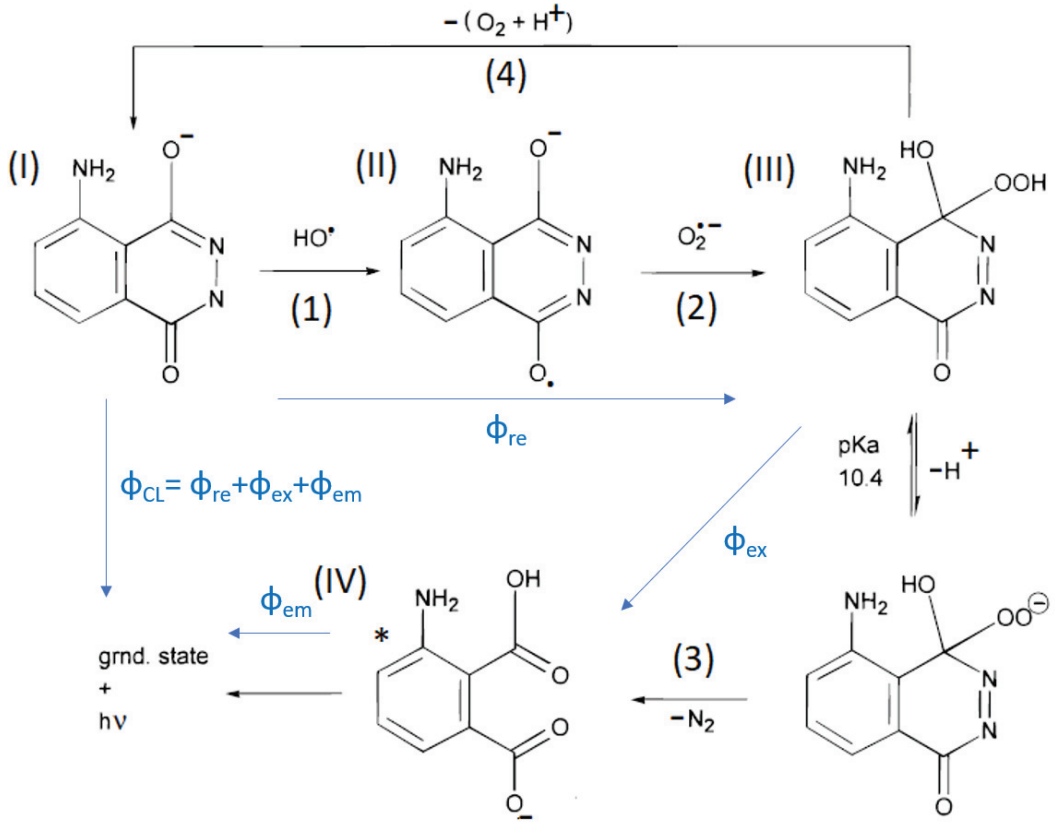

Figure 5.3 - LCL pathway for luminol oxidation by hydroxyl radical and super-oxide ion from a cavitation bubble (adapted from [162]).

The luminol chemiluminescent reaction is essentially the oxidation reaction of luminol [162]. It's a complex multistep reaction, dependent on many parameters, such as pH, temperature, catalysts (metal ions), ionic strength of the medium, and reactive species present, such as the hydroxide and superoxide ion. Many reaction pathways have been suggested during the years of study [162], [177], [178]. Although slightly different to the mechanism proposed by others[88], Figure 5.3 shows one of the rare reaction mechanisms considered in the context of cavitation radical production. Often in biological systems, catalysts (exp.: horseradish peroxidase) are used to induce the oxidation at lower pH values, as not to induce protein denaturization [172]. However, for our purposes these catalysts are not necessary, since our aim is to probe the formation of radicals from the imploding cavitation bubbles.

[88] Mainly the 3-APA excited state formula.

At the end, the LCL reaction produces an emission peak at 425nm. The different proposed mechanisms might vary in the steps of the reaction and reagents (catalysts); however, all of them share the light emission step, since the emission seems to be fixed at the same wavelength. This suggests a unique chemical reaction for light production phase. By the study of the fluorescent properties, an intermediary molecule 3-aminophthalate (3-APA) has been identified as the light emitting species (Figure 5.3 IV). A singlet-singlet radiative relaxation [179], [180] of 3-APA* (* = electronically excited state) to 3-APA, produces the 425nm emission peak, characteristic for the LCL [180].

The quantum efficiency of a CL reaction (applied to Figure 5.3) ϕ_{CL} is the product of three products in the equation below, where the ϕ_{re} is the chemical reaction yield (efficiency of reaction with radicals – step 1 and 2), ϕ_{ex} is the excitation yield (excitation to unstable peroxide – from species III to step IV) and ϕ_{em} is the emission yield (return to ground state by radiative relaxation) [171]:

$$\phi_{CL} = \phi_{re} \cdot \phi_{ex} \cdot \phi_{em} \tag{5.10}$$

For LCL reaction these are about 5% in aprotic media (DMSO) and not more than 1,5% in aqueous solutions.

Due to this relatively low quantum yield, unsuccessful attempts have been made to improve the light yield of the reaction by several **enhancement mechanisms**. The change in amino group position from 5 to 4 (isoluminol) already drastically lowers the ϕ_{CL} to about 0,1%. Chemical alteration of the structure of luminol shows that any modification of the heterocycle ring can even lead to a complete loss of luminescent properties. On the other hand, several modifications to the non-heterocyclic ring forms luminescent analogues, which can vary the quantum efficiency of the reaction or even modify the emission peak. However, these are not used in the scope of the thesis, so the reader is referred to a review on the subject [171] for further reading. Also worth mentioning are the enhancement mechanisms of various nanoparticles (exp.: [181], [182]).

For our study a more important amplification mechanism is the so called CRET (chemiluminescence resonance energy transfer), based on the well-known FRET concept (chapter 3.1), which is discussed in Perspectives (chapter 7.4).

Other effects concerning the emission intensity are the pH, temperature, other substances and the concentration of luminol. Emission of LCL seems highly pH dependent and it is sometimes hard to determine the optimal value, since several steps in the process might be pH sensitive. The LCL seems to be strong and stable around pH 10 [172], which might be the optimum for radiative relaxation step [171]. LCL suppressing mechanisms are usually quenching or inner filter effects (exp.: Fe absorbing strongly at 420nm, which shifts the apparent emission peak to 455nm). While LCL enhancing compounds are either from catalytic activity (peroxidase) or strong oxidation properties towards luminol (hypoclorite, H2O2,etc), while enhancement mechanisms from some species remain unknown [5]. The optimal luminol concentration seems to be in the 0,1mmol to 1mmol range.

5.3. Radical production in cavitating micro-flows

5.3.1. Photon counting technique for radical yield quantification

In this section we present the simple method for quantifying the radical productions in our microfluidic systems. In order to maximize the signal collection (Figure 5.4), the b) PMT R9789 from EMI was placed as close as possible to the cavitation region in the a) microchannel, recording any light produced by the CL reactions.

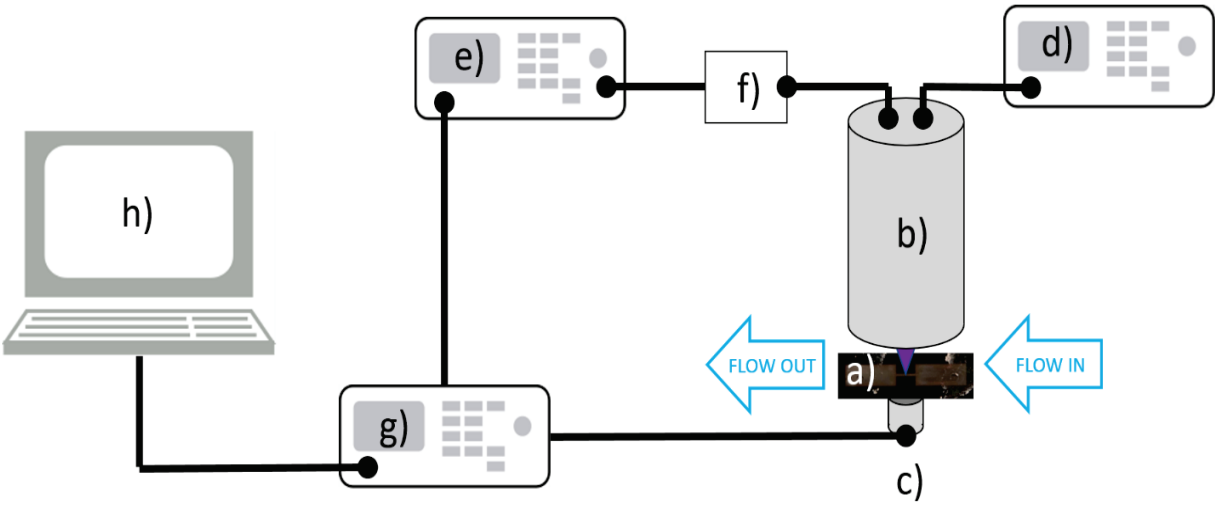

Figure 5.4 - Experimental setup for the CL yield measurements via the photon counting technique. a) microchannel with the b) PMT placed on top and the c) microphone below. d) supplies the voltage to the PMT, f) preamplifier boosts the signal before the e) discriminator. Both signals are collected by the g) data acquisition card and sent to the h) computer.

The PMT has an inherent background signal ~20 counts/s, corresponding to no photons detected. Light tight conditions had to be assured, as not to perturb the PMT measurements by stray light. This called for a home-made c) microphone to be placed just below the constriction region to record cavitation noise. The d) voltage supply powered the PMT with 1250V, producing a signal and passing it along to the f) ORTEC VTI120C 12V pre-amplifier and onwards to the e) ORTEC 935 CFD discriminator. The system produced a voltage spike for every photon detected, which was routed to the counter channel on the g) NI USB-6343 DAQ, thus making it a photon counting technique. A second channel was used to record the cavitation noise with a 50kHz sampling rate, signalling when cavitating flow was occurring, since visual observations were not possible. The two signals were synchronized and analysed with a homemade LabVIEW program on h).

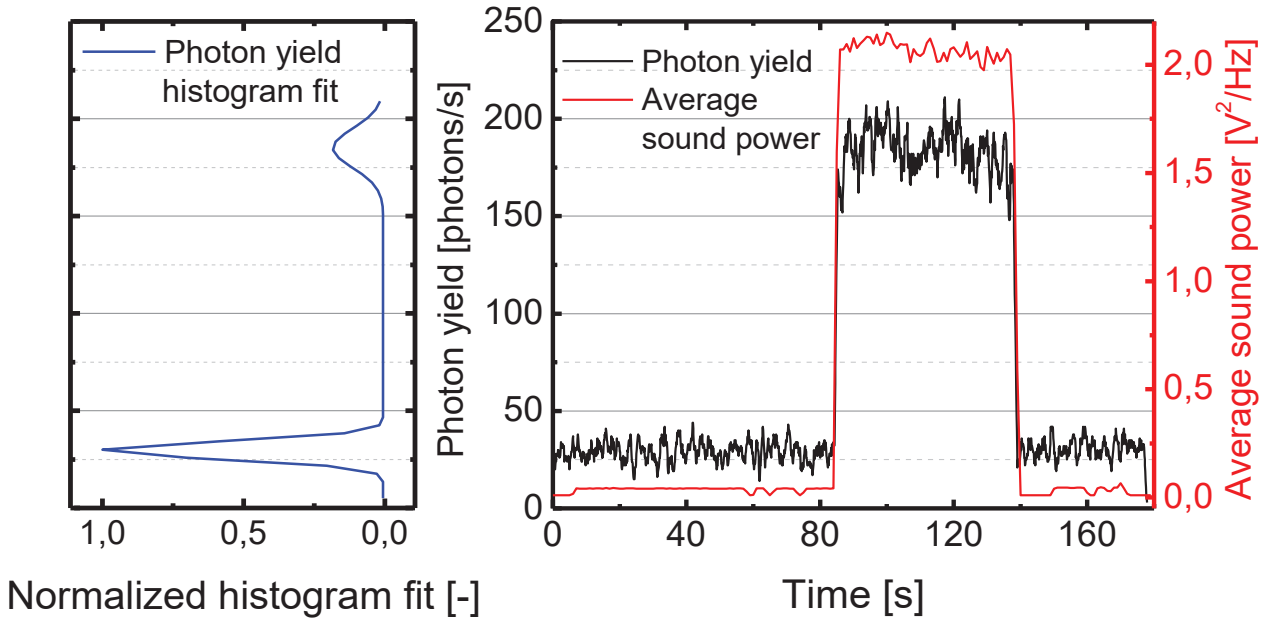

Figure 5.5 - MD L3 at 10bar driving pressure. The graph presents a typical measurement series, producing a histogram (blue line) of the CL signal (black line) on the right. The red signal presents the sound power curve, corresponding nicely to the CL signal.

The working liquid for this microfluidic setup was a 0,1M aqueous Luminol solution. 150mg of NaOH was dissolved in 15ml of deionised water. 170mg of luminol powder (3-aminophthalhydrazide 97% from Sigma-Aldrich) was added, which slowly dissolved in the basic solution. Deionised water from the Barnstead Smart2Pure water purification system was added to make 1L, corresponding to a 3,75mmol NaOH solution at approx. pH=11,6.

The microfluidic setup was identical to the ones reported in chapter 2.3. A separate reservoir, new tubes and filters were used to prevent cross contamination with fluorescent nanoprobes.

Generally, optical techniques are advantageous, due to their non-invasive/intrusive remote sensing abilities and fast acquisitions, another big advantage of these measurement technique is that it needs no liquid extraction to determine the radical production rate. Normally, calibrations are needed to coordinate the signal to the species production yield, complicating the experimental procedure. However, since our technique detects individual photons and the reaction mechanism has a prescribed relationship of photons emitted and radicals consumed by the reaction, a global radical yield can be determined.

However, microfluidic device will inherently produce a reasonable weak signal, due to their small size. Therefore, if the optics are not adapted for the microscale, the signal might be weak or undetectable. For example, in the best-case scenarios, our channels put photon yield below 1000counts/s.

Figure 5.5 shows a typical measurement on the CL photon counting experiment. The photon yield has a step like jump, which is followed nicely by the cavitation noise. The curves are obtained by opening the flow and waiting for the metastability of the system to be overcome. Often, the flow was opened/closed rapidly in order to induce the cavitating flow, as can be seen in slight noise variations at the beginning of the signal (8s flow opened, open closed between 50s and 80s). Cavitation finally occurs at 85s indicated by a jump in both signals[89]. Both signals disappear abruptly as the flow is closed (140s). The PMT data is usually displayed in a histogram, which can be left raw (Figure 5.6) or fitted as in Figure 5.5. The peak maxima are used as the photon yield value at specific conditions. The intensity of the histogram peaks is a arbitrary notion, since it would correspond to the fraction of time the flow was/wasn't cavitating. As seen in Figure 5.5, the background signal is dominating, as the non-cavitating or no CL signal is prevalent. The signal peaks are about twice as wide as the background signal. On Figure 5.6 a unique occurrence for the

[89] A similar method was used on temperature measurements in [94], showing a direct connection to cavitating flow

MD 14 channel is presented; the double step curve indicating two cavitating regimes. As the PMT curves are about 1/3 for each peak, the intensities of the peaks are also such.

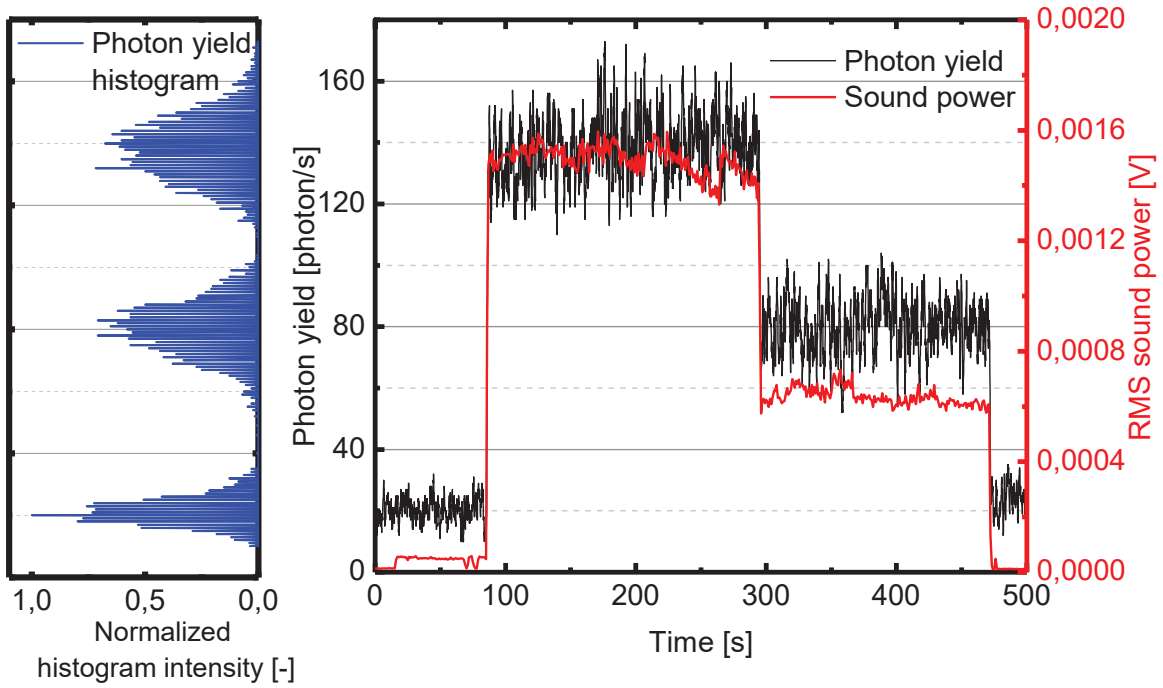

Figure 5.6 – MD 14 CL and cavitation noise signal as a function of time at 9bar, on the right. Left side is the histogram of the CL signal. A double step regime is observed, typical for this channel, indicating two cavitation regimes (high/low). Adapted from [98].

These flows were recorded with the AVT Pike camera, with the results shown on Figure 5.7. Long exposure photography reveals the average vapor cloud in the channel. A clear difference is seen, as the low cav. regime essentially becomes a single cavitating jet. The CL signal drops roughly 40%, corresponding perhaps to the loss of one of the jets. The transition between the regimes is always from high to low cav. regime, usually within a few min or even s. This is most likely why it was not observed in the temperature mapping experiments (chapter 4.2). There seems to be a double regime recorded with the high-speed camera for MD T2 at 10bar (chapter 2.3.2), a similar channel to MD 14.

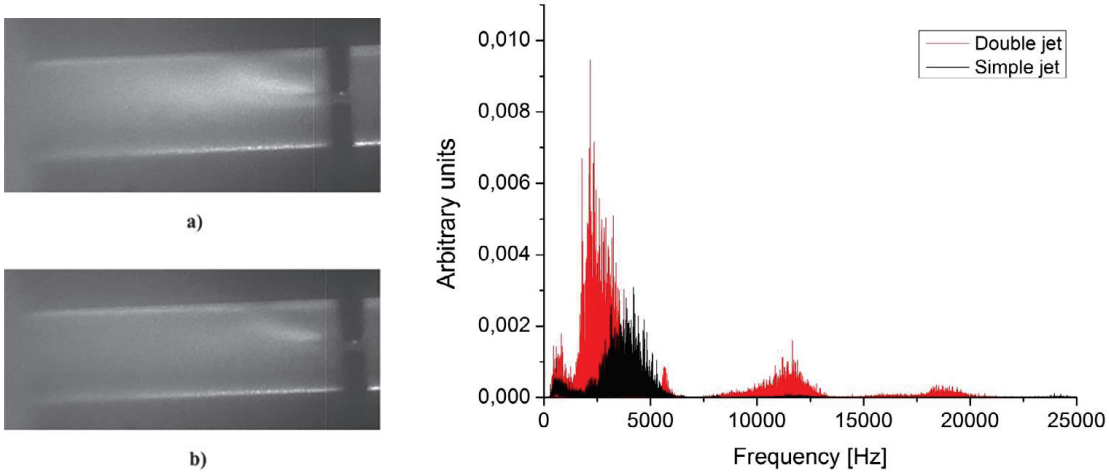

Figure 5.7 – Long exposure time recordings for the MD 14 microchannel vapor clouds downstream of the constriction at 9bar (flow right to left). The two cavitating regimes a) high - double jet and b) low - single jet regimes corresponding to the two steps on Figure 5.6. On the right the cavitation spectrum for both regimes. Adapted from [98].

The transparent MD T3 channel data is presented in Figure 5.8, showing the typical CL signal increase with driving pressure, with cavitation noise following the same linear trend, with some deviations at lower cavitating flows.

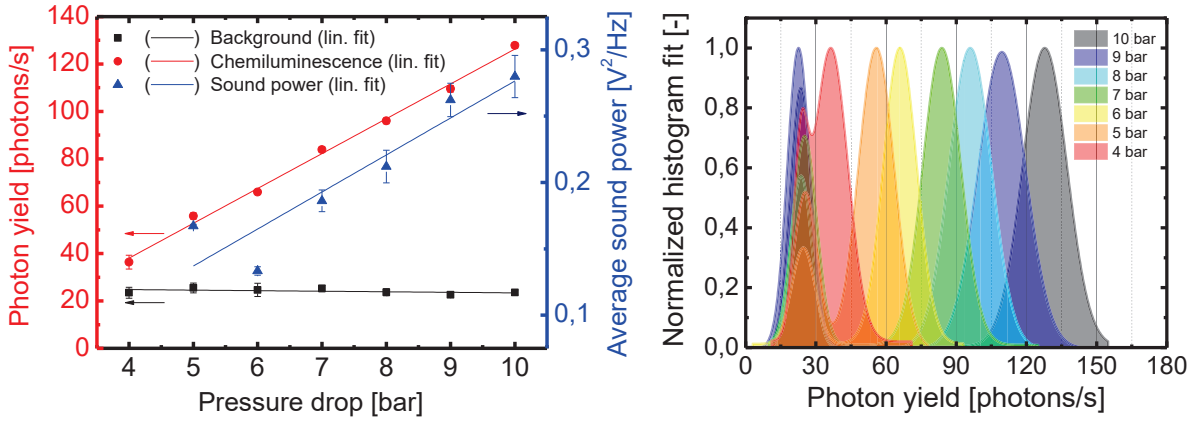

Figure 5.8 – MD T3 CL yield and noise sound power as a function of the pressure drop, with the corresponding linear fits on left. The histogram signal fits on right; peak maxima values plotted on the left (red symbols). The overlapping peaks on left are the PMT background signal, corresponding to non-cavitating regime (right – black squares). Adapted from [98].

MD L3 (Figure 5.9) also shows the linearly increasing trend with pressure, but not for the noise level. In any case, the microphone setup used is a simple homemade setup, probably not well suited for sound analysis. It was never the aim to perform a detailed sound analysis, although as the

results show it might be interesting to probe the cavitation noise at the microscale, as it is a common characterisation parameter at the macroscale. Finally, the microphone was always intended to obtain a cavitation on/off signal.

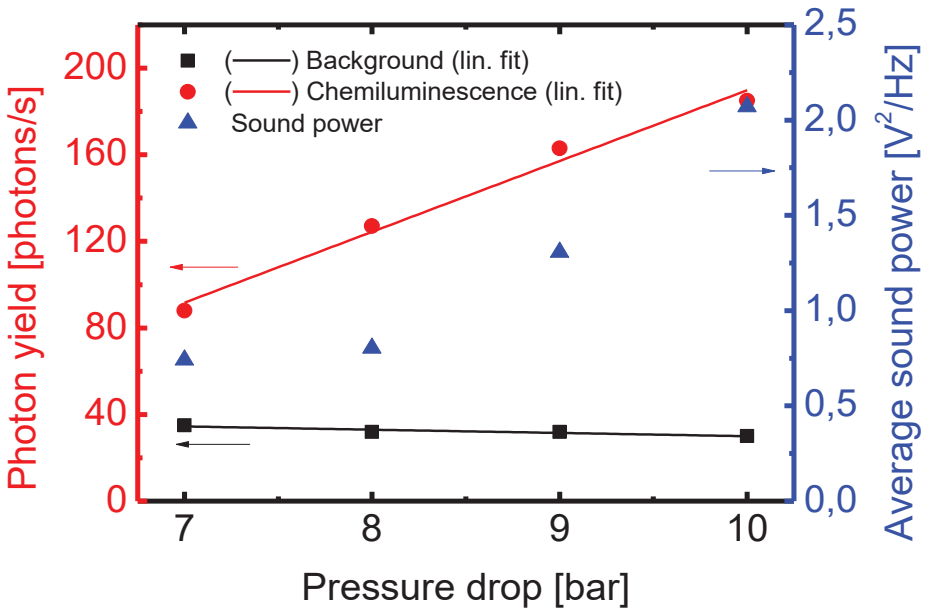

Figure 5.9- MD L3 CL yield and noise sound power as a function of the driving drop.

What is more interesting is the global maxima CL signal among the channels. This is obtained from the MD L3 at 10bar, amounting to 183ph/s at 10 bar and 0,377ml/s, which are the values used later on for radical yield calculations [98]. MD 14 is not far behind at 180ph/s at 10 bar and 0,287ml/s (data not shown).

Figure 5.10 shows the photon yield of different channels compared to two different parameters. On the left is the σ_{cav}/σ value, inception cavitation number divided by the cavitation number, giving an idea of cavitation intensity. Again, linear relationships are observed. Moreover, the high intensity slope of MD 14 follows the L3 trend while the low intensity trend roughly follows the MD T3 measurements. What the σ_{cav}/σ value physically represents or why it follows the two trends is hard to speculate, but similarities in the discharge coefficients [98] might be a partial answer.

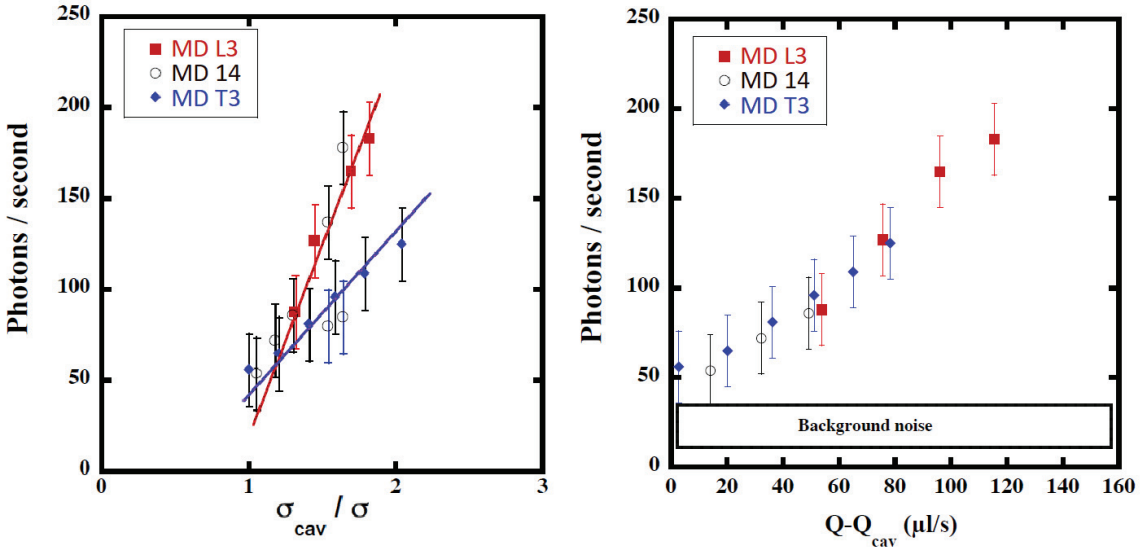

Figure 5.10 – MD L3, 14 and T3 comparison of photon yield compared to σ_{cav}/σ on left and Q-Q_{cav} on right. Adapted from [98].

The right graph shows the same yields, but compared to Q-Q_{cav}, which is the flow above the cavitation inception flow. It seems the intrinsic differences between the channels disappear and a common linear relationship is observed [98]. The Q-Q_{cav} should give an idea of the energy consumption of the generated cavitating flow

The linear relationship between the driving pressure and the flow is quadratic as shown in chapter 2. So, it was surprising to see a linear relationship between the two parameters and the CL signal. However, if one consider the hydraulic power can be estimated from $\Delta p*Q=W_{hyd}$ [98], where these parameters are in linear relation. Since σ_{cav}/σ is proportional to driving pressure and Q-Q_{cav} obviously to the flow, it might indicate that the hydraulic power might then be the key parameter for the CL signal comparison. W_{hyd} values are 0,377W for MD L3 and 0,278W for MD 14. Considering the power consumption caused by the presence of cavitating flow $W_{cav}= \Delta p*(Q-Q_{cav})$; making it 0,05W for MD 14 and 0,12W for L3. A similar approximation was done in [94].

An important aspect of the photon counting technique is the **radical yield** approximation. It's made possible by the CL reaction, in which a photon is produced per radical reaction. Coupling with the ability to count photons allows for the radical production to be obtained. The distance from the PMT to the cavitation area was about 19mm and the PMT opening 10mm. Assuming a point source and isotropic emission of CL, which in microfluidics is a reasonable assumption, we

can calculate the **solid collection angle** $\Omega=2\pi(1-\cos(\beta))$, where β is the calculated angle from the geometrical parameters above, amounting to 14,7º. From the stated above we can calculate that 1,6% of the emitted light is collected[90] by the PMT. Furthermore, the QY being roughly 1%, and the global quantum efficiency for the PMT for the luminol emission range being 15%, shows that the actual radical production was fare more than recorded values.

The radical yield calculation is rudimentary and should be considered as an order of magnitude estimation. To a lesser extent the quantum yield for CL of luminol is derived from literature and does not neccesarely equate to the yield for our specific reaction. At intense cavitation conditions, bubble scattering the CL light might become a factor, however no indications of these effect have been observed so far.

The radical production in the bubble is most-likely much greater, but the technique is a good approximation of the effective radical productions, therefore the radicals that migrate and exist in the liquid long enough to react. In fact, for most practical purposes, this is the relevant information. By using the measurement and reaction efficiency corrections above and the flow parameters we can estimate that at maximum measured conditions the effective radical production[91] is about 6 10^6 •OH/s or 1,6 10^{10} •OH/s/l. The HO-H bond dissociation energy is 493kJ/mol [183], making the energy input for the radical formation 4,9 pW, far from the estimated cavitation energy calculated above (0,12W). The low radical production could also be down to the bubble dynamics, as it should increase with sphericity of the collapse.

A linear relationship was also observed for the pulse radiolysis of luminol solution [177], indicating the initial oxidation of luminol was the rate determining step. As we also observe in Figure 5.8 and Figure 5.9 a linear dependence to the driving pressure, we can determine that cavitation radical production was the rate determining step for the CL signal. This and the calculations above confirm there was a surplus of luminol (~ 6 10^{20}) in the solution for the reaction, compared to the estimated radical production.

Also, preliminary result show (data not presented) pH decreasing linearly with exposure time. After a 6h exposure to cavitation in the microchannels, the pH dropped from 11,5 to 11,2 at 10 bar

[90] Reflections from the bottom of channel assumed negligleble.
[91] Radicals that react with luminol, meaning they exist long enought to react.

driving pressure. This would correspond to a 30 10^6 H^+/s production rate, which is comparable to the $^{\bullet}OH$ production previously discussed. Also not shown due to inconclusive results, are the indications that CL intensity drops sharply at 10,5pH which is the pK indicated for the intermediate reactions of LCL (Figure 5.3). Perhaps an explanation to the linear behavior of the CL yield and the pH rates comes from the observed linear bubble production rate in the high speed images (chapter 2.3.2).

5.3.2. Chemiluminescence mapping

In Figure 5.11 we see the CL mapping experimental setup. Compared to the static version, this technique uses optics to collect the light and allows for the channel movement.

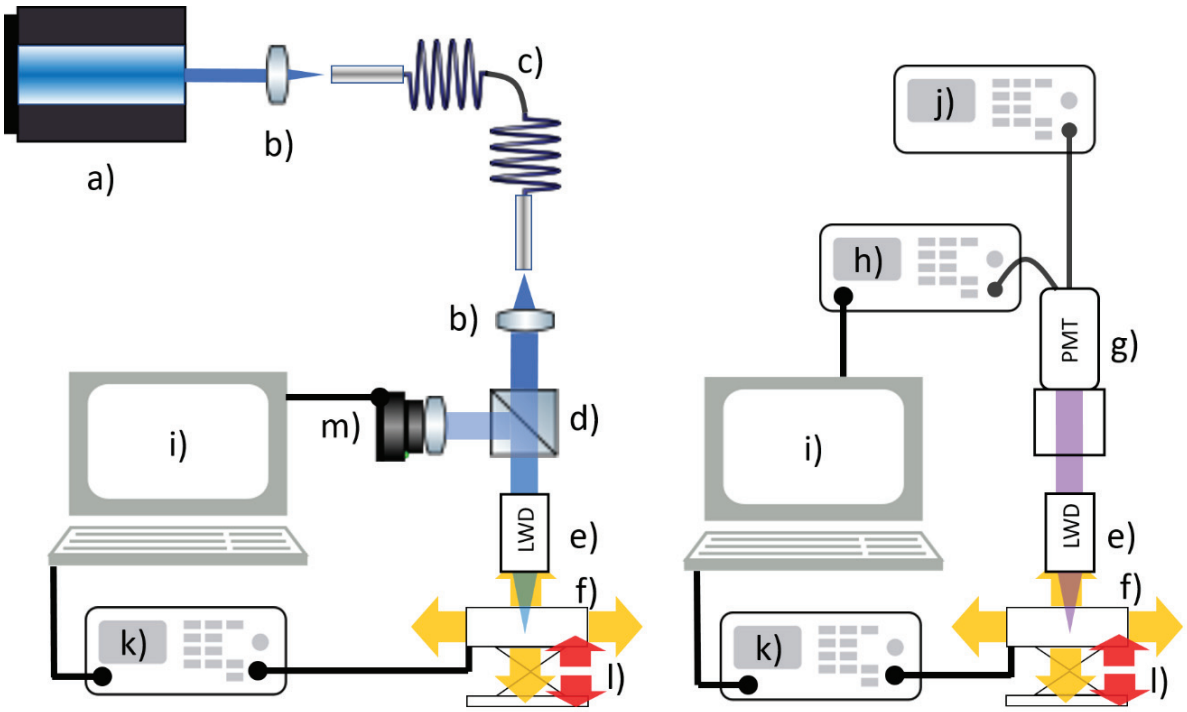

Figure 5.11 - CL mapping experimental setup. On the left the calibration setup and on right the recording setup. The a) 473nm laser with b) fibre injection/collection optical system to collect/inject the light into the c) optical fibre. A d) dichroic mirror passes part of the light through to the e) LWD objective, which gets reflected and is directed to the m) camera for positioning purposes. By replacing the laser with the g) PMT, the light from the reactions will be collected. The h) discriminator with pre-amplifier will pass the signal to the i) computer for recording and analysis. the f) motorized actuators and k) controller operate the x-y movement while the l) height table control the z manually.

The left side shows the setup for calibrating the position of the acquisition point. A a) 473 laser light source is focused by the b) injection optics into the optical fibre. On the other side the beam is collimated by b) collection optics, passed through the d) dichroic mirror to the e) LWD objective OPTEM 20x HR 0,6NA, which focuses the light in the channel. the light is reflected back to the dichroic, where part of the light will pass to the m) MotiCam 1SP 1.3MP CMOS camera form Motic. This allows us to collect the coordinates of the channel, by moving it across the focal point with the f) motorized actuators Z825B controlled by k) KST101 controller, both from Thorlabs. This allows the LabVIEW control program to raster scan the desired area and record the CL rates. The z position is adjusted manually by a l) height control table.

On the right the acquisition setup involves replacing the positioning laser light source by the g) PMT R9789 from EMI and removing the dichroic mirror, leaving a free path for the collimated beam of CL light form the LWD to reach the PMT. The j) voltage supply powering the PMT with 1250V, producing a signal and passing it along to the ORTEC VT120C 12V pre-amplifier and onwards to the h) ORTEC 935 CFD discriminator.

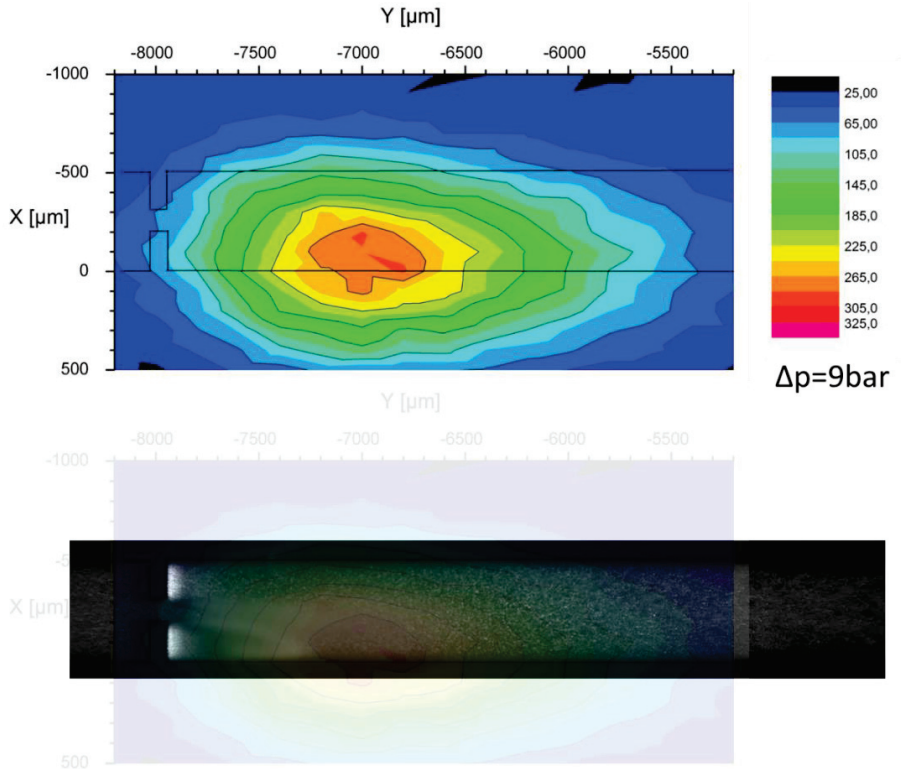

Figure 5.12 – example of MD L4 at 9bar driving pressure. The overlap of the CL map and the long exposure time recording.

The cavitation stream can arbitrarily change side, an effect observed frequently for virgin channels. Used channels tend to lose this tendency with flowtime. Most likely cavitation erosion beats a preferred path in the microchannel, as erosion marks have been observed in the past on the glass surfaces of the channel. The side switching of the flow could easily be overlooked during measurements. Furthermore, slight discrepancies between the coordinates of the position calibration and the measurement conditions are not excluded. Due to the use of an objective with a higher solid collection angle, a signal increase was observed with this method. There might be some losses associated with the optics transmission, however the collection angle increase seems to prevail. Moreover, since we aren't using a confocal setup, the light collection is not coming from a 3D confined volume, but from the entire cone volume, described by numerical aperture and the focal distance of the LWD objective. This of course drastically decreases the resolution of the technique, both in x-y and the z directions, compared to the confocal microscope 1x1x5µm voxel. The best intensity results were obtained by measuring at half way height of the MD. The resolution problems can be clearly seen in Figure 5.12Figure 5.14, as the light is detected even beyond the microchannel walls. However, due to the weak signal, the use of a spatial filter as for the confocal setup is not feasible.

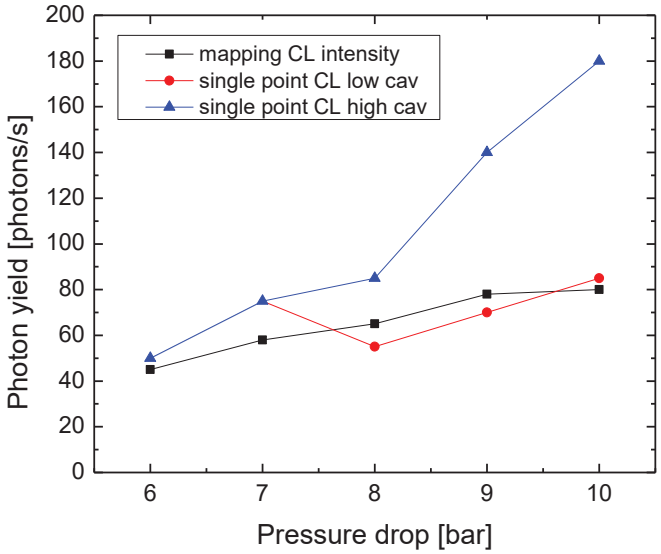

Figure 5.13 - the photon yield for the single point CL measurements and CL mapping data for MD 14 with varying pressure.

Figure 5.12 shows the typical CL mapping. The overlap with the channel shows the maximum CL activity corresponds to the area just after the cavitation cloud. This seems reasonable, due to the

low radical production and the fast relaxation dynamics. After the reactions, 3-APA* relaxes by singlet-singlet transition, therefore ns timescales are expected. It's worth mentioning the overlap above assumes that the cavitating jet in the image and map data swings to the same side, which can't be verified. The CL intensity observed could be a recirculating vortex on the opposite side of the jet swing direction as was observed in chapter 2.3.2 Figure 2.18. However, due to the fitting overlap and the timescale, it's safe to assume the CL maximum intensity spot corresponds to the collapse region of the cavitation bubbles.

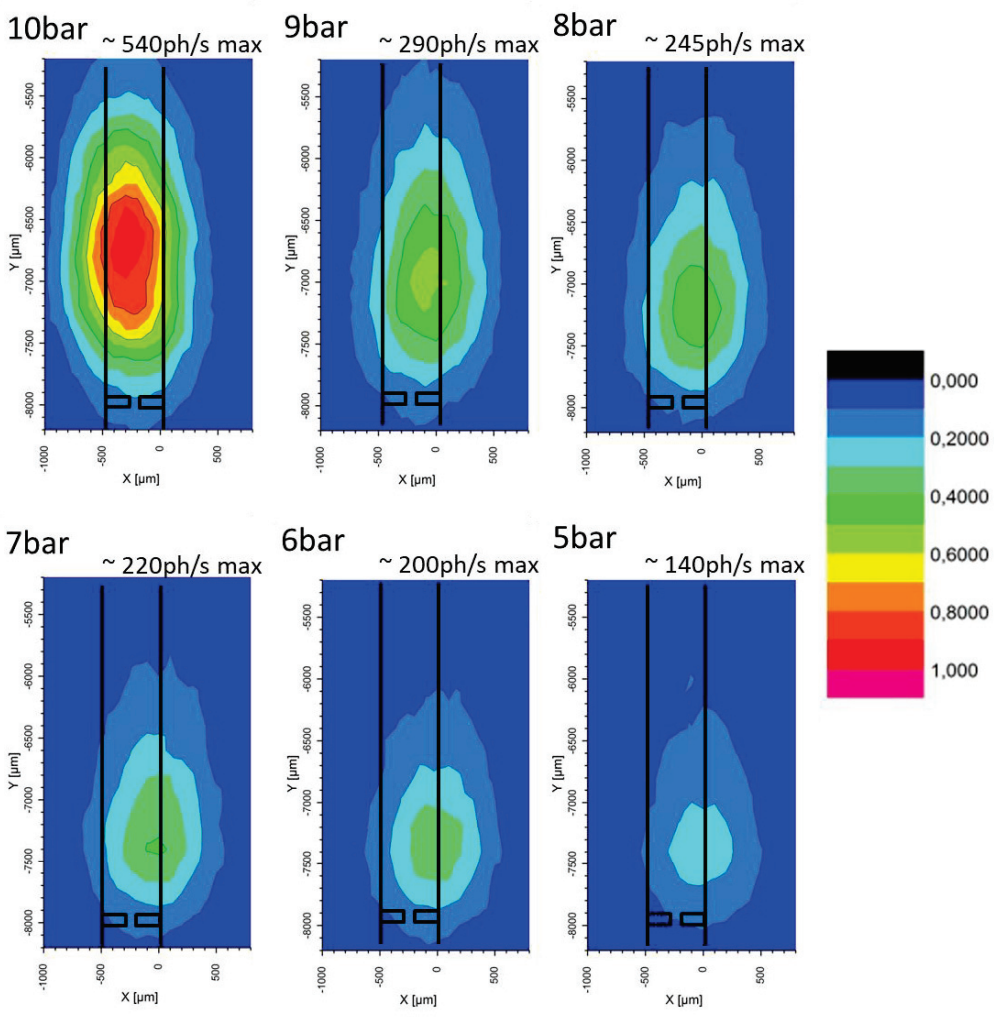

Figure 5.14 – MD L4 CL maps at different pressure drops, normalized to the highest intensity (540ph/s) at 10bar.

Figure 5.13 compares the two CL measurements techniques; the stationary PMT without optics and the CL scanning technique, for the MD 14 microchannel, as it was the only sample tested on

both. The MD 14 with its two cavitation regimes might not be the best comparison, however the transition from high to low regime would occur in seconds or minutes. Therefore, it is likely to have occurred before the slow scanning technique passed over the max intensity point. For this reason, we see the CL map line correspond to the low cavitation regime intensities.

On Figure 5.14 the CL maps are normalized to the highest value in the series. The evolution with pressure can be observed. The resolution of the technique puts the CL activity even beyond the MD walls, as discussed before. But what can be seen is an intensity area of elongated shape in the direction of the flow (along the channel length). The CL activity seems to be highest near the wall, except for the 10bar example. Also, the same case more likely fits the jet swinging the other way.

In the appendix, Figure S. 4 and Figure S. 5 present the CL mapping data overlaped to their corresponding averaged flow images. Another indicator of fast reaction times is the absence of stream of CL activity behind the cavitation cloud. The data is summed up in the figure below (Figure 5.15), with a discrepancy observed at the 10bar point.

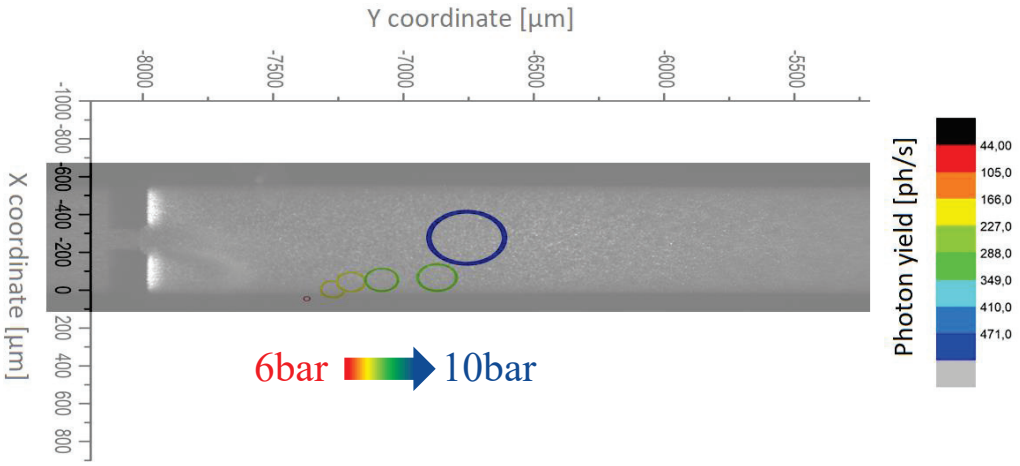

Figure 5.15 - 2D Gaussian fit of CL mapping data of the L4 channel. The maximum coordinates and intensity indicated by the circles are overlapped on channel long exposure time image. The circle size and colour indicate the photon yield; The low intensity red circle at 6bar progressively increasing with driving pressure to the high yield blue circle at 10 bar.

Figure 5.16 shows the reproducibility test. On the left are the CL maximum coordinates of 15 consecutive measurements. The intensity variations are shown on the right graph and are linked to effects of cavitation exposure time effects like dropping pH. After the 15th measurement the intensity dropped substantially and stayed at that level (around 100counts/s) till the end of the

measurements (24h). These results are omitted from the graph for clarity, however their location also changed only slightly downstream, indicating the reaction mechanism might be affected. Luminol is known to be pH sensitive, so this would not be surprising. A study of cavitation exposure time shows on CL intensity, max location and pH evolution was performed but is inconclusive at the time. A repeat was not possible due to time constraints.

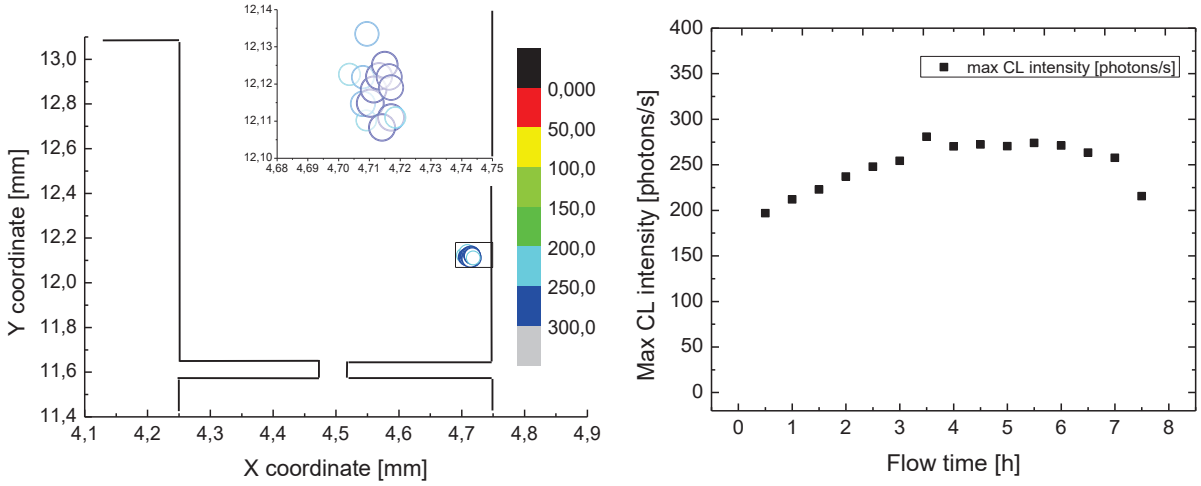

Figure 5.16 - the reproducibility test on MD T2 at 7 bar driving pressure. 15 maps were consequently recorded. Their coordinates are plotted on the left and their intensity evolution on the right. The circle size and colour indicates the intensity.

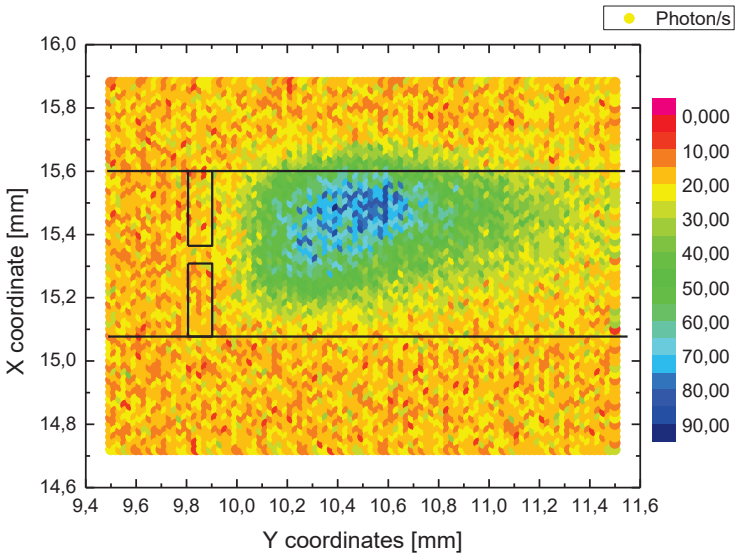

Figure 5.17 - preliminary results on MD T2, at 8 bar driving pressure. The light is passed through an optical fibre, acting as a pinhole before being led to the PMT. This leads to improved resolution. The photon collection is roughly 3 times less than without the fibre.

Figure 5.17 shows a preliminary study with an optical fibre between the PMT and the objective. Since the injection into the fibre works as a pinhole, we observe an improvement in the x,y resolution, making it roughly 50µm. This is most clearly seen on Figure 5.17, at the channel wall, as the signal is confined within the channel dimensions (+50µm). A signal intensity loss due to the fibre is roughly 3-fold, which is acceptable for channels with higher yields.

5.3.3. Void fraction and photon yield comparison

The disappearance of the cavitation cloud should be indicative of the cavitation collapse region. In this section we will compare the results from the void fraction (chapter 4.2.4) and CL mapping in MD 14. As our measurements are all averaging over time, this would of course show where the majority of the bubbles collapse. In the figure below, we are comparing the CL maximum distance from opening to the cavitation cloud area end point (point downstream where α<0,3).

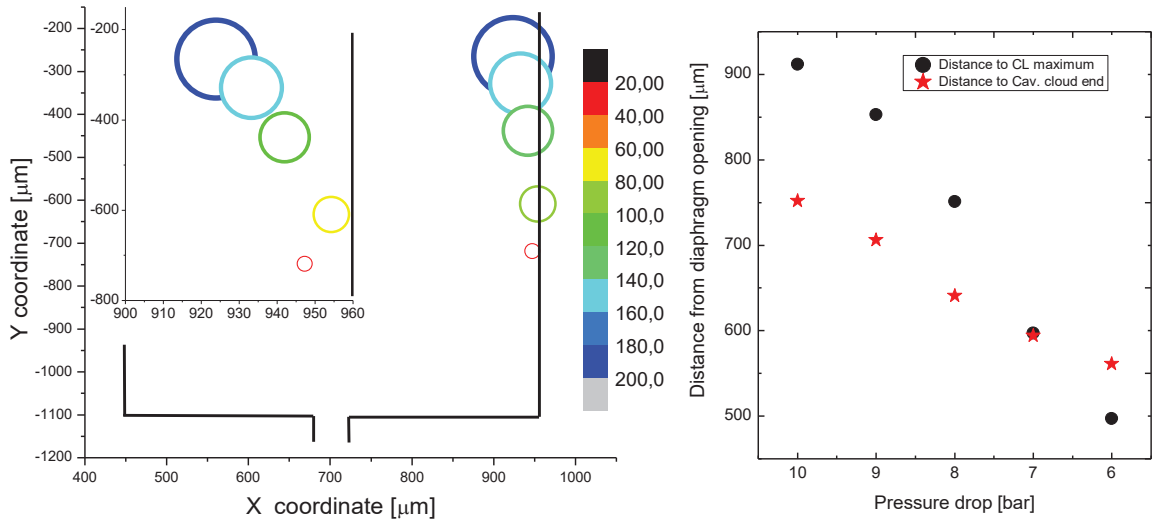

Figure 5.18 – MD 14 coordinates of 2d gaussian peak fit to CL mapping data on left. On right plotted distance from the diaphragm opening. Distance to CL 2d gaussian fit peak (data on left) compared to the distance to the end point of the cavitation cloud (void fraction mapping - 4.2.4).

Both curves are increasing linearly with driving pressure increase. The same applies for the Figure 5.19, the MD L4 graph, with some discrepancies at the maximal pressure drops (10 and 9 bar or at 8 bar) for the cavitation cloud end point.

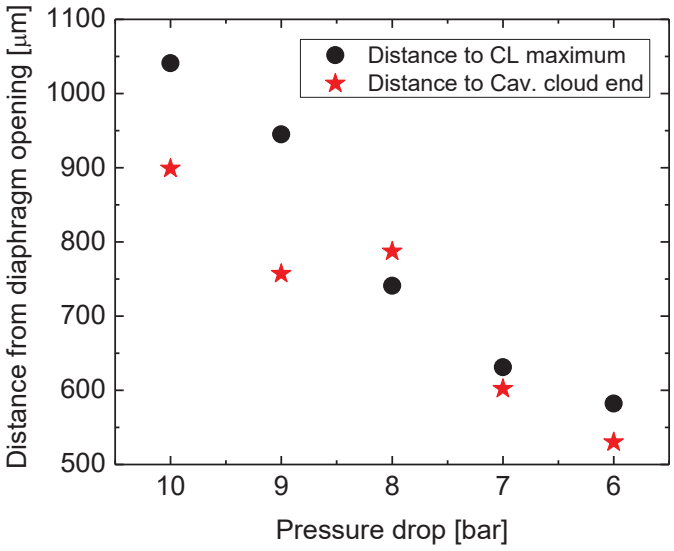

Figure 5.19 – distances plotted from the diaphragm opening for MD L4. Distance to CL 2D Gaussian fit peak compared to the distance to the end point of the cavitation cloud.

Figure 5.20 shows the void fraction maps and the CL maximum plotted as the black circle. It corroborates the observations with the long exposure time images and CL map overlaps, as the CL maxima are located at the end of the cavitation clouds. The 10bar discrepancy originates probably from the jet side switching.

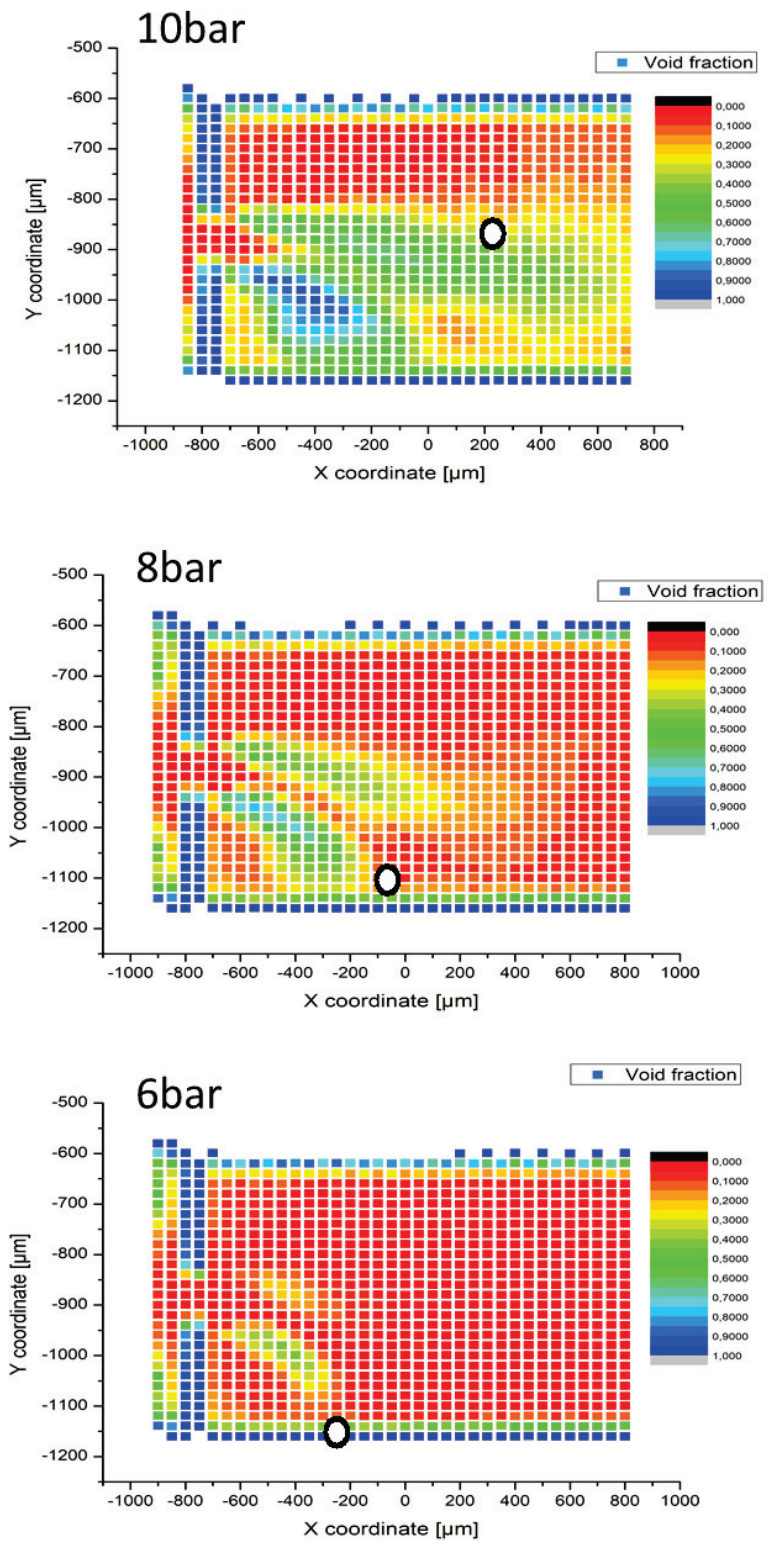

Figure 5.20 - Void fraction maps of L4 at middle of channel for 10, 8 and 6bar. the Black circle marks the CL intensity maximum.

5.4. Chapter conclusions for radical production in cavitating micro-flows

Luminol is a well-established and much used chemiluminescent probe. However, sensitivity to pH, isomerization of the starting product, unclear multistep reaction pathways and long-term stability are all issues, which make it a difficult substance to work with. However, the payoff can be rewarding as it allows for a reasonable quantum yield for a chemiluminescent substance. This enables remote probing[92] of the chemical reactions at the molecular level.

By using the luminol chemiluminescent reaction we managed to probe into the radical production from hydrodynamic cavitation. The reactions taking place in the microfluidic channels are due to bubble collapses releasing radical species, most prominently the hydroxyl radical. The radical undergoes a chemical reaction with the luminol dissolved in the working liquid and emits a photon of light. By using a photomultiplier as the detector, the arrival time of these photons can be recorded, producing the photon yield information. The knowledge of the collection and quantum efficiency of the method allows to approximate the radical production. Due to the sensitivity of the method, light tight conditions were needed around the channel. Therefore, cavitation noise was used to determine the cavitation on/off state.

The first experimental setup with a static acquisition helped us determine the linear relationship between the photon yield and the driving pressure. This relationship seems to hold for all tested channels. The technique showed its sensitivity as it could detect the abrupt changes in cavitation regimes, specific to one of the tested samples. The microfluidic channels tested didn't allow for a conclusive test of the effects of geometrical parameters on radical production. It did show similarities between the two channels, regarding the photon yield and the constriction dimensions. A parameter defined as the volume flow above cavitation threshold flow ($Q\text{-}Q_{cav}$) showed a linear relationship with a common trend for all channels. Moreover, they all seem to follow the same trend, as the inherent differences between them disappear. The radical yield was calculated to be $6 \cdot 10^6$ $^{\bullet}$OH/s or $1{,}6 \cdot 10^{10}$ $^{\bullet}$OH/s/l for the maximum recorded photon yield.

The second experimental was an upgrade of the first, using optics for collection and motorized actuators to allow for scanning of the channels. The CL mapping experiment added additional

[92] without the need for excitation

information of the location of the CL source within the micro-cavitating flow. The expected results were confirmed as the collapse regions seem to overlap with the end of the cavitation clouds. For the one channel tested on both setups, the photon yields were comparable in intensity, perhaps deviating merely due to differences in the collection angle and the transmission efficiency of the optics. The absence of a runoff stream of CL activity confirms the fast reaction and relaxation dynamics. A slight elongation of the CL activity is observed, most-likely due to the non-localized bubble collapse. A way to confirm the overlap of the CL maximum region and the collapse region would be to measure the sonoluminescence activity. For this argonated water should be used to maximize the chance for plasma emission. Also, a more suitable PMT for the wavelength expected from argon emission is to be used, as the one currently used was optimized for the blue part, whereas argon is in the red part of the visible spectrum. The effect of degassing was also attempted, but the results were hard to separate to that of the pH variations with flow time. Therefore, they are inconclusive and were not added to this work.

The other enhancement mechanism was under test during writing (discussed in chapter 7.4). First indications showed that FITC might not be the best suited CRET pair to luminol as the increase was low to none. So, the search for a good CRET pair is currently being investigated. The requirements are a good spectral overlap, stability and suitability for the basic environment of the luminol solution. If a substantial enhancement would be reached, a confocal system could be used, drastically improving the resolution of the mapping. The preliminary results on a similar setup was demonstrated, showing the expected improvements in resolution.

6. Concluding remarks

A broad study, based around the hydrodynamic cavitating flow in silicon based microchannels was conducted in the scope of this thesis. Light based techniques were used to probe the local temperature, void fraction and radical yield information, from the micro cavitating flows. Molecular or nano-composite probes coupled with the working liquid in our experiment and the use of a confocal microscope setup, allows for 2 or even 3D mapping of the parameter in the channel.

Several samples of coinage metals thiolate coordination polymers were tested as potential temperature/pressure probes, with the eventual aim to use them in the microchannels (1-10bar and 0-100ºC). Extensive luminescent studies were performed to help determine the origin of the luminescent properties for each particular sample. The results showed a response to temperature variations, as expected from any luminescent system. Moreover, some samples possess multiple peak emission, making them suitable for self-calibrated ratiometric luminescence thermometry. For pressure however, the response of the materials was not sensitive enough for the use in microchannels. Our studies show they might perhaps be better fitted as a diamond anvil cell manometer. Nevertheless, this group of luminescent materials has only begun to be investigated. The self-assembly of the crystalline structure is highly dependent on the ligands used, leaving the doors open to engineering novel luminescent materials, with possibilities in optical sensorics.

The thread of the study is situated around the use of a light-based probing techniques. Our study offers an unprecedented view on the temperatures and void fraction information in cavitating micro-flows. To our knowledge, it's the first time the cooling regions in cavitating micro-flow was mapped, with the information coming from the bulk working liquid. The three-dimensional confinement of the acquisition voxel allowed us to measure throughout the channel volume. Liquid cooling observed was above what is expected, testifying to the robust intensity independent temperature measurements. As the temperature is obtained from the emission spectrum, it is highly unlikely that any spectral perturbations could be caused by the flow, yielding false measurements. Therefore, a hypothesis was presented, suggesting the temperature of the thermal boundary layer is being measured. However, Raman scattering thermometry in isopropanol yielded similar cooling rates. The latter technique obtains the temperature from the molecular vibration, not nanoprobes, consequently probing the thermal boundary layer would be possible only at high

bubble concentrations with low liquid volume in between. This might indicate the temperatures measured hold even for bulk liquid. A clear comparison could only be made between the luminescence and Raman thermometry in water, therefore the Raman stokes ratiometric intensity measurements (Perspectives – chapter 7.3) of water stretching band should validate or contradict the findings.

The heating region expected due to bubble condensation is not detected, due to a non-localized collapse region, as opposed to a steady and stable bubble growth zone, where cooling was observed. This also points out a drawback of the slow scanning techniques, which is the inability to record the dynamic phenomena in the cavitating flow. For this reason, we purpose the use of a Fluorescence thermographic camera (Perspectives - chapter 7.2), where two cameras acquire the same image, only with a different spectral band. When one acquires the reference and one the temperature variable band, the pixel intensity ratio corresponds to the temperature information.

A parametric study didn't show conclusive results on the dominant geometrical parameters controlling the cavitation events downstream. Some abnormal 3D effects of the flow were observed. Liquid temperature influence on cavitation cloud area (indicative of the cavitation intensity) was reported, being proportional to the liquid vapor pressure variations with temperature, as would be expected. Driving pressure generally increased all measured parameters, with a linear dependency observed only for the transparent Pyrex-Silicon-Pyrex channel design. As it was the only such channel measured it is not a conclusive finding, however the same channel design showed indications of a symmetric flow over the height of the channel, which was not observed on its geometrical copy or other channel geometries in Pyrex-Silicon design.

The luminol chemiluminescence reaction allowed us to estimate the radical production in our microfluidic channels via the photon counting technique. The fast flows over the constriction induce growth times comparable to low frequency ultrasound. This is unusual for hydrodynamic cavitation and perhaps explains the relatively low radical production. Other explanation might be the lack of spherical collapsed due to the fast shearing flows. Linear relationships were observed between the photon yield and the driving pressure for all channels tested. Furthermore, the mapping of the chemiluminescence activity highlighted the collapse region in the channels at the end of the cavitation cloud stream. The technique could be useful for a quick assessment of the cavitation reactor's ability to produce radicals and its optimization to geometrical or flow

parameters. However, the weak signals from the chemiluminescence limit its use. A proposed CRET enhancement mechanism (Perspectives – chapter 7.4) could allow for signal enhancement and the resolution improvement of the CL mapping.

An important parameter not discussed in the results sections is the gas content of the working liquid. As demonstrated by the high-speed images, recirculation of tiny gas bubbles seems to sustain the cavitating flow. These bubbles are probably the degassed remainder of the cavitation bubble. Therefore, the removal of gas might drastically influence the flow parameters and collapse conditions. The high-speed images also demonstrate the importance of knowing the dynamics of the observed flow. However, one aspect is completely missing in our study – the single bubble dynamics in our multi bubble flow. The information on the thermodynamic parameters in a single bubble might be relevant for radical production in the flow. To this end, we developed a novel single bubble excitation setup, enabling the simulation of the growth and collapse of a vapor bubble in the microchannel. The principle is based on inducing tension in the liquid, giving rise to the name Tension cell (Perspectives – chapter 7.1).

Overall, we demonstrated the versatility of optical probing techniques, be it luminescence or Raman scattering based to investigate microfluidic flows. Temperature and void fraction information are important for understanding thermal gradients in two-phase flows, while the chemiluminescent signal can be used to obtain the radical production rates. In both cases the acquisition is fast, non-intrusive and non-invasive, marking the bright future for optical probing techniques in experimental sensorics.

7. Perspectives

In the scope of the thesis, many side projects were proposed and not developed fully due to various reasons, mostly time constraints. Some of them are summed up in this chapter.

7.1. Tension cell – towards a novel single bubble excitation method

In most real-world situations, cavitation will occur as a multi-bubble problematic. When studying multi-bubble systems like acoustic cavitation or hydrodynamic cavitation the information you are obtaining are often values averaged over time. There is therefore a lack of information obtained from a single bubble. As the constituent element of the cavitation process, the information on its behaviour could be detrimental to understanding the process under study.

Single bubble studies however are nothing new. Exiting a single bubble with focused energy sources, such as HIFU (high intensity focused ultrasound) [184], lasers [185], neutron [32] , etc or by pulsed wave sources like tube arrest method [152], [186], [187] have all been used in the past. However, all of these methods lack the temporal control over the bubble dynamics. In other words, after the excitation is initiated, the bubble dynamics will respond to its signal and go through a growth and collapse phase. Little or no control is possible during the two.

What we proposed as a novel excitation technique is the control of the far field pressure. A small amount of liquid is put in a confined volume, without the presence of an expandable medium. One of the container walls can be displaced over several tens of microns. This wall is connected to a piezoelectric actuator in such a manner that it's displacement will cause an expansion of the internal liquid. The pure liquid will resist the expansion, inducing high tensional stress on the confined, calculated from the B[93] - bulk modulus definition[94]:

$$\sigma_{tension} = B \cdot \ln\left(\frac{\Delta V + V_0}{V_0}\right) \tag{6.1}$$

For a small amount of liquid V_0, it will be very sensitive to ΔV. This is defined by the flexible wall area - A multiplied by the Δd – displacement. As the liquid is stretched, tension begins to rise until

[93] B=2200MPa for water.
[94] Assuming a constant B for the equation of state.

the cavitation threshold is reached and bubble nucleation is achieved. Special preparation of the chamber walls and conditioning of the liquid are required to prevent heterogeneous nucleation at low tension. Part of the liquid stretch (piezo movement) will go towards inducing the tension in the liquid (cavitation threshold), but once nucleation occurs the piezo movement would control the bubble size. Thus, control of the bubble interface could be achieved, by the voltage control to the piezo. Furthermore, a Rayleigh type excitation and collapse could be achieved [188], due to the control of the far field pressure[95] in the RPE (chapter 2.1.1). The fast response of the actuator could hopefully replicate the growth times of the bubbles in the microchannel. Also, with the bubble growth and collapse times slowed down, hopefully replicating isothermal or "quasi" adiabatic bubble dynamics.

A micro-diamond (or other material) nucleation point is added to the pure water medium, around which the bubble will grow. Due to the high refractive index, optical trapping can be used to hold it suspended in the liquid. As the bubble grows around it, the lifetime-based thermometry (as shown in chapter 3.2) can be used to determine the temperature in the growing and collapsing bubble. Moreover, different diamond sizes could be introduced, thus controlling the cavitation threshold[96]. Also, other nucleation sites can be imagined like ruby microspheres or infact just a gas bubble[97].

7.2. Fluorescence thermographic camera

The idea for the fluorescence thermographic camera (FTC) is the expansion of the confocal microscope setup used for temperature measurements in chapter 4. The ratiometric intensity measurements in specific parts of the thermally sensitive emission spectrum can yield the temperature information. However, the microscope acquires the spectrum from a monochromator and a CCD, limiting it to a point by point acquisition. This means long scanning times and averaged data over the acquisition time in each point, therefore the technique is completely unsuitable for recording fast dynamic processes in the flow.

[95] As opposed to travelnig pressure waves, the Rayleigh collaps is the responding to an instantaneous and homogeneous pressure change.
[96] Bigger diamond, bigger gas pocket in crevise, lower surface tension.
[97] Reqireing special optical trapping beam profile.

What is suggested with the FTC is the sacrifice of the 3D scanning capabilities and using two identical cameras for the intensity ratio measurements. The image collected by the objective in the channel is split by a dichroic mirror, sending a temperature independent (reference) part of the spectrum to one camera and the temperature sensitive part to the other (Figure 7.1). As every pixel on the device is a light intensity detector, therefore if the same image overlapped on both detectors, a ratio in the two pixels between the devices would yield a ratio proportional to temperature. After calibration, this technique could capture events with the rate determined by the camera and the signal intensity. To improve the latter, a good dye or even better a dye pair should be used. Rhodamine B (RhoB) and Rhodamine 101 (Rho101) is a typical pair, where RhoB suffers from dynamic quenching of fluorescence [120] and the Rho101 does not. As the dynamic quenching is governed by temperature, RhoB turns out to be a sensitive temperature probe in the biological range [189].

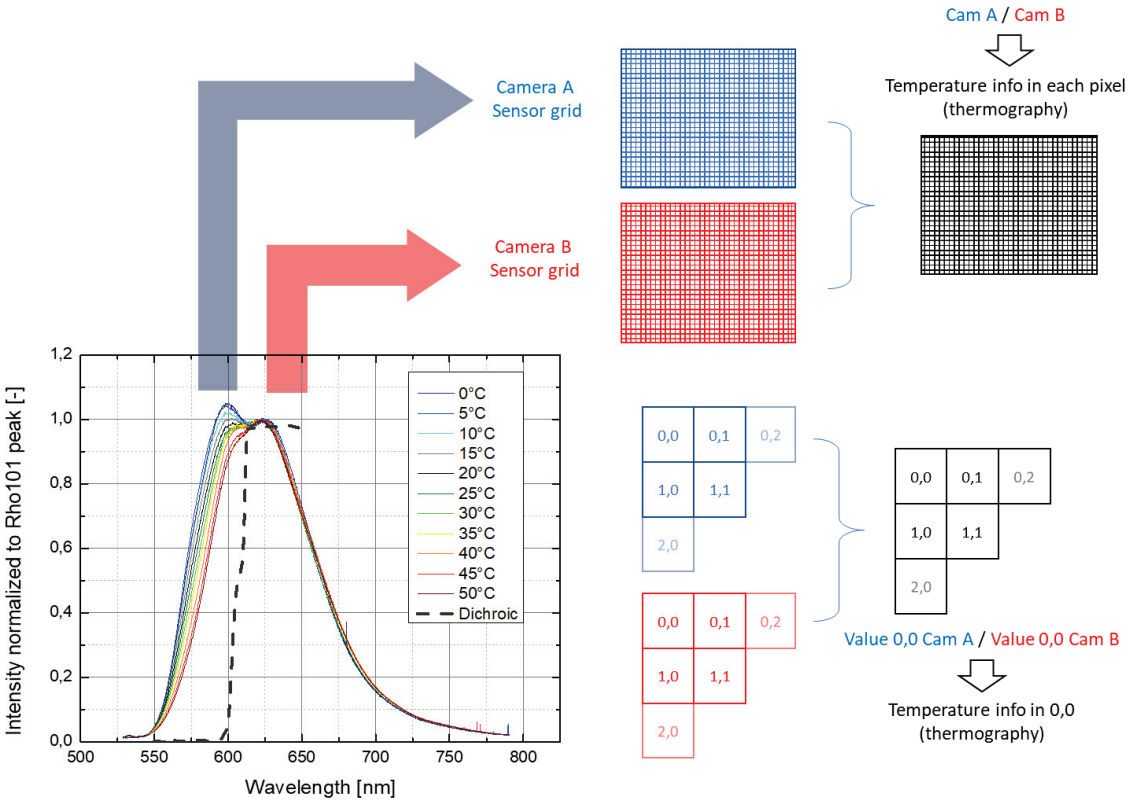

Figure 7.1 - Temperature response of Rhodamine 101 and rhodamine B dye mixture. Normalization is to the Rhodamine 101 peak. The proposed ratiometric temperature information acquisition form the overlapped camera images is proposed.

A reference dye improves the sensitivity and allows the reference camera signal to be used for normal imaging of the flow. The downside of the two dye approach are the potential concentration variations, as cavitation might degrade the two dyes at different rates [190]. This would be problematic if the dye combinations wouldn't degrade at the same rate. Since hydroxyl radicals have a reasonably strong oxidising potential, the rate of bleaching for the dye pair could be in the same range. Using sulphorhodamine dyes might increase their chemical stability. Also, the relatively low radical production observed in chapter 5 might be beneficial in this case. Of course, another option would be dye encapsulation like in chapter 3, inside the shell of the nanoprobes. Or considering only that for dynamic studies short record times would be required, regular replacement of the dye solution could also be an option.

7.3. Raman Stokes ratiometric intensity measurements

The second technique mentioned in chapter 4.3.1 is the Raman Stokes ratiometric intensity measurements. It has been previously used for probing the temperature (and salinity) of water [191] relying once again on a ratiometric technique to determine the temperature in liquid water. Water is examined (OH symmetric stretch [191], [192] and the OH overtone [193]), which was also a popular method for probing into the hydrogen bond network of water. A similar technique was used in microchannels on pure water [156].

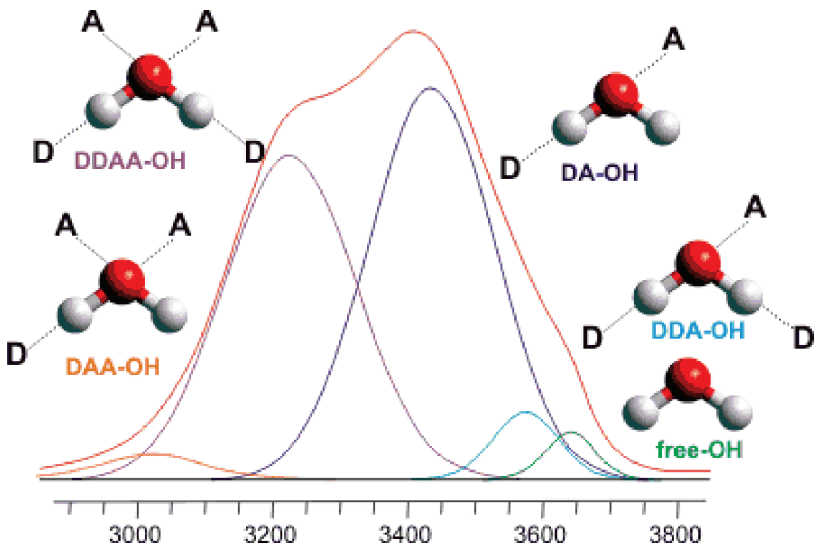

Figure 7.2 - Raman symmetric stretch stokes peak at 3400/cm (convolution of 5 gaussian peaks, each corresponding to a particular water molecule interaction with its surroundings). Image reprinted from [194].

As the hydrogen network is probed, the technique could be se sensitive to water under tension, which is the case in metastable flow. Also, the free radicals produced in the cavitation cloud could influence the signal. At the time of writing unfortunately, the results on Raman thermometry in water were inconclusive (perhaps, due to the reasons stated above) and therefore not presented in the study. We present the calibrations curves in Figure 7.3, showing the temperature dependence of the Raman peak, highlighting its potential use for thermometry.

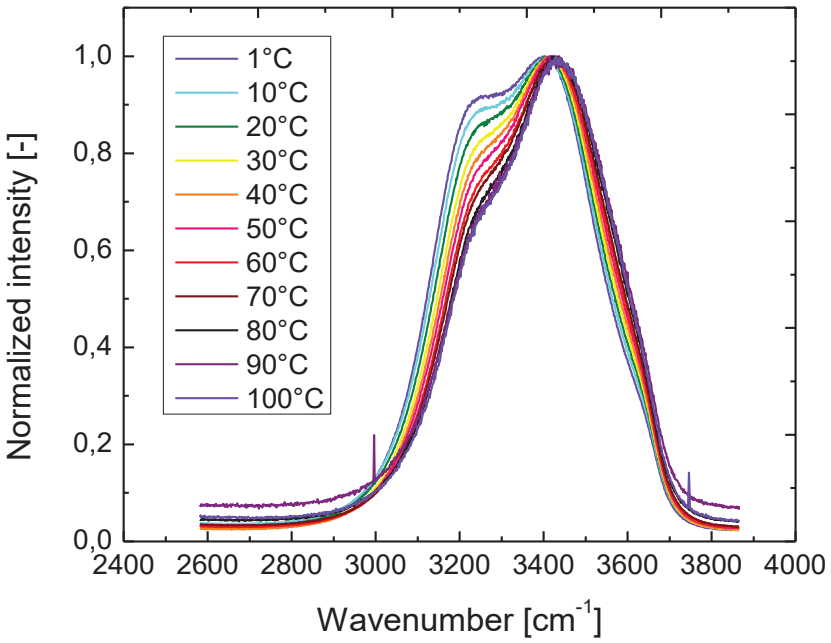

Figure 7.3 - Water stretching band Raman scattering signal as a function of temperature.

7.4. CRET enhancement mechanism

The idea is based on improving the emission of our luminescent system, by introducing an efficient emitter like FITC (improvement of ϕ_{CL} by increasing the ϕ_{em} - Figure 5.3). As for FRET, the requirements for efficient energy transfer are the intermolecular distance and spectral overlap (energy resonance) of the donor and acceptor molecules. As the results were inconclusive at the time of writing, the discussion on CRET was relocated to perspectives.

As mentioned in the main body of the thesis, the aim of using the CRET mechanism is to increase the inherently weak CL signal, by transferring the energy to the more efficient emitter via the resonance energy transfer mechanism (chapter 3.1). Fluorescein has been used as a CRET pair

with luminol [195]. Here fluorescein or FITC (Fluorescein isothiocyanate) is used as an acceptor for the non-radiative energy transfer from the excited 3-APA* state (Figure 7.4). Do to the reasonable spectral overlap of luminol and FITC, a several fold enhancement should be observed, as the FITC (QY>90%) is a much more efficient emitter than luminol, while emitting in the 525nm range makes it more efficient for most detection devices [195]. Essentially, the ϕ_{CL} could be improved by augmenting ϕ_{em}. However, a fourth component should be considered in the case of CRET and that is energy transfer between the molecules, which would be highly distance dependent ($1/r^6$).

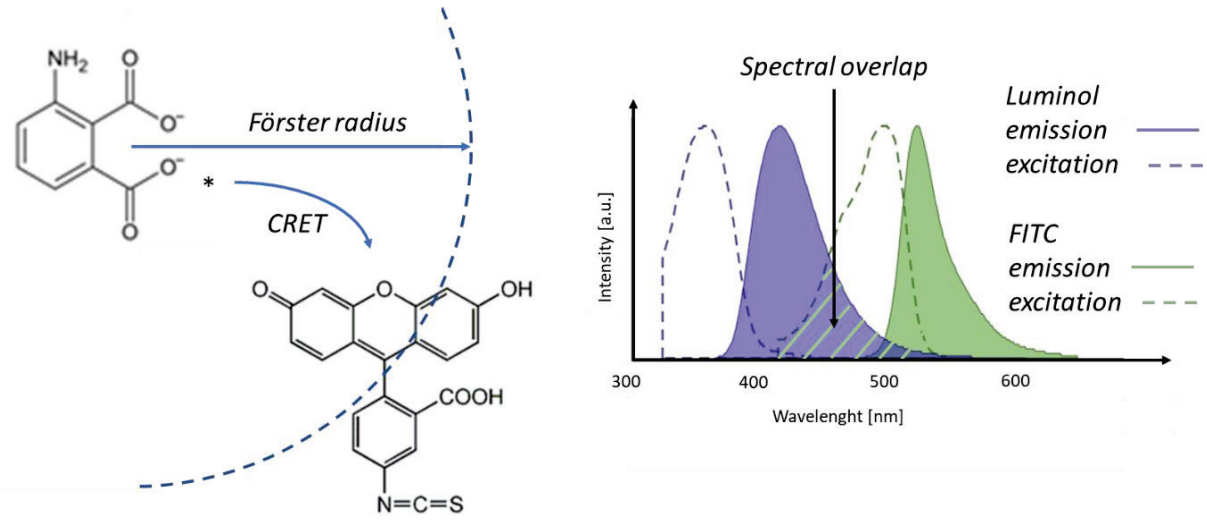

Figure 7.4 - CRET mechanism for luminol/FITC pair. On left the Forsters distance requirement and on the right the spectral overlap requirement.

However, from the initial results, a significant increase wasn't observed. This could be due to the other two parameters of the ϕ_{CL} remaining low or the CRET critical distance wasn't obtained. Also the overlap as seen in Figure 7.4 is not perfect, so a search for a luminol/organic dye CRET pair continues. One of the Coumarin dyes was identified as a good candidate, with nice spectral overlap. However, the dye emission and solubility should be adapted for the basic luminol solution environment.

8. Appendix

The appendix serves as a repository for large format data, not of immediate concern to the narrative, offering an additional insight to the topic.

Table 5 – Device list for the microfluidic experiment setup. Tags refer to the individual elements indicated on Figure 2.11.

Tag	Device	Maker/model	Description
a)	Nitrogen tank with pressure reducing valve	Air liquide	Driving pressure for microfluidic system.
b)	One-way valve		Preventing backflow during refilling, inducing a pressure difference for the BPR to work.
c)	Back-pressure regulator	Equilibar - LF Series Precision Back Pressure Regulator	Pressure regulation during reservoir refiling.
d)	Piezoelectric pressure sensor	Keller PAA-33x	Absolute pressure sensor.
e)	Release valve		System depressurisation
f)	Recirculation pump	TSC micropump – MG2000S	Refilling reservoir
g)	Pump control	EQI-MG2000	Pump control
h)	One-way valve		Preventing backflow after pumping.
i)	Liquid bottom reservoir		Liquid collection
j)	Liquid level sensor	Carlo Gavazzi – VC5510PNOP	Indicating empty/full levels
k)	Valves		Flow regulation
l)	High pressure liquid reservoir	Aquapresso – ADF 8.10	Liquid in butyl rubber subjected to pressure from nitrogen bottle.
m)	Filter	Whatman GR/D and Millipore nylon net filter – NY1004700	1 or 2,7 µm glass fibre filter 10 µm nylon net to contain the fibres from GR/D filter.

n)	Piezoelectric pressure sensor	Keller PAA-33x	Absolute pressure sensor.
o)	Mass flow meter	Flomega Brooks instruments - 5892	Mass flow measurements.
p)	Liquid to liquid heat exchanger	Koolance HXP - 193	High pressure liquid to liquid heat exchanger.
q)	Thermistor	Thorlabs Pt100	PT100 standard thermistor.
r)	Thermocouple	K type	
s)	Data acquisition card	NI USB X-series 6232	Data acquisition
t)	Chiller with temperature control	Solid state cooling – oasis 160 chiller	Liquid temperature control via heat exchanger.
u)	Channel holder	Made in-house	
v)	Channel XY micro positioning	Mad city labs –M drive	Channel x,y control
w)	Micro positioning controller	Mad city labs – Nanoview	Micromechanical x,y manipulator for channel positioningt
x)	Micro positioning controller	Thorlabs APT DC servo control	Objective z control
y)	LWD Z micro positioning	Thorlabs – Z812B	Micromechanical z manipulator for LWD objective movement
z)	Computer		Labview program control and data acquisition.

Table 6 - Device list for high speed shadography recording setup.

Tag	Device	Maker/model	Description
a)	532nm laser	Spectra physics - Millennium pro	High power light source (15W) for fast camera imaging
b)	Mirror	Thorlabs	Beam expander
c)	Lens	Thorlabs	
d)	Pinhole	Newport - 150µm hole	"beam profile cleaning"
e)	Optical density		Laser power attenuation
f)	Channel holder with transparent channel	In-house	Holder modified to allow for high speed shadography
g)	Lens system	Navitar - Zoom 6000	Optical zoom
h)	High speed camera	Vision Research - Phantom v711	High speed imaging

Table 7 - list of devices used in spectroscopic experiments. Tags refer to the individual elements indicated on Figure 3.8, Figure 3.10 and Figure 3.11.

Tag	Device	Maker/model	Description
a)	Laser driven Xenon lamp	ENERGETIQ ED-99	
b)	Excitation monochromator	Jobin Yvon / GEMINI 180	
c)	Lens		
d)	Mirror		
e)	Sample on silicon wafer		
f)	Optical fibre		
g)	Filter holder	-	Many filter options available – removing n-order harmonics
h)	Acquisition monochromator	JOBIN YVON / TRIAX320	
i)	EMCCD camera	Andor	Electron multiplying charge-coupled device camera.
j)	PMT	Hamamatsu/	Photomultiplier
k)	Control and acquisition computer		Computer with Labview excitation/acquisition control program.
l)	Multichannel scaler	Fast ComTec - MCS6A	800ps resolution.
m)	Pulsed laser light source	Hamamatsu	379nm; 1Hz to 100MHz with 1mW to 150mW power output.
n)	Pulse control	Hamamatsu	
o)	Acquisition monochromator	Andor - SR163	
p)	iCCD camera	Andor istar	Intensified charge-coupled device
r)	Laser light source		355nm; 10mW CW

Table 8 - device list for achromatic confocal microscope as shown in Figure 4.1.

Tag	Device	Maker/model	Description
a)	Doubled Nd:YAG laser	Spectra Physics – Millenium PRO	15W 532nm laser source.
b)	Ti:Sapphire laser	Spectra Physics - Tsunami	700 to 1000nm tunable emission wavelength -880nm used.
c)	Faraday isolator		Preventing reflected light return
d)	Frequency doubler crystal		Frequency doubling, yielding 440nm excitation light
e)	Long pass filter		
f)	Beam dump		Absorbing unwanted light
g)	Mirror		
h)	Lens		Beam expander and laser profile clean up.
i)	Pinhole		
j)	Optical densities		Laser power attenuation
k)	Dichroic mirror		Beam splitter
l)	Long working distance objective	Optem – 20x NA0.6	13mm working distance
m)	Microchannel holder		
n)	diode	Thorlabs	Excitation power monitoring
o)	Mirror		Optional mirrof for ATV PIKE camera
p)	Camera	ATV PIKE	F-421
q)	Filter		Removing excitation light
r)	Monochromator	Andor technology - Shamrock	300gr/mm (blazed at 500nm)
s)	EMCCD	Andor technology - Newton	
t)	PMT	Hamamatsu R2949	

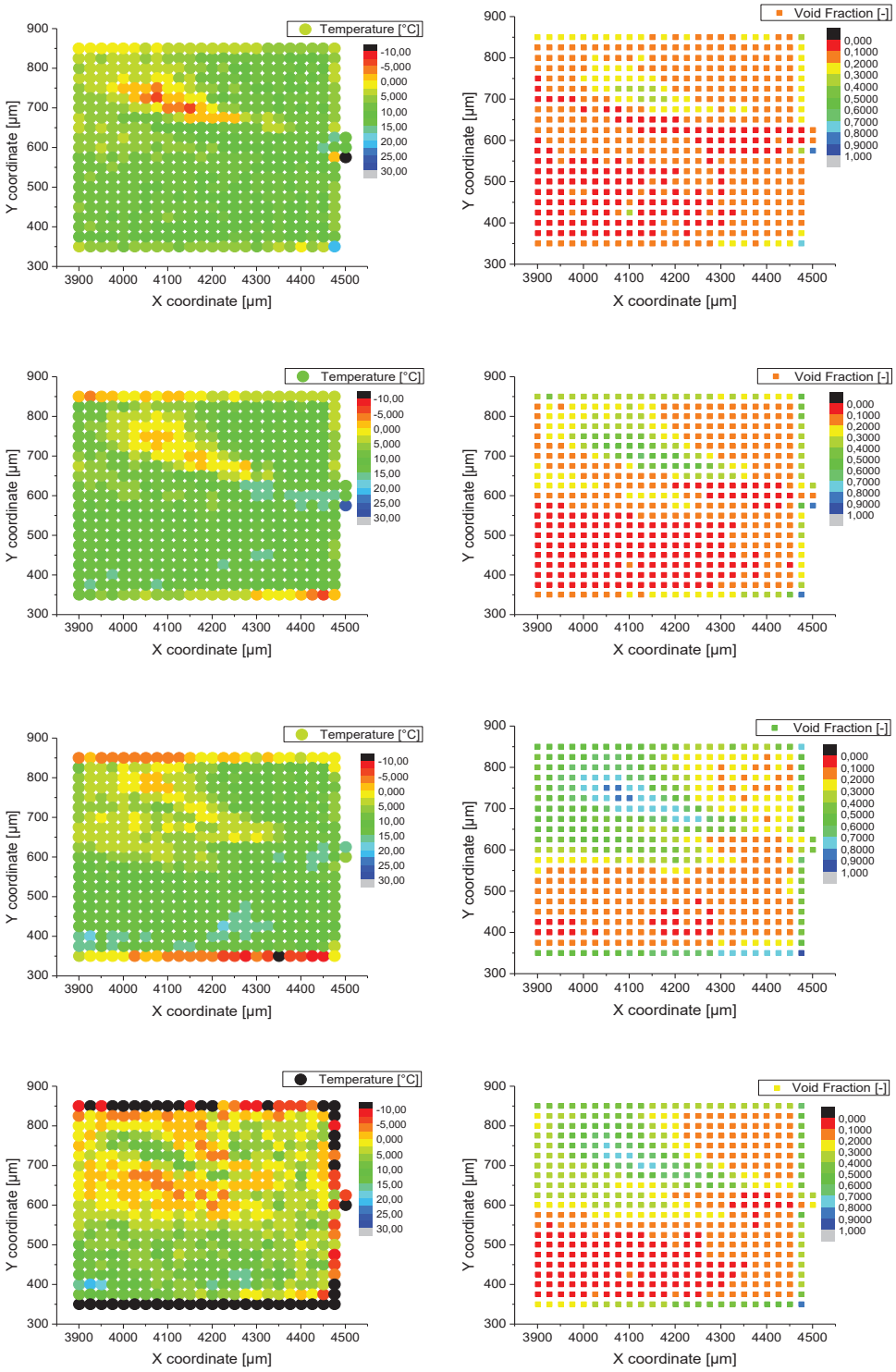

Figure S.1 - MD10 temperature (left) and void fraction (right) mapping at 10, 40, 60 and 80µm from glass (order from top to bottom). Flow is from right to left at 10 bar driving pressure. Diaphragm walls are best seen on lower right temperature map.

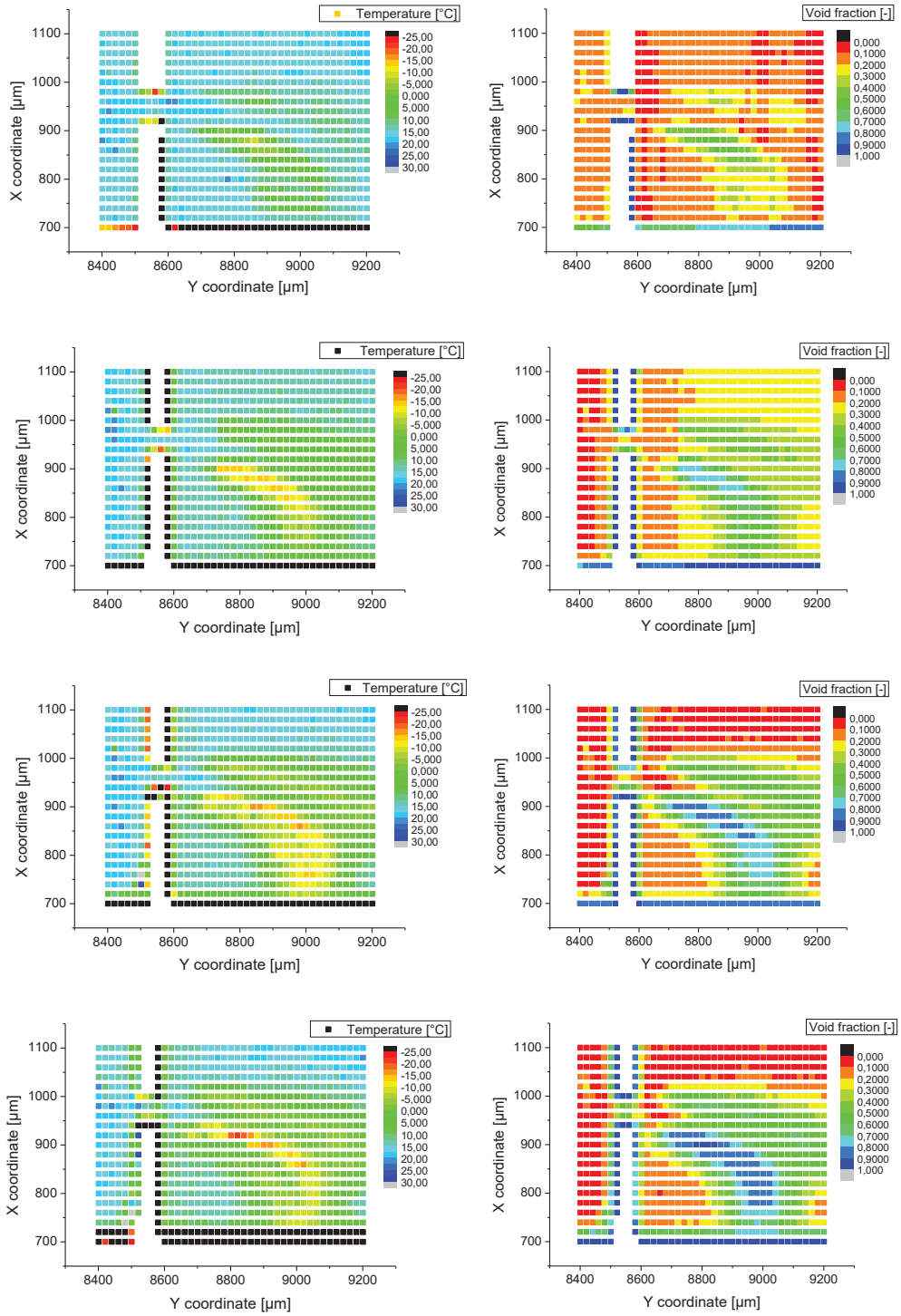

Figure S.2 - MD L6 temperature (left) and void fraction (right) mapping at 20, 50, 70 and 90µm from glass (order from top to bottom). Flow is from left to right at 10 bar driving pressure.

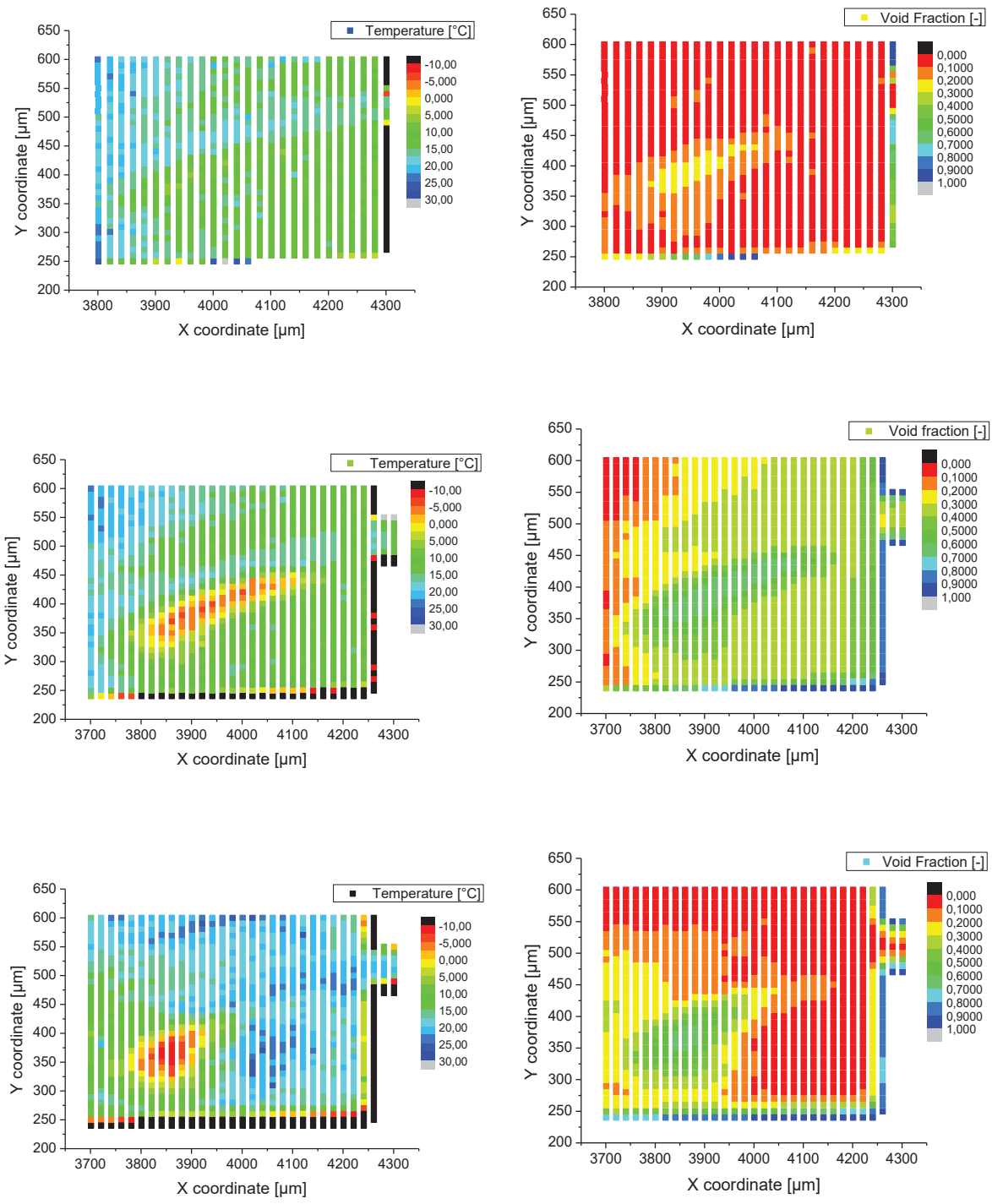

Figure S.3 - text MD 10 at 8 bar driving pressure. Analysis at different height; 20, 50 and 80 from glass (in descending order). Left plots are temperature and right are the void fraction maps. Flow is from right to left.

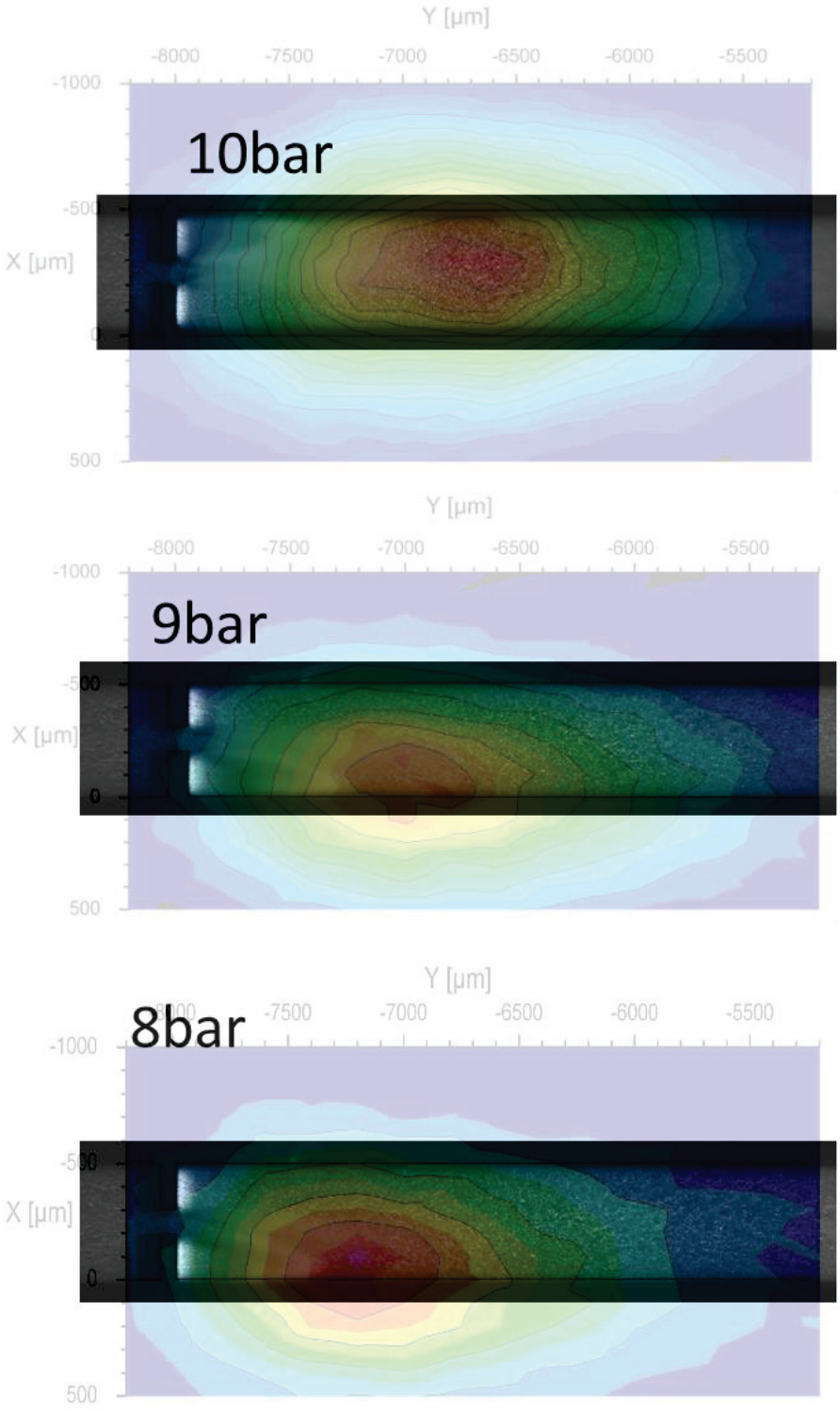

Figure S. 4 - long exposure time recordings of MD L4 overlapped with the CL intensity maps as a function of driving pressure 10-8bar.

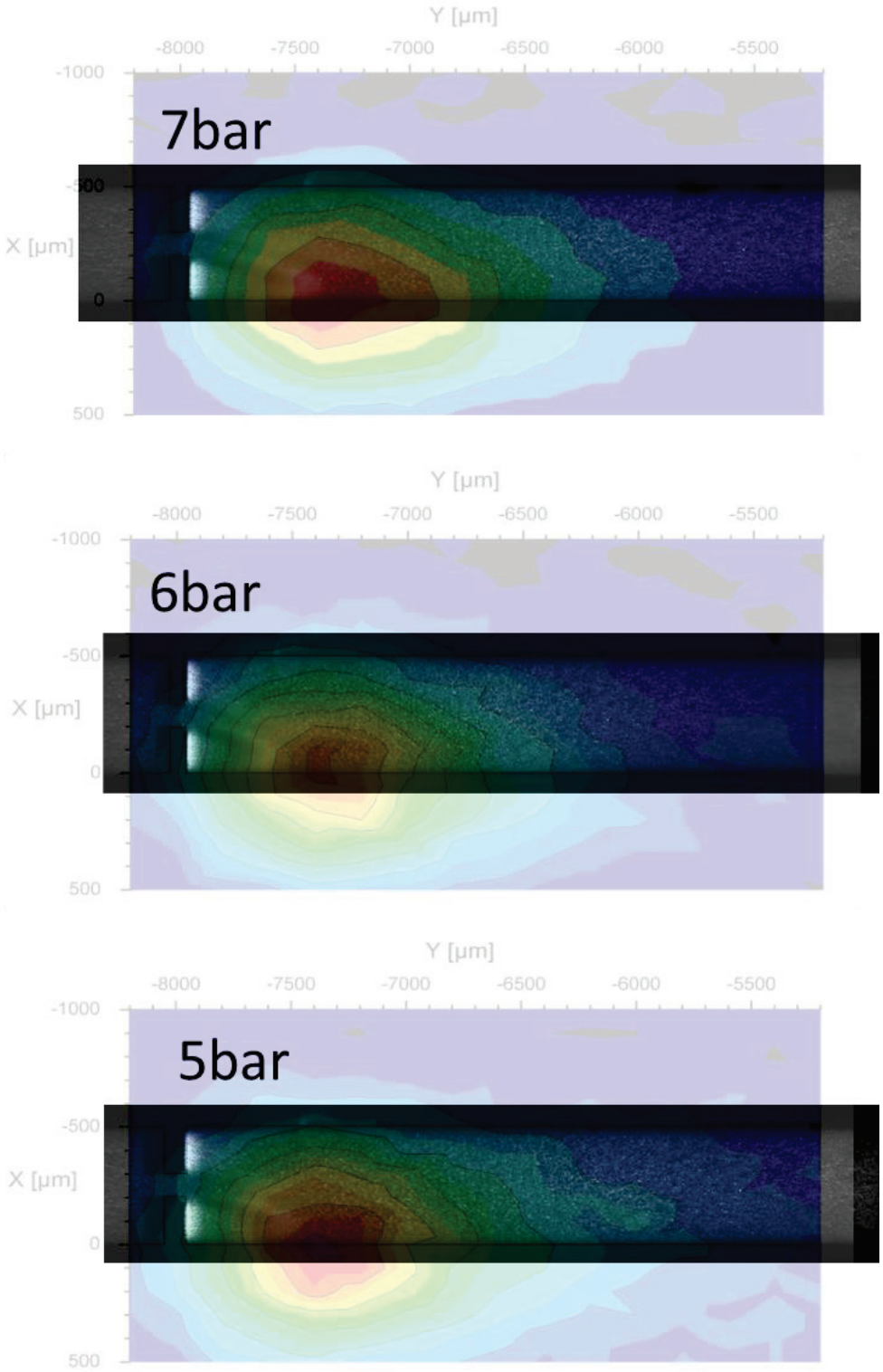

Figure S. 5 - long exposure time recordings of MD L4 overlapped with the CL intensity maps as a function of driving pressure 7-5bar.

9. Literature

[1] R. E. A. Arndt, “Cavitation in Fluid Machinery and Hydraulic Structures,” *Annu. Rev. Fluid Mech.*, vol. 13, no. 1, pp. 273–326, 1981.

[2] F. R. Young, *Cavitation*. Imperial College Press, 1999.

[3] M. Dular and M. Petkovšek, “New insights into the Mechanisms of Cavitation Erosion,” *J. Phys. Conf. Ser.*, vol. 656, no. 1, p. 012046, 2015.

[4] M. Hugens, “An Extract of a Letter of M. Hugens to the Author of the Journal des Scavans of July 25. 1672. Attempting to Render the Cause of That Odd Phaenomenon of the QuickSilvers Remaining Suspended Far above the Usual Height in the Torricellian Experiments,” *Philos. Trans. 1665-1678*, vol. 7, pp. 5027–5030, 1672.

[5] Sir Isaac Newton, *Optics*. .

[6] J. I. Thornycroft and S. W. Barnaby, “Torpedo-boat destroyers. (including appendix and plate at back of volume).,” *Minutes Proc. Inst. Civ. Eng.*, vol. 122, no. 1895, pp. 51–69, Jan. 1895.

[7] C. E. Brennen, *Cavitation and Bubble Dynamics*. New York: Oxford University Press, 1995.

[8] K. Yasui, “Acoustic Cavitation,” in *Acoustic Cavitation and Bubble Dynamics*, Springer, Cham, 2018, pp. 1–35.

[9] X. Luo, B. Ji, and Y. Tsujimoto, “A review of cavitation in hydraulic machinery,” *J. Hydrodyn. Ser B*, vol. 28, no. 3, pp. 335–358, Jun. 2016.

[10] F. Grieser *et al.*, *Sonochemistry and the acoustic bubble*. Elsevier, 2015.

[11] B. Verhaagen and D. Fernández Rivas, “Measuring cavitation and its cleaning effect,” *Ultrason. Sonochem.*, vol. 29, pp. 619–628, Mar. 2016.

[12] L. A. Crum, “Resource Paper: Sonoluminescence,” *J. Acoust. Soc. Am.*, vol. 138, no. 4, pp. 2181–2205, Oct. 2015.

[13] S. I. Nikitenko and R. Pflieger, “Toward a new paradigm for sonochemistry: Short review on nonequilibrium plasma observations by means of MBSL spectroscopy in aqueous solutions,” *Ultrason. Sonochem.*, vol. 35, pp. 623–630, Mar. 2017.

[14] Z. Zhang, G. Wang, Y. Nie, and J. Ji, “Hydrodynamic cavitation as an efficient method for the formation of sub-100nm O/W emulsions with high stability,” *Chin. J. Chem. Eng.*, vol. 24, no. 10, pp. 1477–1480, Oct. 2016.

[15] B. Sajjadi, A. R. Abdul Aziz, and S. Ibrahim, “Mechanistic analysis of cavitation assisted transesterification on biodiesel characteristics,” *Ultrason. Sonochem.*, vol. 22, pp. 463–473, Jan. 2015.

[16] J. Kosel, I. Gutiérrez-Aguirre, N. Rački, T. Dreo, M. Ravnikar, and M. Dular, “Efficient inactivation of MS-2 virus in water by hydrodynamic cavitation,” *Water Res.*, vol. 124, no. Supplement C, pp. 465–471, Nov. 2017.

[17] A. Šarc, M. Oder, and M. Dular, “Can rapid pressure decrease induced by supercavitation efficiently eradicate Legionella pneumophila bacteria?,” *Desalination Water Treat.*, vol. 57, no. 5, pp. 2184–2194, Jan. 2016.

[18] M. Gągol, A. Przyjazny, and G. Boczkaj, “Wastewater treatment by means of advanced oxidation processes based on cavitation – A Review,” *Chem. Eng. J.*, vol. 338, Apr. 2018.

[19] M. Dular *et al.*, “Use of hydrodynamic cavitation in (waste)water treatment,” *Ultrason. Sonochem.*, vol. 29, pp. 577–588, Mar. 2016.

[20] E. P. Stride and C. C. Coussios, “Cavitation and contrast: the use of bubbles in ultrasound imaging and therapy,” *Proc. Inst. Mech. Eng. [H]*, vol. 224, no. 2, pp. 171–191, 2010.
[21] A. Vilagrosa, E. Chirino, J. J. Peguero-Pina, T. S. Barigah, H. Cochard, and E. Gil-Pelegrín, “Xylem Cavitation and Embolism in Plants Living in Water-Limited Ecosystems,” in *Plant Responses to Drought Stress*, Springer, Berlin, Heidelberg, 2012, pp. 63–109.
[22] S. N. Patek and R. L. Caldwell, “Extreme impact and cavitation forces of a biological hammer: strike forces of the peacock mantis shrimp Odontodactylus scyllarus,” *J. Exp. Biol.*, vol. 208, no. 19, pp. 3655–3664, Oct. 2005.
[23] G. Iosilevskii and D. Weihs, “Speed limits on swimming of fishes and cetaceans,” *J. R. Soc. Interface*, vol. 5, no. 20, pp. 329–338, Mar. 2008.
[24] P. R. Gogate, “Hydrodynamic Cavitation for Food and Water Processing,” *Food Bioprocess Technol.*, vol. 4, no. 6, pp. 996–1011, Aug. 2011.
[25] R. Ciriminna *et al.*, “Beer produced via hydrodynamic cavitation retains higher amounts of xanthohumol and other hops prenylflavonoids,” *LWT*, vol. 91, pp. 160–167, May 2018.
[26] G. Kuiper, “Cavitation Research and Ship Propeller Design,” *Appl. Sci. Res.*, vol. 58, no. 1–4, pp. 33–50, Mar. 1997.
[27] E. Alyanak, R. Grandhi, and R. Penmetsa, “Optimum design of a supercavitating torpedo considering overall size, shape, and structural configuration,” *Int. J. Solids Struct.*, vol. 43, no. 3, pp. 642–657, Feb. 2006.
[28] J. Yang, L. J. Zhou, Z. W. Wang, and F. L. Zhi, “The effect of cavitation on the hydrofoil dynamic characteristics,” *IOP Conf. Ser. Mater. Sci. Eng.*, vol. 52, no. 6, p. 062018, 2013.
[29] P. A. Carling, M. Perillo, J. Best, and M. H. Garcia, “The bubble bursts for cavitation in natural rivers: laboratory experiments reveal minor role in bedrock erosion,” *Earth Surf. Process. Landf.*, vol. 42, no. 9, pp. 1308–1316, Jan. 2017.
[30] K. S. Suslick, N. C. Eddingsaas, D. J. Flannigan, S. D. Hopkins, and H. Xu, “Extreme conditions during multibubble cavitation: Sonoluminescence as a spectroscopic probe,” *Ultrason. Sonochem.*, vol. 18, no. 4, pp. 842–846, Jul. 2011.
[31] D. J. Flannigan, S. D. Hopkins, C. G. Camara, S. J. Putterman, and K. S. Suslick, “Measurement of Pressure and Density Inside a Single Sonoluminescing Bubble,” *Phys. Rev. Lett.*, vol. 96, no. 20, p. 204301, May 2006.
[32] R. P. Taleyarkhan, C. D. West, J. S. Cho, R. T. Lahey, R. I. Nigmatulin, and R. C. Block, “Evidence for Nuclear Emissions During Acoustic Cavitation,” *Science*, vol. 295, no. 5561, pp. 1868–1873, Mar. 2002.
[33] C. G. Camara, S. D. Hopkins, K. S. Suslick, and S. J. Putterman, “Upper Bound for Neutron Emission from Sonoluminescing Bubbles in Deuterated Acetone,” *Phys. Rev. Lett.*, vol. 98, no. 6, p. 064301, Feb. 2007.
[34] B. Naranjo, “Comment on ‘Nuclear Emissions During Self-Nucleated Acoustic Cavitation,’” *Phys. Rev. Lett.*, vol. 97, no. 14, Oct. 2006.
[35] J. P. Padilla-Martinez, C. Berrospe-Rodriguez, G. Aguilar, J. C. Ramirez-San-Juan, and R. Ramos-Garcia, “Optic cavitation with CW lasers: A review,” *Phys. Fluids*, vol. 26, no. 12, p. 122007, Dec. 2014.
[36] M. Futakawa, T. Naoe, H. Kogawa, K. Haga, and K. Okita, “Cavitation erosion induced by proton beam bombarding mercury target for high-power spallation neutron sources,” *Exp. Therm. Fluid Sci.*, vol. 57, pp. 365–370, Sep. 2014.
[37] E. Herbert, S. Balibar, and F. Caupin, “Cavitation pressure in water,” *Phys. Rev. E Stat. Nonlin. Soft Matter Phys.*, vol. 74, no. 4 Pt 1, p. 041603, Oct. 2006.

[38] Q. Zheng, D. J. Durben, G. H. Wolf, and C. A. Angell, “Liquids at large negative pressures: water at the homogeneous nucleation limit,” *Science*, vol. 254, no. 5033, pp. 829–832, Nov. 1991.
[39] G. Pallares, M. A. Gonzalez, J. L. F. Abascal, C. Valeriani, and F. Caupin, “Equation of state for water and its line of density maxima down to −120 MPa,” *Phys. Chem. Chem. Phys.*, vol. 18, no. 8, pp. 5896–5900, Feb. 2016.
[40] F. Caupin, “Liquid-vapor interface, cavitation, and the phase diagram of water,” *Phys. Rev. E*, vol. 71, no. 5, p. 051605, May 2005.
[41] V. Holten *et al.*, “Compressibility Anomalies in Stretched Water and Their Interplay with Density Anomalies,” *J. Phys. Chem. Lett.*, vol. 8, no. 22, pp. 5519–5522, Nov. 2017.
[42] F. Caupin, “Escaping the no man’s land: Recent experiments on metastable liquid water,” *J. Non-Cryst. Solids*, vol. 407, pp. 441–448, Jan. 2015.
[43] G. Pallares *et al.*, “Anomalies in bulk supercooled water at negative pressure,” *Proc. Natl. Acad. Sci.*, vol. 111, no. 22, pp. 7936–7941, Jun. 2014.
[44] N. Bruot and F. Caupin, “Curvature-dependence of the liquid-vapor surface tension beyond the Tolman approximation,” *Phys. Rev. Lett.*, vol. 116, no. 5, Feb. 2016.
[45] M. E. M. Azouzi, C. Ramboz, J.-F. Lenain, and F. Caupin, “A coherent picture of water at extreme negative pressure,” *Nat. Phys.*, vol. 9, no. 1, pp. 38–41, Jan. 2013.
[46] K. A. Mørch, “Reflections on cavitation nuclei in water,” *Phys. Fluids*, vol. 19, no. 7, p. 072104, 2007.
[47] K. A. Mørch, “Cavitation Nuclei: Experiments and Theory,” *J. Hydrodyn. Ser B*, vol. 21, no. 2, pp. 176–189, Apr. 2009.
[48] K. A. Mørch, “Cavitation inception from bubble nuclei,” *Interface Focus*, vol. 5, no. 5, Oct. 2015.
[49] F. E. Fox and K. F. Herzfeld, “Gas Bubbles with Organic Skin as Cavitation Nuclei,” *J. Acoust. Soc. Am.*, vol. 26, no. 6, pp. 984–989, Nov. 1954.
[50] A. A. Atchley and A. Prosperetti, “The crevice model of bubble nucleation,” *J. Acoust. Soc. Am.*, vol. 86, no. 3, pp. 1065–1084, Sep. 1989.
[51] A. R. Klotz, “Bubble dynamics in N dimensions,” *Phys. Fluids*, vol. 25, no. 8, p. 082109, Aug. 2013.
[52] William Henry Besant, *A treatise on hydrostatics and hydrodynamics*. Deighton, Bell, 1859.
[53] “An introduction to fluid dynamics. G. K. Batchelor, F.R.S., London (Cambridge University Press), 1967. Pp. xvii, 615; Plates 24; Numerous Figures. 75s. in U.K., $13.50 in U.S.A,” *Q. J. R. Meteorol. Soc.*, vol. 94, no. 401, pp. 435–435.
[54] L. R. O. M. F.R.S, “VIII. On the pressure developed in a liquid during the collapse of a spherical cavity,” *Lond. Edinb. Dublin Philos. Mag. J. Sci.*, vol. 34, no. 200, pp. 94–98, Aug. 1917.
[55] H. Poritsky, *Proceedings of the first U.S. National Congress of Applied Mechanics: held at Illinois Institute of Technology, Chicago, Illinois, June 11-16, 1951.* New York: American Society of Mechanical Engineers, 1952.
[56] E. A. Neppiras and B. E. Noltingk, “Cavitation Produced by Ultrasonics: Theoretical Conditions for the Onset of Cavitation,” *Proc. Phys. Soc. Sect. B*, vol. 64, no. 12, p. 1032, 1951.
[57] B. E. Noltingk and E. A. Neppiras, “Cavitation produced by Ultrasonics,” *Proc. Phys. Soc. Sect. B*, vol. 63, no. 9, p. 674, 1950.
[58] J.-P. Franc and J.-M. Michel, *Fundamentals of cavitation*. Kluwer Publ, 2004.

[59] T. G. Leighton, "The Rayleigh–Plesset equation in terms of volume with explicit shear losses," *Ultrasonics*, vol. 48, no. 2, pp. 85–90, Apr. 2008.
[60] J. Lam, J. Lombard, C. Dujardin, G. Ledoux, S. Merabia, and D. Amans, "Dynamical study of bubble expansion following laser ablation in liquids," *Appl. Phys. Lett.*, vol. 108, no. 7, p. 074104, Feb. 2016.
[61] V. H. Man, M. S. Li, P. Derreumaux, and P. H. Nguyen, "Rayleigh-Plesset equation of the bubble stable cavitation in water: A nonequilibrium all-atom molecular dynamics simulation study," *J. Chem. Phys.*, vol. 148, no. 9, p. 094505, Mar. 2018.
[62] E. A. F. Hutli and M. S. Nedeljkovic, "Frequency in Shedding/Discharging Cavitation Clouds Determined by Visualization of a Submerged Cavitating Jet," *J. Fluids Eng.*, vol. 130, no. 2, pp. 021304-021304–8, Jan. 2008.
[63] M. Farhat, A. Chakravarty, and J. E. Field, "Luminescence from hydrodynamic cavitation," *Proc. R. Soc. Math. Phys. Eng. Sci.*, vol. 467, no. 2126, p. 591, Feb. 2011.
[64] S. Arrojo, C. Nerín, and Y. Benito, "Application of salicylic acid dosimetry to evaluate hydrodynamic cavitation as an advanced oxidation process," *Ultrason. Sonochem.*, vol. 14, no. 3, pp. 343–349, Mar. 2007.
[65] Y. T. Didenko, W. B. McNamara Iii, and K. S. Suslick, "Molecular emission from single-bubble sonoluminescence," *Nature*, vol. 407, no. 6806, pp. 877–879, Oct. 2000.
[66] D. Lohse, M. P. Brenner, T. F. Dupont, S. Hilgenfeldt, and B. Johnston, "Sonoluminescing Air Bubbles Rectify Argon," *Phys. Rev. Lett.*, vol. 78, no. 7, pp. 1359–1362, Feb. 1997.
[67] B. D. Storey and A. J. Szeri, "Argon Rectification and the Cause of Light Emission in Single-Bubble Sonoluminescence," *Phys. Rev. Lett.*, vol. 88, no. 7, p. 074301, Jan. 2002.
[68] D. J. Flannigan and K. S. Suslick, "Inertially confined plasma in an imploding bubble," *Nat. Phys.*, vol. 6, no. 8, pp. 598–601, Aug. 2010.
[69] F. R. Young, *Sonoluminescence*. Taylor & Francis, 2004.
[70] A. Bass, S. J. Ruuth, C. Camara, B. Merriman, and S. Putterman, "Molecular dynamics of extreme mass segregation in a rapidly collapsing bubble," *Phys. Rev. Lett.*, vol. 101, no. 23, p. 234301, Dec. 2008.
[71] K. S. Suslick and D. J. Flannigan, "Inside a Collapsing Bubble: Sonoluminescence and the Conditions During Cavitation," *Annu. Rev. Phys. Chem.*, vol. 59, no. 1, pp. 659–683, 2008.
[72] Y. T. Didenko, W. B. McNamara, and K. S. Suslick, "Hot Spot Conditions during Cavitation in Water," *J. Am. Chem. Soc.*, vol. 121, no. 24, pp. 5817–5818, Jun. 1999.
[73] R. J. Wood, J. Lee, and M. J. Bussemaker, "A parametric review of sonochemistry: Control and augmentation of sonochemical activity in aqueous solutions," *Ultrason. Sonochem.*, vol. 38, pp. 351–370, Sep. 2017.
[74] K. S. Suslick, M. M. Mdleleni, and J. T. Ries, "Chemistry Induced by Hydrodynamic Cavitation," *J. Am. Chem. Soc.*, vol. 119, no. 39, pp. 9303–9304, Oct. 1997.
[75] R. E. Apfel, "7. Acoustic Cavitation," in *Methods in Experimental Physics*, vol. 19, P. D. Edmonds, Ed. Academic Press, 1981, pp. 355–411.
[76] J. Rooze, E. V. Rebrov, J. C. Schouten, and J. T. F. Keurentjes, "Dissolved gas and ultrasonic cavitation – A review," *Ultrason. Sonochem.*, vol. 20, no. 1, pp. 1–11, Jan. 2013.
[77] S. Hiramatsu and Y. Watanabe, "On the mechanism of relaxation oscillation in sonoluminescence," *Electron. Commun. Jpn. Part III Fundam. Electron. Sci.*, vol. 82, no. 2, pp. 58–65, Jan. 1999.

[78] B. Gielen, S. Marchal, J. Jordens, L. C. J. Thomassen, L. Braeken, and T. Van Gerven, "Influence of dissolved gases on sonochemistry and sonoluminescence in a flow reactor," *Ultrason. Sonochem.*, vol. 31, no. Supplement C, pp. 463–472, Jul. 2016.
[79] C. Mishra and Y. Peles, "Cavitation in flow through a micro-orifice inside a silicon microchannel," *Phys. Fluids*, vol. 17, no. 1, p. 013601, Dec. 2004.
[80] Y. Peles, "Cavitation in Microdomains," in *Encyclopedia of Microfluidics and Nanofluidics*, D. L. Prof, Ed. Springer US, 2008, pp. 197–201.
[81] J. Judy, D. Maynes, and B. W. Webb, "Characterization of frictional pressure drop for liquid flows through microchannels," *Int. J. Heat Mass Transf.*, vol. 45, no. 17, pp. 3477–3489, Aug. 2002.
[82] R. Baviere, F. Ayela, S. Le Person, and M. Favre-Marinet, "Experimental characterization of water flow through smooth rectangular microchannels," *Phys. Fluids*, vol. 17, no. 9, p. 098105, Sep. 2005.
[83] Y. Peles and B. Schneider, "Hydrodynamic Cavitation and Boiling in Refrigerant (R-123) Flow Inside Microchannels," pp. 1323–1332, Jan. 2006.
[84] G. S. Cole, R. P. Scaringe, R. P. Roth, and Y. Peles, "System Evaluation of Cavitation Enhanced Heat Transfer in Microchannels," SAE International, Warrendale, PA, SAE Technical Paper 2006-01–3062, Nov. 2006.
[85] C. Mishra and Y. Peles, "Flow visualization of cavitating flows through a rectangular slot micro-orifice ingrained in a microchannel," *Phys. Fluids*, vol. 17, no. 11, p. 113602, Nov. 2005.
[86] C. Mishra and Y. Peles, "An experimental investigation of hydrodynamic cavitation in micro-Venturis," *Phys. Fluids*, vol. 18, no. 10, p. 103603, Oct. 2006.
[87] C. Mishra and Y. Peles, "Development of Cavitation in Refrigerant (R-123) Flow Inside Rudimentary Microfluidic Systems," *J. Microelectromechanical Syst.*, vol. 15, no. 5, pp. 1319–1329, Oct. 2006.
[88] C. Mishra and Y. Peles, "Flow visualization of cavitating flows through a rectangular slot micro-orifice ingrained in a microchannel," *Phys. Fluids*, vol. 17, no. 11, p. 113602, Nov. 2005.
[89] C. Mishra and Y. Peles, "Size scale effects on cavitating flows through microorifices entrenched in rectangular microchannels," *J. Microelectromechanical Syst.*, vol. 14, no. 5, pp. 987–999, Oct. 2005.
[90] C. Mishra and Y. Peles, "Cavitation in flow through a micro-orifice inside a silicon microchannel," *Phys. Fluids*, vol. 17, no. 1, p. 013601, Dec. 2004.
[91] A. Nayebzadeh, Y. Wang, H. Tabkhi, J.-H. Shin, and Y. Peles, "Cavitation behind a circular micro pillar," *Int. J. Multiph. Flow*, vol. 98, pp. 67–78, Jan. 2018.
[92] R. Singh and Y. Peles, "The effects of fluid properties on cavitation in a micro domain," *J. Micromechanics Microengineering*, vol. 19, no. 2, p. 025009, 2009.
[93] M. Medrano, P. J. Zermatten, C. Pellone, J. P. Franc, and F. Ayela, "Hydrodynamic cavitation in microsystems. I. Experiments with deionized water and nanofluids," *Phys. Fluids*, vol. 23, no. 12, p. 127103, Dec. 2011.
[94] F. Ayela *et al.*, "Experimental evidence of temperature gradients in cavitating microflows seeded with thermosensitive nanoprobes," *Phys. Rev. E Stat. Nonlin. Soft Matter Phys.*, vol. 88, no. 4, p. 043016, Oct. 2013.

[95] F. Ayela *et al.*, "Hydrodynamic Cavitation through 'Labs on a Chip': From Fundamentals to Applications," *Oil Gas Sci. Technol. – Rev. D'IFP Energ. Nouv.*, vol. 72, no. 4, p. 19, Jul. 2017.
[96] M. Medrano, C. Pellone, P. J. Zermatten, and F. Ayela, "Hydrodynamic cavitation in microsystems. II. Simulations and optical observations," *Phys. Fluids*, vol. 24, no. 4, p. 047101, Apr. 2012.
[97] S. Mossaz, D. Colombet, and F. Ayela, "Hydrodynamic cavitation of binary liquid mixtures in laminar and turbulent flow regimes," *Exp. Therm. Fluid Sci.*, vol. 80, no. Supplement C, pp. 337–347, Jan. 2017.
[98] D. Podbevsek, D. Colombet, G. Ledoux, and F. Ayela, "Observation of chemiluminescence induced by hydrodynamic cavitation in microchannels.," *Ultrason. Sonochem.*
[99] X. Qiu, W. Cherief, D. Colombet, and F. Ayela, "A simple process to achieve microchannels geometries able to produce hydrodynamic cavitation," *J. Micromechanics Microengineering*, vol. 27, no. 4, p. 047001, 2017.
[100] M. Ghorbani, A. Mohammadi, A. R. Motezakker, L. G. Villanueva, Y. Leblebici, and A. Koşar, "Energy Harvesting in Microscale with Cavitating Flows," *ACS Omega*, vol. 2, no. 10, pp. 6870–6877, Oct. 2017.
[101] M. Ghorbani, A. K. Sadaghiani, L. G. Villanueva, and A. Koşar, "Hydrodynamic cavitation in microfluidic devices with roughened surfaces," *J. Micromechanics Microengineering*, vol. 28, no. 7, p. 075016, 2018.
[102] M. Ghorbani *et al.*, "Biomedical device prototype based on small scale hydrodynamic cavitation," *AIP Adv.*, vol. 8, no. 3, p. 035108, Mar. 2018.
[103] J. Rooze *et al.*, "Hydrodynamic cavitation in micro channels with channel sizes of 100 and 750 micrometers," *Microfluid. Nanofluidics*, vol. 12, no. 1–4, pp. 499–508, Jan. 2012.
[104] T. Gothsch *et al.*, "High-pressure microfluidic systems (HPMS): flow and cavitation measurements in supported silicon microsystems," *Microfluid. Nanofluidics*, vol. 18, no. 1, pp. 121–130, Jan. 2015.
[105] J. Kim *et al.*, "Monitoring the orientation of rare-earth-doped nanorods for flow shear tomography," *Nat. Nanotechnol.*, vol. 12, no. 9, pp. 914–919, Sep. 2017.
[106] T. Stieger, H. Agha, M. Schoen, M. G. Mazza, and A. Sengupta, "Hydrodynamic cavitation in Stokes flow of anisotropic fluids," *Nat. Commun.*, vol. 8, p. 15550, May 2017.
[107] S. Prakash and S. Kumar, "Fabrication of microchannels: A review , Fabrication of microchannels: A review," *Proc. Inst. Mech. Eng. Part B J. Eng. Manuf.*, vol. 229, no. 8, pp. 1273–1288, Aug. 2015.
[108] F. Laermer and A. Schilp, "Method of anisotropically etching silicon," US5501893A, 26-Mar-1996.
[109] S. Arrojo and Y. Benito, "A theoretical study of hydrodynamic cavitation," *Ultrason. Sonochem.*, vol. 15, no. 3, pp. 203–211, Mar. 2008.
[110] G. G. Stokes, "On the Effect of the Internal Friction of Fluids on the Motion of Pendulums," *Trans. Camb. Philos. Soc.*, vol. 9, p. 8, 1851.
[111] C.-Y. Lee, C.-L. Chang, Y.-N. Wang, and L.-M. Fu, "Microfluidic Mixing: A Review," *Int. J. Mol. Sci.*, vol. 12, no. 5, pp. 3263–3287, May 2011.
[112] "Glossary of terms used in photochemistry, 3rd edition (IUPAC Recommendations 2006) : Pure and Applied Chemistry." [Online]. Available: https://www.degruyter.com/view/j/pac.2007.79.issue-3/pac200779030293/pac200779030293.xml. [Accessed: 25-Jun-2018].

[113] E. Wiedemann, “Ueber Fluorescenz und Phosphorescenz I. Abhandlung,” *Ann. Phys.*, vol. 270, no. 7, pp. 446–463.
[114] N. H. Bings, A. Bogaerts, and J. A. C. Broekaert, “Atomic Spectroscopy: A Review,” *Anal. Chem.*, vol. 82, no. 12, pp. 4653–4681, Jun. 2010.
[115] G. Peach and F. Schuller, “The Pressure Broadening and Shift of Spectral Lines Produced in an Intense Monochromatic Radiation Field,” *AIP Conf. Proc.*, vol. 874, no. 1, pp. 178–178, Nov. 2006.
[116] G. Peach, “Unified theories of the pressure broadening and shift of spectral lines. I. General formulation for multipole interactions,” *J. Phys. B At. Mol. Phys.*, vol. 17, no. 13, p. 2599, 1984.
[117] G. Ashkenazi and R. Kosloff, “The Uncertainty Principle and Covalent Bonding.,” *Chem. Educ.*, vol. 11, pp. 67–76, Jan. 2006.
[118] P. D. B. Valeur and P. M. N. Berberan-Santos, *Molecular Fluorescence: Principles and Applications, Second Edition*, vol. 2012. .
[119] J. R. Lakowicz, *Principles of Fluorescence Spectroscopy*, 3rd ed. Springer US, 2006.
[120] G. Arnaoutakis and D. Näther, *Quenching of Fluorescence with Temperature*. 2016.
[121] X. Wang, O. S. Wolfbeis, and R. J. Meier, “Luminescent probes and sensors for temperature,” *Chem. Soc. Rev.*, vol. 42, no. 19, pp. 7834–7869, Sep. 2013.
[122] M. Dramicanin, *Luminescence Thermometry: Methods, Materials, and Applications*. 2018.
[123] E. Homeyer, S. Pailhès, R. Debord, V. Jary, C. Dujardin, and G. Ledoux, “Diamond contact-less micrometric temperature sensors,” *Appl. Phys. Lett.*, vol. 106, no. 24, p. 243502, Jun. 2015.
[124] Y. Egami *et al.*, “Development of fast response bi-luminophore pressure-sensitive paint by means of an inkjet printing technique,” *Meas. Sci. Technol.*, vol. 26, no. 6, p. 064004, 2015.
[125] N. Banerjee, Y. Xie, S. Chalaseni, and C. H. Mastrangelo, “Particle-based optical pressure sensors for 3D pressure mapping,” *Biomed. Microdevices*, vol. 17, no. 5, p. 97, Oct. 2015.
[126] N. Banerjee and C. H. Mastrangelo, “Microballoon Pressure Sensors for Particle Imaging Manometry in Liquid and Gaseous Mediums,” *Analyst*, vol. 141, Jan. 2016.
[127] N. Banerjee, Y. Xie, S. S. Pandey, and C. H. Mastrangelo, “Pressure sensing in microfluidic environments with low-leakage microballoons,” in *18th International Conference on Miniaturized Systems for Chemistry and Life Sciences, MicroTAS 2014*, 2014, pp. 114–116.
[128] H. Yamaoka *et al.*, “Ruby pressure scale in a low-temperature diamond anvil cell,” *J. Appl. Phys.*, vol. 112, no. 12, p. 124503, Dec. 2012.
[129] R. A. Forman, G. J. Piermarini, J. D. Barnett, and S. Block, “Pressure measurement made by the utilization of ruby sharp-line luminescence,” *Science*, vol. 176, no. 4032, pp. 284–285, Apr. 1972.
[130] C. Lavenn *et al.*, “Highly luminescent Au(I)-Thiolate coordination polymers,” Jul. 2014.
[131] C. Lavenn *et al.*, “Shedding light on an ultra-bright photoluminescent lamellar gold thiolate coordination polymer [Au(p-SPhCO2Me)]n,” *Chem. Commun.*, vol. 52, no. 58, pp. 9063–9066, Jul. 2016.
[132] F. Baril-Robert, M. A. Radtke, and C. Reber, “Pressure-Dependent Luminescence Properties of Gold(I) and Silver(I) Dithiocarbamate Compounds,” *J. Phys. Chem. C*, vol. 116, no. 3, pp. 2192–2197, Jan. 2012.
[133] O. Veselska and A. Demessence, “d10 coinage metal organic chalcogenolates: From oligomers to coordination polymers,” *Coord. Chem. Rev.*, Oct. 2017.

[134] V. W.-W. Yam, V. K.-M. Au, and S. Y.-L. Leung, "Light-Emitting Self-Assembled Materials Based on d8 and d10 Transition Metal Complexes," *Chem. Rev.*, vol. 115, no. 15, pp. 7589–7728, Aug. 2015.
[135] O. Veselska *et al.*, "Intrinsic Dual-Emitting Gold Thiolate Coordination Polymer, [Au(+I)(p-SPhCO 2 H)] n , for Ratiometric Temperature Sensing," *J Mater Chem C*, vol. 5, Sep. 2017.
[136] J. Gao, X. Huang, H. Liu, F. Zan, and J. Ren, "Colloidal Stability of Gold Nanoparticles Modified with Thiol Compounds: Bioconjugation and Application in Cancer Cell Imaging," *Langmuir*, vol. 28, no. 9, pp. 4464–4471, Mar. 2012.
[137] D. H. Brown and W. E. Smith, "The chemistry of the gold drugs used in the treatment of rheumatoid arthritis," *Chem. Soc. Rev.*, vol. 9, no. 2, pp. 217–240, Jan. 1980.
[138] O. Veselska, D. Podbevsek, G. Ledoux, A. Fateeva, and A. Demessence, "Intrinsic Triple-Emitting 2D Copper Thiolate Coordination Polymer as a Ratiometric Thermometer Working over 400 K Range," *Chem Commun*, Oct. 2017.
[139] O. Veselska, A. Demessence, N. Guillou, G. Ledoux, D. Podbevsek, and A. FATEEVA, "Structural and photophysical studies of lamellar M(I)-thiophenolate coordination polymers (M = Au, Ag, Cu)," in *GECOM CONCOORD 2017*, Forges-les Eaux , France, 2017.
[140] C. Lavenn *et al.*, "Shedding light on an ultra-bright photoluminescent lamellar gold thiolate coordination polymer [Au(SPhCO2Me)]n," *Chem Commun*, vol. 52, Feb. 2016.
[141] A. Demessence *et al.*, "Luminescence switching upon thermally-induced solid-state amorphous-to-crystalline phase transition in gold(I)-thiophenolate coordination polymer," 2015.
[142] O. Veselska *et al.*, "New Lamellar Silver Thiolate Coordination Polymers with Tunable Photoluminescence Energies by Metal Substitution," *Submitt. Inorg. Chem.*
[143] O. Veselska *et al.*, "Structural Diversity of Coordination Polymers Based on a Heterotopic Ligand: Cu(II)-Carboxylate vs Cu(I)-Thiolate," *Inorg. Chem.*, vol. 57, no. 5, pp. 2736–2743, Mar. 2018.
[144] S. Albahrani *et al.*, "Quantum dots to probe temperature and pressure in highly confined liquids," *RSC Adv.*, vol. 8, pp. 22897–22908, Jun. 2018.
[145] M. Martini *et al.*, "How Gold Particles Suppress Concentration Quenching of Fluorophores Encapsulated in Silica Beads," *J. Phys. Chem. C*, vol. 113, no. 41, pp. 17669–17677, Oct. 2009.
[146] E. Marín, "Characteristic dimensions for heat transfer," *Lat.-Am. J. Phys. Educ.*, vol. 4, Jan. 2010.
[147] S. Mossaz, D. Colombet, G. Ledoux, and F. Ayela, "Role of the thermal entrance length on the viscous heating in microchannels," *Microfluid. Nanofluidics*, vol. 19, no. 6, pp. 1325–1333, Dec. 2015.
[148] R. Sekita, A. Watanabe, K. Hirata, and T. Imoto, "Lessons learned from H-2 failure and enhancement of H-2A project," *Acta Astronaut.*, vol. 48, no. 5, pp. 431–438, Mar. 2001.
[149] J.-P. Franc, C. Rebattet, and A. Coulon, "An Experimental Investigation of Thermal Effects in a Cavitating Inducer," *J. Fluids Eng.*, vol. 126, no. 5, pp. 716–723, Dec. 2004.
[150] J. Hord, Lewis Research Center., and National Bureau of Standards., *Cavitation in liquid cryogens. IV, Combined correlations for venturi, hydrofoil, ogives, and pumps*. Washington, D.C. : Springfield, Va.: National Aeronautics and Space Administration ; For sale by the National Technical Information Service [distributor], 1974.

[151] S. Shi and G. Wang, “Numerical calculation of thermal effect on cavitation in cryogenic fluids,” *Chin. J. Mech. Eng.*, vol. 25, no. 6, pp. 1176–1183, Nov. 2012.
[152] M. Dular and O. Coutier-Delgosha, “Thermodynamic effects during growth and collapse of a single cavitation bubble,” *J. Fluid Mech.*, vol. 736, pp. 44–66, Dec. 2013.
[153] M. Petkovšek and M. Dular, “IR measurements of the thermodynamic effects in cavitating flow,” *Int. J. Heat Fluid Flow*, vol. 44, no. Supplement C, pp. 756–763, Dec. 2013.
[154] M. Petkovšek and M. Dular, “Observing the thermodynamic effects in cavitating flow by IR thermography,” *Exp. Therm. Fluid Sci.*, vol. 88, no. Supplement C, pp. 450–460, Nov. 2017.
[155] N. Rimbert, G. Castanet, and D. Funfschilling, “Measurement of thermal effects in a cavitating channel flow by 2cLIF,” presented at the ICMF 2013 International Conference on Multiphase Flow, 2013.
[156] A. Ewinger, G. Rinke, A. Urban, and S. Kerschbaum, “In situ measurement of the temperature of water in microchannels using laser Raman spectroscopy,” *Chem. Eng. J.*, vol. 223, pp. 129–134, May 2013.
[157] H. Fujimori, M. Kakihana, K. Ioku, S. Goto, and M. Yoshimura, “Advantage of anti-Stokes Raman scattering for high-temperature measurements,” *Appl. Phys. Lett.*, vol. 79, no. 7, pp. 937–939, Aug. 2001.
[158] E. A. Pozzi, A. B. Zrimsek, C. M. Lethiec, G. C. Schatz, M. C. Hersam, and R. P. Van Duyne, “Evaluating Single-Molecule Stokes and Anti-Stokes SERS for Nanoscale Thermometry,” *J. Phys. Chem. C*, vol. 119, no. 36, pp. 21116–21124, Sep. 2015.
[159] R. J. Hall, J. A. Shirley, and A. C. Eckbreth, “Coherent anti-Stokes Raman spectroscopy: spectra of water vapor in flames,” *Opt. Lett.*, vol. 4, no. 3, pp. 87–89, Mar. 1979.
[160] R. J. Hall and J. A. Shirley, “Coherent Anti-Stokes Raman Spectroscopy of Water Vapor for Combustion Diagnostics,” *Appl. Spectrosc.*, vol. 37, no. 2, pp. 196–202, Mar. 1983.
[161] K. Niiyama, Y. Yoshida, S. Hasegawa, M. Watanabe, and M. Oike, “Experimental Investigation of Thermodynamic Effect on Cavitation in Liquid Nitrogen,” 2012, pp. 153–157.
[162] H. N. McMurray and B. P. Wilson, “Mechanistic and Spatial Study of Ultrasonically Induced Luminol Chemiluminescence,” *J. Phys. Chem. A*, vol. 103, no. 20, pp. 3955–3962, May 1999.
[163] P. Braeutigam, M. Franke, Z.-L. Wu, and B. Ondruschka, “Role of Different Parameters in the Optimization of Hydrodynamic Cavitation,” *Chem. Eng. Technol.*, vol. 33, no. 6, pp. 932–940, Jun. 2010.
[164] K. Yasui, “Bubble Dynamics,” in *Acoustic Cavitation and Bubble Dynamics*, Springer, Cham, 2018, pp. 37–97.
[165] B. P. Barber and S. J. Putterman, “Observation of synchronous picosecond sonoluminescence,” *Nature*, vol. 352, no. 6333, pp. 318–320, Jul. 1991.
[166] K. S. Suslick, “Sonoluminescence and sonochemistry,” *Proc. IEEE Ultrason. Symp.*, vol. 1, pp. 523–532, 1997.
[167] Y. Shen, K. Yasui, Z. Sun, B. Mei, M. You, and T. Zhu, “Study on the spatial distribution of the liquid temperature near a cavitation bubble wall,” *Ultrason. Sonochem.*, vol. 29, pp. 394–400, Mar. 2016.
[168] D. G. Aseev and A. A. Batoeva, “Effect of hydrodynamic cavitation on the rate of OH-radical formation in the presence of hydrogen peroxide,” *Russ. J. Phys. Chem. A*, vol. 88, no. 1, pp. 28–31, Jan. 2014.

[169] K. Yasui, T. Tuziuti, and Y. Iida, "Optimum bubble temperature for the sonochemical production of oxidants," *Ultrasonics*, vol. 42, no. 1, pp. 579–584, Apr. 2004.
[170] K. Yasui, "Unsolved Problems," in *Acoustic Cavitation and Bubble Dynamics*, Springer, Cham, 2018, pp. 99–124.
[171] C. Dodeigne, L. Thunus, and R. Lejeune, "Chemiluminescence as diagnostic tool. A review," *Talanta*, vol. 51, no. 3, pp. 415–439, Mar. 2000.
[172] P. Khan *et al.*, "Luminol-Based Chemiluminescent Signals: Clinical and Non-clinical Application and Future Uses," *Appl. Biochem. Biotechnol.*, vol. 173, no. 2, pp. 333–355, May 2014.
[173] Radziszewski B. R., "Ueber einige phosphorescirende organische Körper," *Berichte Dtsch. Chem. Ges.*, vol. 10, no. 1, pp. 321–322, Jan. 2006.
[174] H. O. Albrecht, "Über die Chemiluminescenz des Aminophthalsäurehydrazids," *Z. Für Phys. Chem.*, vol. 136U, no. 1, pp. 321–330, 1928.
[175] T. A. Skripnikova, S. S. Lysova, Y. E. Zevatskii, L. V. Myznikov, S. V. Vorona, and T. V. Artamonova, "Physico-chemical properties of isomeric forms of luminol in aqueous solutions," *J. Mol. Struct.*, vol. 1154, pp. 59–63, Feb. 2018.
[176] R. Petre and G. Hubcă, "A performing synthesis strategy of luminol, a standard chemiluminescent substance," *UPB Sci. Bull. Ser. B Chem. Mater. Sci.*, vol. 75, pp. 23–34, Jan. 2013.
[177] G. Merenyi and J. S. Lind, "Role of a peroxide intermediate in the chemiluminescence of luminol. A mechanistic study," *J. Am. Chem. Soc.*, vol. 102, no. 18, pp. 5830–5835, Aug. 1980.
[178] G. Merényi, J. Lind, and T. E. Eriksen, "Luminol chemiluminescence: chemistry, excitation, emitter," *J. Biolumin. Chemilumin.*, vol. 5, no. 1, pp. 53–56, Mar. 1990.
[179] D. L. Pavia, G. M. Lampman, G. S. Kriz, and R. G. Engel, *Introduction to Organic Laboratory Techniques: A Small Scale Approach*. Cengage Learning, 2005.
[180] E. H. White and M. M. Bursey, "Chemiluminescence of LUminol and Related Hydrazides: The Light Emission Step," *J. Am. Chem. Soc.*, vol. 86, no. 5, pp. 941–942, Mar. 1964.
[181] S. Li *et al.*, "Enhanced chemiluminescence of the luminol-AgNO3 system by Ag nanoparticles," *Lumin. J. Biol. Chem. Lumin.*, vol. 27, no. 3, pp. 211–216, Jun. 2012.
[182] A. Karabchevsky, A. Mosayyebi, and A. V. Kavokin, "Tuning the chemiluminescence of a luminol flow using plasmonic nanoparticles," *Light Sci. Appl.*, vol. 5, no. 11, p. e16164, Nov. 2016.
[183] A. L. Lehninger, D. L. Nelson, M. M. Cox, and U. M. M. Cox, *Lehninger Principles of Biochemistry*. W. H. Freeman, 2005.
[184] H. Cao, M. Wan, Y. Qiao, S. Zhang, and R. Li, "Spatial distribution of sonoluminescence and sonochemiluminescence generated by cavitation bubbles in 1.2MHz focused ultrasound field," *Ultrason. Sonochem.*, vol. 19, no. 2, pp. 257–263, Mar. 2012.
[185] I. Akhatov *et al.*, "Dynamics of laser-induced cavitation bubbles," *Exp. Therm. Fluid Sci.*, vol. 26, no. 6, pp. 731–737, Aug. 2002.
[186] A. Chakravarty, T. Georghiou, T. E. Phillipson, and A. J. Walton, "Stable sonoluminescence within a water hammer tube," *Phys. Rev. E*, vol. 69, no. 6, p. 066317, Jun. 2004.
[187] C. Sun, E. Can, R. Dijkink, D. Lohse, and A. Prosperetti, "Growth and collapse of a vapour bubble in a microtube: the role of thermal effects," *J. Fluid Mech.*, vol. 632, pp. 5–16, Aug. 2009.

[188] A. Kapahi, C.-T. Hsiao, and G. L. Chahine, "Shock-Induced Bubble Collapse versus Rayleigh Collapse," *J. Phys. Conf. Ser.*, vol. 656, no. 1, p. 012128, 2015.
[189] J. J. Shah, M. Gaitan, and J. Geist, "Generalized Temperature Measurement Equations for Rhodamine B Dye Solution and Its Application to Microfluidics," *Anal. Chem.*, vol. 81, no. 19, pp. 8260–8263, Oct. 2009.
[190] X. Wang, J. Wang, P. Guo, W. Guo, and C. Wang, "Degradation of rhodamine B in aqueous solution by using swirling jet-induced cavitation combined with H2O2," *J. Hazard. Mater.*, vol. 169, no. 1, pp. 486–491, Sep. 2009.
[191] T. A. Dolenko, I. V. Churina, V. V. Fadeev, and S. M. Glushkov, "Valence band of liquid water Raman scattering: some peculiarities and applications in the diagnostics of water media," *J. Raman Spectrosc.*, vol. 31, no. 8–9, pp. 863–870, Aug. 2000.
[192] A. V. Kargovsky, "On temperature dependence of the valence band in the Raman spectrum of liquid water," *Laser Phys. Lett.*, vol. 3, no. 12, p. 567, Aug. 2006.
[193] W. B. Monosmith and G. E. Walrafen, "Temperature dependence of the Raman OH-stretching overtone from liquid water," *J. Chem. Phys.*, vol. 81, no. 2, pp. 669–674, Jul. 1984.
[194] C. Choe, J. Lademann, and M. E. Darvin, "Depth profiles of hydrogen bound water molecule types and their relation to lipid and protein interaction in the human stratum corneum in vivo," *Analyst*, vol. 141, no. 22, pp. 6329–6337, Oct. 2016.
[195] H. Xu, C.-M. Liu, Y. He, H.-W. Tang, and Q. Wu, "Study on the chemiluminescence resonance energy transfer between luminol and fluorescent dyes using a linear CCD spectrometer," *J. Lumin.*, vol. 130, no. 10, pp. 1872–1879, Oct. 2010.

Articles published in the scope of the thesis:

[94] F. Ayela *et al.*, "Hydrodynamic Cavitation through 'Labs on a Chip': From Fundamentals to Applications," *Oil Gas Sci. Technol. – Rev. D'IFP Energ. Nouv.*, vol. 72, no. 4, p. 19, Jul. 2017.
[134] O. Veselska *et al.*, "Intrinsic Dual-Emitting Gold Thiolate Coordination Polymer, [Au(+I)(p-SPhCO 2 H)] n , for Ratiometric Temperature Sensing," *J Mater Chem C*, vol. 5, Sep. 2017.
[137] O. Veselska, D. Podbevsek, G. Ledoux, A. Fateeva, and A. Demessence, "Intrinsic Triple-Emitting 2D Copper Thiolate Coordination Polymer as a Ratiometric Thermometer Working over 400 K Range," *Chem Commun*, Oct. 2017.
[138] O. Veselska, A. Demessence, N. Guillou, G. Ledoux, D. Podbevsek, and A. FATEEVA, "Structural and photophysical studies of lamellar M(I)-thiophenolate coordination polymers (M = Au, Ag, Cu)," in *GECOM CONCOORD 2017*, Forges-les Eaux , France, 2017.
[139] C. Lavenn *et al.*, "Shedding light on an ultra-bright photoluminescent lamellar gold thiolate coordination polymer [Au(SPhCO2Me)]n," *Chem Commun*, vol. 52, Feb. 2016.
[141] O. Veselska *et al.*, "New Lamellar Silver Thiolate Coordination Polymers with Tunable Photoluminescence Energies by Metal Substitution," *Submitt. Inorg. Chem.*
[195] D. Podbevsek, D. Colombet, G. Ledoux, and F. Ayela, "Observation of chemiluminescence induced by hydrodynamic cavitation in microchannels," *Ultrason. Sonochem.*, vol. 43, pp. 175–183, May 2018.

Abstract

Optical probing of thermodynamic parameters and radical production in cavitating micro-flows

Abstract: A constriction in the microchannel can be used to establish a two-phase flow, when a sufficient liquid flux is introduced. This is known as hydrodynamic cavitation. The latent heat resulting from the growing and collapsing vapor bubbles makes it interesting to observe the temperature conditions in the flow downstream of the constriction. Using fluorescence microscopy, with the addition of temperature sensitive nano probes into the working fluid, we can determine the temperature at a single point, averaged over the integration time. Coupled with a confocal microscope, we were able to produce two- and three-dimensional temperature maps of the steady state flow in the microchannel by the use of ratiometric intensity measurements. This technic allows us to observe temperature gradients in two-phase flow as well yielding the void fraction information. Areas of substantial cooling are observed downstream the constriction in the two-phase flow, linked to the bubble growth, while heating regions due to condensations are missing. A complementary, yet less sensitive probe-less technique using the inherent Raman scattering signal of the liquid, was used to confirm the findings. A separate study evaluating a new group of luminescent materials for optical temperature and pressure probes is performed and discussed herein. Finally, the luminol chemiluminescent reaction with radicals produced by the cavitating flow, is used to obtain a corresponding photon yield. By counting the photons produced, an estimate on the radical yield can be obtained. Additionally, rudimentary mapping of the chemiluminescence signal allows the localization of the bubble collapse regions.

Keywords: microchannel, hydrodynamic cavitation, optical thermometry, luminescent probes, temperature gradients, radical production, luminol

---

Mesure optique de paramètres thermodynamiques et production de radicaux dans des micro-écoulements cavitants

Resume: Une zone de constriction dans un micro-canal fluidique peut générer, si le débit est suffisant, un écoulement bi-phasique. Ceci est l'origine de la cavitation hydrodynamique. Les échanges de chaleur latente générés par l'apparition et l'implosion des bulles impliquent une variabilité importante de la température dans les zones au-delà de la constriction. En ajoutant des sondes de température nanométriques dans le fluide et en utilisant un microscope confocal on peut déterminer la température en un point. Ainsi on a pu établir des cartographies thermiques en 2 et 3 dimensions à l'intérieur d'un écoulement stationnaire bi-phasique. La technique permet en outre d'avoir accès à la quantité de gaz ce qui permet de corréler les gradients de température avec les zones de transitions de phases. Des zones de très forts refroidissements sont observées après la constriction, là où les bulles apparaissent. Par contre on n'observe pas les zones d'échauffement attendu à cause de la condensation. Une méthode complémentaire, moins sensible, utilisant la spectroscopie Raman a aussi été utilisée pour confirmer ce résultat. Par ailleurs une nouvelle classe de matériaux luminescents sensible à la température et la pression a été étudiée. Enfin une étude de la production de radicaux lors de l'implosion des bulles a été menée en utilisant la chimiluminescence du luminol. La technique utilisée par comptage de photons a permis de quantifier cette production et une cartographie de l'émission du luminol a permis d'associer celle-ci avec la zone d'implosion des bulles.

Mot cles: micro-canaux, cavitation hydrodynamique, thermométrie optique, sondes luminescentes, gradients de température, production de radicaux, luminol.